SYNCHRONOUS FOCAL PLANE DETECTION OF WEAKLY MODULATED IMAGES WITH THE INTERLINE TRANSFER CCD

by

Chad William Fisher

ProQuest Number: 10796871

All rights reserved

INFORMATION TO ALL USERS
The quality of this reproduction is dependent upon the quality of the copy submitted.

In the unlikely event that the author did not send a complete manuscript
and there are missing pages, these will be noted. Also, if material had to be removed,
a note will indicate the deletion.

ProQuest 10796871

Published by ProQuest LLC (2019). Copyright of the Dissertation is held by the Author.

All rights reserved.
This work is protected against unauthorized copying under Title 17, United States Code
Microform Edition © ProQuest LLC.

ProQuest LLC.
789 East Eisenhower Parkway
P.O. Box 1346
Ann Arbor, MI 48106 – 1346

A thesis submitted to the Faculty and the Board of Trustees of the Colorado School of Mines in partial fulfillment of the requirements for the degree of Doctor of Philosophy (Engineering Systems).

Golden, Colorado

Date 11/13/2000

Signed: _____

Chad W. Fisher

Approved: _____

Dr. Nigel T. Middleton
Associate Professor of Engineering
Thesis Advisor

Approved: _____

Dr. Mark A. Linne
Professor of Engineering
Thesis Co-Advisor

Golden, Colorado

Date 11/13/2000

_____

Dr. Joan Gosink
Department Head
Engineering Division

ABSTRACT

An imaging system that extracts a weakly modulated image from a large constant background irradiance and from noise is developed and mathematically analyzed. Focal plane processing functions that synchronously manipulate charge are incorporated into the interline transfer CCD. The focal plane processing improves the imaging system's signal-to-noise ratio through synchronous integration.

An integration threshold feature, specifically implemented in the interline transfer CCD architecture, is also investigated. This feature creates a dead-band threshold, which accumulated charge must surpass prior to integration. The mechanism is designed to reduce the integrated amount of constant background irradiance.

The imaging system and the incident irradiance are mathematically modeled using fundamentals from linear systems theory. The focal plane processing functions give rise to two operational modes; a gated integration mode and a heterodyne detection mode. Both modes are analyzed with the irradiance model. The analysis is made in the context of extracting modulation depth in a pump-probe absorption spectroscopy diagnostic.

The framework of the analysis included throughout this investigation is constructed from flexible and fundamental tools. These tools are based on communications and linear systems theories. The results of the analysis show that complex systems can be successfully modeled and investigated with this underlying approach.

The work has relevance in the advancement of imaging technologies for specialized applications and scientific diagnostics.

TABLE OF CONTENTS

ABSTRACT v

LIST OF FIGURES xv

LIST OF TABLES xxi

NOMENCLATURE xxiii

ACKNOWLEDGMENTS xxix

DEDICATION xxxi

Chapter 1 INTRODUCTION 1

1.1 General Introduction 1
1.2 Benefits and Application Extensions 3
1.3 Laser Diagnostics 6
1.3.1 Mathematical Description of Objective 8
1.3.2 Single Point Detection 11
1.3.3 Diagnostic Imaging 14
1.4 Statement of Work 15
1.5 Advancements In Sensor Level Processing 16
1.5.1 Synchronous Detection Arrays and Systems 18
1.5.2 Dynamic Range Enhancement 19
1.6 Temporal Analysis 20
1.7 Imaging System Description 21
1.8 Contributions of this Work 22
1.8.1 Two-Dimensional Gated Integration With A CCD 24
1.8.2 Integration Threshold Implementation and Investigation . . . 24
1.8.3 Heterodyne Detection With A CCD 25
1.8.4 Input Irradiance Model Development 25
1.8.5 Imaging System Model Development 26
1.8.6 Modeling Foundation 26
1.8.7 Diagnostic Imaging Performance Predictions 27
1.9 Thesis Summary 27

Chapter 2 DIAGNOSTIC IMAGING SYSTEM DESCRIPTION 31

2.1 General Description 31
2.1.1 Hardware 32
2.1.2 Software 35
2.2 Charge-Coupled Devices 36
2.3 Charge-Coupled Device Concept 37
2.3.1 Charge Collection 39
2.3.2 Charge Transfer 42
2.3.3 Charge Output Conversion 44
2.4 CCD Architecture 46
2.4.1 Linear CCD 47
2.4.2 Full Frame CCD 48
2.4.3 Frame Transfer CCD 49
2.4.4 Interline Transfer CCD 51
2.5 Sony ICX085 Interline Transfer CCD 52
2.6 Illustrative interline transfer CCD Representation 53
2.6.1 Charge Flow Under Normal Operation 57
2.7 Imaging System Parameters 58
2.7.1 Transfer Gain 59
2.7.2 Digital Resolution 59
2.7.3 Frame Rate 60
2.7.4 Read Noise 60
2.7.5 Photon Transfer Curve 61
2.7.6 Linearity 63
2.7.7 Flat-field Correction 64

Chapter 3 FOCAL PLANE DETECTION PROCESS 67

3.1 General Introduction 67
3.2 CCD Illustration Review 68
3.3 Multiple Exposure Integration 68
3.3.1 General Signal-to-Noise Ratio Improvement Expectations . . . 74
3.4 Integration Threshold 76
3.4.1 Antiblooming 78
3.4.2 Background Reduction 79
3.4.3 Threshold Mechanism Examples 81
3.4.4 Expected Signal-to-Noise Ratio Improvement 82

Chapter 4 ANALYSIS FRAMEWORK AND FUNDAMENTALS 83

4.1 General Introduction 83
4.2 Linear Systems Approach 84
4.3 Spectral Analysis 87
4.4 General Frequency Conversion 87
4.4.1 Homodyne Detection 88
4.4.2 Heterodyne Detection 92
4.4.3 Optical Modulation and Demodulation 94
4.5 System Bandwidth 96
4.6 Sampling Theory 97
4.6.1 Temporal Sampling 98
4.6.2 Spatial Sampling 99
4.7 General Noise Analysis Considerations 100
4.7.1 Correlation 103
4.7.2 Noise Power Transfer 105
4.7.3 Equivalent Noise Bandwidth 109
4.8 Conventional Laser Diagnostic Instrumentation 111
4.8.1 Lock-In Amplifier 112
4.8.2 Boxcar Averager 113

Chapter 5 REPRESENTATION OF SIGNALS AND NOISE . . . 117

5.1 Input Signal Definition 118
5.2 Transfer Of Units 121
5.3 Background Component 124
5.4 Stochastic Process Definitions 128
5.5 Photon Noise 131
5.5.1 Spectral Shape Of Photon Noise 132
5.5.2 Photon Noise Power 139
5.5.3 Fundamental Detection Limit 145
5.5.4 Probability Description 146
5.6 $1/f$ Noise 149
5.6.1 Spectral Approximation 151
5.6.2 $1/f$ Noise Power 153
5.7 Total Input Noise 155
5.7.1 Spatial Noise 157
5.8 Information Bearing Signal 158
5.8.1 Modulation Waveforms 162
5.8.2 Modulated Signal 167
5.9 Input Attributes 173

5.10 Imaging System Noise 177
5.10.1 Shot Noise 177
5.10.2 Dark Charge 179
5.10.3 Fixed Pattern Noise 179
5.10.4 Charge Transfer Noise 180
5.10.5 On-Chip and Off-Chip Amplifier Noise 181
5.10.6 Reset Noise 181
5.10.7 Electronic $1/f$ Noise 182
5.10.8 Thermal Noise 182
5.10.9 Quantization Noise 183
5.10.10 Read Noise 185

Chapter 6 GATED INTEGRATION SYSTEM MODEL 187

6.1 General Introduction 187
6.2 Charge Flow Under Normal Operation 188
6.3 Linear Systems Model Development 189
6.3.1 Natural Sampling Function 192
6.3.2 Integrate And Dump Filter 195
6.3.3 CCD Specific Gain 198
6.4 Gated Integrator Model 199
6.4.1 System Function 200
6.4.2 Input Review 201
6.5 Gated Integrator Output 204
6.5.1 Signal Output 204
6.5.2 Background Output 205
6.5.3 Noise Output 206
6.6 Modulation Depth Determination 210
6.7 Signal-To-Noise Ratio 212
6.8 Detection Limits 215
6.8.1 Detection Summary 218

Chapter 7 HETERODYNE DETECTION SYSTEM MODEL . . 221

7.1 General Introduction 221
7.2 Heterodyne Detection Model 222
7.2.1 Sample And Hold Filter 222
7.2.2 Post Processing 225
7.2.3 System Function 226
7.2.4 Input Review 228
7.3 Heterodyne System Output Without Demodulation 229

7.3.1 Background Output 230
7.3.2 Photon Noise Output 231
7.3.3 1/f Noise Output 231
7.3.4 Combined Output 232
7.4 Heterodyne System Output With Demodulation 233
7.4.1 Signal Output 233
7.4.2 Photon Noise Output 237
7.4.3 1/f Noise 239
7.4.4 Combined Output 242
7.5 Modulation Depth Determination 242
7.6 Signal-To-Noise Ratio 244
7.7 Detection Limits 245
7.8 Applications 247

Chapter 8 PROCESSING DEMONSTRATION 249

8.1 General Introduction 249
8.2 Experiment Configuration 250
8.2.1 Light Source 251
8.3 On-chip Integration 252
8.4 Integration Threshold 257
8.5 Modulation Depth 261
8.5.1 Source Configuration 262
8.5.2 Calibration Measurements 262
8.5.3 Imaging System Results 265
8.5.4 Detection Limit 270
8.6 Alternate Applications 274
8.6.1 Object Recognition 274
8.6.2 Heterodyne Detection 276

Chapter 9 DISCUSSION AND OBSERVATIONS 279

9.1 System Performance 279
9.2 Industrial Collaboration 280
9.3 Project Breadth 280

Chapter 10 CONCLUSIONS 283

10.1 General Summary 283
10.2 Contributions of this Work 283
10.2.1 Two-Dimensional Gated Integration with a CCD 284
10.2.2 Integration Threshold Implementation and Investigation . . . 284

10.2.3 Heterodyne Detection with a CCD 285
10.2.4 Input Irradiance Model Development 286
10.2.5 Imaging System Model Development 286
10.2.6 Diagnostic Imaging Performance Prediction 287
10.3 Limitations of this Work 287
10.3.1 Spatial Noise Considerations 288
10.3.2 Irradiance Source 288
10.3.3 Diagnostic Application 289
10.3.4 Signal Enhancement with Image Processing Algorithms 289
10.4 Suggestions For Future Work 289
10.5 Conclusion 290

REFERENCES 291

APPENDIX A. 301

APPENDIX B. 303

B.1 Charge Collection in a Semiconductor 303

APPENDIX C. 311

APPENDIX D. 313

D.1 Photon Transfer Technique 313

APPENDIX E. 315

E.1 Natural Sampling Function Model 315

APPENDIX F 321

F.1 Integrate and Dump Filter Model 321
F.1.1 Noise Equivalent Bandwidth 326

APPENDIX G. 329

G.1 Sample and Hold Filter Model 329
G.1.1 Noise Equivalent Bandwidth 332

APPENDIX H **335**

H.1 Homodyne Detection System Function 335
H.1.1 Sinusoidal Mixer 336
H.1.2 Lowpass Filter 336
H.2 System Output 337
H.2.1 Signal Output 337
H.2.2 Background Output 339
H.2.3 Noise Output 339
H.3 Signal-To-Noise Ratio 342

APPENDIX I **345**

I.1 Determination of Modulation Depth 345
I.1.1 Waveform Definition 346
I.1.2 Fourier Series Representation 347
I.1.3 Harmonic Relation To Modulation Depth 351
I.1.4 Determiniation of Fundamental Harmonic 354

APPENDIX J **357**

J.1 Integration Threshold Circuit 357
J.2 Circuit Design 359
J.3 PCB Layout 360
J.3.1 Top Layer 360
J.3.2 Bottom Layer 361

APPENDIX K **364**

K.1 Application Manual 364

LIST OF FIGURES

1.1 Signal of interest contained over a series of images in the time domain 2

1.2 Probe beam modulation through interaction with the sample volume, which has been perturbed by the modulated pump beam 8

1.3 Probe irradiance illustration 9

1.4 Frequency domain illustration of probe beam components 12

2.1 Imaging system hardware illustration 32

2.2 Buried-channel CCD illustration: (a) semiconductor structure, (b) potential profile 40

2.3 Charge packet transfer through coordinated gate voltage clocking . 43

2.4 Linear CCD 47

2.5 Full Frame CCD 48

2.6 Frame Transfer CCD 50

2.7 Interline Transfer CCD 51

2.8 On-chip mircolens structure 53

2.9 Sony ICX085 interline transfer CCD semiconductor structure 54

2.10 Simplified cross-section illustration of the Sony ICX085 interline transfer CCD 56

2.11 CCD signal conversion factor representation 58

2.12 Photon transfer curve 62

2.13 Photon transfer histogram 63

2.14 Flat-field gain correction value histogram 65

2.15 Pixel-to-pixel noise improvement with flat-field gain correction 66

3.1 Simplified cross-section illustration of the Sony ICX085 interline transfer CCD 69

3.2 CCD initialization prior to image acquisition 71

3.3 Integrating the *first* exposure in the vertical register 72

3.4 Draining unwanted charge into the substrate while holding the *first* exposure in the vertical register 72

3.5 Integration of consecutive exposures in the vertical register 73

3.6 Multiple exposures integrated in the vertical register; the integrated image is ready to be read from the array 74

3.7 Antiblooming function under normal interline transfer CCD configuration and operation 78

3.8 Regulation of ROG barrier to create a charge dead band between the sensor and vertical register 80

3.9 Background charge contained in the sensor is discarded by lowering the OFD barrier 81

4.1 Block diagram comparison of a general communication system and diagnostic imaging system 86

5.1 Unit conversion from CCD input to output of the read out electronics, prior to analog-to-digital conversion (ADC) 122

5.2 Transfer of magnitude spectrum ($F(f)$) and power spectrum ($S(f)$) through the system function ($H_s(f)$) that describes the imaging system 123

5.3 Maximum incident power per pixel according to sampling time 126

5.4 Maximum beam irradiance according to sampling time 127

5.5 Expected peak signal for modulation depths of 10^{-2} (1.0%), 10^{-4} (0.01%), and 10^{-6} (0.0001%),for a range of background power, compared to the photon noise limit 147

5.6 Poisson distribution with its density function compared to a Gaussian density function 149

5.7 1/f noise power spectral density function variations 152

5.8 Input noise power spectral density functions 156

5.9 Input noise power spectral density (positive frequency values) plotted on a logarithmic scale 157

5.10 Example power spectral density function for a pulse train modulated signal, $S_{\mathrm{Ap}}(f)$ 169

5.11 Example power spectral density function for a sinusoidally modulated signal, $S_{\mathrm{As}}(f)$ 172

5.12 Input signal-to-noise ratio 174

5.13 Ratio of signal power at the fundamental frequency component to the total noise spectrum power at f_m 176

5.14 Electronic noise sources 178

6.1 General cross-section of the interline transfer CCD 189

6.2 Natural sampling function power spectrum 193

6.3 Amplitude spectrum of periodic natural sampling function with constant sampling rate and variable dwell time 194

6.4 Amplitude spectrum of periodic natural sampling function with constant dwell time and variable sampling rate 195

6.5 Integrate and dump filter power response 196

6.6 Gated integrator block diagram 200

6.7 Illustration of the natural sampling performed by the gated integrator on the input waveform 202

6.8 Transfer of $1/f$ noise through gated integrator system function 208

6.9 SNR improvement gained from integration threshold factor, ρ 214

6.10 SNR improvement gained from averaging $(n_p \cdot n_f)$ 215

6.11 Comparison of SNR_g with SNR_o using the same parameters 217

6.12 Comparison of SNR_g with SNR_o using different constraints 219

6.13 Predicted SNR improvement when utilizing the integration threshold mechanism 219

6.14 Predicted SNR improvement when averaging 220

7.1 Block diagram of the imaging system operated as a heterodyne detector with post processing functions 223

7.2 Sample and hold filter power response 224

7.3 Processing with and without $|D(f)|^2$ 227

7.4 Numerical integration of $K_W(f_d)$ 238

7.5 Ratio of noise contribution from $S_L(f \pm f_s)$ to the total $1/f$ noise . . 240

7.6 Numerical integration of $K_L(f_d)$ 242

7.7 Modulation depth-to-noise ratio (MDNR) as a function of demodulation frequency, f_d 246

7.8 Ratio of signal power from $|H_e(f)|^2$ to the signal power from $|H_g(f)|^2$ 247

8.1 Equipment and instrumentation used to demonstrate and test the imaging system's functions 250

8.2 Block diagram of LED array 252

8.3 Wavelength scan of LED Array 253

8.4 Applied dc voltage vs. total LED current draw 254

8.5 On-chip exposure integration using 10μs exposure time 255

8.6 On-chip exposure integration using 100μs exposure time 255

8.7 On-chip exposure integration using 500μs exposure time 256

8.8 Input arrival rate when applying 4V dc to the LED array 257

8.9 Mean integration per read out gate (ROG) voltage setting 258

8.10 Integration threshold coefficient (ρ) determination 259

8.11 Noise power per read out gate (ROG) voltage setting 260

8.12 Noise power per read out gate (ROG) voltage setting 261

8.13 Modulation depth measurements with a lock-in amplifier and a boxcar averager 265

8.14 Modulation depth measurement with the combination of a lock-in amplifier and a multimeter 266

8.15 Modulation depth measurement with 20mV input signal modulation . 267

8.16 Modulation depth measurement with 5mV input signal modulation . 268

8.17 Modulation depth measurement with 2mV input signal modulation . 268

8.18 Modulation depth measurement with 1mV input signal modulation . 269

8.19 Calculated steady state background irradiance for both a single pixel and the photodiode, compared to the expected peak signal value for modulation depths of 10^{-2}, 10^{-4}, and 10^{-6}, and compared to the photon noise limit 273

8.20 Experimental configuration for fringe analysis 275

8.21 Fringe analysis example 276

8.22 Heterodyne detection output with difference between sampling frequency and modulation frequency set to 2Hz 277

8.23 Power spectrum of the 2Hz IF example from Figure 8.22 278

B.1 Buried-Channel CCD Illustration: (a) semiconductor structure, (b) charge density profile, (c) electric field profile, (d) potential profile. . . 306

D.1 CCD signal conversion factor representation 313

E.1 Time domain illustration of the natural sampling function 316

E.2 Spectral coefficients and spectral envelope of the natural sampling function 319

E.3 Natural sampling function: magnitude squared spectrum 320

F.1 Causal impulse response of the integrate and dump filter 322

F.2 Non-causal integrate and dump impulse response 323

F.3 Integrate and dump filter power response 326

G.1 Sample and hold filter power response 332

H.1 Simplified lock-in amplifier (homodyne detector) block diagram . . . 335

H.2 Transfer of $1/f$ noise through the simplified lock-in amplifier system function 341

I.1 General probe intensity along a time axis 345

I.2 General detection system input waveform 347

I.3 Modulation depth calculation using the dc component and the fundamental modulation frequency component 355

J.1 Bill of materials (BOM) 362

J.2 Bill of materials (BOM) 363

K.1 WinView/32 menu for application specific settings 365

K.2 Exposure time resolution setting 366

K.3 Integration dead-band threshold setting 366

K.4 ROG barrier voltage as a function of digital-to-analog converter settings (DAC) 367

K.5 Setting the number of integrated exposures 369

LIST OF TABLES

8.1 Calculation of photon arrival rate (λ_p) and steady state background irradiance (I_p) from the integration rate (ν_I) on a per-pixel basis . . . 272

NOMENCLATURE

$a(t)$	Information bearing signal
$A(f)$	Information bearing signal spectrum
$A(t)$	Random phenomenon of a physical parameter
$\bar{A}$	Mean, normalized power of $a(t)$
a_p	General time domain magnitude component
A_p	Pixel area: cm^2
A_1	Gain of read out electronics
A_2	Analog-to-digital conversion gain
A_λ	Average photon arrival rate
ADC	Analog-to-digital converter
AO	Acousto-optic modulator
APS	Active pixel sensor
B	Bandwidth: hertz
B_{id}	Noise Equivalent Bandwidth for $H_{id}(f)$
B_{rd}	Noise Equivalent Bandwidth for $H_{rd}(f)$
B_{sh}	Noise Equivalent Bandwidth for $H_{sh}(f)$
b_m	General time domain magnitude component
c	Speed of light
C	General magnitude variable
c_i	Pixel column location
CCD	Charge Coupled Device
CMOS	Complimentary metal-oxide-semiconductor
CTE	Charge transfer efficiency
d_B	Beam diameter: cm
DAC	Digital-to-analog converter
DN	Digital number = Analog-to-digital count value
EO	Electro-optic modulator
f	Frequency: hertz
f_c	Modulation carrier frequency
f_d	Demodulation frequency
f_f	Sample and hold frequency: System frame rate
f_h	General high frequency limit
f_i	Integrate and dump frequency
f_{IF}	Intermediate frequency
f_l	General low frequency limit
f_m	Modulation frequency

f_o	General frequency variable
f_s	Natural sampling frequency
$\Im(\bullet)$	Fourier transform
G_c	Lowpass filter, $H_c(f)$, gain
G_d	Demodulation function, $D(f)$, gain
G_s	Imaging system gain
h	Planck's Constant
$h_{id}(t)$	Integrate and dump filter impulse response
$h_s(t)$	Imaging system impulse response
$h_{sh}(t)$	Sample and hold filter impulse response
$h(\tau)$	Impulse response of a general detector
$H_c(f)$	Second order lowpass filter transfer function
$H_e(f)$	Heterodyne detection system function with demodulation
$H_{ft}(f)$	Flat-top sampling transfer function
$H_g(f)$	Gated integrator system function
$H_{ge}(f)$	Heterodyne detection system function without demodulation
$H_{id}(f)$	Integrate and dump filter transfer function
$H_s(f)$	Imaging system transfer function
$H_{sh}(f)$	Sample and hold filter transfer function
I_B	Beam irradiance: $Watts/cm^2$
I_p	Mean irradiance per pixel: $Watts$.
I_{off}	Probe beam intensity when pump beam is off
I_{on}	Probe beam intensity when pump beam is on
$I_N(t)$	Additive noise irradiance
$I_L(t)$	$1/f$ noise irradiance
$I_W(t)$	Photon noise irradiance
IT	Integration threshold
K	Photon transfer curve factor
K_1	General magnitude variable
K_s	Imaging system gain
$K_\lambda(t)$	Instantaneous photon arrival rate
$m(t)$	General modulation waveform
$m_p(t)$	Rectangular pulse train modulation waveform
$m_s(t)$	Sinusoidal modulation waveform
$M(f)$	General modulation function spectrum
$M_p(f)$	Rectangular pulse train modulation spectrum
$M_s(t)$	Sinusoidal modulation spectrum
MDNR	Modulation depth-to-noise ratio
n	Integer summation variable
n_p	Instantaneous number of photons

N_a	Number of doped acceptor atoms
N_d	Number of doped donor atoms
N_f	Number of frames
$N_{1/f}$	Average $1/f$ noise power
N_i	Number of integrated exposures
N_p	Average photon noise power
N_t	Average total noise power
N_{si}	Number of samples integrated per frame
N_{if}	Number of integrations per frame
$\bar{n_p}$	Mean number of photons
OFD	Over flow drain
$p_r(t)$	Time domain representation of imaging system input
$P_r(f)$	Frequency domain representation of imaging system input
P_B	Probe beam power
PPAS	Pump-probe absorption spectroscopy
PSD	Power spectral density
PSP	Pressure sensitive paint
$q(t)$	Natural sampling function
$Q(f)$	Natural sampling spectrum
Q_g	Surface charge density at metal gate
r_j	Pixel row location
$r(t)$	Flat-top sampling pulse
$R(f)$	Flat-top sampling spectrum
ROG	Read out gate
ROI	Region of interest
$S(DN)$	Signal value in digital number units
$S_{\mathrm{A}}(f)$	Unmodulated signal input power spectrum
$S_{\mathrm{Ap}}(f)$	Signal input power spectrum, modulated with $m_p(t)$
$S_{\mathrm{As}}(f)$	Signal input power spectrum, modulated with $m_s(t)$
$S_B(f)$	Steady state background input power spectrum
$S_L(f)$	$1/f$ noise input power spectrum
$S_W(f)$	Photon noise input power spectrum
S_T	Total input power spectrum
S_v	CCD output amplifier gain
SNR	Signal-to-noise ratio
t	Time in seconds
T_f	Sample and hold filter period, also system frame rate
T_m	Modulation function period
T_o	General period variable
T_s	Natural sampling period

$v(t)$	Time domain representation of a general function
$V(f)$	Frequency domain representation of a general function
V_g	CCD gate voltage
V_{g1}	Vertical register phase 1 gate voltage
V_{g2}	Vertical register phase 2 gate voltage
V_{g3}	Vertical register phase 3 gate voltage
V_n	Harmonic components of a general function
V_{sub}	CCD substrate voltage
x	Distance into semiconductor device
x_d	Depletion depth
x_o	Oxide layer thickness
$y(t)$	General system output: Time domain
$y_B(t)$	Time domain output: Background component only
$y_n(t)$	Time domain output: Noise components only
$y_s(t)$	Time domain output: Signal components only
$Y(f)$	General system output: Frequency domain
$Y_{\mathrm{A}g}(f)$	Signal spectrum out of $H_g(f)$
$Y_{Bg}(f)$	Background spectrum out of $H_g(f)$
$Y_{Lg}(f)$	$1/f$ noise spectrum out of $H_g(f)$
$Y_{Wg}(f)$	Photon noise spectrum out of $H_g(f)$
$Z_{\mathrm{A}e}(f)$	Signal spectrum out of $H_e(f)$
$Z_{Le}(f)$	$1/f$ noise spectrum out of $H_e(f)$
$Z_{We}(f)$	Photon noise spectrum out of $H_e(f)$
$Z_{Bge}(f)$	Background spectrum out of $H_{ge}(f)$
$Z_{Lge}(f)$	$1/f$ noise spectrum out of $H_{ge}(f)$
$Z_{Wge}(f)$	Photon noise spectrum out of $H_{ge}(f)$
α_{mod}	Modulation depth
ϵ	Energy per photon
ϵ_o	Permittivity of free space
η	CCD quantum efficiency
$\Lambda(\bullet)$	Photon arrival rate process
λ	Instantaneous photon arrival rate
λ_p	Mean photon arrival rate per pixel: *photons/sec*
λ_w	Laser wavelength
κ	Dielectric constant
ρ	Integration threshold coefficient
σ_{A}^2	Variance of $A(t)$
σ_n^2	Photon arrival rate variance
σ_n	Photon arrival rate standard deviation
σ_L^2	Incident $1/f$ noise power

σ_{Le}^2	$1/f$ noise power out of $H_e(f)$
σ_{Lg}^2	$1/f$ noise power out of $H_g(f)$
σ_{Lge}^2	$1/f$ noise power out of $H_{ge}(f)$
σ_r^2	Imaging system read noise variance
σ_{Tg}^2	Total noise power out of $H_g(f)$
σ_W^2	Incident photon noise power
σ_{We}^2	Photon noise power out of $H_e(f)$
σ_{Wg}^2	Photon noise power out of $H_g(f)$
σ_{Wge}^2	Photon noise power out of $H_{ge}(f)$
τ_a	Accumulation interval
τ_h	Flat-top sampling pulse width
τ_i	Integration period of integrate and dump filter
τ_m	Modulation function pulse width
τ_o	General pulse width variable
τ_s	Natural sampling pulse width
ψ_m	Modulation function duty cycle
ψ_o	General duty cycle
ψ_s	Natural sampling function duty cycle
ϕ	Electrostatic potential
$\phi_1(x)$	Metal SiO_2 interface potential
$\phi_2(x)$	P-type region potential
$\phi_3(x)$	N-type potential
ϕ_c	Modulation carrier phase
ϕ_d	Phase of demodulation function
ϕ_e	Phase error

ACKNOWLEDGMENTS

This investigation could not have been completed without the support of others. I am thankful for the efforts put forth by my advisors, my committee members, and my fellow graduate students. I am also grateful for the relationships that developed over the years from working with those that shared common goals.

I especially thank my advisor, Dr. Nigel Middleton, for all his support. My extreme gratitude lies in the breadth of opportunities that are afforded me because of the techniques and methodologies I have learned. I thank him for giving me the latitude to investigate, struggle, fail, and inevitably discover. I deeply appreciate Nigel's insightful nature. He often nudged me in the right direction with the knowledge that I would eventually find my way, guided me when appropriate, and offered unwavering encouragement. Nigel is an exceptional mentor and fascinating friend.

I also am grateful for the support given by Dr. Mark Linne. I thank Mark for presenting me with a challenge and then providing an amazing amount of support for pursuing that challenge. Mark's ability to foster industrial partnerships and incorporate them into advanced research unquestionably enhanced my graduate career and professional development. Mark's guidance greatly facilitated my learning and technical breadth, which opened my eyes to new opportunities. I enjoyed our many discussions on ways to promote and capitalize on our developments.

I would also like to thank the other members of my committee, Drs. Ronald Klusman, Chris Debrunner, and Robert Woolsey for their valuable time and recommendations. I appreciate all their efforts and support.

A research internship at Roper Scientific (Princeton Instruments, Inc.) in Tren-

ton, New Jersey, was an integral portion of my graduate career. During this time I was given resources and the support of others to learn the design of a scientific imaging system. I would like to thank Sam Khoo, Jim Paton, Dave Lafferty, Ishai Nir, Mark Schultz, Mike Narozniak, Hai Hguyen, and Victor Guzman for their time, support, and friendship.

My fellow graduate students have also made my graduate career a memorable period in my life. I enjoyed the interactions and discussions that arose on a daily basis. The assistance and support offered by each is something I hope to also find in my professional career. I would especially like to acknowledge Tom Settersten, Scott Spuler, John Fowler, and Ryan Swartzendruber for their assistance and friendship.

Outstanding support for this investigation was also supplied by several agencies. I would like to thank the National Aeronautics and Space Administration (NASA) for their support through the Center for Commercial Applications of Combustion in Space (CCACS) under the Cooperative Agreement Number NCCW-0096. The National Science Foundation (NSF) provided support through the acquisition of equipment with the MRI Grant CTS-9711889 and the Air Force Wright Laboratories provided support under contracts F33615-96-C-2632 and F33615-98-C-2859.

DEDICATION

This dissertation is dedicated to my parents,

Tom and Sue Fisher

Your support is endless,

Your encouragement perpetual,

And your love is absolute;

I am blessed beyond belief.

Chapter 1

INTRODUCTION

1.1 General Introduction

Charge-coupled devices (CCD) have long been the transducer of choice for acquiring spatially resolved, two-dimensional data in the form of images. Complimentary metal-oxide-semiconductor (CMOS) active pixel sensors (APS) have also made an impact in the imaging market, albeit less of an impact in the scientific imaging community (Janesick *et al.*, 1987; Fossum, 1993). The ability for both technologies to acquire spatially resolved information is widely understood and, thus, commonly used to enhance instrumentation and measurement systems.

In many implementations, the data, in the form of images, is first acquired and stored and then digital processing is performed to extract, from the images, useful information. The desired information is often in the form of spatial anomalies that are contained in the image space of an image frame. In this case, spatial data processing or image processing is performed to extract object features (Snyder *et al.*, 1993; Chitti, 1997).

An imaging system can also provide information in other dimensions. Spatial information from an imaging system accounts for two of the four possible dimensions that can be used to provide information about the object space. The other two dimensions are the time dimension and the spectral dimension (Haas *et al.*, 1979). Temporal information can be acquired by processing a series of frames. Spectral

information is contained in the imaging system's electrical response to the wavelength of light incident on the array, which is defined as the quantum efficiency of the device.

The focus of this thesis is on temporal information that is gathered in two spatial dimensions, as images. The temporal operation of an imaging system is investigated. The intent is to determine a method for extracting temporally resolved information from the object space projected onto the detector plane. The signals of interest are, therefore, contained in a set or a series of frames, as shown in Figure 1.1.

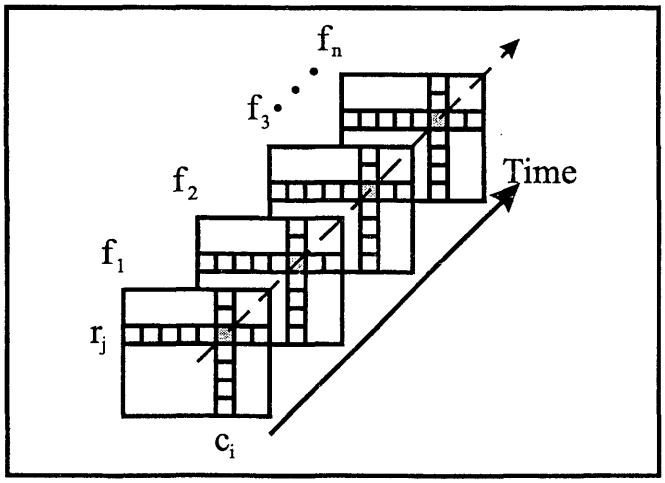

FIG. 1.1. Signal of interest contained over a series of images in the time domain

Because of the time required to transfer an image out of an array and digitize each pixel, use of CCDs and CMOS APS for acquiring temporally resolved information is not very common. In order to make imaging systems more attractive as transducers that can provide temporally resolved information, processing functions have been incorporated into the array at the focal plane or pixel level (Takeda & Kitoh, 1991; Spirig *et al.*, 1995; Povel, 1995; Eklund *et al.*, 1996; Mendis *et al.*, 1997). Focal plane processing functions provide the means to extract images of interest and attenuate unwanted components prior to image readout and digitization. This technique opens

up temporal processing possibilities by operating on the temporal information before the high temporal frequency (in distinction from spatial frequency) components of the object space are eliminated by the read out process (Fossum, 1993; Seitz, 1996)

It is difficult to incorporate sophisticated focal plane processing while maintaining high spatial resolution. As the complexity of the focal plane processing functions increases, so too does the chip area required to develop the processing circuitry (Fossum, 1989; Fossum, 1993; Seitz, 1996; Eklund *et al.*, 1996; Mendis *et al.*, 1997). An increase in the area of each pixel, therefore, results in a decrease in spatial resolution. A compromise must be made between the focal plane processing complexity and the spatial resolution.

This thesis investigates the temporal resolution that can be obtained by incorporating elementary processing functions at the focal plane in a commercially available interline transfer CCD. Since the CCD used in this work is a commercially available device, it has well defined spatial characteristics and is not specifically designed for temporal processing. Based on the interline transfer architecture, however, synchronous charge maneuvering operations are incorporated into the imaging system. These operations are then used in conjuction with post processing calculations to extract a weakly modulated image from a large background irradiance.

1.2 Benefits and Application Extensions

The developments and findings in this work will prove beneficial to those pursuing research with selected laser based diagnostics and in particular laser based camera imaging applications. Because of the foundation upon which this work is based, its products, both physical and academic, contribute to the advancement of instrumentation and camera technology for laser based diagnostics. Certain laser

diagnostic procedures and combustion studies can profit from the imaging system that is developed (Settersten, 1999; Drouillard *et al.*, 2000). The camera imaging system contributes to the set of detection tools that are available for nonintrusive investigations that rely on modulated irradiance to extract information.

The technique with which the imaging system is analyzed will also benefit further studies in detection systems and instrumentation. Both the input irradiance and the imaging system's detection process are modeled in the temporal frequency domain using linear systems analysis fundamentals. This modeling approach provides a broad representation and understanding of all the system parameters and processes, from the input irradiance to the power in the signal at the output. With this end-to-end understanding, design and development efforts can be prioritized toward those specific parameters and processes that will enhance the entire diagnostic system. The definition of the input irradiance and the analysis approach can also be extended to comparable investigations. Many of the models are created in a general manner and can be utilized in other optical signal processing investigations by inserting specific details that comply with the parameters of the comparable investigation.

Besides the application and analysis performed in this work, the problem of detecting a small modulated image in the presence of a large background irradiance and accompanying noise is exhibited in many applied imaging fields. As an example, guidance systems must be able to detect dim targets embedded in background clutter and noise (Haas *et al.*, 1979; Tao *et al.*, 1979). Also, in the medical diagnostic industry, imaging systems, which are constrained by excitation levels that maintain patient safety, must be optimized for the detection of small signals (Cunningham & Shaw, 1999; Pelli & Farell, 1999). The results from this work, therefore, can prove to be beneficial to other such imaging applications.

As this investigation has progressed, background free imaging applications and enhancements have also become apparent. The imaging system can be used to extract interference patterns, or fringes, generated with a coherent light source. This enhanced data, in the form of images, can be used by an intelligent computing system to measure objects and perform object recognition operations (Arai *et al.*, 1996b). As a result, improvements in industrial robotic systems or systems that search for product defects may be realized.

Other background free applications that may benefit from the results contained in this work are, for example, three dimensional mapping and imaging in harsh weather conditions. Recovering phase information, with a heterodyne detection process, in images can lead to the measurement and mapping of terrain in the object plane. Finally, if processing similar to that which is discussed in this investigation is incorporated into devices that can detect infrared irradiance, imaging systems that are unconstrained by harsh weather, such as fog, may be developed.

A direct result of this work and a collaborative effort with an industrial partner is a commercially available imaging system that captures two separate, full-frame images with very small temporal separation. The ability to accurately control the potential barrier between the sensor and the vertical register on the interline transfer CCD provides a mechanism for capturing two images on the CCD chip prior to read out. By capturing both images on the chip before read out begins, the time separation between the two images is accurately controlled and, at the minimum, can be set on the order of nanoseconds. This is the first such imaging system of its kind to be developed and deployed in laboratory applications at the Colorado School of Mines and also at Stanford University.

This commercially available system has already been applied to pressure sensi-

tive paint (PSP) diagnostics. PSP investigations, which use a specialized paint that fluoresces with an intensity that is a function of oxygen quenching, is used to determine the pressure and temperature of a structure under operating conditions. Often the characteristics of turbine blades and airfoils are analyzed with this diagnostic technique, which facilitates understanding of failure modes and provides knowledge that can be used to improve future designs. Development of the imaging system has resulted in the ability to produce elaborate, two-dimensional PSP fluorescence decay models (avoiding the "wind-off" measurement) and has extended the ability to gain knowledge in PSP investigations (Drouillard *et al.*, 2000).

The results of this work have also promoted the current development of a new solid-state imaging device that contains focal plane processing functions. The focal plane processing functions are designed specifically to extract a small modulated signal from a very large background irradiance. The results from this work have been used to direct the design of this new device, overcoming some of the application specific limitations that were set by the imaging system used in this investigation. As of this writing, fabrication of the new imaging device is underway.

In summary, this work has contributed to the state-of-the-art in instrumentation-quality imaging systems, through both a rigorous theoretical development and the practical development and testing of a prototype device. Although the work has centered around laser diagnostics in reacting flow fields, related applications are quite extensive and open new opportunities for two-dimensional imaging.

1.3 Laser Diagnostics

Motivating this investigation is the desire to acquire spectroscopic information in three dimensions, the time dimension and two spatial dimensions (a moving image).

In this work, the irradiance is assumed to be monochromatic, thus, the spectral data dimension is not considered as a useful source of information.

The particular diagnostic application used to analyze the performance of the imaging system is pump-probe absorption spectroscopy (PPAS). PPAS is a temporally and spatially resolved laser diagnostic technique that can be used to measure concentrations of radical species in reacting flows. Detailed discussion on PPAS can be found in the dissertation by Settersten (1999).

PPAS is one of a variety of laser diagnostics well suited for investigating combustion systems to increase upon the body of knowledge in this arena. Increasing the knowledge base of combustion systems is critical to the pursuit of efficient and environmentally safe energy sources (Eckbreth, 1996). An imaging system designed as the transducer for PPAS would enhance the tool set available to those seeking to contribute to the combustion knowledge base.

In the case of PPAS, the input to an optical transducer is the probe laser beam, after both it and the pump beam have crossed paths in a reacting flow field. The probe beam is comprised of a large steady state background, low frequency noise, photon noise, and a modulated information bearing signal that is orders of magnitude smaller than the steady state background (Linne *et al.*, 1995b; Settersten, 1999). The ratio of the weakly modulated signal irradiance to the steady state background irradiance is defined as the probe beam's modulation depth (Fiechtner & Linne, 1994). After measuring the probe beam with an optical transducer and determining the modulation depth, linear spectroscopic calculations can be performed to acquire number density information about the species being examined (Settersten, 1999). In order for the spectroscopic calculations to have merit, the transducer must be able to resolve a modulation depth of at least 10^{-4}. A more desirable system would be able to resolve

lower levels.

1.3.1 Mathematical Description of Objective

The probe beam is defined as the linear combination of four components; a steady state background, photon noise, low frequency noise, and a modulated information bearing signal. After a sample volume in the reacting flow field has been perturbed with a modulated pump beam, modulation is placed on the probe beam through molecular interactions within the sample volume (Settersten, 1999). The sample can, therefore, be considered the medium through which modulation on the pump beam is impressed onto the probe beam. Figure 1.2 provides an oversimplified illustration of the interaction process.

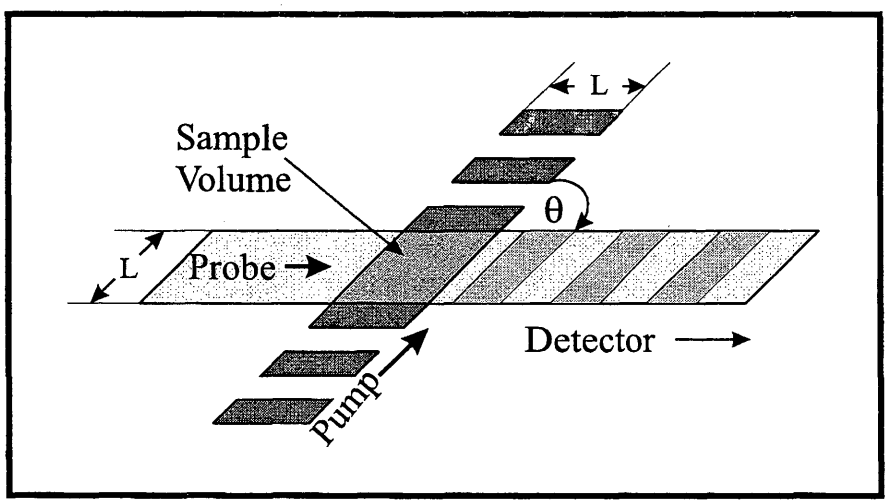

FIG. 1.2. Probe beam modulation through interaction with the sample volume, which has been perturbed by the modulated pump beam

Before the probe beam passes through the sample volume, it is comprised of only the steady state background level and noise. Considering for a moment only the steady state background, the probe beam is a constant irradiance. Once the probe

beam passes through the sample volume, additional irradiance, which represents the modulated information bearing signal, is added to the constant irradiance. After passing through the sample volume, without considering noise, the probe beam is the superposition of a modulated irradiance and a steady state background irradiance, which is illustrated in Figure 1.3.

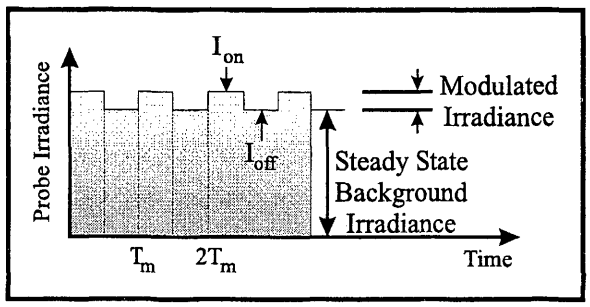

FIG. 1.3. Probe irradiance illustration

The modulated signal added to the steady state background in Figure 1.3 is assumed to be the result from directly modulating the pump beam with a rectangular pulse train that has a period T_m. In this case, the pump cycles "on" and "off" at the modulation frequency, f_m, which is $1/T_m$. As a result, the probe beam irradiance, once it passes through the sample, increases when the pump beam is "on" and remains at its background level when the pump beam is "off".

When the pump is "on", the probe beam irradiance is defined as I_{on}, and when the pump is "off", the probe irradiance is defined as I_{off}. In order to calculate modulation depth, I_{on} and I_{off} need to be accurately measured. Once these irradiance values are known, the modulation depth, α_{mod}, is calculated by dividing the difference by the steady state background, which is I_{off}.

$$\alpha_{mod} = \frac{I_{\text{on}} - I_{\text{off}}}{I_{\text{off}}} \tag{1.1}$$

There is also noise in the probe beam irradiance, which is not illustrated in Figure 1.3. Intrinsically, the beam contains photon noise and low frequency noise that has a tapering $1/f$ spectrum (Linne *et al.*, 1995b). Light sources by nature contain photon noise, which is a statistical property of the number of photons received during a given time period. $1/f$ noise, which presents itself as low frequency fluctuations in power, is also present in light sources and laser systems (Dereniak & Crowe, 1984; Eckbreth, 1996).

In order to mathematically model the probe beam irradiance, photon noise irradiance, $I_W(t)$, and $1/f$ noise irradiance, $I_L(t)$, are linearly combined with the steady state background, I_p. The complete definition of the probe beam, $P_r(t)$, after it passes through the sample volume, also contains the modulated information bearing signal $(A(t) \cdot m(t))$, so that

$$P_r(t) \;=\; I_p \;+\; I_W(t) \;+\; I_L(t) \;+\; A(t) \cdot m(t) \tag{1.2}$$

where $A(t)$ is the information bearing signal and $m(t)$ is the modulation waveform.

It is assumed that $A(t)$ is a random phenomenon that represents a physical parameter of interest. In this case, $A(t)$ is proportional to the modulation depth, α_{mod}. In order to obtain modulation depth images, the information bearing irradiance, $A(t)$, is the parameter that needs to be recovered with the imaging system, since

$$A(t) \;\propto\; \alpha_{mod} \tag{1.3}$$

The stochastic nature of noise prohibits direct application of equation 1.2 in analyzing the system's ability to extract $A(t)$. Since the noise is stochastic and since an understanding of the temporal processing capability of the imaging system is

desired, the components of $P_r(t)$ are analyzed in the frequency domain. The power spectral density of $P_r(t)$, which is defined as $S_T(f)$, provides a way to mathematically analyze stochastic noise and study the temporal characteristics of both the input irradiance and the imaging system.

The complete spectrum of $P_r(t)$ is also the linear combination of the four components. The general spectral shape of each component, the steady state background, $S_B(f)$, photon noise, $S_W(f)$, low frequency noise, $S_L(f)$, and the modulated information bearing signal, $S_{\mathrm{A}p}(f)$, are illustrated in Figures 1.4(a), 1.4(b), 1.4(c), and 1.4(d) respectively.

Combining each of the individual spectra in Figures 1.4(a)–1.4(d) produces the total probe beam spectrum, shown in Figure 1.4(e). The temporal processing capability of the imaging system is, therefore, derived from its ability to recover $S_{\mathrm{A}p}(f)$ from $S_T(f)$.

$$S_T(f) = S_B(f) + S_W(f) + S_L(f) + S_{\mathrm{A}p}(f) \tag{1.4}$$

where

$$S_{\mathrm{A}p}(f) = [\mathrm{A}(f) * M(f)]^2 \tag{1.5}$$

1.3.2 Single Point Detection

The modulation waveform, $m(t)$, is directly impressed upon the pump beam and then indirectly impressed upon the probe beam. Both the frequency and phase of the modulation waveform is, therefore, known *a priori*. Knowing this information provides a means to synchronize the detection system with the signal of interest.

Conventional detection systems, for measuring the probe beam in a PPAS diagnostic, are single point systems that typically use a photodiode as the optical trans-

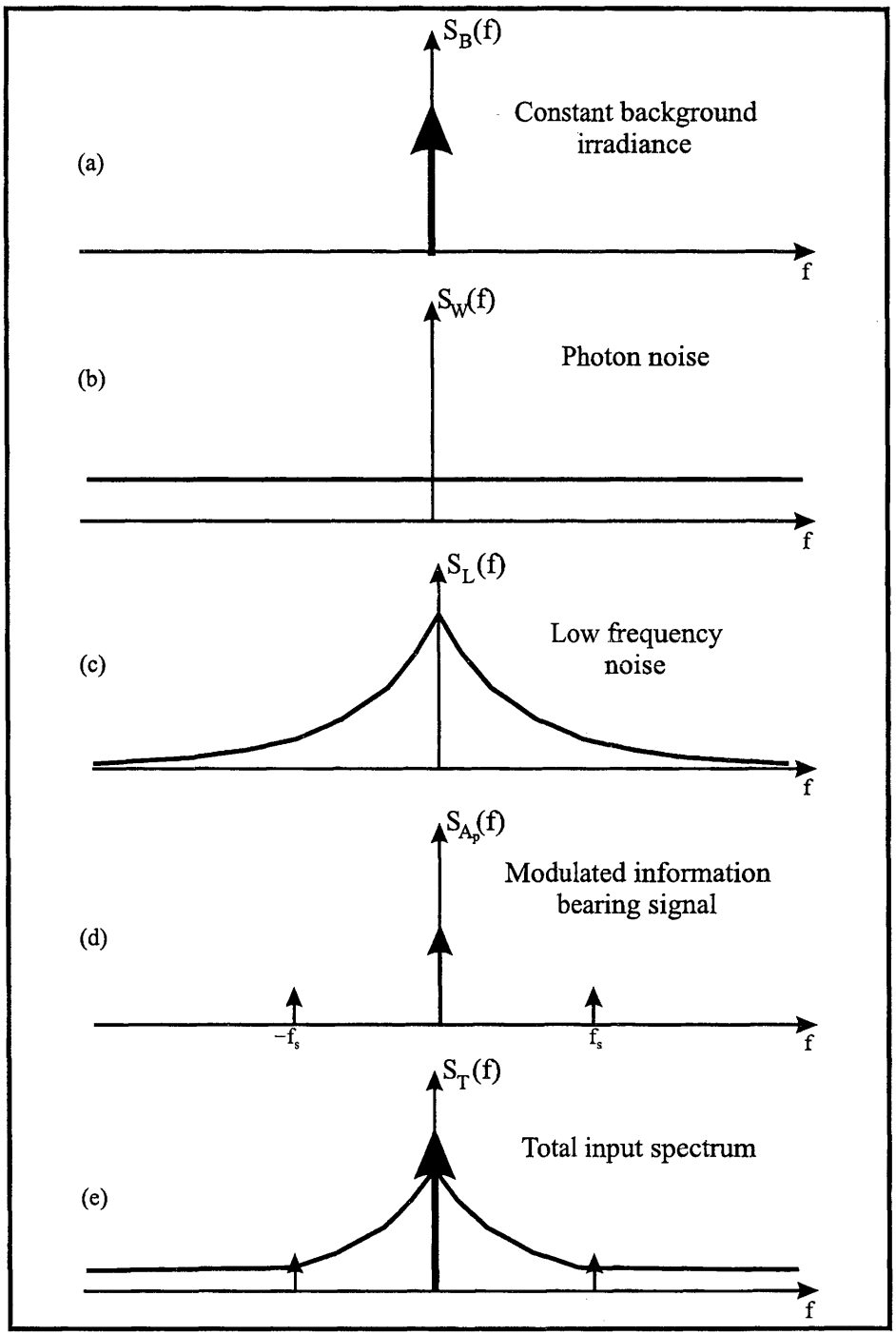

FIG. 1.4. Frequency domain illustration of probe beam components

ducer. The signal processing required to extract the information bearing signal from the large background irradiance limits the measurement to a single point. In order to measure the modulated irradiance and, hence, determine the modulation depth, a photodiode is typically used in conjuction with a lock-in amplifier (Fiechtner & Linne, 1994; Settersten, 1999).

A lock-in amplifier mixes the input, transferred from a single photodiode element, with a reference sinusoid that is "locked" to the frequency and phase of the modulated signal. The reference sinusoid is a zero mean waveform that is generated internally by the lock-in amplifier's electronics that are phase locked with an external reference, which follows the modulation waveform. Mixing the input with a zero mean sinusoid transfers the signal from its modulation frequency, f_m, to the baseband. At the same time the steady state background and low frequency noise components are transferred to a higher frequency band around f_m. A lowpass filter is then used to eliminate the higher frequency components, retaining at the output the information bearing signal (Stanford Research Systems, 1999; Settersten, 1999).

Another conventional instrument used in laser diagnostics to measure periodic information is the boxcar averager. The boxcar averager, or gated integrator, is also a single point measurement system that measures the input only when the information bearing signal is present. Using a reference that is synchronized to the signal's frequency and phase, a gate or switch circuit at the input to the boxcar is "opened" and "closed". "Closing" the gate circuitry only when the signal is present provides a mechanism for eliminating noise when the signal is not present (Stanford Research Systems, 1999; Fowler, 2000).

1.3.3 Diagnostic Imaging

Single point detection methods that utilize a photodiode in conjuction with a lock-in amplifier or a boxcar averager do not exploit the spatial resolution inherent in many laser diagnostic systems. Employing a solid-state imaging system as the optical transducer would, on the other hand, take full advantage of the spatial resolution afforded by laser based diagnostics.

Two-dimensional imaging of radical species concentrations (e.g. OH, CH, NO, etc.) in reacting flow fields has yielded a large amount of useful information. As an example, Planar Laser Induced Fluorescence (PLIF) has become the two-dimensional imaging technique of choice for turbulent flame studies (Hanson, 1986; Paul, 1991).

Other laser diagnostics techniques and instruments that utilize two-dimensional solid-state imaging systems are, for example, Particle Imaging Velocimetry (PIV), Pressure Sensitive Paint (PSP) measurements, and CCD based spectrometers. PIV is an optical technique for measuring and calculating the velocity profile in flow fields (Drouillard, 1998). PSP measurements use specialized fluorescent paint, that is dependent on oxygen quenching rates, and a laser excitation source to measure pressure and temperature effects on items such as airfoils. The application of imaging systems to PSP provides a way to measure pressure profiles over the object plane without mechanical scanning instruments (Drouillard *et al.*, 2000). Also, common to laser diagnostics are spectrometers that use a CCD as the transducer for measuring spectral profiles (Ratzlaff & Paul, 1979).

An initial investigation in the use of a solid-state imaging system as the transducer in a PPAS diagnostic has also been performed (Linne *et al.*, 1995a). This approach, which used a liquid crystal mounted in front of a conventional CCD camera to modulated optical gain, had several limitations, but proved sufficient as a

concept demonstration. This investigation showed that it is possible to capitalize on the spatial resolution afforded by PPAS and acquire modulation depth images, by incorporating temporal processing functions at the imaging systems focal plane.

Similar ideas have also been demonstrated in the field of phase fluorimetry for medical imaging (French, 1996). In the work by French (1996) an intensifier, mounted in front of a CCD camera, was used as a mixer to create a heterodyne detection system. The intensifier was gated "on" and "off" at a rapid rate to mix a high frequency (MHz) fluorescence signal down to an intermediate frequency that is lower than the CCD camera's frame rate.

1.4 Statement of Work

In an effort to expand upon the initial work performed by Linne *et al.* (1995), this thesis investigates the ability of an imaging system, that uses an interline transfer CCD as the optical transducer, to extract a weakly modulated image from a large background. The imaging system is modified to synchronize its on-chip sampling process with the modulated signal of interest. Once the phase of both the modulated signal and the sampling performed by the CCD are synchronized, two detection modes are realized. A gated integration mode, which samples the modulated signal at the same frequency used for modulation, can be used to restore the signal to a constant value at the baseband. The second mode, which is a heterodyne detection mode, samples the modulated signal at a frequency that is different than the modulation frequency. In this case, the signal is transferred to an intermediate frequency at the imaging system's output.

In order to alleviate quick saturation brought on by the large background irradiance in a probe type irradiance, an integration threshold feature is also proposed,

implemented on the CCD chip, tested, and analyzed. Using a method that can be compared to anti-blooming, the signal, represented as charge accumulated in the sensor, must surpass a threshold, created by a potential barrier, before it is able to flow into the vertical register, where it is integrated.

The two detection modes, the gated integrator and the heterodyne detector modes, and the integration threshold are mathematically analyzed to predict the system's ability to extract a weakly modulated image. The modulation depth that can be resolved, based on the definitions used at the input, is then analyzed and performance predictions stated.

Functional demonstrations of the two operating modes and the integration threshold are presented. Using a controllable irradiance source, the system's ability to integrate multiple exposures is first demonstrated. The integration threshold feature is tested and the characteristics of the mechanism are presented. Using the demonstrated operating modes, modulation depth experiments and a heterodyne detection process are then presented.

1.5 Advancements In Sensor Level Processing

Extensive efforts in the research and development of imaging transducers is widely apparent (Fossum & Barker, 1984; Fossum, 1989; Seitz *et al.*, 1993; Eklund *et al.*, 1996; Seitz, 1996). Intrinsically, most solid-state imaging systems, especially those used for scientific applications, can be described, in general, as two-dimensional integrators (Janesick *et al.*, 1987; Fossum, 1993). The input irradiance is converted to photoelectrons, through the photoelectric process (Appendix B), and integrated for a specified exposure time. The integrated charge from a CCD, or the integrated voltage from a CMOS array, is then digitized with an analog-to-digital converter (ADC) and

sent to a computer for display, further processing, and storage. A finite length of time is required to convert the charge packet, or proportional voltage, from each pixel to a digital value with the ADC. Although conversion for a single pixel may take only $1\mu s$ or less, the total time to convert an entire array of thousands, or millions, of pixels may be on the order of seconds.

Obtaining complete images at low frame rates, even at 30Hz or 60Hz frame rates, can eliminate the possibility of extracting, from a set of image frames, temporal information that resides at higher frequency bands. In many imaging systems, the ADC, which may actually include multiple ADCs operating in parallel, is the bottleneck that limits the system's ability to extract and process temporal information from high frequency components. Post processing algorithms cannot extract high frequency, temporal information from a set of frames in which the temporal information has been attenuated or eliminated by a low frequency frame rate. In other words, the only information that can be resolved is that which is limited by the Nyquist rate, which is set by the ADC process.

In an attempt to recover high frequency, temporal information from an image prior to the ADC bottleneck, research and development efforts have incorporated processing functions at the pixel level prior to image read out (Pain *et al.*, 1993; Spirig *et al.*, 1995; Seitz, 1996; Eklund *et al.*, 1996). Research is being performed in many arenas including investigations in CMOS active pixel sensors (Fossum, 1993; Mendis *et al.*, 1997), and focal plane spatial processing functions (Marshall & Collins, 1998; Hakkarainen & Lee, 1993). Of particular relevance to this work is the research and development of arrays that extract a modulated image (Spirig *et al.*, 1995; Seitz *et al.*, 1995b; French, 1996), and arrays that increase the dynamic range at the sensor level (Burke & Dan L. Smythe, 1983; Fossum & Barker, 1984; Pain *et al.*, 1993;

Johnston, 1995; Spirig *et al.*, 1997).

1.5.1 Synchronous Detection Arrays and Systems

A "lock-in CCD" sensor that incorporates focal plane processing functionality similar to that of a lock-in amplifier has been developed for two-dimensional synchronous detection of modulated optical inputs (Spirig *et al.*, 1995; Seitz *et al.*, 1995b; Seitz *et al.*, 1995a). This sensor integrates four independent samples, of a modulated irradiance, per carrier period, per pixel. Charge is integrated during four time intervals and each integration is stored at a different spatial location adjacent to the photo-sensor. The four integrated samples can then be processed, after reading them from the array, to recover the modulation depth, relative phase, and mean brightness (background) of the modulated irradiance. Initial results show the array can be used to detect a modulation depth of 5%. The lock-in CCD has, however, only been fabricated in a 3x3 array.

A single CCD has also been used to demodulate rapidly modulated light (Povel *et al.*, 1990; Povel, 1995). In this case, an opaque mask was placed over every second row of the CCD, creating two interlaced image planes. A row of pixels separates the integrated light as charge is transferred back and forth between the two image planes in phase with the modulated light. This method provides a way to capture both an in-phase image and anti-phase image (180° out of phase) in one frame. Since two image planes are created and the two images are separated by another row, the CCD's resolution is, however, sacrificed.

Arai *et al.* (1996) have demonstrated the use of a linear CCD for high speed fringe analysis. Fringes created with an interferometer are imaged with a linear CCD. The time sequential data from the CCD is frequency demodulated, resulting in

the recovery of the carrier fringes. Results show that this type of system can update fringe measurements every 10ms, which should prove useful to industrial applications such as object recognition (Arai *et al.*, 1996b; Arai *et al.*, 1996a).

As of this writing, a phase sensitive CMOS APS is being developed for the specific task of extracting weakly modulated images from an intense background irradiance. Background reduction circuitry is incorporated at the front end of each pixel to alleviate saturation of down steam processing functions. Since the intense background irradiance is a fairly constant value, and contains no useful information, the initial background reduction circuitry, essentially, ac couples the input. In this case, only changes in irradiance are processed. In order to extract the weakly modulated information bearing image, after background reduction has been performed, down stream processing, per pixel, is synchronized with the modulated image.

1.5.2 Dynamic Range Enhancement

The "lock-in CCD" developed by Spirig *et al.* (1997) has also been developed with offset subtraction circuitry. In this device, an offset control gate (OCG) is implemented between the photo-gate and the read out register. The OCG acts as a barrier such that the accumulation of additional charge past the barrier is allowed to be skimmed from the photo-gate to the register. By implementing the offset subtraction, the dynamic range of the device improved from 60dB to 94dB. An increase in noise variance was, however, noticed and attributed to non-ideal charge subtraction with the OCG barrier (Spirig *et al.*, 1997).

Johnson (1995) demonstrates a method for increasing the dynamic range of a CCD based imaging system through a non-linear (logarithmic) detection process. The implementation described in the work uses both anti-blooming circuit features

and time varying control voltages to shift the signal-to-noise characteristics to a larger range of illumination (Johnston, 1995).

Similar functions have been included in other charge-coupled devices. Burke and Smythe, Jr. (1983) present a time-integrating correlator using the charge-couple device concept. This device is not an imaging device but is an analog processing chain created with CCD technology, which was the original intent of CCDs (Amelio *et al.*, 1970; Boyle & Smith, 1970). A charge skimming circuit is incorporated into this device. This circuit provides a mechanism for transferring a small portion of the integrated charge, which contains correlation information, from a large bias charge. The charge at the output is reduced by tenfold, yielding a dynamic range of 67dB (Burke & Dan L. Smythe, 1983).

1.6 Temporal Analysis

In order to better understand the image acquisition process and to find ways to improve upon this process, mathematical models for a commercially available imaging system are developed. Using linear systems theory as a tool, an in depth study of the detection process, when using an interline transfer charge-coupled device (CCD) as the optical transducer, is performed. The detection process for one pixel in the array is analyzed both in the time and frequency domains. The results of the analysis are used to determine the signal-to-noise ratio (SNR) at the detector output, thus, expressing a figure-of-merit for the system.

Using signal and noise transfer concepts is not new to imaging system analysis (Haas *et al.*, 1979; Burns, 1989; Burns, 1990; Harada *et al.*, 1992). This type of analysis is often performed on medical imaging systems (Cunningham & Shaw, 1999; Pelli & Farell, 1999; Burgess, 1999). The analysis is often performed, however,

in the spatial domain on systems that capture a single image or a single integrated image. Rather than spatial characteristics or spatial response, this work focuses on the system's temporal response and ability to recover temporal information. Along these lines, the input irradiance is also defined temporally, rather than spatially.

This investigation uses as the input to the imaging system a general, linear systems description of the probe beam from a pump/probe absorption spectroscopy (PPAS) experiment (Fiechtner & Linne, 1994; Settersten, 1999; Linne *et al.*, 1995a). In this specific case, the input is defined as the combination of the steady state background irradiance and noise, which are inherent in a probe beam, and an additional modulated information bearing signal. Using a linear systems model, the analysis objective is, therefore, to determine how to extract the useful information from the general probe input.

Even though this investigation is based on the specific task of determining the modulation depth in a PPAS diagnostic, many of the results can be applied to other imaging diagnostics. The analysis performed in this investigation assumes a modulated information signal as the input. The methodology used in this work invites general use from other detection system investigations that have as an input a modulated irradiance.

1.7 Imaging System Description

The diagnostic imaging system under study is a modified version of the commercially available MicroMAX 1300Y camera, designed and manufactured by Roper Scientific, Inc., (Princeton Instruments). The MicroMAX 1300Y is a cooled, high-resolution digital camera that is designed for scientific and industrial applications (Roper Scientific, 1998a). In order to meet our research objectives, hardware modifications have

been made to the imaging system's controller and camera head.

The CCD chip used in the system is the Sony ICX085AL, 2/3 inch, interline transfer image sensor. The CCD's pixels are 6.7μm square and are developed with microlenses that focus the incident light onto each pixel's sensor area. The active area consists of 1030 rows and 1300 columns, which results in over 1.3 million total active pixels. Since the CCD has an interline transfer architecture, the sensor features an electronic shutter, which makes it possible to accurately control the image exposure time without using a mechanical shutter.

1.8 Contributions of this Work

Not only does the problem of detecting a small signal value in the presence of a larger background and noise arise in laser diagnostics that are used to extract information from physical systems, but it also arises in medical imaging and other non-destructive evaluation applications. Detecting a small anomaly embedded in a large background and noise is essential to the development of selected medical imaging systems (Burgess, 1999). Other than diagnostic techniques, night vision systems or vision applications under restricted circumstances, such as harsh weather and fog, face technical obstacles that are similar to those presented in this work.

The material presented in this thesis offers a range of contributions to the fields of two-dimensional diagnostic imaging and temporal analysis of a solid-state imaging system. Of particular value are;

- Implementation of synchronous focal plane processing functions in an imaging system,
- Development of a mathematical model describing the imaging system's processing functions,

- Development of a mathematical model describing the input irradiance,
- Imaging system analysis and performance predictions, and
- Demonstration of the imaging system's processing functions and comparison with performance predictions.

Other than the developments and results, the framework of this research is important. It is presented in a form that can be easily adapted to other imaging developments that face similar concerns. As an example, the mathematical definition of the input irradiance can be used to analyze other detection systems, with a range of values for the background, noise, and signal. An analysis of this type would provide insight to the relationship between the total input irradiance and the detection system's processing functions, which can lead to design changes and optimization.

Supporting mathematical models and experimental hardware, which were required to complete this investigation, can be used to expand the direction of complementary investigations and to expedite further investigations. Supporting mathematical models, which include a model of a simplified lock-in amplifier (homodyne detector) and an expression for determining modulation depth from both a lock-in amplifier measurement and a dc voltage measurement, can be used to compare new instrumentation performance. The hardware developed to demonstrate the imaging system's ability can also be used in other investigations that require a controlled irradiance source.

This work, therefore, not only extends the state-of-the-art in diagnostic imaging systems, but also provides a mathematical framework for analyzing weakly modulated images and for analyzing an instrument's ability to resolve them. The following subsections elaborate on the contributions offered to the field of diagnostic imaging.

1.8.1 Two-Dimensional Gated Integration With A CCD

A commercial interline transfer CCD is used as a two-dimensional gated integrator. In an effort to extract a modulated image from both a large background and noise, the CCD's exposure mechanism is synchronized with the modulation waveform. Using both the frequency and phase synchronization and the intrinsic interline transfer architecture, the input irradiance is either integrated or rejected at the focal plane. The results show that an interline transfer system can, therefore, be operated as a two-dimensional gated integrator.

1.8.2 Integration Threshold Implementation and Investigation

An integration threshold feature is proposed, implemented, and investigated in the interline transfer CCD architecture. A potential barrier between the CCD's sensor and storage well is used to create a "dead-band", which accumulated charge in the sensor must surpass before it is integrated in a storage well. The process is similar to anti-blooming, which is implemented with another potential barrier and the substrate potential well.

The motivation for implementing a dead-band threshold is to increase the number of exposures that can be integrated prior to saturation and, thus, improve upon the SNR. The input irradiance is assumed to contain a large constant value and only a small signal value. The purpose of the integration threshold is, therefore, to remove as much of the constant value as possible and retain the small signal.

The results show that a dead-band threshold can be implemented in a commercially available interline transfer CCD. The number of exposures that can be integrated without saturating the CCD are shown to increase as the dead-band threshold is raised. Also apparent from the results, however, is an increase in noise, which miti-

gates the SNR improvement achieved by acquiring an increased number of exposures.

1.8.3 Heterodyne Detection With A CCD

It is shown that an interline transfer CCD can operate as a heterodyne detector. Both the CCD's electronic shutter and charge accumulation mechanism are synchronized and phase locked to a modulated image. Using the synchronized detection process, which operates at a different frequency than the modulated image, the image is translated to an intermediate frequency. By selecting an intermediate frequency that is less than the imaging system's frame rate, both the frequency and phase information, from the modulated image, can be resolved at the output.

1.8.4 Input Irradiance Model Development

The irradiance that enters the imaging system as the input is defined as a continuous time function. The specific irradiance source introduced is the probe beam irradiance from a pump-probe absorption spectroscopy diagnostic (Fiechtner & Linne, 1994; Linne *et al.*, 1995a; Settersten, 1999). The probe beam is not, however, presented with a spectroscopic representation. Instead, the irradiance is defined as a linear function that is the sum of a steady state background component, photon noise, $1/f$ noise, and a modulated information bearing signal. The power spectral density of each component is developed individually and the power spectrum of the total irradiance is expressed through superposition.

Defining the input irradiance as the sum of individual spectra provides both flexibility and convenience in analyzing the imaging system. With these definitions, it is possible to investigate the spectral composition of each component after it passes, individually, through the imaging system model. The analysis can, therefore, be

performed in general terms independent of both the specific diagnostic technique and the transducer model.

1.8.5 Imaging System Model Development

Mathematical models of the imaging system are presented and analyzed. The focal plane processing functions, incorporated into the imaging system, are defined and modeled mathematically. A complete temporal frequency response is presented that is used to determine the spectral content of the images at the output of the imaging system.

Based on the focal plane processing functions, the imaging system can be operated in two modes. Both modes, the gated integration mode and the heterodyne detection mode, are modeled and analyzed. The irradiance model, introduced in the previous sub-section, is applied to the imaging system model to predict its ability to resolve modulation depth. The results of the analysis show the gated integration mode is better suited for resolving modulation depth. The heterodyne detection mode does, however, retain phase information, which the gated integration mode does not. Phase information in the form of images can be used in other applications, such as ranging and mapping.

1.8.6 Modeling Foundation

The foundation for the mathematical models are built from communications and linear systems theory. Using this model development practice and analysis procedure, provides insight to the detection process at a systems level. An understanding of the system level parameters and processes is obtained on a broad scope. This scope of understanding facilitates design and development efforts, which can be focused

on specific sub-systems that most influence the entire imaging system's processing ability.

1.8.7 Diagnostic Imaging Performance Predictions

By applying the input irradiance mathematical model to the imaging system's mathematical model, a mathematical description of the imaging system's expected output is obtained. The analysis is made specifically to determine the system's ability to extract modulation depth from a probe beam in a PPAS diagnostic. The results show the gated integration mode will perform better than the heterodyne detection mode in this context. Based on the output signal-to-noise ratio, when using the gated integration mode, the imaging system can extract a modulation depth of 10^{-4}.

1.9 Thesis Summary

This work investigates an imaging system's capacity to extract a weakly modulated image that is superimposed on a large background and is embedded in noise. In order to perform this investigation, the foundation of this work is first built with developments and mathematical fundamentals from multiple, supporting disciplines. To begin with, CCD functionality is used to develop the foundation for the pixel level charge maneuvering proposed in this work. The CCD's charge maneuvering capability provides renders input processing at each pixel. The processing functions are defined and analyzed using mathematical fundamentals from communication theory. Also utilized in the foundation of this work are probabilistic and statistical descriptions of the signal and noise components. In particular, the mathematical fundamentals used to describe the physical nature of light are incorporated into the analysis foundation.

An introduction to CCD technology is presented in Chapter 2. While omitting

the extensive technological background of CCD's, this chapter briefly covers the fundamental theory behind detection of photons with such a device. Three conventional CCD architectures are then described to demonstrate the attractiveness of the interline transfer architecture. Chapter 2 then concludes with characteristics that are specific to the interline transfer CCD used in this investigation.

After introducing, in Chapter 2, the functionality of an interline transfer CCD, Chapter 3 presents the charge maneuvering operations that are incorporated into the architecture. Two application specific features are implemented in the imaging system by synchronously controlling the manipulation of photoelectrons at each CCD pixel. These features, which are a gated exposure integrator and an integration threshold are discussed in Chapter 3.

In order to fully develop the mathematical analysis, a summary of some mathematical techniques is first presented in Chapter 4. This chapter, like Chapter 2, is not exhaustive. It merely serves as a review of the mathematical functions, taken from communication and linear systems theory, that are used in the imaging system analysis.

The first step in analyzing the imaging system is to mathematically define the input components. Chapter 5, therefore, presents a mathematical description of the input to the imaging system. The input to the imaging system is defined as the sum of three components; the steady state background, the modulated information bearing signal, and noise. Mathematical descriptions of each of the three components are developed, which, when combined, create a description of the total input. The mathematics developed in Chapter 5 are crucial to the analysis of the imaging system performed in later chapters.

The imaging system's detection capability is then mathematically defined with

linear processing functions. Two operational modes are presented. A gated integration mode is presented in Chapter 6 and a heterodyne detection mode is presented in Chapter 7. Both of the operating modes are mathematically modeled in their respective chapters. After developing models, or system functions, the mathematical description of the input, from Chapter 5, is applied to each model. Chapters 6 and 7 conclude with imaging system performance expectations based on the modulated input and operating parameters.

Chapter 8 then presents operational results. Experiments were performed to test the functionality of the gated exposure integration and integration threshold features. The results from these experiments are presented in this chapter. The two modes of operation, the gated integrator and heterodyne detector, are tested using a light-emitting-diode (LED) as a source. The imaging system's ability, in the gated integrator mode, to extract a small modulated image from a large background is tested and the results are presented. Finally, results from testing the heterodyne detection mode are presented.

The thesis concludes with discussions and conclusions in Chapters 9 and 10 respectively. Chapter 9 discusses the imaging system's performance and desired performance. Also included in this chapter are observations on the level of collaboration with Roper Scientific, Inc., and the breadth of disciplines incorporated into this investigation.

Chapter 10 concludes with a review of the investigation. The contributions made by this work to the fields of imaging in laser diagnostics and other selected imaging applications are reviewed. The limitations of this work are outlined and suggestions for future work are offered. A final summary is then given in conclusion.

Chapter 2

DIAGNOSTIC IMAGING SYSTEM DESCRIPTION

This chapter introduces the imaging system's technical infrastructure. A general description of the imaging system is given, followed by specific information about the hardware and software. Three different CCD architectures are then discussed, focusing on the interline transfer architecture. Finally, this chapter concludes with discussion on characteristics specific to the CCD detector and overall imaging system used in this work.

2.1 General Description

The diagnostic imaging system is a modified version of the commercially available MicroMAX 1300Y camera, designed and manufactured by Roper Scientific, Inc., (Princeton Instruments). The MicroMAX 1300Y is a cooled, high-resolution digital camera that is designed for scientific and industrial applications. The MicroMAX 1300Y data sheet is included in Appendix A. In order to meet our research objectives, hardware modifications have been made to the imaging system's controller and camera head.

The WinView software package, also developed by Roper Scientific, Inc., is used in conjuction with the imaging system to collect and store data. WinView is used to set up all configuration options prior to data acquisition. This includes configuration options for the modifications made to the camera hardware. Some image processing, such as flat-field correction, is performed with the WinView package, but most post

processing and data analysis is performed in MatLAB.

2.1.1 Hardware

The imaging system is comprised of a hardware controller, a camera head, and a computer interface, as illustrated in Figure 2.1. The controller contains a serial

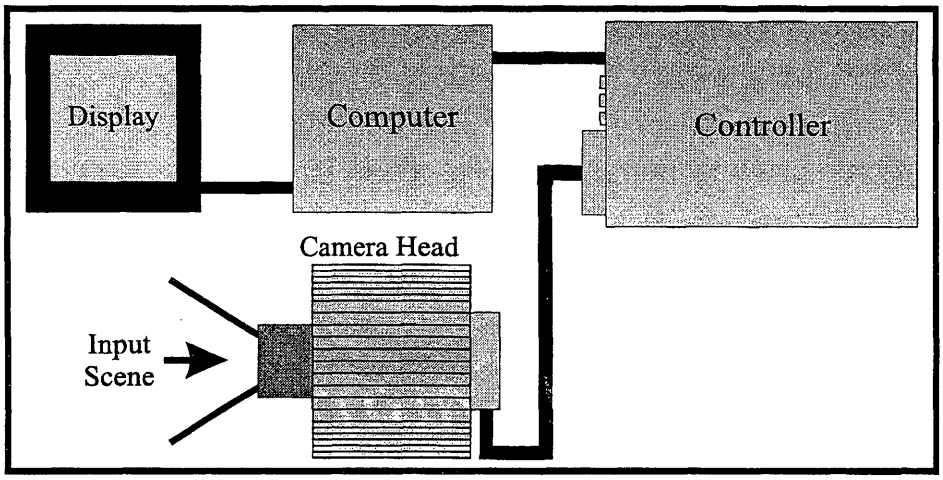

FIG. 2.1. Imaging system hardware illustration

data communication interface card and a controller card. The serial interface card receives, from the computer, hardware setup instructions and transmits, to the computer, digital image data. The controller card contains electrically programmable logic devices (EPLDs) that control the operation of the camera head, which is designed as a slave device. The imaging system's analog-to-digital converter (ADC) is also part of the controller card. Further information about the controller can be found in the MicroMAX System Manual from Roper Scientific, Inc., (Roper Scientific, 1998a).

Controller initialization and parameter configuration is accomplished with the WinView software package. After the controller is configured with the imaging pa-

rameters, such as integration time, region of interest (ROI), imaging mode, etc., it then generates the necessary clock and logic signals for operating the camera head. Once configured, the controller, therefore, autonomously manages the image integration process, the image read out process, the digital conversion process, and, finally, the flow of data to the computer.

The camera head contains the CCD imaging array, CCD driver circuitry, an EPLD, and low noise read out electronics. The camera head is a slave device and only responds to signals sent from the controller. Some logic is incorporated into the camera head's EPLD. This logic converts the clock signals sent from the controller to alternate clock signals required to operate the particular CCD device utilized in this imaging system.

The CCD chip used in the imaging system is the Sony ICX085AL, 2/3 inch, interline transfer image sensor. The CCD's pixels are $6.7\mu m$ square and are developed with micro-lenses that focus the incident light onto each pixel's sensor area. The active area consists of 1030 rows and 1300 columns, which results in over 1.3 million total active pixels. Since the CCD has an interline transfer architecture, the sensor features an electronic shutter, which makes it possible to accurately control the image exposure time without using a mechanical shutter. Further discussion on this particular CCD array is presented in section 2.5.

After an image is captured and stored in the CCD, low noise electronics, incorporated into the camera head, amplify the CCD's output signal during read out. Once the analog output signals are amplified, they then propagate to the controller via shielded twisted pair wire, for digitization. Digital logic from the camera head's EPLD is also used to generate clocking signals for the amplification stages during the read out process.

A thermoelectric cooler is also incorporated into the camera head. This device cools the CCD chip in order to reduce the amount of dark charge that builds up over time in the CCD's pixels. Dark charge is treated as noise and is discussed in section 5.10.2. The temperature is set by the user in software and is monitored and regulated by electronics in the controller.

In order to develop the diagnostic imaging system described in this thesis, both the controller and camera head are modified from their original configuration. However, much of the original functionality, as designed by Roper Scientific, Inc., has been retained. Controller modifications were made in the digital logic, and camera head modifications include both digital logic and additional analog circuitry.

The controller's digital logic is implemented in electronically programmable logic devices (EPLDs). Additions to the logic include a camera head initialization mode, which generates a pre-trigger that instructs the camera head to clean the CCD. Other changes include logic for the integration of multiple exposures on the CCD chip prior to read out, exposure timing functions, and imaging sequence control.

The digital logic in the camera head is reconfigured and circuitry is added to control the CCD barrier voltages during an exposure. The camera head's digital logic is also implemented in an EPLD. The logic includes an initialization mode, which creates clocks to clean the CCD and varied control over the electronic shutter mechanism. The additional circuitry, added to the camera head, provides an on-chip integration threshold mechanism, which is discussed in section 3.4. The integration threshold circuit design and discussion on its functionality in included in Appendix J

Parameters for two of the imaging system modifications need to be configured with the software interface. A counter in the controller is added to provide flexibility and control over the number of exposures that are integrated, on the CCD chip, into

a single frame. The counter is configured prior to imaging, via the software interface, with a twelve bit value. The system can, therefore, be set up so that a single frame may range from a single exposure to the on-chip integration of 4095 discrete exposures.

The second parameter that needs to be configured is a voltage level in the camera head's additional integration threshold circuitry. Two eight bit digital-to-analog converters (DAC) are used to set the integration threshold in a range from 0V to 5V. This voltage level is set, through the software interface, with an Inter-Integrated Circuit (I^2C) serial interface between the controller and the camera head.

The integration threshold controls the CCD's readout gate (ROG) during an exposure. The CCD's ROG separates the sensor and adjacent charge storage site. The ROG acts as a variable barrier for controlling the flow of electrons from the sensor to the storage site. Since the ROG is a variable barrier, its level can be used to control the amount of charge that must accumulate in the sensor before additional charge will spill over the barrier into the storage site. Setting the ROG barrier level to a level above its minimum, during the dwell time of an exposure creates a dead-band threshold between the sensor and the storage site. Once accumulated charge exceeds the dead-band, then it will be integrated. Further discussion on this modification is included in section 3.4.

2.1.2 Software

The WinView software package from Roper Scientific, Inc. is used to configure the controller and camera head. The user configures the controller with the imaging parameters, such as integration time, timing mode, binning operations, etc., by entering the parameters into the software package. Detailed information about WinView can be found in the WinView User's Manual provided by Roper Scientific,

Inc., (Roper Scientific, 1998b).

The exposure counter and integration threshold voltage, discussed above, are also configured with the WinView software package. The exposure counter is set with the controller register diagnostic utility. The integration threshold voltage is configured with the get/set parameter diagnostic utility. Discussion on these settings and other software features used for the diagnostic imaging system is included in Appendix K, as a user's manual.

2.2 Charge-Coupled Devices

The imaging system's transducer is an interline transfer charge-coupled device (CCD). The CCD concept was developed by Boyle and Smith in 1970 at Bell Laboratories (Boyle & Smith, 1970). The first functional device was later developed in the same year by Amelio, Tompsett, and Smith, also at Bell Laboratories (Amelio *et al.*, 1970). By using the CCD concept, a multi-element device can be developed, and the signal in each element can be manipulated and recovered, without a maze of wires, bonds, and amplifiers (Dereniak & Crowe, 1984).

A charge-coupled device can be developed for purely electronic applications, such as a shift register, a sample multiplexer, a signal processor, or as a memory device. The most common application, however, is as an imaging device (Kopeika, 1998). The development of highly effective two-dimensional image sensors is facilitated by the responsivity of silicon (Si) to visible radiation, the ability to arrange Si based charge-coupled devices into an array, and the ability to recover the signal from each device in the array. CCDs are now commonly used in many consumer devices and industrial systems. They are used in professional video equipment, home video cameras, and auto focusing sensors. Also, product inspection and manufacturing systems,

or robotic systems, typically use CCDs to collect optical information (Holst, 1996).

The CCD, as an optical input transducer, has for many years been the technology of choice for imaging applications in the scientific community (Fossum, 1993). The development of CCDs with better noise performance, larger array formats, far larger than those needed for professional video applications, and greater well depths have enabled the scientific community to acquire multi-dimensional images and data. The CCD's intrinsic ability to provide spatially quantized and temporally sampled data, which can be transferred directly to a computer for processing and display, also make the device attractive for scientific studies (Janesick *et al.*, 1987).

2.3 Charge-Coupled Device Concept

A CCD is basically a collection of closely spaced metal-oxide-semiconductor (MOS) capacitors. The MOS capacitors can be configured into many different formats; the most common is either in a one-dimensional linear array or a two-dimensional area array. In an array, each MOS capacitor gives rise to an individual pixel.

A CCD's ability to perform three primary functions, which are charge collection, charge transfer, and charge output conversion, results from the use of MOS capacitors and their arrangement into a closely spaced array. Since the device is made of a doped Si material, the MOS capacitors can collect and store charge packets, which represent optical information, in localized potential wells (Barbe, 1975). Once the charge packets are collected, they are transfered to adjacent capacitors, and eventually to the output capacitor, by successive manipulation of potential wells. The information is then detected as a voltage at the CCD's output by converting the charge packet through capacitive coupling (Barbe, 1975).

The charge-coupled device concept is well defined (Séquin & Tompsett, 1975;

Janesick *et al.*, 1987; Schroder, 1987). Semiconductor manufacturers have, however, implemented the concept in different ways and developed a diverse range of structural and architectural types. This section discusses common structural features and the following section will describe some common CCD architectures.

The two basic structures are the surface-channel structure and the buried-channel structure. Surface-channel devices were developed first. The buried-channel structure was later designed to improve CCD noise performance. A buried-channel device reduces the effects of charge interface traps, which are present in surface-channel structures, by moving the charge packet away from the surface into the bulk of the material. In a surface-channel device, the charge interface traps (which randomly collect or pass on charge at the Si and silicon-dioxide (SiO_2) interface) randomly add or subtract charge to a packet as it passes through the MOS capacitor, thereby distorting the packet's value. In order to reduce the effects of charge trapping, a constant charge, called a fat zero, is passed through the potential wells along with the signal packet. Statistically, this process reduces the charge trapping noise, however, it also reduces the dynamic range in surface-channel CCDs (Dereniak & Crowe, 1984). Since a fat zero is not required in a buried-channel CCD, its structure provides greater dynamic range.

Today, most CCD sensors, including the CCD used in the imaging system for this work, are developed with a buried-channel structure. Therefore, the remaining discussion in this section focuses on buried-channel design concepts. Further information on surface channel design concepts can be found in texts on semiconductor design and semiconductor devices (Séquin & Tompsett, 1975; Dereniak & Crowe, 1984; Schroder, 1987).

2.3.1 Charge Collection

Using the definitions made in Appendix B, we can analyze the buried-channel CCD as depicted in Figure 2.2. The general buried-channel MOS capacitor consists of an N-type substrate that is diffused with a P-type faction. A cross section of the MOS capacitor structure is shown in Figure 2.2(a), in which x is a function of material depth.

Figure 2.2 illustrates the cross section of a single MOS capacitor. An imaging array contains thousands or millions of MOS capacitors organized in rows and columns. The metal layer, as shown in Figure 2.2, is placed over the array in organized strips, which leave gaps where no metal layer exists. In the case of a front illuminated CCD, incident light will enter the semiconductor (from the left in Figure 2.2) where the metal layer is not present.

N-type and P-type semiconductor material is produced by doping pure silicon with impurities. Doping silicon with donor impurities creates an N-type material that has an abundance of extra free electrons and doping with acceptor impurities creates a P-type material that has an abundance of extra holes (Horenstein, 1990). Using an extrinsic MOS capacitor, as shown in Figure 2.2(a), a structure is developed which uses majority carriers to represent the information packet, as opposed to minority carriers, which are used in a surface-channel device (Dereniak & Crowe, 1984).

The buried-channel CCD collects charge, produced by photons, and confines it in a potential well. When a gate voltage, V_g, is applied to the metal gate, as shown in Figure 2.2, a potential profile is produced. The potential profile is found by integrating the electric field, which is derived from Poisson's equation, over the depth of the material. Derivation of the potential profile is included in Appendix B.

The potential profile, shown in Figure 2.2, is modeled with three equations based

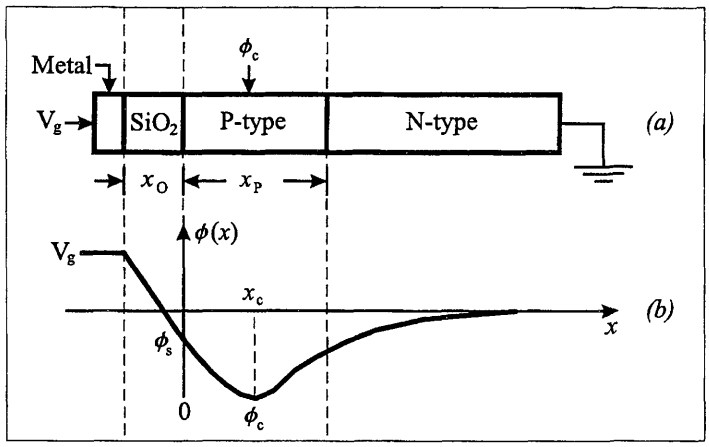

FIG. 2.2. Buried-channel CCD illustration: (a) semiconductor structure, (b) potential profile

on the boundaries between different materials (see Appendix B). The potential at the interface between the metal and the silicon-dioxide, SiO_2, is simply the voltage applied to the gate. The potential, $\phi_1(x)$, in the SiO_2 material is expressed in the following form.

$$\phi_1(x) = V_g - \frac{Q_g(x + x_o)}{\kappa_o \epsilon_o} \qquad -x_o < x \leq 0. \tag{2.1}$$

The potential in the P-type region from $x = 0$ to $x = x_p$ is given by equation 2.2 and the potential in the N-type substrate for $x > x_p$ is given by equation 2.3.

$$\phi_2(x) = V_g - \frac{Q_g x_o}{\kappa_o \epsilon_o} - \frac{1}{\kappa_s \epsilon_o}\left[Q_g x - \frac{1}{2} q N_a x^2\right] \qquad 0 < x \leq x_p. \tag{2.2}$$

$$\phi_3(x) = V_g - \frac{Q_g x_o}{\kappa_o \epsilon_o} - \frac{1}{\kappa_s \epsilon_o}\left[Q_g - q N_a x x_p + \frac{1}{2} q N_a x_p^2 + \frac{1}{2} q N_d (x - x_p)^2\right]. \tag{2.3}$$

The potential profile, therefore, is a function of the doping concentrations, N_a and N_d,

the oxide thickness, x_o, which affects the capacitance, and the metal gate potential V_g with surface charge density Q_g. Since like charges repel, applying a positive voltage to the gate forces the holes in the P-type material to migrate to the N-type substrate. Thus, a region in the P-type material has been depleted of holes and is referred to as the depletion region. As a result of forcing the holes into the substrate, the potential energy in the depletion region is reduced, creating a potential minimum, or potential well. The location of the potential well and the depletion depth, x_d, is determined by the charge density at the gate, Q_g, and the requirement that the electrical charge remain neutral across the whole structure (Dereniak & Crowe, 1984).

$$Q_g = qN_a x_p - qN_d x_d \tag{2.4}$$

When a photon with energy that is greater than the band gap of silicon is absorbed in the depletion region, an electron-hole pair is produced. If the energy of a photon, ϵ, is greater than the energy required to break the covalent bond of a valence electron in a silicon atom, then the electron in the valence band is excited into the conduction band, as a free electron. Since an electron is excited into the conduction band, a positive charge, or hole, remains in the valence band. The hole, however is mobile and is forced to migrate into the N-type substrate. The free electron is held in the depletion region at the potential minimum.

$$\epsilon = \frac{hc}{\lambda_w} \tag{2.5}$$

The potential well, or simply *well*, reaches a minimum in the capacitor's P-type region, as shown in Figure 2.2(b), which results in a barrier between the potential

well and both the SiO_2 material and the N-type substrate. As charge is collected in the potential minimum, the barriers, which are at a higher potential, confine the charge packet and prevent it from moving. A fluid flow analogy is often used when describing a potential well. If a charge packet is considered a volume of fluid, then for visualization purposes we imagine that the fluid will flow to the deepest part of the well.

2.3.2 Charge Transfer

After collecting photoelectrons in the MOS capacitor potential well, the charge packet must then be transferred to the CCD's output. In a typical CCD, as shown in Figure 2.3, the gate voltages applied to adjacent MOS capacitors are independent. If the gate voltages and their phases are clocked in a coordinated fashion, the charge packets can be forced to physically travel in a lateral direction. Notice in Figure 2.3 that the transfer direction, y, is orthogonal to the previously defined depth, x, of the material, shown in Figure 2.2. Also, to facilitate a qualitative discussion, the potential profile is depicted as a well and the fluid flow analogy is utilized.

In Figure 2.3(a) the voltage, V_{g1}, applied to the phase 1 gate is greater than the voltage applied to either the phase 2 or the phase 3 gates. Therefore, a potential well is created under the phase 1 gate. Also, a barrier in the carrier region is created between phase 1 and phase 2 since the potential under phase 1 is ϕ_m and the potential under phase 2 is ϕ_o. Photons absorbed in the depletion region under the phase 1 gate will , therefore, be collected as photoelectrons and contained in the well.

Increasing the voltage, V_{g2}, on phase 2 gate so that $V_{g2} = V_{g1}$ will lower the barrier between phase 1 and phase 2, thus, creating a potential well under phase 2 that is as deep as the well under phase 1. In this case, the barrier shifts between

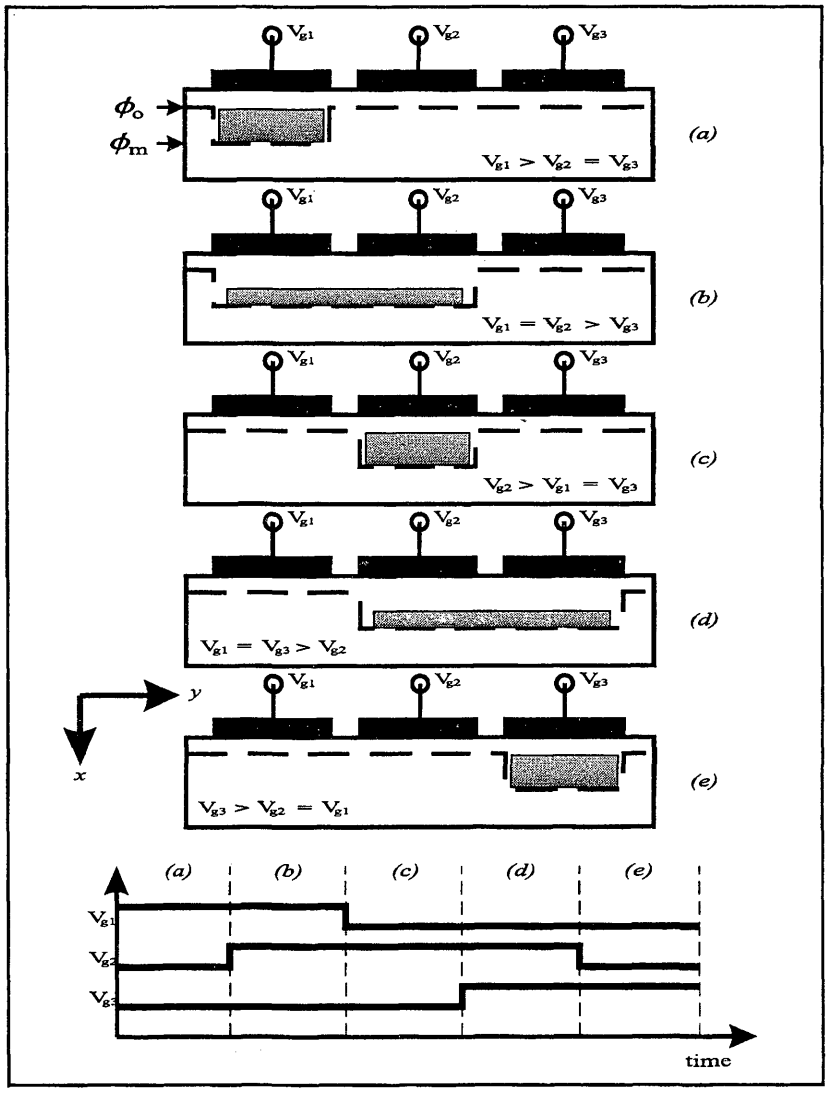

FIG. 2.3. Charge packet transfer through coordinated gate voltage clocking

phase 2 and phase 3, as shown in Figure 2.3(b). Since the potential well under both phase 1 and 2 is now the same, the charge packet is shared between the two wells.

After the charge packet is distributed between the wells in phase 1 and phase 1, the voltage on the phase 1 gate can be lowered, as shown in Figure 2.3(c). Lowering V_{g1} will force the entire charge packet to flow into the well under phase 1, since the well is removed under phase 1 and is retained under phase 1. At this point, a barrier exists on both sides of the phase 1 well, where the entire charge packet is now contained.

The same clocking cycle used to transfer the charge packet from phase 1 to phase 2 is also used to transfer the packet from phase 2 to phase 3 as shown in Figures 2.3(d) and 2.3(e). If the MOS capacitors are grouped in sets of three, as used in this illustration, then all the charge packets in an entire array can be transferred in parallel using the same clocking scheme. Other phase grouping arrangements can also be developed. Typically, CCD arrays are manufactured with three, four, or six phases. Two phase CCDs can also be developed with proper doping structures that force the charge packet to flow in one direction only (Holst, 1996).

2.3.3 Charge Output Conversion

Figure 2.3 illustrates a technique for transferring charge packets laterally through adjacent MOS capacitors. The technique is applied, in parallel, to the entire array to transfer the charge packets from each pixel to a single output point. Once the charge packet arrives at the output point, it is converted, through capacitive coupling, to a measurable quantity.

An on-chip, output preamplifier is typically used to covert the charge packet to a measurable voltage. Multiple read out techniques have been developed which convert

the charge packet to a voltage. The most common output technique uses a floating diffusion amplifier (Schroder, 1987; Holst, 1996).

The floating diffusion amplifier incorporates a preamplifier, an output MOS capacitor, a screen capacitor, and a reset capacitor. A reset pulse, on the reset capacitor, or gate, is first used to clear the output gate. The charge packet, or pixel, to be read out is then transferred to the output gate through the screen gate. This process results in a change in the preamplifier's output voltage, ΔV_{out}, which has a magnitude proportional to the change in charge, ΔQ_{out}, on the output capacitor, of capacitance C_{out}, and the preamplifier gain, G_{pa}. The conversion factor from electrons to volts is normally on the order of $1\mu V/e^{-}$.

$$\Delta V_{out} = \frac{\Delta Q_{out}}{C_{out}} G_{pa} \tag{2.6}$$

In order to mitigate drifts in the absolute value of the output voltage that occur after the output gate is reset, a differential sampling process is often used. Low frequency drifts in the output voltage can add noise, with a $1/f$ shaped power spectrum, to the output voltage. Sampling the reset voltage, sampling the change in voltage after the charge packet is transferred to the output gate, and then differencing the two samples produces an output signal that is not corrupted by the $1/f$ noise. Differentially sampling a CCD's output in this fashion is commonly know as correlated double sampling (CDS) (Dereniak & Crowe, 1984).

After the charge is converted to a voltage with the output amplifier, the voltage is then digitized with an analog-to-digital converter (ADC). Often there is only a single channel ADC through which each pixel voltage is digitized. The digitization process often requires only microseconds to convert the voltage to its corresponding digital count value, or digital number (DN). Converting an entire array, which may

contain hundreds of thousands or millions of pixels, however, requires hundreds of milliseconds or seconds. The ADC is, therefore, often the bottleneck in the read out process, which dictates the speed at which frames can obtained.

2.4 CCD Architecture

As previously stated, CCD manufacturers have not only developed different structural schemes, but also developed different architectural schemes. The most widely used are the linear, full frame, frame transfer, and interline transfer architectures.

In order to better discuss the interline transfer CCD that is used in the imaging system, its basic characteristics are introduced in this section. The characteristics of other CCD architectures are also introduced for comparative purposes.

The four architectures described below have fundamental similarities. Since a CCD is comprised entirely of MOS capacitors, each capacitor, or pixel, has the capability to collect photoelectrons if it is exposed to light. However, it is desirable to prevent photoelectrons from collecting in specific sections of the CCD, such as the section used only for transferring charge packets or the read out section. Once an image is collected, additional photoelectrons generated in the read out circuitry from direct exposure to incident light would add unwanted noise to the signal.

Therefore, an opaque mask is placed over sections of the CCD to block light from entering the semiconductor material and prevent the covered section from collecting photoelectrons. Placing a mask over an entire row or column of pixels creates a register that is used to shift, or transfer, charge packets without adding noise from additional exposure. A CCD's read out circuitry is also covered to prevent direct generation of photoelectrons in this region. As shown in the following sections, the

placement of the opaque mask, which determines a CCD's active pixel and masked pixel arrangement, is a major component in a CCD's architecture.

2.4.1 Linear CCD

The linear CCD, as illustrated in Figure 2.4, is comprised of one row of active pixels and one row of masked pixels, with corresponding columns. The exposed pixels collect the photoelectrons, which are then shifted to the masked pixels for read out. Thus, the masked row is normally referred to as a read out register. Once the previous exposure is transferred to the read out register, the subsequent exposure can begin immediately.

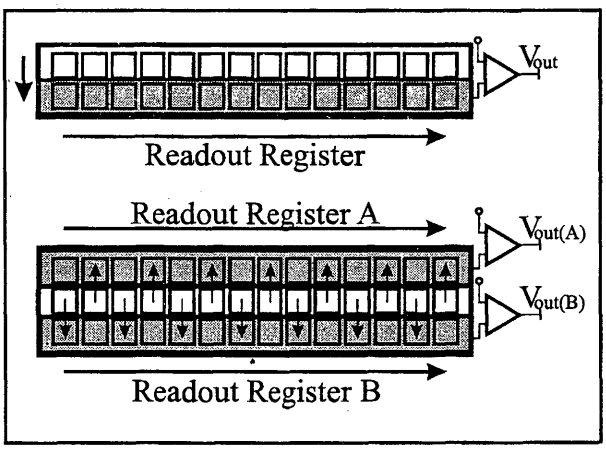

FIG. 2.4. Linear CCD

Very fast frame rates can be achieved with a linear array since only one row is read out of the array per frame (Holst, 1996). Multiple read out registers can also be used, as shown in Figure 2.4(b), to increase the CCD's frame rate. With multiple read out registers and corresponding outputs, multiple pixels can be read from the array simultaneously. Proper arrangement of the pixels is then accomplished with software.

Although a linear array can achieve high frame rates, complex imaging optics and motion control systems are needed to image a two-dimensional scene. Therefore, linear arrays are often used in an environment in which the object plane is fixed, such as document copy machines and image scanning machines. Linear arrays are also used for component inspection, where, the CCD is fixed and the item moves through the object plane.

2.4.2 Full Frame CCD

The full frame CCD (FFCCD) is comprised of multiple columns and more than one row of active pixels, as shown in Figure 2.5. Using this type of array, the object plane can be imaged in a single frame. In the FFCCD the active pixels are also used to transfer the image, one row at a time, to the horizontal register for read out. After an image is acquired in the active pixels, then the charge packets are read out one row at a time.

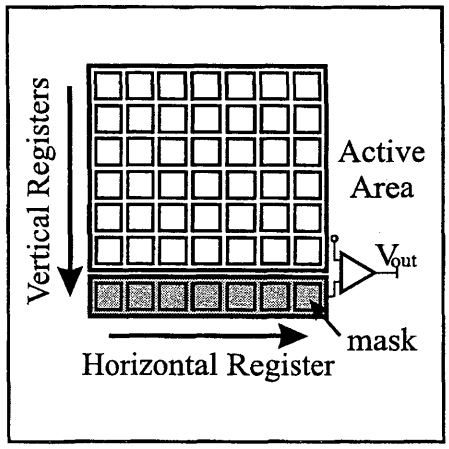

FIG. 2.5. Full Frame CCD

Since the active pixels are used to transfer the image, one row at a time, to the horizontal register for read out, image smearing can result. As the charge packets are

transferred along the active pixels, towards the read out register, additional photoelectrons collect in the potential wells. During the transfer sequence, the potential wells are essentially moving, therefore, additional photoelectrons produce a smearing effect in the image.

To prevent image smear, a mechanical shutter is often used with a full frame CCD. Image smearing will not be present if read out is performed while the mechanical shutter is completely closed (Holst, 1996). Since the active pixels in a FFCCD are continuously collecting photoelectrons, a mechanical shutter also controls the exposure time. An exposure is initiated by opening the shutter and then terminated by closing the shutter in front of the array.

A FFCCD architecture is typically used in digital snapshot cameras or low frame rate security cameras. In scientific applications, the FFCCD is used for imaging in experiments that have pulsed events, such as particle imaging velocimetry (PIV) experiments. The FFCCD is also extensively used in intensified cameras. An intensifier, which can be gated in nanosecond time scales, is often used as the shutter for a FFCCD camera.

2.4.3 Frame Transfer CCD

The frame transfer CCD (FTCCD) is very similar to the full frame CCD. A FTCCD, however, incorporates a masked portion of the array that is equal in size to the active portion of the array. This type of array is illustrated in Figure 2.6.

After an image is acquired in the active pixels of an FTCCD, the image is quickly shifted down under the masked portion of the array. While shifting the image from the active area to the masked area, the pixels are clocked at a much higher rate than they are during read out. Transferring charge packets down to the masked area

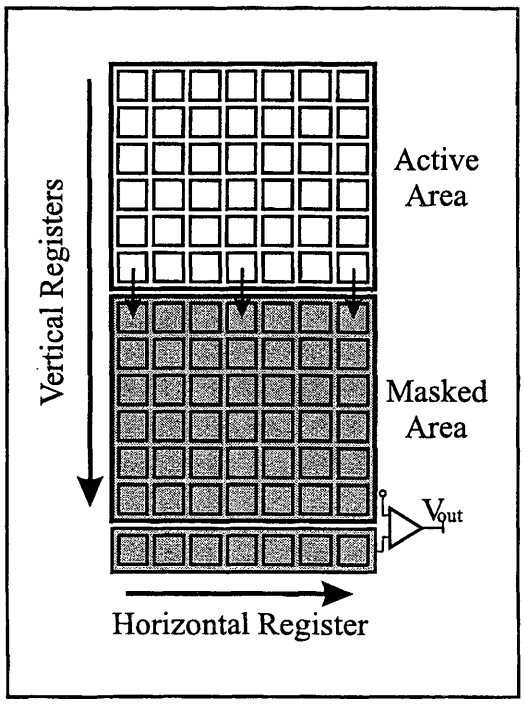

FIG. 2.6. Frame Transfer CCD

requires less time than the analog to digital conversion (ADC) process, and, thus, is performed at a faster clock rate. The addition of a mechanical shutter is not required because of the speed at which the image is transferred from the active area to the masked area.

After an image is transferred under the masked area, the slower read out and ADC process is then performed on only the charge packets under the mask area. While the charge packets under the mask are read out, a new image is acquired in the active pixels. The frame rate is, therefore, limited by the time required to read out and digitize the charge packets under the mask.

2.4.4 Interline Transfer CCD

The interline transfer CCD is similar to both the full frame and frame transfer architectures. The interline transfer CCD, as shown in Figure 2.7, has interlaced active columns and masked columns. After photoelectrons are collected in an active column, the charge packets are transferred to an adjacent column, which is covered with the mask. Once the charge packets are in the masked column, typically referred to as the vertical register, they are then read out without serious image smearing effects (Holst, 1996).

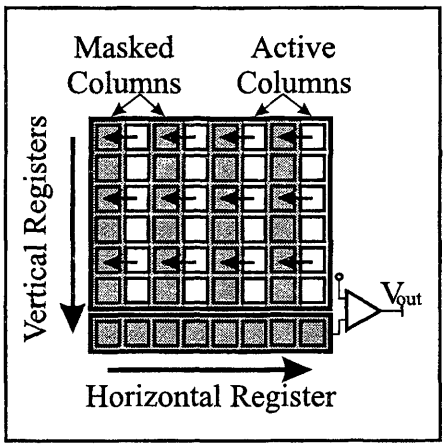

FIG. 2.7. Interline Transfer CCD

The interline transfer architecture provides a way to quickly shift the charge packets from an active pixel to a masked pixel, which results in accurate control over the image exposure time. The next image can be acquired in the active column immediately after the previous image is shifted under the masked vertical registers.

The drawback, however, is that the fill factor in an interline transfer CCD is less than that of the FFCCD or FTCCD. The fill factor is the ratio of image sensing area to total array area. Since the interline transfer CCD requires more physical area to

make one sensor, which includes an active pixel and a masked pixel, smaller pixels are incorporated into this architecture. Smaller pixels result in smaller well depths, which is the total amount of charge the pixel can contain at saturation.

2.5 Sony ICX085 Interline Transfer CCD

The CCD array used in the imaging system is an interline transfer CCD, manufactured by Sony. The CCD, model ICX085, is a 2/3-inch progressive scan image sensor. This CCD has 1300 horizontal pixels and 1030 vertical pixels, and each pixel is $6.7\mu m$ square.

Each pixel is comprised of a photo-sensor (or simply sensor) and three vertical MOS capacitors. The CCD is, therefore, defined as a three phase device. Since each pixel includes multiple capacitors, the sensor area is only a fraction of the total pixel area. Light that does not enter the sensor area will not be detected. In order to increase the amount of light that is incident on the sensor area, on-chip micro-lenses, as shown in Figure 2.8, are attached directly to the CCD during the manufacturing process (Sony, 1998). These lenses increase the device's effective fill factor.

The micro-lenses not only focus light into the sensor area, but also divert light away from the vertical register. Charge that enters the vertical register through means other than the exposure mechanism is considered noise. Even though the vertical register is masked with aluminum, a small amount of photons do penetrate the mask and enter directly into the vertical register. The micro-lenses, therefore, assist in reducing image noise by diverting photons away from the mask and vertical register.

Because of their optical properties, the micro-lenses place a restriction on the detectable wavelengths. The micro-lenses are plastic and, therefore, rapidly cutoff blue

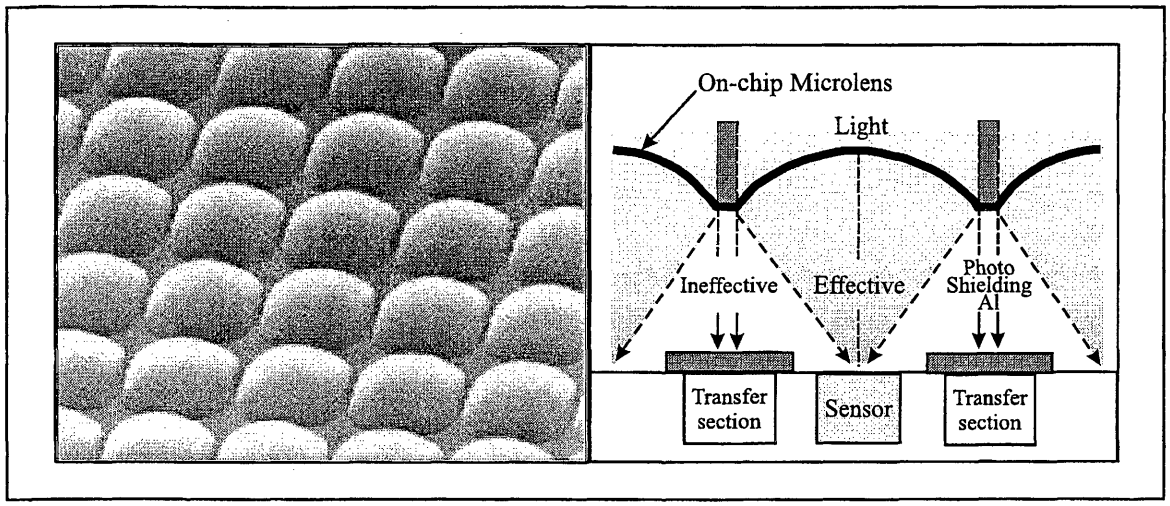

FIG. 2.8. On-chip mircolens structure

wavelengths and severely limit the detection capability in the ultraviolet region. This effect is seen in the CCD's quantum efficiency curve, which is included in Appendix C.

Included in the CCD's architecture is a variable speed electronic shutter. The electronic shutter provides the interline transfer CCD with the capability to capture images with variable and accurate exposure times. When an image is not to be acquired, the electronic shutter is activated and charge accumulated in the sensor is discarded into the substrate. The interline transfer CCD does not require an additional mechanical shutter. The electronic shutter also provides a mechanism to control pixel blooming. Blooming results when additional charge, beyond a pixels full well, spills over into adjacent pixels.

2.6 Illustrative interline transfer CCD Representation

As previously mentioned, each pixel in the interline transfer CCD includes a sensor, three MOS transfer capacitors and an electronic shutter. The semiconductor structure for one pixel is illustrated in Figure 2.9 (The on-chip microlens is not in-

cluded in this figure). As shown, the interline transfer CCD is a buried-channel CCD that has an N-type substrate. The sensor potential is developed in the 1st P–well and the vertical register potentials are developed in the 2nd P–well.

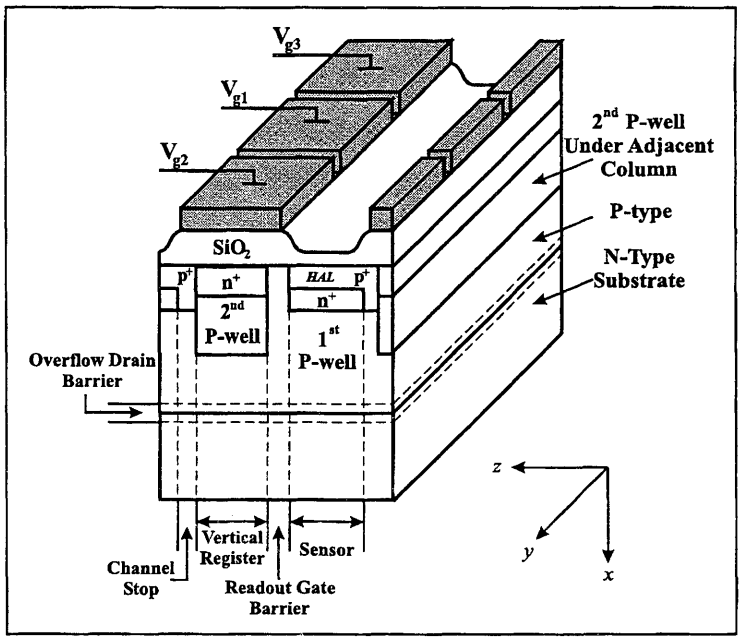

FIG. 2.9. Sony ICX085 interline transfer CCD semiconductor structure

For consistency, the coordinate system in Figure 2.9 is the same as the coordinates used in Figures 2.2 and 2.3. The buried-channel potential profile, in Figure 2.9, extends along the x direction. Based on the discussion in section 2.3, the interline transfer CCD has two buried-channel potential well profiles per pixel. The sensor's potential profile extends from the p^+ material, through the 1st P-well, and into the N-type substrate. The potential profile for the adjacent vertical register extends from the aluminum gate, through the 2nd P–well, and into the N-type substrate.

Photoelectrons are collected in the sensor well, which is the 1st P–well. Charge collected in the sensor can be transferred in one of two directions. The charge can either be drained and discarded into the substrate by transferring the charge in the

x direction, or it can be stored in the vertical register by shifting the charge in the z direction.

After a charge packet is shifted and stored in the vertical register, it can then be transferred to the CCD's output amplifier. Coordinated manipulation of the three gate voltages, as illustrated in Figure 2.3, forces the charge stored in the vertical register to move in the y direction.

Figure 2.9 is the cross section of one pixel in the CCD array. Each pixel in the array has the same cross section and each pixel is controlled in parallel. The ROG barrier and the OFD barrier in each pixel are connected in parallel and, therefore, perform the same operation across the array. Each pixel is not and cannot be controlled independently.

The flow of charge is controlled by manipulating the depth and location of potential wells. The sensor's well depth is a function of the heavily doped p^+ type region above the 1st P–well. Unlike the fixed potential used to analyze the buried-channel CCD in Figure 2.2, the potential applied to the N-type substrate in this device is variable. The potential profile from the 1st P–well to the N-type substrate is, therefore, controlled by the voltage applied to the substrate. In relation to Figure 2.2, $\phi(x)$ for $x > x_p$ is also a function of the substrate voltage.

Increasing the voltage applied to the substrate lowers the potential well in the substrate. In other words, raising the substrate voltage forces the deepest part of the sensor's well to migrate from the 1st P–well toward the substrate. When the substrate voltage is raised, charge in the sensor's well, therefore, flows to the deepest part of the substrate and is discarded.

The same process is used to transfer the charge packet from the sensor to the vertical register. Increasing the voltage applied to gate 2, V_{g2}, increases the well depth

in the 2nd P–well. When the potential well under gate 2 is deeper than the sensor's potential well, the charge packet will shift to the deeper well and into the vertical register.

In order to better facilitate discussion about charge flow in the remainder of this thesis, the two dimensions x and z are depicted along the same axis, as illustrated in Figure 2.10. This figure shows the potential wells for the sensor, substrate, and vertical register. Between the wells are barriers that prevent charge from moving. The overflow drain (OFD) barrier prevents the charge from moving from the sensor to the substrate, and the readout gate (ROG) barrier prevents the charge from moving from the sensor to the vertical register. The barriers OFD and ROG are controlled by the substrate voltage, V_{sub}, and the vertical register gate voltage, V_{g2}, respectively.

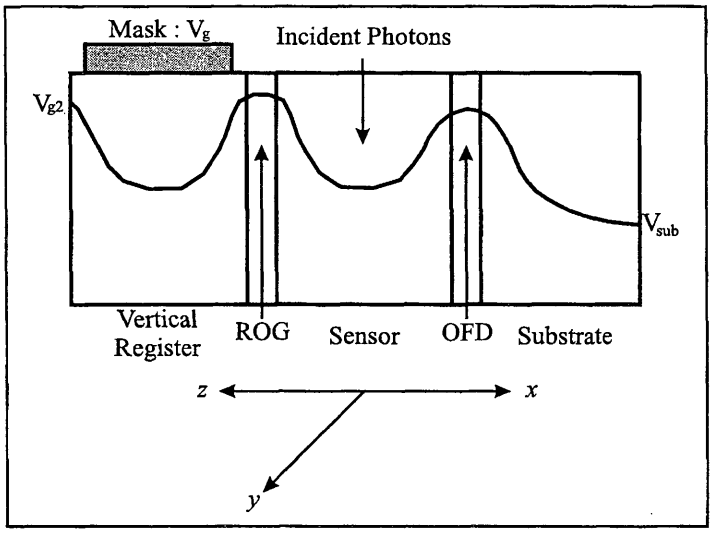

FIG. 2.10. Simplified cross-section illustration of the Sony ICX085 interline transfer CCD

2.6.1 Charge Flow Under Normal Operation

In a normal detection process, the OFD barrier is initially lowered by raising the substrate voltage. This forces all charge accumulated in the sensor to immediately drain into the substrate. The electronic shutter mechanism is, therefore, controlled with the OFD barrier.

Image acquisition is initiated by raising the OFD barrier. Once this barrier is raised, all photoelectrons are accumulated in the sensor area. After the desired exposure time has elapsed, which began when the OFD barrier was raised, the charge packet accumulated in the sensor is shifted to the vertical register by lowering the ROG barrier.

After the charge packet is stored in the vertical register, the ROG barrier is then raised to its original level. The OFD barrier is once again lowered to drain new photoelectrons from the sensor to the substrate. Finally, the charge packet stored in the vertical register is transferred, along the y direction, out of the CCD by clocking the three vertical register phases. While the image is being read from the array, the process starts over and the next exposure is captured in the sensor.

The OFD barrier, as its name would suggest, is also the mechanism that controls the anti-blooming feature. When an image is acquired and charge is integrated in the sensor, the OFD barrier is set lower than the ROG level. If the sensor is saturated, meaning the sensor's well is full of charge, additional charge accumulated in the sensor will spill over the OFD barrier and drain into the substrate. Setting the OFD barrier lower than the ROG barrier prevents additional sensor charge from spilling over the ROG barrier and into the vertical register or into adjacent sensor wells.

2.7 Imaging System Parameters

In order to characterize the imaging system several baseline measurements were performed to do an initial assessment of the imaging system's performance under normal operating conditions. This section highlights some results from standard CCD system tests. Some of the imaging system's attributes are also discussed toward the end of this section.

A block diagram for a typical CCD detection system is illustrated in Figure 2.11 (Janesick *et al.*, 1985). Photoelectrons collected in the CCD are converted to a voltage by the CCD's output amplifier. The CCD's output voltage is then amplified prior to converting it to a digital value with the ADC.

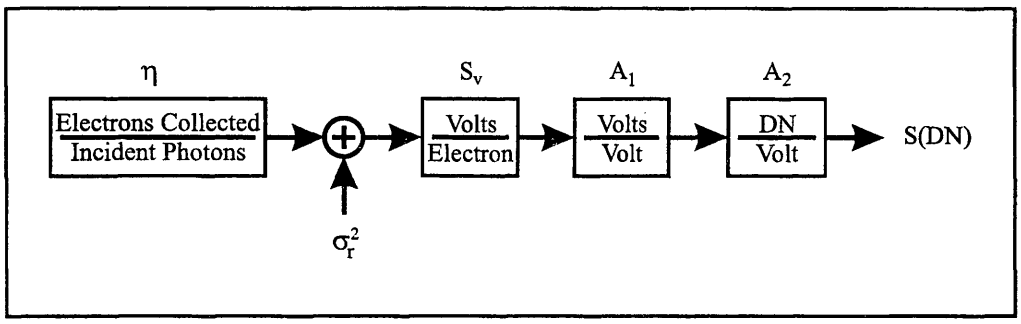

FIG. 2.11. CCD signal conversion factor representation

The parameters in Figure 2.11 can be either measured or taken from device specifications. Quantum efficiency (QE), η, is a linear factor that relates the number of incident photons to the number of electrons that accumulate in the sensor. The QE is a function of wavelength and is specified as a QE curve across the device's spectral operating region. The QE curve is taken from device specifications and is shown in Appendix C. The QE is also considered a constant when the input irradiance is monochromatic.

The conversion factor for the ADC, A_2, can also be taken directly from manufacturers specifications. The read out noise floor, σ_r^2, and the camera gain, A_1, which is the amplification from the CCD's output to the ADC's input, can be measured. After finding A_1, A_2, and σ_r^2, the gain in the CCD's output amplifier, S_v, can be determined with the photon transfer technique (Janesick *et al.*, 1985; Janesick *et al.*, 1987).

2.7.1 Transfer Gain

The signal between the CCD's output and ADC's input passes through three gain stages, which are combined into the single gain parameter A_1. Analytically, the total gain from the CCD output to the ADC input, A_1, is determined to be 4.5 V/V. Experimentally, however, A_1 was shown to be closer to 4.1 V/V.

2.7.2 Digital Resolution

The imaging system's analog to digital converter (ADC) is a 16-bit converter that has a 1MHz sample rate. The ADC generates a digital count value from 0 to 65535, therefore, producing a dynamic range of 96dB. Since the CCD saturates at approximately 28,000 counts, the dynamic range of the ADC exceeds the dynamic range of the CCD by about 50dB.

The input to the ADC can range from 0 to 10 volts. The actual signal from the camera, however, only has a range of 0 to 5 volts, which limits the maximum digital count value to 32768. Since the input range is set at 0 to 10 volts, the ADC's transfer gain, A_2, is 1 DN per 0.1526 mV, (DN is digital number or number of counts).

2.7.3 Frame Rate

The CCD is has 1300 by 1030 active pixels, plus some dummy columns and rows that are incorporated before and after the active area. Based on the maximum sampling rate of the system's ADC, which is $1\mu s$ per pixel, the system requires about 1.34 seconds to read out the entire array.

Smaller regions of interest (ROI) can be specified, which increase the system's frame rate, albeit at the cost of total data pixels. The pixels that are not in the ROI are not digitized and simply discarded, thus, increasing the frame rate. A single horizontal strip of pixels can be read from the array at a maximum frame rate of 30 Hz.

Binning is an on-chip process which reduces the number of pixels to be digitized and, therefore, increases the frame rate. Pixel binning is the process of summing, on the array, the charges from multiple pixels into a single super-pixel. The super-pixel is then converted to a voltage at the CCD's output and then digitized with the ADC.

2.7.4 Read Noise

The read noise floor, σ_r^2, is the intrinsic noise associated with the imaging system during read out. Read noise is the noise seen at the output when imaging a dark field and performing both background subtraction and flat-field correction. Read noise is, therefore, a combination of dark charge, noise in the CCD's output amplifier, noise in the amplification stages between the CCD and the ADC, and any other noise source that is independent of signal level (Janesick *et al.*, 1987). Much of the noise that comprises the read noise floor can be considered Johnson noise.

When the CCD is cooled to -10^oC, the read noise standard deviation was measured to be 5.02 DN, which, as will be shown below, corresponds to 6.16 electrons.

The read noise variance is, therefore, 25.2 DN, which is 37.9 electrons.

2.7.5 Photon Transfer Curve

Once both the system gain, A_1, and the ADC conversion factor, A_2, are known, the CCDs output amplifier gain, in terms of volts/electron, can be calculated using the photon transfer technique (Janesick *et al.*, 1987). The photon transfer technique is a common test method for evaluating CCD performance characteristics in absolute units (Janesick *et al.*, 1985).

A factor K is defined (Appendix D) that relates the unknown output amplifier gain, S_v, to the known gains A_1 and A_2. In order for the units on S_v to be volts/electron, the units on K must be electrons/DN.

$$K = \frac{1}{S_v \, A_1 \, A_2} \tag{2.7}$$

The constant K can be determined using two different methods. Both methods are based on data from a uniform illumination source. First, K can be found graphically by plotting the photon transfer curve. The photon transfer curve is a plot of the standard deviation of the signal, $\sigma_s(DN)$, as a function of the mean value of the signal, $S(DN)$. Both $\sigma_s(DN)$ and $S(DN)$ are represented as a digital number. As the irradiance increases the output becomes dominated by photon noise and the slope of the graph becomes 1/2, as shown in Figure 2.12. The point at which a line, fit to the photon transfer curve, having a slope of 1/2, intersects the abscissa is the constant K (Janesick *et al.*, 1985).

Photon noise is the fundamental noise limit of irradiance set according to the random incidence of photons as described by Poisson statistics (Dereniak & Crowe, 1984). The photon noise standard deviation is often considered as the square root of

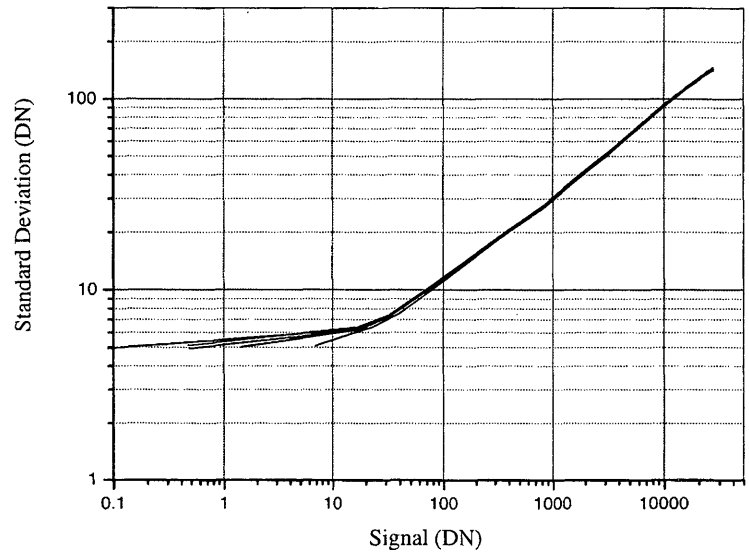

FIG. 2.12. Photon transfer curve

the number of detected photons. Plotting the square root of the abscissa in a log-log plot produces a line that has a slope of 1/2, which is the approximate slope of the lines given in Figure 2.12.

A second method that is more accurate is to calculate a K value directly from the mean signal value, standard deviation of the signal, and read noise floor.

$$K = \frac{S(DN)}{\sigma_s^2(DN) - \sigma_r^2(DN)} \tag{2.8}$$

A histogram of K values, as shown in Figure 2.13, is accumulated by applying equation 2.8 to multiple data sets and to different sub-arrays across the CCD. The mean of the histogram becomes an accurate representation of the system's K value. From the histogram shown in Figure 2.13, the mean K value is 1.228 e^-/DN. The variance of K is 0.0048 e^-/DN. The CCD's output amplifier gain, S_v can now be determined

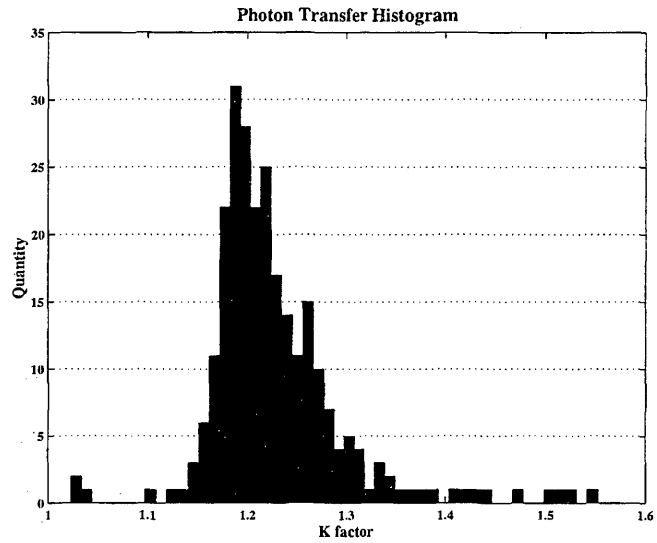

FIG. 2.13. Photon transfer histogram

with equation 2.7. Based on K, A_1, and A_2, the CCD's output amplifier gain is $30.3\mu\text{v}/\text{e}^-$.

The CCD's full well depth can also be determined from the K value and the point at which saturation occurs. Based on the data taken to determine the K conversion factor, the count value at saturation occurs is approximately 28,000. Multiplying 28,000 counts by 1.228 e^-/DN indicates that the mean pixel saturation level is approximately 34,000 electrons.

2.7.6 Linearity

CCDs, operating below their saturation level are typically linear sensors. Using a uniform irradiance source, the linearity of the CCD is examined from the mean signal value as a function of exposure time. After performing a least squares fit to the data, the CCD's percent linearity is indicated by the coefficient of regression. Using this technique, the imaging system used in this work is determined to be 99.989%

linear over the digital output range from 32 counts to 28560 counts, which is just prior to saturation. Conversely, the imaging system is only 0.011% non-linear over the majority of its operating range.

2.7.7 Flat-field Correction

Charge-coupled devices have small nonuniformities in gain, which need to be accounted for in order maintain a low noise system. If these variations are left uncorrected, then at high signal levels the noise is dominated by the pixel-to-pixel variations (Janesick *et al.*, 1987). Pixel-to-pixel variations are typically constant over a wide signal range and can be accounted for during data acquisition.

Using a uniform, diffuse light source, raw data files are collected over the detector's linear operating region. The raw data file's global average (average digital count value over all 1300x1030 pixels) is calculated and then each pixel value is divided by the global average. At incremental steps over the system's linear operating region, a per pixel gain correction factor data file is obtained for the entire array. All the gain correction factor data files are then averaged together to obtain a final gain correction factor file to be used for any exposure level. In order to account for the CCD's pixel-to-pixel nonuniformity, all raw data files are divided by the gain correction factor data file, which is more aptly referred to as the flat-field correction file.

The flat-field correction factor data file has a mean of 1.0000 DN and a standard deviation of 0.0221 DN. A histogram of all the gain correction values is shown in Figure 2.14. Since all the pixels in the CCD are developed with the same manufacturing process and in the same material, one would expect the gain of each pixel to be very close to the same value, as shown by the histogram. The histogram appears to contain two normal distributions, rather than a single normal distribution as expected.

Since the entire CCD chip covers a large area of silicon, multiple distributions may be required to represent the full array.

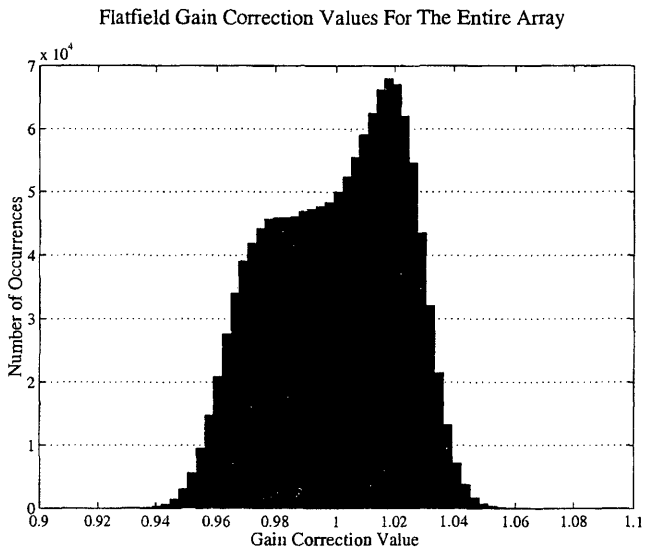

FIG. 2.14. Flat-field gain correction value histogram

The reduction of noise obtained when a flat-field correction file is utilized is quite significant, as shown in Figure 2.15. Without the flat-field correction, the output is limited by noise from pixel-to-pixel nonuniformities. When using the flat-field correction data file, the output is limited by shot noise (assuming a uniform, diffuse light source is used), which is the fundamental detection limit (Dereniak & Crowe, 1984; Janesick *et al.*, 1987).

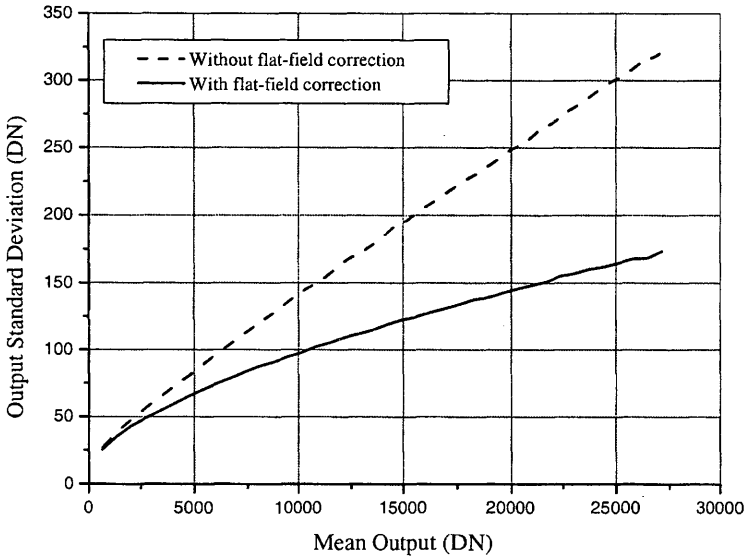

FIG. 2.15. Pixel-to-pixel noise improvement with flat-field gain correction

Chapter 3

FOCAL PLANE DETECTION PROCESS

3.1 General Introduction

There are two application specific features incorporated into the imaging system. These features maneuver charge in a controlled sequence that can be synchronized to a modulated input. Since charge is maneuvered at the pixel level, in the interline transfer CCD, processing is primarily performed at the focal plane.

The first feature is an on-chip gated exposure integrator and the second is termed an "integration threshold". The gated exposure integration feature can be set to integrate multiple exposures into one image, on the CCD chip, prior to read out. The second feature, the integration threshold (IT), creates a charge dead-band. In order for charge to be captured, the amount of charge that is generated in the sensor must surpass the threshold of the dead-band.

This chapter describes these application specific features, how they are implemented in the CCD architecture, and how the features are used to enhance signal detection. A brief review of the interline transfer CCD architecture is first presented. The gated exposure integrator is then discussed. Finally, the IT feature, which is an extension of the gated integration capability, is presented.

3.2 CCD Illustration Review

Figure 3.1 was introduced in section 2.6 to illustrate charge flow in the interline transfer CCD. This figure shows the potential wells for the sensor, the substrate, and the vertical register, as well as the barriers between the potential wells. An aluminum mask resides over the vertical register, which prevents incident photons from creating electron hole pairs directly in the vertical register. Micro-lenses (shown previously in Figure 2.8) also focus incident photons to the sensor area.

Incident photons are converted to photoelectrons in the sensor region (Appendix B). The photoelectrons, or charge, that accumulate in the sensor's potential well can flow either to the vertical register or to the substrate. Charge flow is controlled by the barriers that separate the sensor's potential well from the potential well of the vertical register and substrate. The overflow drain (OFD) barrier controls charge flow from the sensor to the substrate, and the readout gate (ROG) barrier controls charge flow from the sensor to the vertical register.

Figure 3.1 is used in this chapter as a visual aid, to assist in explaining the application specific features that are incorporated into the system. In particular, the features described below depend on the ROG and OFD barriers and the ability to accurately control these barriers. Figure 3.1 illustrates, as a single curve across the device, the potential wells and the potential barriers.

3.3 Multiple Exposure Integration

In general, a gated integrator is a device that synchronously acquires an input only when the signal of interest is known to be present. Often, the input signal's frequency and phase are known *a priori*, which provide a means for synchronizing the detection process. Once the detection process is synchronized, data is acquired only

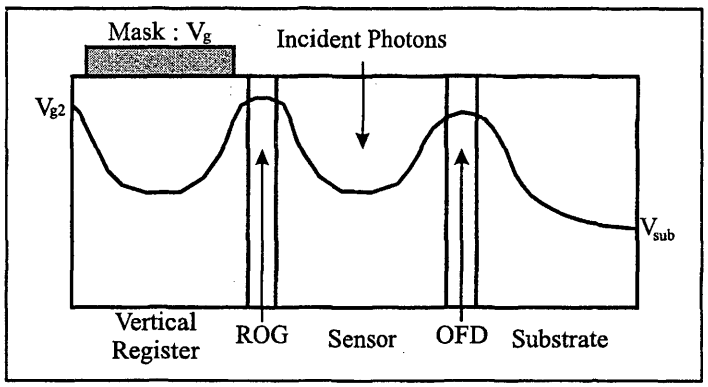

FIG. 3.1. Simplified cross-section illustration of the Sony ICX085 interline transfer CCD

when the signal is present. Signal enhancement is achieved both by rejecting noise when the signal is *not* present and by averaging repeated acquisitions (Wang *et al.*, 1992).

A similar process is incorporated into the imaging system, which synchronously integrates exposures. An exposure is the timed accumulation, considered the dwell time, of charge in the potential well of the sensor region. The exposure is integrated, during the dwell time, by transferring the accumulated charge from the sensor to the vertical register.

There is no temporal separation between the exposure process and the integration of an exposure in the vertical register. The charge accumulated in the sensor is immediately transferred to the vertical register. Each transfer of charge to the vertical register is, therefore, considered to be an exposure. Transferring multiple exposures to the vertical registers for all sensors creates an image array that is the integrated charge from each exposure.

An external trigger, which is synchronized to the signal of interest using a pulse/delay generator (Stanford Research Systems DG535), is connected to the con-

troller. Each trigger received by the controller, unless the controller is reading the image from the CCD array, initiates an exposure. The number of exposures that are integrated in the vertical register is set in the controller logic, via software, prior to image acquisition. Once the desired number of exposures is integrated, the integrated image is read from the array. Appendix K contains further information and instructions on configuring the imaging system's hardware and software to perform gated exposure integration.

Prior to the integration process, the controller and camera remain in a standby mode. While in the standby mode, one in which no images are acquired, the controller continuously reads out the CCD and discards the output. Photoelectrons are continuously accumulated in the array and, therefore, they need to be continuously read from the array. The process of reading out an array while not acquiring data is often called "cleaning" the array.

Once acquisition of an image is activated, using the WinView software package (Roper Scientific, 1998b), the controller finishes its current cleaning operation and then waits for the camera head to initialize. Control over the array cleaning process is, at this point, passed to the logic in the camera head. The camera head is initialized once both the cleaning process resumes, under the control of the camera head logic, and the OFD barrier is lowered, activating the electronic shutter. At this point, charge accumulated in the vertical register, whether dark charge or mask bleed-through, is discarded with the cleaning process and charge accumulated in the sensor is drained to the substrate, since the electronic shutter is active.

The array cleaning and initialization process is important since it is often unknown exactly when the first external trigger will arrive at the controller. If there is a long time lapse between initial setup and the arrival of the first trigger, dark charge

and other noise can build up in the array while waiting. When waiting for the first trigger, charge is, therefore, discarded by cleaning the vertical register and activating the electronic shutter. This initial state is shown in Figure 3.2 (assuming all three phases of the vertical register are being clocked accordingly to clean the array).

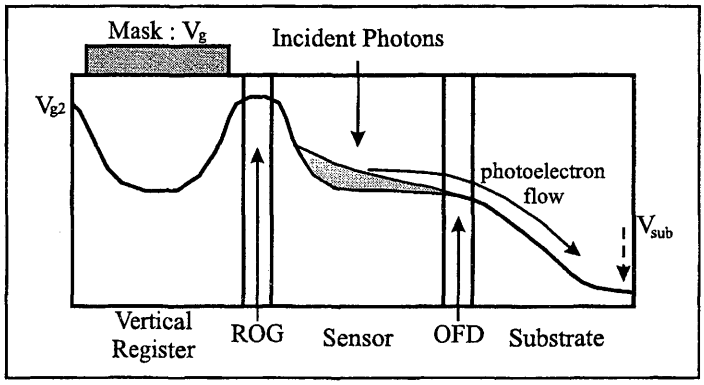

FIG. 3.2. CCD initialization prior to image acquisition

Once the first external trigger is received, the vertical register cleaning process immediately stops and the first exposure begins. At this time, the OFD barrier is raised and the ROG barrier is simultaneously lowered and remains low for the dwell time. Charge generated in the sensor now flows directly into the vertical register. Figure 3.3 illustrates the CCD's state when integrating the first exposure in the vertical register.

Once the dwell time, as set in the software (Appendix K), has elapsed, the ROG barrier is raised, halting the flow of charge from the sensor to the vertical register. The OFD barrier is, once again, lowered and unwanted charge is drained into the substrate. The charge integrated during the first exposure remains in the potential well of the vertical register, under the aluminum mask, as shown in Figure 3.4.

The cleaning process performed prior to the first exposure does not resume after the integration process begins. Since the integrated charge is held in the vertical

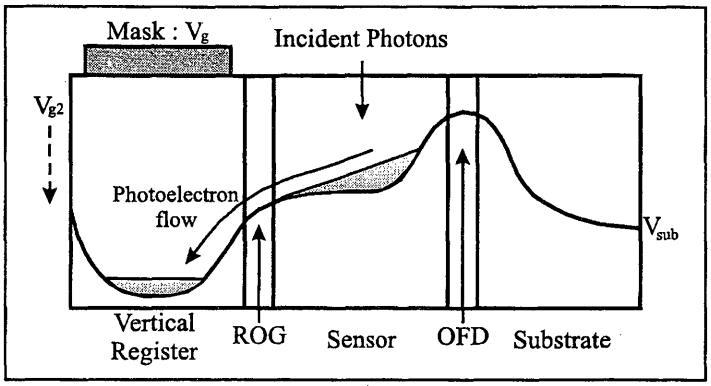

FIG. 3.3. Integrating the *first* exposure in the vertical register

register, the vertical register must remain in its current potential state until the desired number of exposures are integrated. The integrated exposures will then be read from the array. Only after the integrated image has been read from the array will the vertical register cleaning process resume.

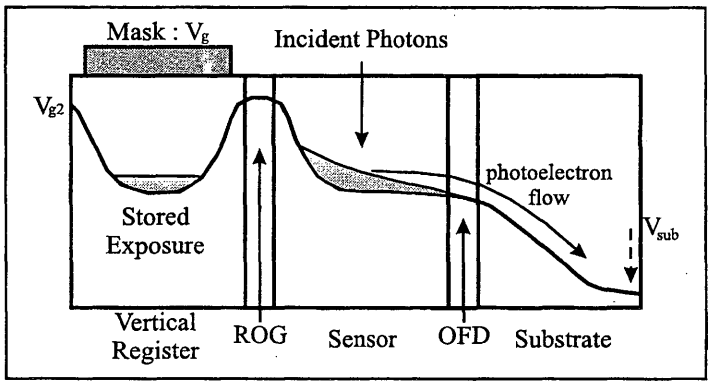

FIG. 3.4. Draining unwanted charge into the substrate while holding the *first* exposure in the vertical register

Another exposure can be added to the first exposure by performing the same process that was described above. In order to add another exposure to the first exposure, the OFD barrier is raised and the ROG barrier is simultaneously lowered for the same dwell time. Charge generated in the sensor, once again, flows into the

vertical register (assuming the potential well of the vertical register is not full). The current exposure is, therefore, integrated with the first exposure held in the vertical register, as shown in Figure 3.5. The illustration in Figure 3.5 separates the integrated exposures with a dashed line for demonstrative purposes. It is, however, impossible to discern which portions of the total charge, held in the vertical register, were generated per exposure. The total number of photoelectrons contained in the vertical register is now the sum of two separate exposures.

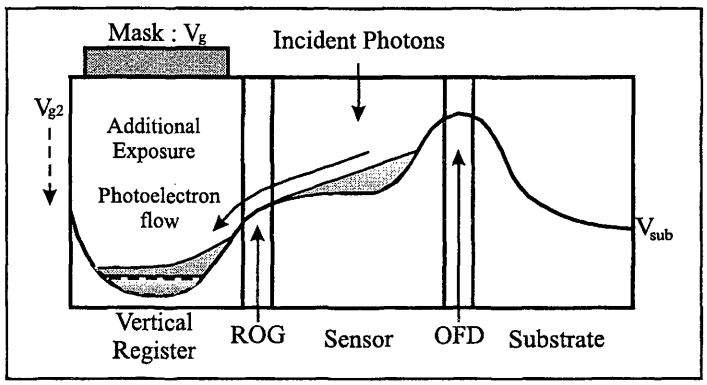

FIG. 3.5. Integration of consecutive exposures in the vertical register

This process can continue as long as the vertical register is not saturated. Based on the logic implemented in the controller, the maximum number of exposures that can be integrated is 4000. Performing 4000 integrations requires that each exposure be on average no more than 6.5 photoelectrons. Integrating a greater number of photoelectrons per exposure, at the maximum number of integrations, will result in a saturated image that exceeds the CCD's linear operating region. In most cases, the number of photoelectrons integrated per exposure will be much larger, thus, the total number of integrations must be much smaller. The total number of integrated exposures per image (1 - 4000) is set using the software as discussed in Appendix K.

Once the desired number of integrations has been performed, as shown in Fig-

ure 3.6, the final integrated image is read from the array. Since the integration process uses the vertical register and the vertical register is used to read the image from the array, acquisition of the next integrated image cannot begin until the previous image is entirely read from the array.

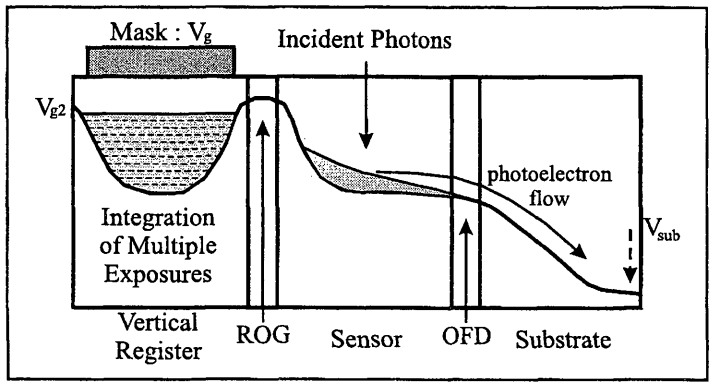

FIG. 3.6. Multiple exposures integrated in the vertical register; the integrated image is ready to be read from the array

3.3.1 General Signal-to-Noise Ratio Improvement Expectations

In general, statistical averaging of a periodic signal is a well known and extensively utilized signal enhancement technique (Dereniak & Crowe, 1984; Horowitz & Hill, 1989; Pallás-Areny & Webster, 1991; Wang *et al.*, 1992; Eckbreth, 1996). Averaging techniques, which are also comparable to lowpass filtering operations, produce a value that approaches an ensemble's mean value. The root-mean-squared (rms) error in the final average value is reduced by the square-root of the number of averages and, therefore, the signal-to-noise ratio (SNR) is improved (Cooper & McGillem, 1999).

The boxcar averager or gated integrator are conventional instruments that improve SNR through averaging. By capturing and averaging multiple samples over time, the output value approaches the actual mean value of the signal (Eckbreth,

1996; Fowler, 2000). Further discussion on the boxcar averager is included in section 4.8.2.

Averaging techniques have also been demonstrated as a way to improve the SNR of images that are acquired with CCDs (O'Malley & O'Mongain, 1992). By adding multiple frames together, in software after the frames have been read from the CCD, the SNR is improved by the square-root of the number of frames added together.

The noise in an image is typically defined as the combination of photon noise (n_w) and electronic noise (n_r) (Kopeika, 1998). The total noise, n_t, is the square root of the sum of the squared noise components. (The noise is presented here in general terms to point out the expected increase in SNR. Chapter 5 presents mathematical descriptions of the system's noise components.) If the output signal is defined as s_o, then the SNR at the output is,

$$\text{SNR} = \frac{s_o}{\sqrt{(n_w)^2 + (n_r)^2}} = \frac{s_o}{n_t} \tag{3.1}$$

Frame adding has been shown to increase the SNR by $\sqrt{N_f}$, where N_f is the number of frames that are summed (O'Malley & O'Mongain, 1992). Since each frame is read from the array prior to averaging, each frame is considered to contain the same noise power. In this case, the SNR improvement has been shown to be,

$$\text{SNR} = \frac{N_f \cdot s_o}{\sqrt{N_f\left[(n_w)^2 + (n_r)^2\right]}} = \frac{N_f \cdot s_o}{\sqrt{N_f\,(n_t)^2}} = \sqrt{N_f}\frac{s_o}{n_t} \tag{3.2}$$

A similar improvement in SNR can be anticipated by performing integration on the CCD chip, as described in the previous section. In this case, the frame is integrated, or averaged, prior to reading the image from the array. The noise from the read out electronics is added to the final integrated image, rather than to each image

prior to integration. The photon noise, which is a function of the input irradiance, is still added to each integration.

The initial expected SNR from integrating exposures on the CCD chip is,

$$SNR = \frac{N_i \cdot s_o}{\sqrt{N_i\left[(n_w)^2\right] + (n_r)^2}} = \sqrt{N_i}\frac{s_o}{\sqrt{(n_w)^2 + \frac{(n_r)^2}{N_i}}} \tag{3.3}$$

where N_i is the number of integrations performed per frame. The maximum SNR, as calculated by equation 3.3, depends on the number of integrations that can be performed at the pixel level. The achievable SNR, therefore, depends on the CCD's well depth. Larger wells will allow for more integrations per frame.

The on-chip integration technique can also be combined with frame averaging to further improve the SNR. Combining both techniques produces an expected SNR,

$$SNR = \frac{N_i \cdot N_f \cdot s_o}{\sqrt{N_f\left\{N_i\left[(n_w)^2\right] + (n_r)^2\right\}}} = \sqrt{N_i \cdot N_f}\frac{s_o}{\sqrt{(n_w)^2 + \frac{(n_r)^2}{N_i}}} \tag{3.4}$$

that is a function of both N_i and N_f. A more involved estimation of the SNR improvement achieved from on-chip averaging is given in Chapter 5.

3.4 Integration Threshold

Background intensive diagnostics, such as pump-probe absorption spectroscopy, limit the total number of exposures that can be integrated prior to detector saturation. The possible number of integrations can, in this case, be fairly restricted or even limited to a single exposure. This can be true even when the exposure time is set to the minimum limit of 1μs.

In such cases, the information bearing signal is only a fraction of the total irra-

diance that is captured during an exposure. Much of the total exposure is comprised of background photoelectrons that represent a dc level and contain no useful information.

In order to increase the number of exposures that can be integrated into the vertical register and, therefore, increase the potential SNR (equation 3.3), an on-chip "integration threshold" (IT) feature is proposed and investigated. Fundamentally, the IT feature is a dc offset, or dead-band threshold, that must be exceeded before the photoelectrons generated in the sensor will be able to flow into the vertical register. The background charge, which is considered to be the charge that does not exceed the IT, contained in the sensor is discarded into the substrate after the exposure time has elapsed. The purpose of the IT feature, therefore, is to increase the number of possible integrations by integrating, in the vertical register, only a representative fraction of each exposure.

The IT feature is derived from the interline transfer CCD's antiblooming capability. The basic idea is to shift the antiblooming process from the OFD barrier to the ROG barrier. Antiblooming keeps a saturated pixel from saturating adjacent pixels by draining off excess charge into the substrate. When a pixel saturates, the excess charge in the sensor "spills" over the OFD barrier and is discarded. The objective of the IT feature is to allow charge that accumulates beyond a dead-band threshold, which is established with the ROG barrier level, to "spill" over the ROG barrier. Only the portion of charge that "spills" over the ROG barrier is, therefore, integrated in the vertical register.

3.4.1 Antiblooming

To better explain the operation of the IT feature, the interline transfer CCD's antiblooming feature is first presented. When imaging with an interline transfer CCD under *normal* conditions, both the ROG barrier and the OFD barrier are raised during an exposure period. The image is captured and contained in the sensor's potential well, which is created by raising both barriers. If antiblooming control were not implemented, additional photoelectrons, generated after the sensor's potential well is full, will migrate to other areas of the detector that have additional well capacity. Blooming is apparent on the output image when a saturated pixel causes other pixels to saturate.

In order to prevent a sensor's surplus charge from migrating to other pixels, the OFD barrier is held at a slightly lower level than the ROG barrier, which is shown in Figure 3.7. Surplus charge, generated in a saturated pixel, will migrate to the lower potential of the substrate and, therefore, "spill" over the OFD barrier, instead of migrating to adjacent, unsaturated pixels. Once charge "spills" over the OFD barrier it is discarded into the substrate.

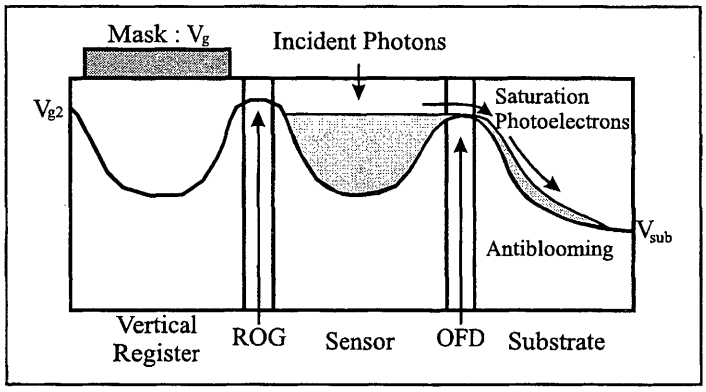

FIG. 3.7. Antiblooming function under normal interline transfer CCD configuration and operation

Under *normal* operating conditions as discussed above, once the exposure time has elapsed, the ROG barrier is pulsed to transfer the charge in the sensor to the vertical register. The maximum amount of charge that will be transferred to the vertical register is based on the sensor's full well capacity. Antiblooming control drained off excess charge into the substrate.

Before continuing with the IT feature description, it is noted that antiblooming control is not active when operating the imaging system with the integration feature as described above in section 3.3. When integrating multiple exposures into the vertical register, the charge generated in the sensor is transferred directly into the vertical register. It is, therefore, possible for the integrated charge to exceed the well depth of the vertical register. No path exists to drain excess charge directly from the vertical register to the substrate. Excess charge in the vertical register will unavoidably migrate to other pixels resulting in blooming. Care must be taken when setting the dwell time and the number of integrations, as described in Appendix K, to avoid saturation and blooming effects.

The same care must also be taken when utilizing the IT feature. In order to incorporate the IT feature, the OFD barrier is set to a higher level than the ROG barrier and, thus, the antiblooming control is rendered inactive.

3.4.2 Background Reduction

Section 3.3 describes how multiple exposures are integrated in the vertical register by repeatedly lowering and raising the ROG barrier. The purpose of the IT feature is to transfer only a fraction of each exposure to the vertical register for integration.

In order to implement the IT feature the ROG barrier is not completely lowered but is controlled with a predetermined voltage. Setting the ROG barrier to a prede-

termined voltage creates a dead-band that charge in the sensor must exceed before it "spills" into the vertical register. Figure 3.8 illustrates the dead-band that is created by the ROG barrier when it is not lowered completely. As photoelectrons build up in

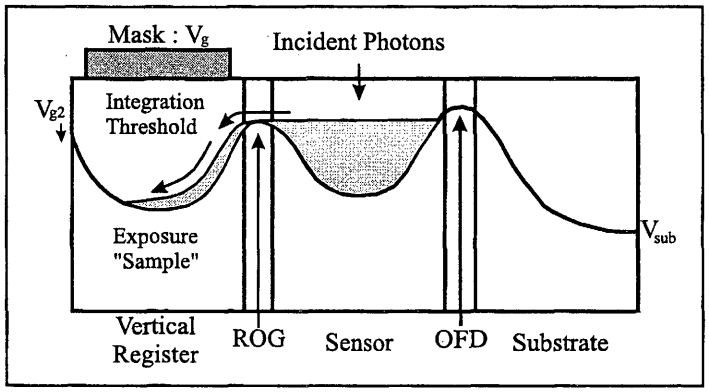

FIG. 3.8. Regulation of ROG barrier to create a charge dead band between the sensor and vertical register

the sensor region, the sensor eventually reaches its full well capacity. Additional photoelectrons generated in the sensor "spill" over the ROG barrier and are integrated in the vertical register.

Once the exposure is complete, the ROG barrier is raised to its maximum height and the OFD barrier is completely lowered, which activates the electronic shutter. The charge contained in the sensor's potential well, which represents a large portion of the input's dc value, is drained into the substrate and discarded, as illustrated in Figure 3.9.

The integration process then proceeds in the same format that was described in section 3.3. In this case, however, the ROG barrier creates a dead-band that the charge from each exposure must overcome during the dwell time before it is integrated in the vertical register. Since less charge from each exposure is integrated, more integrations should be possible.

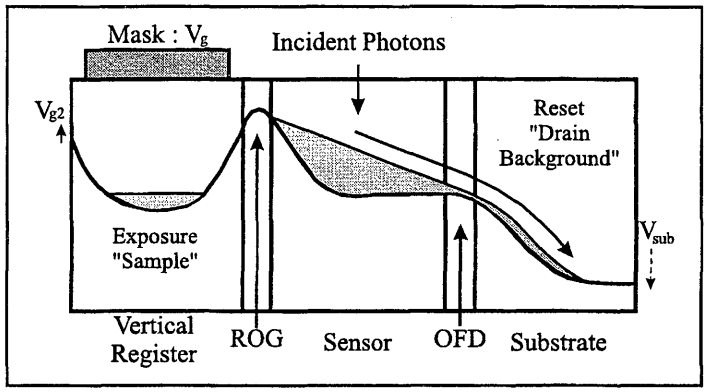

FIG. 3.9. Background charge contained in the sensor is discarded by lowering the OFD barrier

3.4.3 Threshold Mechanism Examples

Charge transfer efficiency (CTE) is a measure of how efficiently a charge packet is transferred between registers, while reading the packet out of the array. CTEs less than one indicate that some of the charge in a packet is left as residual charge along a read out chain of registers. CTE is actually an additive noise component which is discussed further in section 5.10.4.

CTE is presented here as an example of a widely documented loss mechanism that is similar to the IT feature (Barbe, 1975; Dereniak & Crowe, 1984; Janesick *et al.*, 1987; Johnson-Cole & Clark, 1991). Inter-electrode gaps can create a slight barrier between the potential wells of two shift registers. When transferring a charge packet from one register to the next, the charge must cross over the small barrier. The barrier, therefore, impedes the flow of charge and some of the charge packet is left behind, resulting in loss (Séquin & Tompsett, 1975; Dereniak & Crowe, 1984; Janesick *et al.*, 1987).

The small barrier produced from inter-electrode gaps, which generates a loss mechanism, is similar to the barrier created by the ROG. Setting the level of the

ROG barrier in a controlled manner, force a loss mechanism to exist between the sensor and the vertical register. The ROG barrier, thus, impedes charge flow from the sensor to the vertical register in a way that reduces the total amount of charge that actually enters the vertical register.

3.4.4 Expected Signal-to-Noise Ratio Improvement

Predictions on the SNR improvement obtained by implementing the IT feature are based upon the maximum dead-band threshold setting, the repeatability of the threshold, and the uniformity of the threshold over the entire array. Setting the dead-band threshold to its maximum will reduce the greatest amount of background, which will improve the SNR in two ways. First, the number of integrations per frame, N_i, can be improved, which will increase the SNR as shown in equation 3.3. Second, since the photon noise is a function of the background (Chapter 5), the photon noise is reduced by draining much of the background to the substrate. An estimate of the SNR improvement achieved by implementing the IT feature is given in Chapter 6.

Chapter 4

ANALYSIS FRAMEWORK AND FUNDAMENTALS

4.1 General Introduction

This chapter introduces the fundamental approach taken in this work, which provides a foundation to the imaging system's mathematical models and analysis. The basis for a linear systems analysis is discussed, as well as the mathematical foundations required to perform such an analysis. Specifically, spectral analysis is discussed as an essential tool. As background, other parameters and processes that arise in linear systems analysis, such as bandwidth and sampling, are also discussed.

A primary concern in the design of any electronic instrument is noise. Noise that enters an instrument as input or noise that is generated internally, determines the instrument's fidelity. Information bearing signals falling below an instrument's noise floor cannot be extracted and accurately measured. The amount of noise in a measurement system sets a lower bound on the system resolution. In order to clearly state the system's limitations, the amount of noise at the input and at the output need to be carefully defined and modeled. This chapter, therefore, also introduces general probabilistic and statistical methods that can be used to define noise.

Finally, this chapter concludes with discussion on two conventional instruments that are often utilized in laser diagnostics. The measurement and processing capabilities of these instruments, which are the lock-in amplifier and the boxcar integrator, are qualitatively outlined. The primary signal enhancement techniques that are em-

ployed by these instruments are then related to the processing functions contained in the imaging system.

4.2 Linear Systems Approach

Linear systems theory is used in this work as a tool to analyze a CCD-based imaging system developed for laser-based diagnostics. The analysis methods and mathematical models used throughout this work are often found in the design and development of electronic communication systems. The objective, in designing communication systems, is often to develop a transmission system that conveys information with minimal errors. Linear systems analysis is, therefore, performed on the portions of a communication system that allow for design and control.

In a general communication system, information, represented as a rapidly changing signal, is sent from a transmitter, through a channel, and is detected by a receiver. As the information propagates from one physical location to another, the information is contaminated by random noise and errors are introduced. Communicating over long distances or through harsh (*noisy*) environments, requires that mathematical operations be performed on the information in preparation for transmission, and corresponding, or inverse, mathematical operations be performed to extract the information at the receiver (Taub & Schilling, 1986).

Linear systems theory and communication theory provide the foundation for developing continuous time, mathematical models. These models describe basic subsystems, such as transmitters, channels, receivers, and system inputs and outputs that, when combined, model a complete communication system. Mathematical models may include characteristic transfer functions, power spectra for the signal and noise factors, and probability descriptions. Each can then be used to configure the

subsystem parameters in an effort to achieve the highest possible signal-to-noise ratio (SNR), within given constraints.

In order to gain a systems level perspective of both the laser based diagnostic technique, which is pump-probe absorption spectroscopy (PPAS), and the imaging system's detection process, mathematical foundations from linear systems theory are used in this investigation. By developing a systems-level model of the interaction between a laser diagnostic technique and the imaging system, efforts can be focused on the portions of the system that allow for design and control. A comparative illustration between a communication system and a diagnostic imaging system is given in Figure 4.1.

In this context, the imaging system is separated into subsystems and models of the subsystems are developed. Combining the subsystem models creates a complete model of the detection process. The input irradiance is also separated into fundamental parameters and they are defined mathematically. Combining the irradiance model with the imaging system model results in a complete system model that can be used to define operating parameters that will achieve a high SNR, within operational constraints.

On the premise that laser diagnostic instruments, in general, can be treated as a communication system, laser diagnostics non-intrusively transfer information through harsh environments to a receiver. From a systems level perspective, the sample volume under investigation is the transmitter. Excitation sources (lasers) can also be considered a subsystem of the transmitter, since mathematical operations (such as modulation) are typically performed on the excitation source to prepare the information for transmission.

After the interaction or excitation process, an information bearing signal is trans-

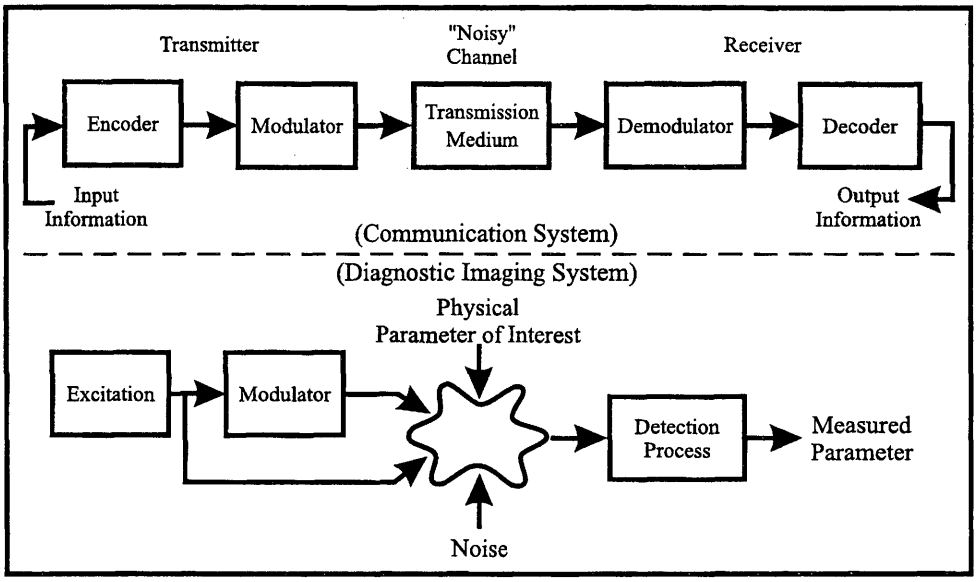

FIG. 4.1. Block diagram comparison of a general communication system and diagnostic imaging system

mitted from the sample volume to the receiver. As the signal travels to the receiver, it propagates through a channel, which may simply be the air or the background irradiance of a continuous wave (cw) laser beam. The signal can be, therefore, embedded in the background, which may be much larger than the signal itself. The receiver must be capable of processing the input to extract the useful information bearing signal from the background and noise elements.

The imaging system developed in this work is considered to be the receiver in the communication system analogy. The analysis, which is performed on the portions of the imaging system that allow for design modifications, is performed with the objective of enhancing detection capabilities and achieving the highest possible SNR, within given constraints. The mathematical models that describe the imaging system's amplification, attenuation, and frequency translation characteristics can be used to massage the transmitter's modulation scheme and the receiver's signal

extraction process to achieve a good level of performance.

4.3 Spectral Analysis

Spectral analysis is an essential part of communication theory's foundation. Spectral analysis provides the mathematical tools to describe waveforms, both deterministic and stochastic, in the frequency domain, with a mathematical correspondence to the time domain description. Analyzing waveforms in the frequency domain can produce mathematical descriptions of a waveform's harmonic content and spectral location that is not directly apparent in the waveform's time domain representation. These descriptions can then be used to determine the probability of detecting useful, information bearing waveforms, and to design systems that will increase detection probability (Taub & Schilling, 1986).

4.4 General Frequency Conversion

A very common design technique, which results from the ability to perform spectral analysis, is frequency translation. Frequency translation is the process of moving a waveform from one spectral location to another. The process of translating the spectral makeup of a waveform in frequency can also be called frequency conversion, frequency mixing, heterodyning, modulation, or demodulation.

Frequency translation is performed for various reasons. Specifically in communications systems, waveforms are modulated at the transmitter in preparation for transmission through a medium that requires a certain transmission band, such as AM or FM radio. Many systems, other than systems designed specifically for data communications, utilize frequency translation techniques in order to move a waveform, that contains useful information, to a spectral location that has lower levels

of noise and less interference from other information-bearing waveforms. In order to extract a waveform from its prepared state configured by the transmitter, frequency translation techniques are also used in receivers or detectors to move a waveform to a spectral band that can be processed by other subsystems in the receiver.

Two general frequency translation processes, homodyne and heterodyne, are used to describe the imaging system's detection capabilities. Homodyne and heterodyne techniques are typically implemented in detection processes to extract signals that have been modulated and reside at a carrier frequency. Carrier frequencies are normally higher than the detector's electronic processing bandwidth and, therefore, the modulated waveform must be converted to a lower frequency that is inside the detector's pass band.

General definitions for homodyne detection and heterodyne detection are given in the following sections. Their relationship to the imaging system's detection functions becomes apparent in Chapters 6 and 7.

4.4.1 Homodyne Detection

Homodyne and heterodyne techniques are very similar. The distinction between the two is based on the output that results from performing either homodyne or heterodyne detection. Likewise, the distinction also corresponds to the mixing frequency or sampling frequency. A homodyne detector returns a modulated carrier waveform to its original baseband state, which is the waveform's spectral location prior to modulation. Heterodyning, on the other hand, converts a modulated waveform to another *intermediate frequency* (IF), which is typically higher than the original baseband, but lower than the modulation carrier frequency. Heterodyne techniques, therefore, require a second frequency translation step to convert the output of the heterodyne

process to the waveform's original baseband (Stremler, 1990).

A simple homodyne detection process can be described with an amplitude modulation example. Let $f(t)$ be a band-limited signal that is amplitude modulated by the modulation function, $m(t)$, shown in equation 4.1.

$$m(t) = a(t)\ cos\,(2\pi f_c t + \phi(t)) \tag{4.1}$$

In equation 4.1, $a(t)$ is the modulation carrier gain, or envelope, and f_c is the carrier frequency. In amplitude modulation systems, the phase term, $\phi(t)$, is a constant value and is often set to zero. The constant phase characteristic of amplitude modulated signals is important because it provides a mechanism for recovering signals, at a known carrier frequency and fixed phase.

Assuming the envelope $a(t)$, in equation 4.1, is constant at unity, the amplitude modulated signal $\gamma(t)$, is the product of a general, band-limited function, $f(t)$, and the modulation function, $m(t)$.

$$\gamma(t) \;=\; f(t) \cdot m(t) \;=\; f(t)\ cos\,(2\pi f_c t) \tag{4.2}$$

Since multiplication in the time domain corresponds to convolution in the frequency domain, the amplitude modulation process shifts the complete baseband, spectral shape of $f(t)$ in the frequency domain to the positive carrier component, f_c, and to the negative carrier component, $-f_c$. As the modulated signal propagates through lossy channels to a detector, interference and noise outside of the bandwidth of the signal, $f(t)$, centered at the carrier frequency, f_c, will not affect the spectral

content of the signal $f(t)$. Also, if the system is designed to mitigate errors, noise and interference inside the bandwidth of the signal, centered at the carrier frequency, should not seriously degrade the signal's spectral content.

In order to detect the original signal, $f(t)$, at the receiver, the modulation property of the Fourier transform is again utilized. The modulated signal, $\gamma(t)$, is once again multiplied in the time domain with another sinusoid that has the same frequency and phase as the modulation function, $m(t)$. The demodulation function, $d(f)$, or signal used for homodyne detection, is set equal to the modulation function, $m(t)$.

$$d(f) \;=\; m(t) \;=\; a(t)\; cos\,(2\pi f_c t) \tag{4.3}$$

The output of the demodulator, or homodyne detector, is then the original signal, $f(t)$, multiplied by the square of the modulation function,

$$\gamma(t).d(t) \;=\; f(t)\; cos^2\,(2\pi f_c t)\,, \tag{4.4}$$

which, using a trigonometric half-angle relationship, can be rewritten as equation 4.5.

$$\gamma(t).d(t) = \frac{1}{2}\, f(t) \;+\; \frac{1}{2}\, f(t)\; cos\,(4\pi f_c t) \tag{4.5}$$

The modulated signal is, in the ideal case, convolved in the frequency domain with delta functions at the demodulation frequency, f_c, which is the same as the modulation frequency. The demodulation, or homodyne, process transfers the spectra of the modulated waveform from f_c to twice the modulation frequency, $2f_c$, and to the frequency domain origin, which is the signal's original baseband state. This is

easily seen in the Fourier transform of equation 4.5, which is

$$\begin{aligned} \Im\left[\gamma(t).d(t)\right] &= \Im\left[\frac{1}{2}f(t) + \frac{1}{2}\ f(t)\ cos\,(4\pi f_c t)\right] \\ &= \frac{1}{2}F(f) + \frac{1}{4}F(f+2f_c) + \frac{1}{4}F(f-2f_c)\ , \end{aligned} \tag{4.6}$$

where $\Im(\bullet)$ is used for the Fourier transform. Finally, a lowpass filter can be used, following the homodyne process, to filter out the double-frequency terms from the original spectral components and recover the original signal, $f(t)$.

As shown, homodyning is a synchronous detection technique used to recover a modulated signal. In order to recover the signal, the detector must generate a mixing function, often defined as a local oscillator, that has the same frequency and phase as the modulated signal. Since homodyne detection is sensitive to phase differences between the carrier and the local oscillator, the detection process is also referred to as phase sensitive detection.

Both the correct phase and frequency of the modulated signal must be known to perform synchronous or phase sensitive detection. A phase error, ϕ_e, in the detection system will cause a variable gain factor in the recovered signal that is proportional to the cosine of the phase error. Although small phase errors are tolerable, the signal is eliminated when the error approaches $\pm 90^o$ (Stremler, 1990).

$$\gamma(t).d_e(t) = \frac{1}{2}\ f(t)cos\,(\phi_e)\ \ +\ \frac{1}{2}\ f(t)\ cos\,(4\pi f_c t + \phi_e) \tag{4.7}$$

On the other hand, if there is a frequency error, the signal $f(t)$ is multiplied by a low frequency sinusoid producing unacceptable distortion in the context of homodyne detection. A frequency error may, however, be used in a controlled manner to translate

the modulated signal from the carrier frequency to an intermediate frequency that is also higher the original baseband frequency location. In this case, heterodyne detection is performed.

4.4.2 Heterodyne Detection

Heterodyne detection is very similar to homodyne detection. The difference between the two schemes lies in the frequency of the local oscillator used for frequency translation. As shown in the previous section, homodyne detection utilizes a local oscillator that has its frequency and phase terms matched to a modulated input signal. The heterodyne detector mixes the modulated signal with a sinusoidal function that has a frequency term that is different than the modulated signal's carrier frequency, f_c.

The same modulated signal, $\gamma(t)$, from equation 4.2, is used to illustrate the heterodyne detection process. A carrier phase term, ϕ_c, is added to the modulated signal to show how phase information is also retained at the output of the heterodyne receiver.

$$\gamma(t) = f(t)\ cos\,(2\pi f_c t + \phi_c) \tag{4.8}$$

In order for the receiver to translate $\gamma(t)$ in frequency, $\gamma(t)$ is once again multiplied in the time domain with another sinusoid, $d(t)$. In the case of the heterodyne receiver, the demodulation frequency, f_d, differs from the modulation carrier frequency, f_c. The demodulation function is again defined as a sinusoid with frequency f_d and phase ϕ_d, as shown in equation 4.9. The gain term, $a(t)$, in the demodulation function, is again assumed to be a unity constant.

If the modulation function, $m(t)$, (used to generate the modulated signal $\gamma(t)$)

and the demodulation function, $d(t)$, are generated with phase locked clocks, then their difference in phase can be considered a constant. The phase term in the demodulation function is, in this case, set to zero. The resulting output, after the heterodyne process, is then dependent on the phase term of the modulated input, $\gamma(t)$.

$$d(t) \;=\; a(t)\; cos\,(2\pi f_d t + \phi_d) \;=\; cos\,(2\pi f_d t) \tag{4.9}$$

It is helpful to perform the analysis of the heterodyne process in the frequency domain. The Fourier transform of the modulated signal, $\gamma(t)$, is,

$$\begin{aligned} \Im\left[\gamma(t)\right] \;=\; \Gamma(f) \;&=\; \Im\left[f(t)\; cos\,(2\pi f_c t + \phi_c)\right] \\ \Gamma(f) \;&=\; \frac{1}{2}F\left(f - f_c\right)e^{j\phi_c} + \frac{1}{2}F\left(f + f_c\right)e^{-j\phi_c} \end{aligned} \tag{4.10}$$

which is the spectrum of the original signal, $f(t)$, translated to the modulation carrier frequency, f_c. In the ideal case, the Fourier transform of the demodulation function, $d(t)$, is a pair of impulses at the positive and negative mixing frequency components.

$$\Im\left[d(t)\right] \;=\; D(f) \;=\; \Im\left[cos\,(2\pi f_d t)\right] \;=\; \frac{1}{2}\left(f - f_d\right) + \frac{1}{2}\left(f + f_d\right) \tag{4.11}$$

Multiplying the modulated signal, $\gamma(t)$, with the demodulation function, $d(t)$, results in two sinusoidal components. In the frequency domain, this is apparent in the result obtained from convolving the Fourier transform of the modulated signal, $\Gamma(f)$, with the Fourier transform of the heterodyne function, $D(f)$.

$$\begin{aligned} \Gamma(f) * D(f) \;&=\; \left[\frac{1}{2}F\left(f - f_c\right)e^{j\phi_c} + \frac{1}{2}F\left(f + f_c\right)e^{-j\phi_c}\right] * \left[\frac{1}{2}\left(f - f_d\right) + \frac{1}{2}\left(f + f_d\right)\right] \\ &=\; \frac{1}{4}F\left[f - (f_c \pm f_d)\right]e^{j\phi_c} + \frac{1}{4}F\left[f + (f_c \pm f_d)\right]e^{-j\phi_c} \end{aligned} \tag{4.12}$$

The original signal's spectrum, $F(f)$, is now located at the sum and difference frequencies that are generated from mixing the modulation and demodulation functions. The absolute value of the difference between the two mixing frequencies, $|f_c - f_d|$, is defined as the intermediate frequency (IF). The inverse Fourier transform of equation 4.12 is,

$$\gamma(t).d(t) = \frac{1}{2}f(t)\ cos\,(2\pi|f_c - f_d|t + \phi_c) + \frac{1}{2}f(t)\ cos\,(2\pi|f_c + f_d|t + \phi_c) \qquad (4.13)$$

Lowpass filtering can again be used to eliminate the sum frequency term, $|f_c + f_d|$, and retain the IF term, as long as the IF term is located in the filter's passband. The heterodyne process is typically incorporated into a system to transfer the modulated signal down to a frequency band that can be processed by downstream subsystems in a receiver.

A heterodyne detector also transfers an unwanted frequency component to the intermediate frequency. When the heterodyne process is performed, the entire modulation signal spectrum is convolved with the demodulation spectrum. Thus, the frequency components that have an absolute value equal to twice the intermediate frequency plus the modulation carrier frequency, $|f_c + 2f_{IF}|$, are also mixed down to the intermediate frequency. The frequency $|f_c + 2f_{IF}|$ is called the image frequency. To improve signal fidelity at the intermediate frequency, a signal at the image frequency, if it exists, must be filtered away prior to demodulation (Stremler, 1990).

4.4.3 Optical Modulation and Demodulation

The mathematical descriptions of the modulation and demodulation functions, described in the previous sections, represent electronic processes. The polarity, of such processes, can be altered between positive and negative states. Since both positive

and negative values can be realized in electronic systems, waveforms can be created that do not have a dc component.

Frequency translation techniques can also be utilized in optical systems. Modulation waveforms can be impressed upon light sources, typically laser beams, by passing the light through an optical modulator. Optical modulators provide to the user the ability to modulate laser beams with a range of waveforms that extend from simple to complex.

Optical modulators range from the simple mechanical chopper to the more complex acousto-optic modulator (AO) and electro-optic modulator (EO). The mechanical chopper time gates the light with a rotating metal disk that either allows the beam to pass through an aperture or blocks the beam with a solid portion of the disk. The resulting modulation function is a, low frequency, square pulse train, which typically oscillates at 5kHz or less (Fowler, 2000). Since the modulation waveform generated by a mechanical chopper is a square pulse train, higher order harmonics exist and can also be considered the carrier frequency.

The AO and the EO, on the other hand, can be used to modulate a laser beam with high frequency waveforms. These types of optical modulators are typically driven by a function generator or arbitrary waveform generator, which provides greater flexibility in terms of the modulation function. Modulation waveforms, applied to a laser beam, can range from simple sinusoidal waveforms to other complex forms derived from an equation that is programmed into an arbitrary waveform generator (Fowler, 2000).

The resulting modulation waveform, at the output of an optical modulator, will, however, contain a dc component. The mathematical description of the modulation function itself, whether generated with a mechanical chopper, an AO, or an EO,

has a non-zero mean value. If for example, a laser beam, with a magnitude that is considered normalized, is sinusoidally modulated with an EO, the modulator's output can be described as,

$$m(t) = \frac{1}{2} + \frac{1}{2} cos\,(2\pi f_c t + \phi_c) \tag{4.14}$$

which is similar to equation 4.1, albeit with an added constant component.

The non-zero mean value, or dc component, inherent in a modulated laser beam is derived from the physical nature of light. In order to impress the temporal representation of a modulation waveform onto a laser beam, an optical modulator attenuates the beam accordingly. The level of attenuation, and attenuation rate, are regulated by the desired modulation function. Without considering transmission losses from optical apertures, the level of attenuation ranges from 0% to 100%. Thus, there is an inherent dc value in modulated laser beams.

4.5 System Bandwidth

Essentially, there are three bandwidth categories, optical bandwidth, electronic bandwidth, and spatial bandwidth, that can be considered when analyzing an optical diagnostic system that utilizes a CCD as the transducer. The optical bandwidth describes the output. The electronic bandwidth describes the frequency domain processing capability of the imaging system from the input at the CCD to the output from the ADC. The spatial bandwidth describes the CCD's ability to resolve two-dimensional objects.

Optically, frequencies are extremely high. The range of wavelengths that can be detected by the imaging system are in the visible spectrum from 300nm to about 900nm. Thus, the optical frequencies are in the thousands of terahertz.

In this work, the continuous wave (cw) mode-locked laser actually emits a string of short pulses at a rate of 82MHz. The pulse width can be set to 50fs, 1ps, or 60ps. The Fourier transform limited bandwidth of the pulses is, therefore, in on the order of gigahertz. The repetition rate and the length of the pulses are considered to be at such high frequencies that the bandlimited electronic components interpret the input as a continuous-time signal.

The electronic bandwidth of the imaging system is much smaller than any optical bandwidth contained in the entire diagnostic system. The electronic bandwidth is the primary bandwidth of importance in this investigation. The information bearing signals are modulated at relatively low frequencies, on the order of kHz. Detection processes, incorporated at the pixel level, can operate in the MHz, while the image read out process, or frame rate, operates on the order of Hz.

The spatial bandwidth of an imaging system can be determined by its modulation transfer function (MTF). The MTF is a function that describes how spatial frequencies can propagate through an imaging system from the input to the output. An MTF is very similar to the temporal transfer function of a single channel electronic system, however, it is beyond the scope of this work (Kopeika, 1998).

4.6 Sampling Theory

The imaging system's input is considered a continuous time signal, as described in the previous section. Assuming the input is temporally bandlimited, the continuous time input can be completely represented and reconstructed from discrete samples taken at equally spaced intervals.

The sampling theorem states that a band-limited signal can be exactly reconstructed from samples of the signal if certain conditions are met. To show this, first

let $x(t)$ be a band-limited signal with a spectrum, $X(f)$, that is zero for frequencies higher than $|f_x|$. Acquiring samples of $x(t)$ at $x(nT_s)$, where

$$f_s = \frac{1}{T_s} \quad \text{sampling frequency,} \tag{4.15}$$

generates spectral replicas of $X(f)$ at integer multiples of the sampling frequency, f_s.

If the sampling frequency, f_s, is at least two times the absolute value of the highest frequency, f_x, contained in the continuous signal,

$$f_s > 2f_x \quad \textit{Nyquist Rate} \tag{4.16}$$

then the spectral replicas of $X(f)$ will not overlap in the sampled spectrum. Aliasing occurs if equation 4.16 is not satisfied and the original spectrum $X(f)$ is altered by interactions in frequency with adjacent sampled spectra.

The band-limited signal can be completely recovered by satisfying equation 4.16, often referred to as the *Nyqyist Rate.* If this equation is satisfied, spectral aliasing is avoided, and a lowpass filter can be used to recover the initial continuous signal. Passing the samples, $x(nT_s)$, through a lowpass filter that removes the spectral replicas of $X(f)$ but passes the original baseband spectrum will smooth the samples, reconstructing the original signal (Oppenheim & Willsky, 1997).

4.6.1 Temporal Sampling

The imaging system's temporal sampling capability is divided into two different processes. The on-chip sampling can be performed at a high frequencies while the imaging system's frame rate is limited to low frequencies.

Each pixel in the CCD array can acquire a discrete sample of the continuous time

input. Each pixel has a minimum sample duration of approximately $1\mu s$. If a 50% duty cycle is used to generate the sampling function in each pixel, then the sampling function's period is $2\mu s$. According to equation 4.15, the sampling frequency is then 500kHz. In order to satisfy equation 4.16, signals of interest must be band-limited to no more than 250kHz.

After the input is sampled at the pixel level, it must then be read from the array prior to acquiring the next frame. Reading only a single row from the CCD results in a maximum frame rate of 30Hz. Increasing the region-of-interest (ROI), which is the total number of pixels digitized, slows the frame rate down considerably (Roper Scientific, 1998a). Since data is contained in a succession of frames, and the maximum frame rate is 30Hz, the information bearing signal is band-limited to a maximum of 15Hz.

4.6.2 Spatial Sampling

The imaging system also spatially samples the continuous input. The continuous scene is converted into a grid of discrete values, contained in each pixel of the array. The discrete values can then be processed with discrete processing algorithms. If the samples are sufficiently close together, the image may appear to be spatially continuous to an observer.

Spatial frequency is, much like temporal frequency, the spatial rate at which the irradiance can fluctuate across the CCD plane. If there is no fluctuation in irradiance, and it is completely uniform, then the spatial frequency is zero or dc. The modulation transfer function (MTF) of an imaging system can be used to determine the system's capability to transfer spatial frequencies from the input to the output (Kopeika, 1998).

In this work, the irradiance across the CCD is considered to be uniform and,

thus, contains no spatial frequencies other than dc. The actual irradiance across the CCD does, however, vary. The spatial frequency of the input and the imaging system's MTF should be considered in future investigations.

4.7 General Noise Analysis Considerations

In most cases, the qualitative and quantitative descriptions of noise must be handled differently than that of deterministic signals. Signals are most often made to contain some known characteristic that can be used for identification and detection. Noise, on the other hand, is often described as a random or stochastic process.

In order to characterize a stochastic noise process, probabilistic descriptions are developed to represent the random process mathematically. A probabilistic description is the most complete and it contains all the available information about a stochastic process. The probabilistic descriptions then constitute statistical definitions that can be more applicable to the mathematical basis of system designs. A probabilistic description is not always in the realm of possibility and the extended development of probability models are not always warranted. In many engineering situations, a statistical description of noise satisfies all design requirements (Cooper & McGillem, 1999). Some important statistical descriptions are the expected value, or mean, the central moments, in particular the variance, correlations, and spectral estimations.

Qualitative assumptions about a stochastic process are often an important starting point, which can simplify the quantitative description. Sometimes the only way to specify noise in terms of its probability and statistical descriptions is to assume the noise has certain properties which validate the mathematical descriptions.

Stochastic processes are often assumed to be ergodic, which specifies that any sample function, $\mathbf{x}(\mathrm{t_i})$ from the stochastic process $x(\bullet)$ completely represents the

statistical nature of the entire ensemble. Thus, any sample function can be used in deriving the statistical properties of an ergodic process (Cooper & McGillem, 1999).

An ergodic process is also a stationary process. This type of stochastic process is independent of time origin. The statistical nature of any sample function does not depend on the time in which the sample was gathered. Thus, the statistical properties for the sample function $\mathbf{x}(\mathrm{t_i})$ will, in this case, be equal to the statistical properties of sample function $\mathbf{x}(\mathrm{t_j})$ for $t_i \neq t_j$. If a process is stationary, it is not always ergodic, but an ergodic process is always stationary (Cooper & McGillem, 1999).

If a process is stationary, then the entire statistical description does not change depending on choice of sample time. If only the first and second central moments are time invariant, the process can be considered wide-sense stationary. A wide-sense stationary process is often considered sufficient when using only the mean value and noise power to analyze and predict a system's detection capabilities.

The ensemble $\{x(t)\}$ of a stochastic process is the entire collection of all possible sample functions that may be acquired from the process. A sample function $x(t)$ is one of any possible outcomes taken from the ensemble. The sample function $x(t)$ is comprised of random variables $\mathbf{x}_\mathrm{i}$ taken at $\mathbf{x}(\mathrm{t_i})$.

In order to develop a probabilistic description of a stochastic process, a probability distribution is developed, which represents the probability of observing a random variable $\mathbf{x}$ that is less than or equal to the possible value x.

$$F_\mathrm{X}(x) \;=\; Pr\,(\mathbf{x} \leq x) \tag{4.17}$$

From the distribution function, the probability density function (pdf) can be acquired. The pdf is the derivative of the distribution function with respect to the

random variable.

$$f_{\mathrm{X}}(x) = \frac{dF_{\mathrm{X}}(x)}{dx} \tag{4.18}$$

The physical significance is contained in each step dx, such that,

$$\begin{aligned} \lim_{\Delta x \to 0} \; f_{\mathrm{X}}(x)\Delta x &= Pr\left[x < \mathbf{x} \leq (x + \Delta x)\right] \\ = \; f_{\mathrm{X}}(x)dx &= Pr\left[x < \mathbf{x} \leq (x + dx)\right], \end{aligned} \tag{4.19}$$

which is the probability that $\mathbf{x}$ lies between the possible values x and $x+dx$ (Cooper & McGillem, 1999). Thus, the information contained in the pdf isn't implicitly obvious, however, the pdf can be used to determine important statistical properties. If the pdf describing a the stochastic process $x(\bullet)$ is known, then the expected value and central moments can be determined. The expected value, $E\left[\mathbf{x}\right]$, is simply the mean value of the process.

$$\overline{\mathrm{X}} = E\left[\mathrm{X}\right] = \int_{-\infty}^{\infty} x\, f_{\mathrm{X}}(x)\, dx \tag{4.20}$$

The second moment, which is the mean-square value, is also determined from the pdf by,

$$\overline{\mathrm{X}^2} = E\left[\mathrm{X}^2\right] = \int_{-\infty}^{\infty} x^2\, f_{\mathrm{X}}(x)\, dx\,. \tag{4.21}$$

When considering noise and how a detection system is effected by the noise, the noise variance is much more useful than the noise mean. The variance is found by

calculating the second central moment, which is derived from the pdf by,

$$\sigma_{\mathrm{X}}^2 = \overline{(\mathrm{X}-\overline{\mathrm{X}})^2} = \int_{-\infty}^{\infty} (x-\overline{\mathrm{X}})^2 \, f_{\mathrm{X}}(x) \, dx \tag{4.22}$$

The variance can also be determined from the difference between the mean-square value and the square of the mean value. In electronic systems, noise often has a mean value of zero. If the mean value is defined as zero, then the variance is equal to the mean-square value. This, however, is not the case for systems that utilize light, since light is always positive, and the mean is some value greater than zero, so

$$\sigma_{\mathrm{X}}^2 = \overline{(\mathrm{X}-\overline{\mathrm{X}})^2} = \overline{\mathrm{X}^2} - (\overline{\mathrm{X}})^2 \tag{4.23}$$

The mean-square value is also related to the total power spectral density function used to describe the stochastic noise in the frequency domain.

$$\overline{\mathrm{X}^2} = \int_{-\infty}^{\infty} S_{\mathrm{X}}(f) df \tag{4.24}$$

4.7.1 Correlation

If the probability description of a stochastic process, such as noise, is not definable or is difficult to work with mathematically, then statistical properties may be obtained more easily with correlation functions. If the statistics for the interaction of different stochastic processes is desired, then a crosscorrelation function is utilized and if statistics for a single stochastic process is desired, then an autocorrelation function is utilized. Also, the output of a linear system can be determined from the specification of a correlation function at the input, even if the probability density function is not known (Cooper & McGillem, 1999).

Correlation functions lead to a function of time that provides insight to the statistical properties of a stochastic process. The autocorrelation of a stochastic process $x(\bullet)$ is found by

$$R(t_1, t_2) \;=\; E\left[\mathrm{X}(t_1), \mathrm{X}(t_2)\right] \;=\; \int_{-\infty}^{\infty} x_1 x_2 f_{\mathrm{X}}\left(x_1, x_2\; t_1 t_2\right) dx_1\, dx_2\ . \tag{4.25}$$

From the correlation function, the mean-square value can be determined at $R_{\mathrm{X}}(0)$.

$$R_{\mathrm{X}}(0) \;=\; \overline{\mathrm{X}^2} \tag{4.26}$$

If the mean value is known, then the variance can be determined by subtracting the square of the mean value from $R_{\mathrm{X}}(0)$.

If the mean value is zero, then the variance is simply equal to the autocorrelation function evaluated at $\tau = 0$. Thus, $R_x(0)$ is equal to the mean-square value, whether the process has a mean value of zero or not (Cooper & McGillem, 1999).

$$\sigma_{\mathrm{X}}^2 \;=\; R_{\mathrm{X}}(0) - \left(\overline{\mathrm{X}}\right)^2 \;=\; \overline{\mathrm{X}^2} - \left(\overline{\mathrm{X}}\right)^2 \tag{4.27}$$

The autocovariance function is often more useful, since the mean value is removed, and the function is only dependent on random fluctuations, or noise (Helstrom, 1991). Subtracting the square of the mean value from the autocorrelation function produces the autocovariance function, $C_{\mathrm{X}}(\tau)$.

$$C_{\mathrm{X}}(\tau) \;=\; R_{\mathrm{X}}(\tau) \;-\; \left(\overline{\mathrm{X}}\right)^2 \tag{4.28}$$

Evaluating the autocovariance at $\tau = 0$ is the same as equation 4.27 and, therefore,

gives the variance of the stochastic process.

$$C_X(0) = \sigma_X^2 = R_X(0) - \left(\overline{X}\right)^2 \tag{4.29}$$

The autocorrelation function can also be used to determine the power spectral density (psd) function. The psd function describes how the power in stochastic noise process is distributed over the frequency domain. The power spectral density function, $S_X(f)$, can be obtained by taking the Fourier transform of the autocorrelation function, $R_X(\tau)$.

$$S_X(f) = \int_{-\infty}^{\infty} R_X(\tau)\, e^{-j2\pi f\tau}\, d\tau \tag{4.30}$$

The psd function is often used when determining a system's output by applying the psd to a system's power transfer function, which is described in the next section. The psd function can also be used to find the mean-squared value for a stochastic process. Integrating the psd function, $S_X(f)$, results in the mean-squared value,

$$\overline{X^2} = \int_{-\infty}^{\infty} S_X(f)\, df\ , \tag{4.31}$$

which is also equal to the result from evaluating the autocorrelation function at $\tau = 0$, as shown in equation 4.26.

4.7.2 Noise Power Transfer

Once a stochastic noise source is defined in terms of its statistical properties, these properties can be used in the design and analysis of a linear time invariant (LTI) system. As shown in the previous section, noise can be statistically described

in terms of it variance, mean-squared value, and its mean value. It can also be described in the time domain, by determining an autocorrelation function, and in the frequency domain, by determining the power spectral density function.

Linear systems theory and spectral analysis techniques can be found in numerous texts such as Taub & Schilling (1986), Stremler (1990), Oppenheim & Willsky (1997), and Cooper & McGillem (1999). A basic premise of linear systems theory is that, given an LTI system, its input and output are related by the system's transfer function, or impulse response. Given the impulse response, $h(t)$, the transfer function, $H(f)$, is found by taking the Fourier transform of $h(t)$.

$$H(f) = \int_{-\infty}^{\infty} h(t)e^{-j2\pi ft}\, dt \tag{4.32}$$

Convolution can be used in the time domain to determine the output of a system, $y(t)$, based on its input, $x(t)$, and the system's impulse response, $h(t)$. In this case, both the input and output signal can be considered to have units of current or voltage.

$$y(t) = \int_{-\infty}^{\infty} x(\tau)h(t-\tau)\, d\tau \tag{4.33}$$

Often, a transformation is used to simplify the previous equation. Performing the convolution process in the time domain is equivalent to performing multiplication in the frequency domain. If the Fourier transform of both the input $x(t)$, which is $X(f)$, and the system's impulse response, $h(t)$, which is $H(f)$, can be found, then the output, $Y(f)$, can be obtained through multiplication.

$$Y(f) = X(f) \cdot H(f) \tag{4.34}$$

The time domain signal at the output, $y(t)$, can then be found by taking the inverse Fourier transform of $Y(f)$.

$$y(t) = \int_{-\infty}^{\infty} Y(f)e^{j2\pi ft}\,df = \int_{-\infty}^{\infty} (X(f)\cdot H(f))\,e^{j2\pi ft}\,df \tag{4.35}$$

In terms of designing a system, the transfer function can instead be specified by dividing the output by the input. If the input is known, and a desired output is specified, then the transfer function and impulse response can be developed.

$$H(f) = \frac{Y(f)}{X(f)} \tag{4.36}$$

and

$$h(t) = \int_{-\infty}^{\infty} H(f)e^{j2\pi ft}\,df \tag{4.37}$$

The same procedures can be used to analyze the transfer of stochastic processes through LTI systems. When analyzing stochastic processes, however, waveforms cannot be specified in terms of a deterministic voltage or a current. The statistical representation of a stochastic process describe it in terms of variations in power. Thus, the power transfer function needs to be used when analyzing stochastic processes.

The power transfer function is the squared magnitude of the transfer function. If $H(f)$ is the transfer function of an LTI system, then it power transfer function is $|H(f)|^2$.

In order to determine the power spectrum of a stochastic process at the output, $S_{\mathrm{Y}}(f)$, of an LTI system, the power transfer function can be applied to the input power spectrum, $S_{\mathrm{X}}(f)$.

$$S_{\mathrm{Y}}(f) = S_{\mathrm{X}}(f)|H(f)|^2 \tag{4.38}$$

As shown in equation 4.37, the previous mathematical statement can also be used to design a transfer function that will produce a desired output based on a given input. If the input power spectrum, $S_{\mathrm{X}}(f)$, is known and the desired output spectrum is $S_{\mathrm{Y}}(f)$, then the power transfer function is,

$$|H(f)|^2 = \frac{S_{\mathrm{Y}}(f)}{S_{\mathrm{X}}(f)} \tag{4.39}$$

The statistical analysis calculations that were described above can also be performed on the system's output. The mean-squared value at the output, $\overline{\mathrm{X}_{\mathrm{o}}^2}$, can then be determined by integrating the output power spectral density function, $S_{\mathrm{Y}}(f)$.

$$\overline{\mathrm{X}_{\mathrm{o}}^2} = \int_{-\infty}^{\infty} S_{\mathrm{Y}}(f)\, df \tag{4.40}$$

If the stochastic process contains a mean value, then the square of the mean value at the output, $\left(\overline{\mathrm{X}_{\mathrm{i}}}\right)^2$, can be determined by,

$$\left(\overline{\mathrm{X}_{\mathrm{o}}}\right)^2 = \left(\overline{\mathrm{X}_{\mathrm{i}}}\right)^2 |H(0)|^2 \tag{4.41}$$

where $\left(\overline{\mathrm{X}_{\mathrm{i}}}\right)^2$ is the square of the mean value at the input. Since the mean value is a dc component, the power transfer function is evaluated at $f = 0$, in the equation above.

The variance at the output, σ_o^2, can be determined by subtracting the square of mean value from the mean-squared value. If the mean value at the input is zero, then the mean value at the output is zero and the variance at the output is equal to the

mean-squared value at the output.

$$\sigma_o^2 = \overline{X_o^2} - \left(\overline{X_o}\right)^2 = \int_{-\infty}^{\infty} S_X(f)|H(f)|^2\, df - \left(\overline{X_i}\right)^2 |H(0)|^2 \tag{4.42}$$

4.7.3 Equivalent Noise Bandwidth

Instead of integrating over the entire frequency spectrum, it is often easier to determine the noise power out of a filter by using the filter's equivalent noise bandwidth. A filter's equivalent noise bandwidth (NEB) is the bandwidth of an ideal filter, which when applied to a white noise source, produces the same noise power at the output as the actual filter (Stremler, 1990). The NEB is defined such that the area under an ideal filter is equal to the area under the real filter over all frequency.

The NEB is determined by dividing the area of a filter from $f = 0$ to $f = \infty$ by the value of the filter at $f = 0$.

$$B_N = \frac{\int_0^{\infty} |H(f)|^2\, df}{|H(0)|^2} \tag{4.43}$$

As an example, the NEB for a second order, lowpass filter, $H_{LP}(f)$, is determined. The lowpass filter is defined as,

$$H_{LP}(f) = \frac{G_{LP}}{\sqrt{1 + \frac{f}{f_c}}}, \tag{4.44}$$

where G_{LP} is the filter gain and f_c is the -3dB cutoff frequency. Integrating $|H_{LP}(f)|^2$ from $f = 0$ to $f = \infty$ results in,

$$\int_0^{\infty} \frac{(G_{LP} f_c)^2}{f_c^2 + f^2}\, df = G_{LP}^2 f_c \frac{\pi}{2}. \tag{4.45}$$

Evaluating $|H_{LP}(f)|^2$ at $f = 0$ is simply the square of the filter's gain, G_{LP}^2. Inserting these values into equation 4.43 produces the NEB for $H_{LP}(f)$.

$$B_N = \frac{G_{LP}^2 f_c \frac{\pi}{2}}{G_{LP}^2} = f_c \frac{\pi}{2} \tag{4.46}$$

The ideal filter the produces the same noise power at the output, defined as the noise equivalent filter, has a gain equal to the real filter's gain that is constant over the noise equivalent bandwidth, B_N. The noise equivalent filter, $H_{LP}^{eq}(f)$, can be written as,

$$H_{LP}^{eq}(f) = G_{LP} \prod \left(\frac{f}{2B_N} \right) = G_{LP} \prod \left(\frac{f}{\pi f_c} \right) \tag{4.47}$$

The rectangular gate function is defined as unity over a specified bandwidth and defined as zero elsewhere, as shown in the following equation.

$$\prod \left(\frac{f}{2B_N} \right) \equiv \begin{cases} 1 & |f| \leq B_N \\ 0 & |f| > B_N \end{cases} \tag{4.48}$$

Rather than integrating over the entire frequency spectrum, the noise at the output of a filter can then be determined by integrating over the noise equivalent bandwidth. If $S_X(f)$ is a zero mean valued white noise source applied to the lowpass filter, $H_{LP}(f)$, the noise power at the output can be found by using the real filter and integrating over all frequency.

$$\sigma_y^2 = \int_{-\infty}^{\infty} S_X(f) |H_{LP}(f)|^2 \, df \tag{4.49}$$

Or, the same output power can be determined by using the noise equivalent filter and

integrating over the noise equivalent bandwidth.

$$\sigma_y^2 = G_{LP}^2 \int_{-f_c\frac{\pi}{2}}^{f_c\frac{\pi}{2}} S_X \, df \tag{4.50}$$

The latter integral is quite often the simpler of the two. It is, therefore, beneficial to determine the NEB of real filters for noise analysis purposes.

4.8 Conventional Laser Diagnostic Instrumentation

Different measurement techniques can be utilized in laser diagnostics to increase the probability of detecting a signal, or determining if a signal exists. Often the measurement technique is classified by its ability to improve the signal-to-noise ratio (SNR). Choosing which basic technique to utilize is determined by how closely the technique's processing functions meet the desired measurement objective (Cunningham & Shaw, 1999).

SNR improvement is often achieved by bandwidth narrowing techniques. Narrowing the detection bandwidth in a controlled manner can reduce the total amount of noise at the output, while preserving, and even amplifying, the desired signal. A few basic techniques of bandwidth narrowing that are in widespread use are signal averaging, transient averaging, boxcar integration, multichannel scaling, pulse-height analysis, and lock-in detection or phase sensitive detection (Horowitz & Hill, 1989).

Two established instruments are the lock-in amplifier and the boxcar integrator. The functionality of each of these instruments is explained to show the relationship between the processing functions incorporated into the imaging system and processing functions that are held as industry standards.

4.8.1 Lock-In Amplifier

A lock-in amplifier is a phase sensitive detection instrument that measures small ac signals in the presence of noise, which may be many thousands of times larger than the signal. A lock-in amplifier is a well established instrument typically used in laser diagnostics to extract a small information bearing signal, when the laser source is cw, and the amplitude-modulated frequency and phase are known *a priori* (Eckbreth, 1996).

Extracting a small ac signal of interest is accomplished, in an elementary form, with mixing and bandwidth narrowing operations. First, the input to the lock-in amplifier, which can be the output from a photodiode, is mixed with a reference sinusoid. The reference sinusoid is normally generated from a phase-locked loop driven by the same waveform used for modulation.

Mixing the input with a sinusoid accomplishes two things. The dc component, which can be much larger than the signal in laser diagnostics, and any low frequency noise are translated to a high frequency band. These are the sum frequency terms in a homodyne process. Likewise, the signal of interest is translated in frequency, albeit back down to the baseband.

After mixing the input with the sinusoidal reference, a lowpass filter removes the sum frequency components, where the dc and low frequency noise now reside. The end result, at the output of the lowpass filter, is comprised of the signal and any noise that existed at the modulation frequency over a bandwidth equal to the noise equivalent bandwidth of the lowpass filter. The extent of noise reduction is, therefore, controlled by the synchronization of the reference sinusoid and the passband of the lowpass filter. A narrower lowpass filter passband increases the SNR, but also reduces the instruments response time (Fowler, 2000; Stanford Research Systems, 1999).

The lock-in amplifier utilizes the homodyne detection method, described in section 4.4.1. The lock-in amplifier is, therefore, sensitive to the phase difference between the modulated signal and the sinusoidal reference. A phase error will reduce the gain applied to the recovered signal; a phase error of $\pm 90^o$ results in a gain of zero, eliminating recovery of the signal. Commercial lock-in amplifiers, however, allow the user to either adjust the phase or lock to the phase that maximizes the signal.

The diagnostic imaging system described in this work has a few characteristics that were extracted from the lock-in amplifier. Using a reference waveform, or trigger, the input is sampled, at the pixel level, with a waveform that is locked to the frequency and phase of the modulation waveform.

Mixing the input with the pixel's sampling waveform translates the modulated information signal down to the baseband. However, since the sampling waveform at each pixel has an inherent dc value, the input's dc term and low frequency noise remain at the baseband and are not completely translated to a higher frequency band. Thus, the processes that occur at the pixel level are not ac-coupled like the processes that are performed by the lock-in amplifier.

The imaging system also has a lowpass filtering capability at the pixel level. Multiple samples can be stored at each pixel, producing an averaging process. The averaging process filters out high frequency components, which can include sum frequency terms, much like the lock-in amplifier.

4.8.2 Boxcar Averager

A boxcar averager, or gated integrator, is a more appropriate instrument for measuring a train of short pulses that are separated by relatively long durations of zero information, which is the case when the duty cycle is much less than 50%. A

boxcar integrator greatly improves the SNR by detecting the signal only when it is present and not detecting anything when there is nothing but noise. The detection is performed by switching, or gating, the input signal, to an amplifier, on and off. Significant amplification of the gated signal, on the order of 10^8, is also possible, which improves the instruments capability of detecting small amplitude signals (Stanford Research Systems, 1999).

The gated input is then fed into a lowpass filter, which integrates all of the on gates. Thus, the boxcar integrator can essentially be considered a gated lowpass filter. The final value at the filter's output is equal to the average value of the pulses over the on interval of the gate. SNR improvement is obtained by reducing the noise bandwidth and patiently gathering information, which is spread out over time (Fowler, 2000).

In its elementary form, the boxcar integrator is a gated averager that is comprised of a simple RC integrating circuit that has a triggerable on-off switch, called a gate, at its input. The gate is controlled with an external trigger that is synchronized to the laser source or experiment. Triggering the gate on allows the input to pass to the RC integrator for the time duration τ.

A boxcar integrator can be operated in three averaging modes, which are based on the relationship between the RC time constant and the gate time duration τ. If τ is much less than RC, the boxcar operates in a linear averaging mode; if τ is approximately equal to RC, it operates in an exponential averaging mode; or if τ is much greater than RC, the boxcar operates in a sample and hold mode.

In the linear averaging mode, the integrated value is a linear weighting of all of the pulses that are sampled. The integrated value increases over time and, thus, the output must be read prior to saturation. If RC/τ pulses are integrated, the output

will approximate the average of all the pulses (Eckbreth, 1996).

The exponential averaging mode is used to continuously measure a signal's steady state value. In this case, when τ is approximately equal to RC, the most recent integrated pulses are more heavily weighted and earlier pulses are forgotten. As the pulses are integrated, the RC integrator will reach a steady state value, from which variations in the input can be determined.

As pulses are averaged in both the linear averaging mode and the exponential averaging mode, the noise contained in the pulses is also averaged. Most noise sources, such as photon noise and $1/f$ noise, have a zero mean value and will, therefore, average out to zero. Any type of offset or additional dc values, other than the signal of interest, will not be eliminated, but will average to their mean values (Stanford Research Systems, 1999).

The final operating mode is typically used in conjunction with an analog-to-digital converter (ADC). If τ is much larger than RC, then each pulse is sampled individually and held on the integrator's output. The integrator's output can be digitized and additional processing can be performed digitally (Eckbreth, 1996).

The diagnostic imaging system also shares characteristics with the boxcar integrator. At the pixel level, the input can be gated, by the read out gate (ROG), either on or off. The information in each pulse or sample is stored in the vertical register. Multiple pulses can be stored in the vertical register, creating a lowpass filtering function, or integrator. Operating the imaging system in a homodyne mode is comparable to operating a boxcar integrator in the linear averaging mode.

Unlike a typical boxcar integrator, the imaging system is not capable of amplifying the signal prior to averaging with the vertical register. In fact, there is actually a slight loss in signal due to the quantum efficiency of the CCD detector. However,

the phase sensitive imaging system can capture two-dimensional data, which is not possible with a single boxcar integrator.

Chapter 5

REPRESENTATION OF SIGNALS AND NOISE

In order to use the mathematical model that represents the diagnostic imaging system's functionality, certain definitions and clarifications about the system's input need to be presented. This chapter introduces mathematical descriptions of the waveforms that when combined, represent the total irradiance entering the detector. This chapter also introduces definitions for noise levels, which are derived from both laser characteristics and electronic characteristics. The definitions made in this chapter will then be used in Chapters 6 and 7, after the imaging system's mathematical models are developed, to predict the signal and noise power present at the output.

This investigation analyzes the imaging system's temporal response, rather than its spatial response, and, therefore, the input is defined in the time and temporal frequency domains, but not in the spatial domain. The definitions developed in this chapter model the irradiance that enters a single pixel. It is assumed that the total irradiance over the entire CCD array is uniform and any pixel of interest is incident with the same input.

An objective of this investigation, as outlined in Chapter 4, is to gain a systems level perspective of the imaging system. The system level model is then used to explore methods to enhance the imaging system's detection capability. In order to perform a linear systems analysis, with mathematical models that describe the imaging system's functionality, a linear mathematical model of the input needs to be realized.

Information about the input signal and noise components that will contribute to a linear systems analysis is specified in the following sections. For example, a power spectral density function for both photon noise and $1/f$ noise is developed. Time domain and temporal frequency domain models of the signal are also defined. The power spectral density functions are then used to provide insight on how the signal and noise components transfer through the imaging system and are manifested at the output.

5.1 Input Signal Definition

The instantaneous optical input signal, $P_r(t)$, is modeled as the composition of three irradiance components: (1) a steady state background irradiance, I_p; (2) an information bearing irradiance, $A(t)$, that is modulated with a periodic waveform $m(t)$; and (3) additive noise irradiance, $I_N(t)$. The information bearing irradiance, $A(t)$, which we are seeking to detect at the imaging system's output, is considered to be a random phenomenon that represents a physical parameter of interest. The frequency and phase of the modulation function, $m(t)$, that is impressed on the information bearing irradiance, are most likely controllable, and, therefore, known *a priori*. Thus, the modulation function, $m(t)$, can be used to represent the periodic nature of a signal employed in a particular diagnostic technique. The steady state background is the mean, or dc, value of the input. Random variations in the input are contained in the noise component, which is the combination of photon noise and $1/f$ noise. Thus, the different components can be manipulated into a form that provides a good representation of a particular experiment's conditions.

$$P_r(t) \;=\; I_p \;+\; I_N(t) \;+\; A(t) \cdot m(t) \tag{5.1}$$

This general mathematical definition of the irradiance incident on a single pixel (equation 5.1) can be used to model a range of input characteristics. The input to a detector from both background free and background intensive diagnostic techniques can be modeled. The steady state background component is the mean value of the optical input. Background intensive and background free diagnostic techniques can be modeled by changing the magnitude of the steady state background component accordingly.

As shown later in this chapter, the level of the two noise sources are a function of the level of the steady state background, I_p. If the background tends to zero, as in a background free diagnostic, then the noise levels become a function of the signal level. A range of case studies can, therefore, be performed by incorporating the characteristics of a particular diagnostic into the general model.

As an example case study, the probe beam, in a pump/probe absorption spectroscopy (PPAS) experiment can be modeled with equation 5.1. In this case, the modulated information bearing signal, $A(t) \cdot m(t)$, is superimposed on a much larger steady state background, I_p. The background irradiance also fluctuates at low frequencies and has an inherent fluctuation in the arrival rate of photons. $A(t)$, therefore, also resides in the $1/f$ noise and photon noise ($I_N(t)$).

In a PPAS experiment, two laser beams, a pump beam and a probe beam, are passed through a spatially overlapping region in a sample. The lasers are tuned in wavelength to the resonant frequency of the species under investigation. Thus, some of the photons in the lasers are absorbed by the species. The change in a beam's irradiance, after it passes through a sample, can then be used to determine characteristics about the species under investigation (Settersten, 1999).

If only the probe beam is passed through the sample, the number of absorbed

photons will reach a steady state value and the beam's irradiance out of the sample will reach a steady state value. Since the species information is contained in the amount the irradiance changes from the sample's input to its output, a very small steady state value at the output would be impossible to measure. The pump beam, which is modulated, is also passed through the sample to impress a predetermined modulation waveform on the probe beam. Knowing the frequency and phase of the modulation waveform *a priori* provides a way to synchronize the probe beam irradiance with a reference.

Before the pump beam enters the sample volume, it is directly modulated. A modulation waveform can be impressed on the pump beam with a mechanical chopper, acousto-optic modulator (AO) or eletro-optic modulator (EO) as discussed in Chapter 4. The modulation waveform that is impressed on the pump beam also appears on the probe beam after it passes through the sample (Fiechtner & Linne, 1994). The probe beam, which is a continuous wave (cw) beam before entering the sample, increases slightly in irradiance at the frequency and phase of the modulated pump beam, which passed through the sample just prior to the probe beam. Information about the sample volume, through which the two beams cross, is contained in the level of attenuation impressed on the probe beam. Since the frequency and phase of modulation waveform impressed on the pump beam are known, the information in the probe beam can be extracted by utilizing the *a priori* knowledge (Fowler, 2000). Extensive information about PPAS can be found in (Settersten, 1999).

The probe beam, after it exits the sample volume, can be modeled using equation 5.1. The steady state value, I_p, is used to represent the average probe beam irradiance, or dc power. The modulated information bearing signal, $A(t) \cdot m(t)$, represents the variations in the probe irradiance that are related to the sample. Random

fluctuations in the probe beam irradiance are assumed to be photon noise and $1/f$ noise. These noise parameters are incorporated in the noise component $I_N(t)$ to complete the probe beam model.

As an example of a background free technique, the model may also be used to describe the fluorescence signal from pressure sensitive paint measurements. In this case, the information bearing signal, $A(t)$, while still small, is comparable to the steady state background, I_p.

In the background intensive case, the $1/f$ noise and photon noise is a function of the background, I_p. The $1/f$ noise and photon noise in a background free diagnostic, on the other hand, can be modeled as a function of the $A(t)$ itself. Thus, the same variables from equation 5.1, albeit with different scales and bounds, can also be used to represent the modulated information bearing signal, steady state background, and the noise present in a background free diagnostic.

5.2 Transfer Of Units

Before determining representative equations for the background, photon noise, and $1/f$ noise, the units of the equations are introduced in this section. As shown in section 5.3, the input to the imaging system can be specified in units of either watts or photons/second.

In general, the noise components in a system are specified in units that are the square of the signal units. For example, if a signal has a mean value with units of volts, then its variance is defined in units of volts^2, which can also be defined as normalized power (referenced to a resistance of 1 ohm) with units of watts.

In this analysis, the magnitude of the inputs are given in units of watts and photons/second. The noise components will, therefore, have units of (watts)^2 and

(photons/sec)^2.

These units for noise appear to be ambiguous. An illustration that shows how units are transferred through the imaging system helps in understanding the noise units. Figure 5.1 illustrates the transfer of units through the imaging system. The quantum efficiency, integration time, CCD's output amplifier conversion, and the gain of the read out electronics are incorporated into Figure 5.1. These parameters are explained in section 2.7. Figure 5.1 does not include the system's analog to digital (ADC) converter.

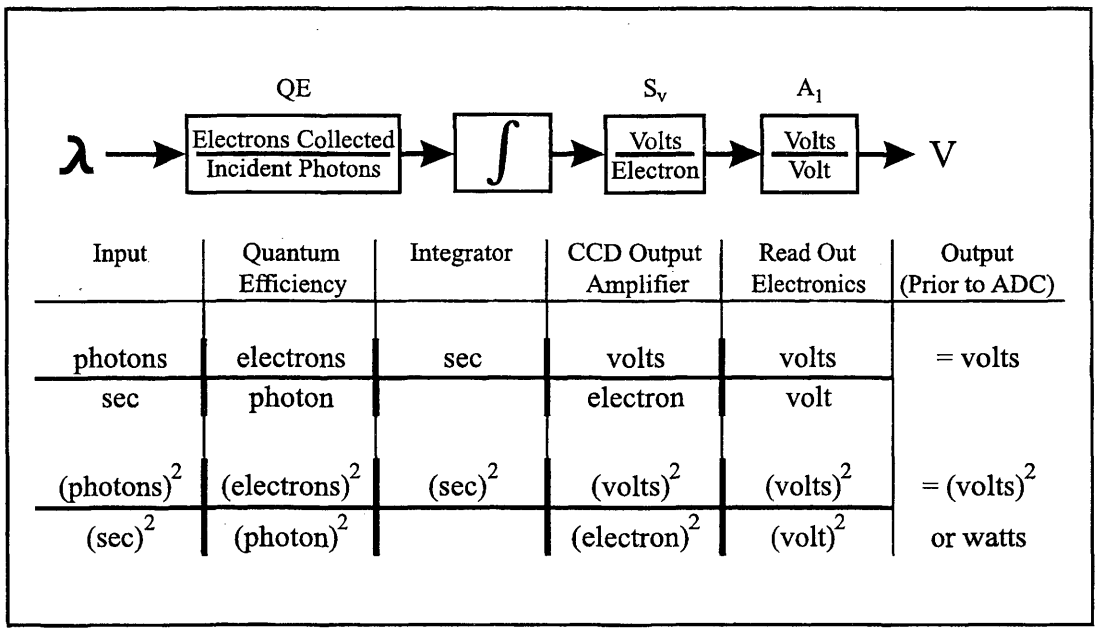

FIG. 5.1. Unit conversion from CCD input to output of the read out electronics, prior to analog-to-digital conversion (ADC)

Based on Figure 5.1, the imaging system's output has units of volts when the input has units of photons/second. Correspondingly, the noise output has units of (volts)^2, or watts, when the input is in units of (photons/sec)^2. The input magnitude units are, therefore, defined as photons/second and the input power units are defined

as (photons/sec)^2. At the input, the units can be converted to watts and (watts)^2 respectively, considering the energy per photon.

The units for the magnitude spectrum and power spectral density are defined accordingly. Figure 5.2 gives spectral definitions and shows the transfer of spectra through the imaging system's transfer function $H_s(f)$.

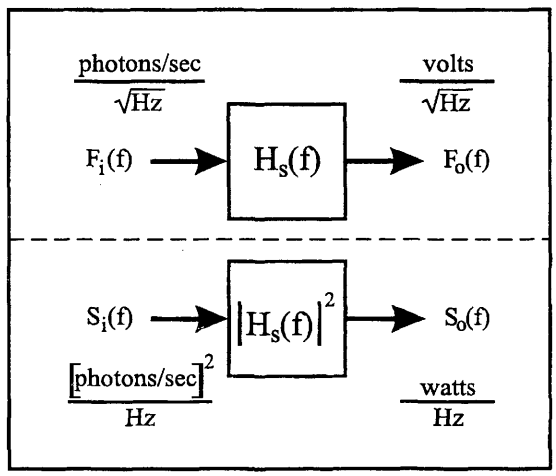

FIG. 5.2. Transfer of magnitude spectrum ($F(f)$) and power spectrum ($S(f)$) through the system function ($H_s(f)$) that describes the imaging system

The input magnitude spectrum has units of (photons/sec)/$\sqrt{\text{Hz}}$. Applying the input magnitude spectrum to $H_s(f)$ results in an output spectrum that has units of volts/$\sqrt{\text{Hz}}$. Based on the noise units defined above, the input power spectral density function, or simply power spectrum, has units of (photons/sec)^2/Hz. The output of the power transfer function, $|H_s(f)|^2$, is in units of (volts)^2/Hz, or watts/Hz.

In the following sections of this chapter, the magnitude spectrum, $F(f)$, and

power spectrum, $S(f)$, are, therefore, defined with the following units.

$$F(f) \Leftrightarrow \frac{\text{photons/sec}}{\sqrt{\text{Hz}}} \quad \text{or} \quad \frac{\text{watts}}{\sqrt{\text{Hz}}}$$
$$S(f) \Leftrightarrow \frac{(\text{photons/sec})^2}{\text{Hz}} \quad \text{or} \quad \frac{(\text{watts})^2}{\text{Hz}}$$

5.3 Background Component

The steady state background component, defined in this section, is derived from the average beam power, P_B. Both an incident power *per pixel*, I_p, and a corresponding photon arrival rate *per pixel*, λ_p, are defined. Initially, the irradiance in the entire laser beam, I_B, is defined for a beam with average power P_B, in watts, and a beam diameter d_B, in centimeters.

$$I_B = \frac{4P_B}{\pi d_B^2} \quad \frac{\text{watts}}{\text{cm}^2} \tag{5.2}$$

The steady state power per pixel, I_p, can then be determined from the beam irradiance, I_B, using the area of a single pixel, A_p. The area of one pixel on the Sony $ICX085$ interline transfer CCD is approximately 4.5x10^{-7} cm^2.

$$I_p = I_B A_p = \frac{4P_B A_p}{\pi d_B^2} \quad \text{watts (per pixel)} \tag{5.3}$$

The background power, I_p, is considered to be the mean power entering a single pixel and is defined as a constant value for all time. Since the incident power is a constant, the background power spectrum, per pixel, is an impulse, $I_p\delta(f)$, at the frequency domain origin. Variances in the power entering each pixel is considered noise, which will be defined in a later section.

The mean per pixel photon arrival rate, λ_p, can also be defined using the beam irradiance, I_B, defined in equation 5.2, and the energy per photon, ϵ. The energy per photon, ϵ, is a function of wavelength, λ_w,

$$\epsilon = \frac{hc}{\lambda_w} \quad \frac{\text{Joules}}{\text{photon}} \tag{5.4}$$

where h is Planck's constant and c is the speed of light. Using the energy per photon, the beam irradiance, I_B, can be converted to the beam's photon flux density, λ_B.

$$\lambda_B = \frac{I_B}{\epsilon} = \frac{\lambda 4 P_B}{hc\pi \left(d_B\right)^2} \quad \frac{\text{photons}}{\text{sec}\cdot\text{cm}^2} \tag{5.5}$$

By incorporating the pixel area, A_p, into the equation above, an expression for the mean photon arrival rate, λ_p, at a single pixel, is obtained.

$$\lambda_p = \lambda_B A_p = \frac{I_B A_p}{\epsilon} = \frac{I_p}{\epsilon} = \frac{\lambda 4 P_B A_p}{hc\pi \left(d_B\right)^2} \quad \frac{\text{photons}}{\text{sec}} \quad \text{(per pixel)} \tag{5.6}$$

Just as the average power, I_p, is considered to be a constant for all time, so too is the photon arrival rate, λ_p. Deviations from the constant photon arrival rate are considered noise. The steady state background is, therefore, defined as an impulse in the frequency domain at dc. Based on the discussion of units in section 5.2, the steady state background power spectrum, $S_B(f)$, can be written in the following two forms.

$$S_B(f) = \left(I_p\right)^2 \delta(f) \quad \frac{(\text{watts})^2}{\text{Hz}} \tag{5.7}$$

or

$$S_B(f) = \left(\lambda_p\right)^2 \delta(f) \quad \frac{(\text{photons/sec})^2}{\text{Hz}} \tag{5.8}$$

For a given exposure time, Δt, the mean number of photons incident on a pixel is $\lambda_p \Delta t$. Based on the exposure time and the CCD's dynamic range, the maximum power that can be incident on each pixel prior to reaching saturation can be determined.

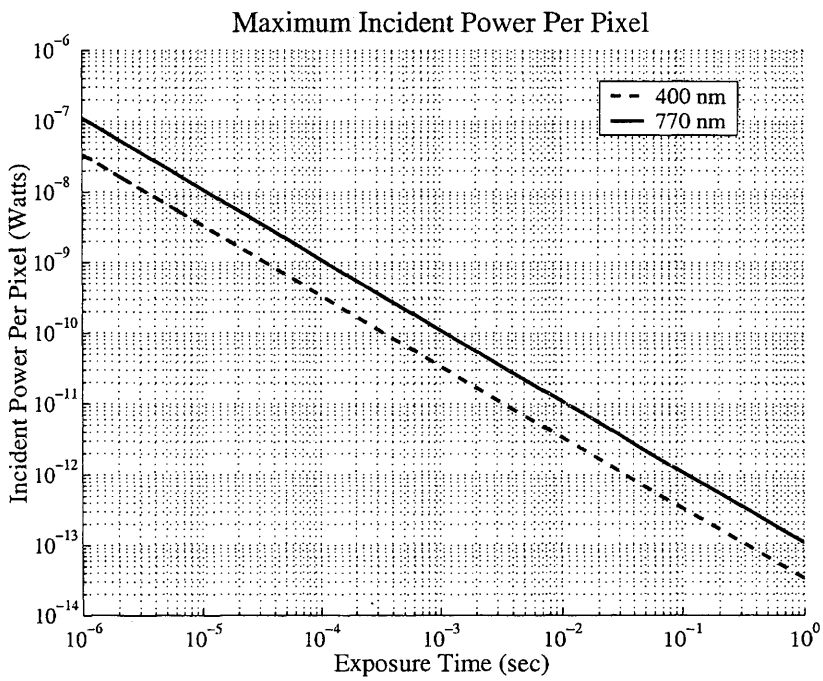

FIG. 5.3. Maximum incident power per pixel according to sampling time

Figure 5.3 illustrates the maximum steady state power, I_p, that can be incident on a single pixel for an exposure time of Δt, without saturating the pixel. The corresponding maximum beam irradiance, I_B, that can be incident on the entire CCD array is illustrated in Figure 5.4. The irradiance in Figure 5.4 is calculated by dividing the maximum incident power per pixel, I_p, in Figure 5.3, by the pixel area, A_p.

The maximum incident power per pixel is based on the CCD's well depth, which, as explained in Chapter 2, is the maximum number of photoelectrons that can be held

in a pixel's potential well. The accumulation of photoelectrons beyond the well depth leads to saturation.

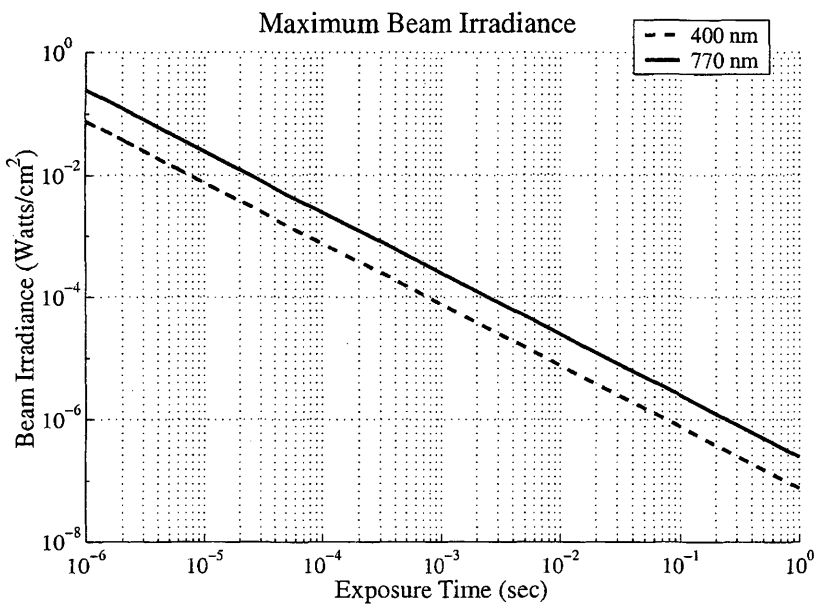

FIG. 5.4. Maximum beam irradiance according to sampling time

As shown in Chapter 2, the well depth of the interline transfer CCD is about 34,000 photoelectrons. Since lasers are typically monochromatic light sources, the number of incident photons required to fill a pixel's potential well is dependent on both the detector's quantum efficiency at the beam's particular wavelength and the photon arrival rate at the detector plane. The photon arrival rate, λ_p, and the corresponding steady state power, I_p, were shown in equation 5.6 to be related by the photon energy, ϵ, which is also a function of wavelength. In this case, wavelengths of 400nm and 700nm and a well depth of 34,000 electrons were used to calculate the maximum values shown in Figures 5.3 and 5.4.

The maximum incident power per pixel and maximum beam irradiance are important parameters that need to be taken into consideration when designing back-

ground intensive diagnostics, such as PPAS. Not only does a beam's power need to be set to operate in the linear region of a diagnostic, but it also needs to be set or attenuated so that the detector operates in the linear region and is not saturated.

The signal-to-noise ratio (SNR) is another factor that also needs to be considered. It will be shown that the SNR, according to the photon limit, increases with increasing beam power. An optimized system would therefore have a high SNR while operating in the detection system's linear operating region.

5.4 Stochastic Process Definitions

Random variations away from the average power, I_p, incident on each pixel, are considered to be noise. The total noise entering a pixel is a combination of low frequency drifts in the incident power and photon noise. Low frequency drift in the background power is considered to be noise with a $1/f$ type power spectral density, or power spectrum. Photon noise, which is inherent in all optical systems because of the discrete nature of photons, is considered to be white noise with a uniform power spectrum. Spatial noise is also discussed below, however, it is not included as a noise source in the temporal model.

Since noise is a random phenomenon, it is advantageous to describe noise with probabilistic and statistical methods. It is not possible to define noise at every instant in time, but it is possible to determine the average power and the distribution of power over frequency for a noise source (Cooper & McGillem, 1999). The following sections will define probability properties and statistical characteristics for photon noise and $1/f$ noise.

Before discussing noise, the stochastic processes used in this work to represent the photon arrival rate and noise need to be defined. The photon arrival rate process

is defined as the stochastic process $\Lambda(\bullet)$ (λ is often used in the literature to represent a rate). This process has a probability density function $f_\Lambda(\lambda)$, where λ is any possible photon arrival rate. In this case, the expected value of the stochastic process $\Lambda(\bullet)$ is,

$$\overline{\Lambda} = E[\Lambda] = \int_{-\infty}^{\infty} \lambda\, f_\Lambda(\lambda)\, d\lambda \quad \text{(mean)} \tag{5.9}$$

The mean-square value of the stochastic process $\Lambda(\bullet)$ is,

$$\overline{\Lambda^2} = E[\Lambda^2] = \int_{-\infty}^{\infty} \lambda^2 f_\Lambda(\lambda)\, d\lambda \quad \text{(mean-square)} \tag{5.10}$$

The variance of the process is the difference between the mean-square value and the square of the mean value.

$$Var\left(\Lambda\left(\bullet\right)\right) = \sigma_\Lambda^2 = \overline{\Lambda^2} - \left(\overline{\Lambda}\right)^2 \quad \text{(variance)} \tag{5.11}$$

A stochastic beam power process that is proportional to the photon arrival rate process, $\Lambda(\bullet)$, could also be defined. Equation 5.6 shows that the photon arrival rate is calculated by dividing the beam power by the energy per photon. Thus, the random nature in beam power can be described by multiplying the photon arrival rate process, $\Lambda(\bullet)$ by the energy per photon, ϵ.

Very similar definitions are made for the photon noise process and the $1/f$ noise process. The photon noise process is defined as the stochastic process $W(\bullet)$ (W is used since photon noise is a **W**hite noise, as shown in the next section). This process has a probability density function $f_W(w)$, where w is any possible photon noise power.

The statistical properties of the stochastic photon noise process, $W(\bullet)$, can be defined with the same format used in equations 5.9, 5.10, and 4.22. Making the

appropriate substitutions into these equations gives the mean value $\overline{W}$, the mean-square value, $\overline{W^2}$, and the variance, σ_W^2, for the photon noise process, $W(\bullet)$.

Finally, the same definitions are made for the $1/f$ noise process. The $1/f$ noise process is defined as the stochastic process $L(\bullet)$ (L is used because this process contains primarily **L**ow frequency noise). This process has a probability density function $f_L(l)$, where l is any possible $1/f$ noise power.

The statistical properties of the stochastic $1/f$ noise process, $L(\bullet)$, can again be defined by making the appropriate substitutions into equations 5.9, 5.10, and 4.22. The statistical parameters for the $1/f$ noise process, $L(\bullet)$, are the mean value $\overline{L}$, the mean-square value, $\overline{L^2}$, and the variance, σ_L^2.

Although the probability density functions (pdf), for each of the stochastic processes above, were introduced, exact definitions for the density functions may not be obtainable. In fact determining the pdf for a stochastic process may not even be necessary. Often, the statistical properties of a stochastic process, such as the mean, mean-squared value, and variance, comprise adequate information to perform a complete design and analysis of a system (Cooper & McGillem, 1999).

In order to find the total noise from the photon noise and $1/f$ noise sources, a final assumption is made about the correlation between the two sources. If noise sources are assumed to be completely uncorrelated, then their correlation coefficient is zero and the noise sources add solely in quadrature. It is assumed in this work that the photon noise and $1/f$ noise sources are uncorrelated. Therefore, the total input noise, N_T, is defined as the square root of the sum of the square of individual noise sources,

$$N_T = \sqrt{(N_W)^2 + (N_L)^2} \quad \frac{\text{photons}}{\text{sec}}, \tag{5.12}$$

where N_W is the photon noise and N_L is the $1/f$ noise.

5.5 Photon Noise

In laser diagnostics there is uncertainty in the total amount of irradiance collected within a fixed time period. The uncertainty in the irradiance can be described as a random fluctuation in the number of photons detected at a focal plane, over a given time interval. The uncertainty in the total number of photons arriving at a focal plane is photon noise, also known as quantum noise.

Photon noise is the result of stochastic fluctuations in the arrival rate of photons. The total number of photons, n, detected in the interval $t+\Delta t$ varies with differences in the selected start time t. In many cases, the signal-to-noise ratio (SNR), for a photon noise limited system, is defined to be proportional to the mean number of photons detected, $\overline{n}$, in the given interval Δt (Dereniak & Crowe, 1984; Kopeika, 1998). Since photon noise is described by a Poisson distribution function, the variance of the process is equal to the mean value. The standard deviation is, therefore, the square root of the mean value, and the SNR limit is,

$$SNR_{limit} = \frac{\overline{n}}{\sqrt{\overline{n}}} = \sqrt{\overline{n}}. \tag{5.13}$$

The above definition, however, does not provide the information required to develop a linear systems model of the input. Developing a time domain and temporal frequency domain representation of the laser radiation requires more information.

In order to gain more information about photon noise, such as descriptive functions in both the time and frequency domains, the *shot noise process* is first analyzed. Section 5.5.1 mathematically describes the shot noise process, which is a Poisson impulse process. Analyzing the shot noise process supports the conclusion that photon

noise is a white noise source.

After determining, in section 5.5.1, that the photon noise spectrum is indeed white, the power level of the photon noise is then determined in section 5.5.2. The power level of the photon noise is determined by investigating the statistical properties of the photon arrival rate process, $\Lambda(\bullet)$.

5.5.1 Spectral Shape Of Photon Noise

The photon noise spectrum can be shown to be white by investigating the shot noise process. A simple current model, describing the current produced from a photodetector affected by light, is first used to describe shot noise. From the shot noise model, the statistical characteristics of the input, which is a light source, can be extracted.

Current pulses are assumed to be generated when light, or a photon stream, hits a photodetector. The total current, $i(t)$, is the sum of all the current pulses, as indicated in equation 5.14. The current pulses are assumed to have a standard shape that is described by an average pulse's impulse response $h(t)$.

$$i(t) = \sum_{k=-\infty}^{\infty} A_k \cdot h\left(t - \tau_k\right) \tag{5.14}$$

The times τ_k, at which current pulses are generated, are random and are assumed to constitute a Poisson point process (Helstrom, 1991). A_k are random response amplitudes proportional to the photon arrival rate (Frey, 1995). Since this random process is assumed to have been active for all time, it is independent of the time selected to gather a sample and is, therefore, a stationary process (Frey, 1995).

In order to derive the statistical nature of the shot noise process, $i(t)$, (since calculating its probability density function is a difficult mathematical problem (Hel-

strom, 1991)) an approximation, $\tilde{i}(t)$, to the shot noise process is first developed. The approximate shot noise process, $\tilde{i}(t)$, is calculated with small intervals of time, Δt such that $\lambda \Delta t \ll 1$. The shot noise process, $i(t)$, is then found by taking the limit of the approximation, $\tilde{i}(t)$, as $\Delta t \rightarrow 0$.

To facilitate the approximation, a binary variable, ε_k, is defined that is governed by Poisson statistics (Helstrom, 1991). In general, if n is any integer number of pulses, the probability that n pulses are emitted during the time Δt is,

$$Pr(n) \;=\; \frac{(A_\lambda \Delta t)^n \, e^{-A_\lambda \Delta t}}{n!} \qquad n \;=\; 0, 1, 2, 3, ... \tag{5.15}$$

where A_λ is the average photon arrival rate, which is also assumed to be present for all time.

The binary variable, ε_k, however, has only two states, 0 and 1. It is defined such that it is one if a pulse is generated in the time interval, Δt, or it is zero if no pulse is generated in the interval. Substituting ε_k into equation 5.15 for n, the probability that ε_k is equal to one is,

$$Pr\left(\varepsilon_k = 1\right) \;=\; A_\lambda \Delta t e^{-A_\lambda \Delta t} \;\approx\; A_\lambda \Delta t \tag{5.16}$$

The approximation in equation 5.16 is made since it was assumed that $A_\lambda \Delta t \;\ll\; 1$, such that the exponential tends toward one.

The sum of all probable outcomes must sum to one, or 100%. Thus, the probability of generating a pulse and the probability of not generating a pulse must sum to one. The probability that ε_k is equal to zero is, therefore,

$$Pr\left(\varepsilon_k = 0\right) = 1 - Pr\left(\varepsilon_k = 1\right) \;\approx\; 1 - A_\lambda \Delta t \,, \tag{5.17}$$

and the expected value of ε_k is (Helstrom, 1991),

$$E[\varepsilon_k] \;=\; Pr\,(\varepsilon_k = 1) \;\approx\; A_\lambda \Delta t. \tag{5.18}$$

Substituting the expected value of ε_k and the small time interval definition, Δt, into equation 5.14, provides the expected value of the approximate current model, $E[\tilde{i}(t)]$.

$$E[\tilde{i}(t)] \;=\; \sum_{k=-\infty}^{\infty} E[\varepsilon_k] h\,(t - k\Delta t) \;=\; \sum_{k=-\infty}^{\infty} A_\lambda\, \Delta t\; h\,(t - k\Delta t) \tag{5.19}$$

The expected value of the shot noise model, $E[i(t)]$, can then found by taking the limit of equation 5.19 as $\Delta t \rightarrow 0$. The result is the integrated value of current pulses, rather than the summation of pulses. The process is assumed stationary, thus, the time dependence can be removed, simplifying the integration.

$$E[i(t)] \;=\; A_\lambda \int_{-\infty}^{\infty} h(t-\tau)\, d\tau \;=\; A_\lambda \int_{-\infty}^{\infty} h(\tau)\, d\tau \tag{5.20}$$

$E[i(t)]$, found in equation 5.20, is the expected value of the shot noise process and it is proportional to the mean photon arrival rate, A_λ (Helstrom, 1991). Since $E[i(t)]$ is determined from the photodetector's impulse response, $h(\tau)$, the shot noise process can be described as the filtered arrival of photons. The arrival of photons is defined statistically as a Poisson impulse process, therefore, shot noise is a filtered Poisson impulse process (Frey, 1995).

The mean photon arrival rate is considered to be a constant value. The photon noise is the difference between the actual photon arrival rate and the mean photon arrival rate. Since the shot noise process models the linear filtering of photon arrivals,

photon noise variance is also linearly proportional to the shot noise variance. The autocovariance function for the shot noise process will, therefore, be derived, which will provide the variance in the shot noise process. Finally, the photon noise variance can be determined from its linear relationship with the shot noise process.

The same binary variable, ε_k, used to approximate the shot noise process, as shown in equation 5.19, will again be used to develop both the approximate autocorrelation function, $R_{\tilde{i}}(t_1, t_2)$, and the approximate autocovarince function, $C_{\tilde{i}}(t_1, t_2)$. Since correlation functions calculate the product of two random samples at times t_1 and t_2, an additional binary variable, ε_j, is defined to represent the second random sample.

By assuming that any sample taken from the shot noise process is statistically independent of any other sample, the expected value of the product of the two binary variables is defined as (Cooper & McGillem, 1999),

$$E[\varepsilon_k \varepsilon_j|_{(k=j)}] = E[\varepsilon_k^2] = E[\varepsilon_k] = A_\lambda \Delta t \tag{5.21}$$

$$E[\varepsilon_k \varepsilon_j|_{(k\neq j)}] = E[\varepsilon_k]E[\varepsilon_j] = (A_\lambda \Delta t)^2 \tag{5.22}$$

The approximate autocorrelation function is,

$$R_{\tilde{i}}(t_1, t_2) = E[\tilde{i}(t_1), \tilde{i}(t_2)] = \sum_{k=-\infty}^{\infty} \sum_{j=-\infty}^{\infty} E[\varepsilon_k \varepsilon_j] h(t_1 - k\Delta t) h(t_2 - j\Delta t) \tag{5.23}$$

which is,

$$
\begin{aligned}
R_{\tilde{i}}(t_1,t_2) &= \sum_{k=-\infty}^{\infty} E[\varepsilon_k]h(t_1-k\Delta t)h(t_2-k\Delta t) \\
&+ \sum_{k=-\infty}^{\infty}\sum_{j\neq k} E[\varepsilon_k]E[\varepsilon_j]h(t_1-k\Delta t)h\left(t_2-j\Delta t\right) \\
&\text{or} \\
R_{\tilde{i}}(t_1,t_2) &= \sum_{k=-\infty}^{\infty} \left(A_\lambda\Delta t\right) h(t_1-k\Delta t)h(t_2-k\Delta t) \\
&+ \sum_{k=-\infty}^{\infty}\sum_{j\neq k} \left(A_\lambda\Delta t\right)^2 h(t_1-k\Delta t)h\left(t_2-j\Delta t\right) \qquad (5.24)
\end{aligned}
$$

The autocovariance, as noted in section 4.7.1, describes the random fluctuations in a process, independent of the mean value. The approximate autocovariance function, $C_{\tilde{i}}(t_1,t_2)$, is obtained by subtracting the product of the approximate expected values from the approximate autocorrelation function.

$$
C_{\tilde{i}}(t_1,t_2) = R_{\tilde{i}}(t_1,t_2) - E[\tilde{i}(t_1)]E[\tilde{i}(t_2)] \qquad (5.25)
$$

The product of the approximate expected values, taken from equation 5.19, is

$$
\begin{aligned}
E[\tilde{i}(t_1)]E[\tilde{i}(t_2)] &= \left[\sum_{k=-\infty}^{\infty} A_\lambda\Delta t\; h\left(t_1-k\Delta t\right)\right]\left[\sum_{j=-\infty}^{\infty} A_\lambda\Delta t\; h\left(t_2-j\Delta t\right)\right] \\
&\text{which is,} \\
E[\tilde{i}(t_1)]E[\tilde{i}(t_2)] &= \sum_{k=-\infty}^{\infty}\sum_{j=-\infty}^{\infty} \left(A_\lambda\Delta t\right)^2\; h\left(t_1-k\Delta t\right) h\left(t_2-j\Delta t\right). \qquad (5.26)
\end{aligned}
$$

The $k \neq j$ terms in equation 5.26 cancel the second term in $R_{\tilde{i}}(t_1,t_2)$ (equation 5.24), which are all statistically independent, simplifying the calculation of

$C_{\tilde{i}}(t_1, t_2)$.

$$\begin{aligned} C_{\tilde{i}}(t_1,t_2) &= \sum_{k=-\infty}^{\infty} (A_\lambda \Delta t)\, h(t_1 - k\Delta t) h(t_2 - k\Delta t) \\ &- \sum_{k=-\infty}^{\infty} (A_\lambda \Delta t)^2\ h\,(t_1 - k\Delta t)\, h\,(t_2 - k\Delta t) \end{aligned}$$

which is,

$$C_{\tilde{i}}(t_1,t_2) = \sum_{k=-\infty}^{\infty} \left[A_\lambda \Delta t - (A_\lambda \Delta t)^2\right] h(t_1 - k\Delta t) h(t_2 - k\Delta t) \tag{5.27}$$

The autocovariance, $C_i(t_1, t_2)$, of the shot noise process is finally found by taking the limit of equation 5.27 as $\Delta t \to 0$. The integrand is initially τ, which is then removed through a substitution to conclude with a more familiar equation.

$$\begin{aligned} C_i(t_1,t_2) &= A_\lambda \int_{-\infty}^{\infty} h(t_1 - \tau) h(t_2 - \tau)\, d\tau \\ \text{(or substituting)}\ u &= t_1 - \tau \\ C_i(t_1,t_2) &= A_\lambda \int_{-\infty}^{\infty} h(u) h(t_2 - t_1 + u)\, du \end{aligned} \tag{5.28}$$

The time dependence, $t_2 - t_1$, can then be removed by remembering that the shot noise process is stationary. The shot noise autocovariance function, also known as *Campbell's theorem* is given in equation 5.29 (Helstrom, 1991).

$$C_i(\tau) = A_\lambda \int_{-\infty}^{\infty} h(t) h(t + \tau)\, dt \tag{5.29}$$

The spectral density of the shot noise process is then found by taking the Fourier transform of the autocovariance function.

$$S_i(f) = A_\lambda \int_{-\infty}^{\infty} \int_{-\infty}^{\infty} h(t) h(t + \tau) e^{-j2\pi f \tau} dt\, d\tau \tag{5.30}$$

$$S_i(f) = A_\lambda \int_{-\infty}^{\infty} \int_{-\infty}^{\infty} h(t) e^{j2\pi ft} h(t+\tau) e^{-j2\pi f(t+\tau)} dt\, d\tau \tag{5.31}$$

$$S_i(f) = A_\lambda \int_{-\infty}^{\infty} h(t) e^{j2\pi ft} dt \int_{-\infty}^{\infty} h(u) e^{-j2\pi fu} du \tag{5.32}$$

where $u = (t + \tau)$. Therefore, the spectral density of the shot noise process is,

$$S_i(f) = A_\lambda |H(f)|^2 = S_p(f)|H(f)|^2, \tag{5.33}$$

where $H(f)$ is the transfer function corresponding to the impulse response $h(t)$, and $S_p(f)$ is the spectrum of the input.

Equation 5.33 can be considered the output of a linear time-invariant filter. In general, the power spectrum, $S_Y(f)$, at the output of a linear time-invariant filter is the product of the input power spectrum, $S_X(f)$, and the filter's power transfer function, $|H(f)|^2$.

$$S_Y(f) = S_X(f)|H(f)|^2 \quad \text{and} \quad S_X(f) = \frac{S_Y(f)}{|H(f)|^2} \tag{5.34}$$

Considering shot noise as the output of a filter, demonstrates that the input to the shot noise process has a constant spectral quantity. It is clear from equation 5.33 that the input spectrum, $S_p(f)$, is uniform.

$$S_p(f) = A_\lambda \tag{5.35}$$

In the time domain, the autocovariance of the input can be determined by taking

the inverse Fourier transform of the power spectrum, $S_p(f)$.

$$C_p(\tau) = \int_{-\infty}^{\infty} S_p(f) e^{j2\pi f\tau} df = A_\lambda \int_{-\infty}^{\infty} e^{j2\pi f\tau} df = A_\lambda \, \delta(\tau) \tag{5.36}$$

Equations 5.35 and 5.36, which express the power spectrum and autocorrelation function of the input to a photodetector, are equivalent to the definition of white noise. Thus, the noise contained in an input stream of photons can be modeled as white noise (Helstrom, 1991).

5.5.2 Photon Noise Power

Photon noise is a white noise source that has a constant power value A_λ, as shown in equation 5.35. The next step in defining the photon power spectrum is to determine the value of A_λ. In order to determine this value, the stochastic photon arrival rate process $\Lambda(\bullet)$ is used as a starting point. The photon arrival rate itself is analyzed as a stochastic process rather than analyzing the number of photons that arrive in a specified interval of time. By analyzing the arrival rate, the interval of time is arbitrary and does not require specification.

The instantaneous value of $\Lambda(\bullet)$ is defined as $K_\lambda(t)$. $K_\lambda(t)$ is the sum of the mean photon arrival rate, λ_p, and the instantaneous value of the stochastic arrival rate, $N_p(t)$, which is considered photon noise.

$$K_\lambda(t) = \lambda_p + N_p(t) \tag{5.37}$$

It is widely known that the collection of a discrete number of photons in a specified time interval is governed by Poisson statistics (Dereniak & Crowe, 1984; Frey, 1995; Winzer, 1997; Kopeika, 1998; Cunningham & Shaw, 1999). The stochastic

photon arrival rate process, $\Lambda(\bullet)$, however, is defined as the rate at which photons, or impulses, arrive at the detector plane, without stating a specific time interval. Since $\Lambda(\bullet)$ describes the arrival of photons, albeit without a specified time interval of accumulation, it is assumed that $\Lambda(\bullet)$ can also be characterized with Poisson statistics. In this case, the probability that the instantaneous photon arrival rate, $K_\lambda(t)$, is equal to the random and discrete arrival rate λ, is,

$$Pr[K_\lambda(t) = \lambda] \;=\; \frac{(\lambda_p)^\lambda}{\lambda!}\mathrm{e}^{-\lambda_p} \quad \lambda \;=\; 0, 1, 2, 3, ... \tag{5.38}$$

where λ_p is, again, assumed to be the mean photon arrival rate for all time.

Because $\Lambda(\bullet)$ is characterized with Poisson statistics, the variance of the process, σ_Λ^2, is equal to the mean value of the process, $\overline{\Lambda}$, (Cooper & McGillem, 1999). As shown in section 4.7, the variance can be defined as the difference between the mean-squared value and the square of the mean value. Using this definition, and the fact that the variance is equal to the mean, the mean-square value, of the photon arrival process, can be determined.

$$\begin{aligned} \sigma_\Lambda^2 &= \overline{\Lambda^2} - \left(\overline{\Lambda}\right)^2 \\ \text{or} \quad \overline{\Lambda} &= \overline{\Lambda^2} - \left(\overline{\Lambda}\right)^2 \\ \text{therefore} \quad \overline{\Lambda^2} &= \left(\overline{\Lambda}\right)^2 + \overline{\Lambda} \end{aligned} \tag{5.39}$$

The photon arrival rate process, $\Lambda(\bullet)$, is a vehicle that is used to determine the statistical characteristics of the photon noise process, $W(\bullet)$. The only difference between $\Lambda(\bullet)$ and $W(\bullet)$ is the mean value. Creating separate, yet related, processes allows the photon noise process, $W(\bullet)$, to be represented as a zero-mean valued process. The arrival rate process, however, is characterized by Poisson statistics and

has a nonzero-mean.

First, a general random process $x(\bullet)$ is analyzed. Equation 5.37 can be expressed in general terms as the sum of a constant value, $\overline{X}$, and an instantaneous zero mean noise term, $N(t)$.

$$X(t) = \overline{X} + N(t) \tag{5.40}$$

The autocorrelation function, $R_x(\tau)$, for the general expression in equation 5.40 is,

$$\begin{aligned} R_x(\tau) &= \left(\overline{X}\right)^2 + E[N(t)N(t+\tau)] \\ \text{or} \quad R_x(\tau) &= \left(\overline{X}\right)^2 + R_n(\tau), \end{aligned} \tag{5.41}$$

which is the sum of the square of the general constant term and the autocorrelation, $R_n(\tau)$, of the general noise term, $N(t)$. Since the generalized noise term has a zero mean value, the autocorrelation of the noise, $R_n(\tau)$, is equal to its autocovariance function, $C_n(\tau)$, as described in section 4.7.1.

$$R_x(\tau) = \left(\overline{X}\right)^2 + C_n(\tau) \tag{5.42}$$

Based on equations 5.37,5.42, and 5.40, the autocorrelation function for $\Lambda(\bullet)$ is,

$$R_\Lambda(\tau) = \left(\overline{\Lambda}\right)^2 + C_\Lambda(\tau) \tag{5.43}$$

which is the sum of the square of the expected value and the autocovariance function, $C_\Lambda(\tau)$.

Referring again to section 4.7.1, the mean-square value, $\overline{\Lambda^2}$, of $\Lambda(\bullet)$ can now be

determined by evaluating $R_\Lambda(\tau)$ at $\tau = 0$. This is true whether the process has a nonzero mean value or not (Cooper & McGillem, 1999).

$$R_\Lambda(0) \;=\; \overline{\Lambda^2} \;=\; \left(\overline{\Lambda}\right)^2 + C_\Lambda(0) \tag{5.44}$$

Equation 5.39 shows that the mean-square value of the arrival rate process is also equal to the square of the mean value plus the mean value. Therefore, $R_\Lambda(\tau = 0)$ can be written as,

$$R_\Lambda(0) \;=\; \left(\overline{\Lambda}\right)^2 + \overline{\Lambda} \;=\; \left(\overline{\Lambda}\right)^2 + C_\Lambda(0). \tag{5.45}$$

Solving for the autocovariance of $\Lambda(\bullet)$ gives,

$$C_\Lambda(0) \;=\; \overline{\Lambda} \quad \text{or} \quad C_\Lambda(\tau) \;=\; \overline{\Lambda}\delta(\tau). \tag{5.46}$$

Equation 5.46 shows that the autocovariance function, of the photon arrival rate process, evaluated at $\tau = 0$ is equal in magnitude to the mean value of the process. This equality is expected, since the nature of this phenomenon is described by a Poisson distribution.

The autocovariance, $C_W(\tau)$, of the photon noise process, $W(\bullet)$ is now set equal to the autocovariance from $\Lambda(\bullet)$.

$$C_W(\tau) \;=\; C_\Lambda(\tau) \;=\; \overline{\Lambda}\delta(\tau) \tag{5.47}$$

The variance of the photon noise, as described by $W(\bullet)$, is equal to the autocovariance function evaluated at $\tau = 0$. The mean value $\overline{W}$ of $W(\bullet)$ is, however, set equal to zero. Thus, the mean-square value, in this case, is equal to the variance. As shown

in equation 5.49, both the variance and the mean-square value of the photon noise are equal to the mean value of the photon arrival rate process, $\overline{\Lambda}$.

$$\sigma_W^2 = C_W(0) = \overline{\Lambda} \tag{5.48}$$

$$\text{and since } \overline{W} = 0$$

$$\overline{W^2} = \sigma_W^2 = \overline{\Lambda} \tag{5.49}$$

The mean value of the photon arrival rate process, $\overline{\Lambda}$, is λ_p, and, therefore, σ_W^2 is also λ_p. The respective units are, however, different. The mean arrival rate, λ_p, has units of photons/sec. Thus, the mean value of the photon arrival rate process, $\overline{\Lambda}$, also has units of photons/sec.

The autocorrelation function's units are, on the other hand, the square of the units of the process. Evaluating the autocorrelation or autocovariance functions requires that the expected value of two samples be calculated. The autocorrelation functions for both the photon arrival rate process, and the photon noise process have units of (photons/sec)^2. The magnitudes of $\overline{\Lambda}$ and σ_W^2, nevertheless, remain the same.

$$\overline{\Lambda} = \lambda_p \quad \frac{\text{photons}}{\text{sec}} \tag{5.50}$$

and

$$\sigma_W^2 = \lambda_p \quad \left[\frac{\text{photons}}{\text{sec}}\right]^2 \tag{5.51}$$

The value for A_λ, from equation 5.35, can now be set equal to the mean photon arrival rate, λ_p. The power spectral density of the photon noise, shown to be white in equation 5.35, is found by evaluating the Fourier transform of the autocovariance

function, $C_W(f)$.

$$S_W(f) = \int_{-\infty}^{\infty} C_W(f) e^{-j2\pi f\tau} d\tau = \lambda_p \quad \frac{(\text{photons/sec})^2}{\text{Hz}}. \tag{5.52}$$

The mean photon arrival rate, λ_p, per pixel, can also be defined in units of watts. Since λ_p is equal to I_p/ϵ, which was shown in equation 5.6, the power spectrum can also be defined as,

$$S_W(f) = \epsilon^2 \cdot \lambda_p = \epsilon \cdot I_p \quad \frac{(\text{watts})^2}{\text{Hz}}. \tag{5.53}$$

The total noise at the detector input depends on the system's bandwidth. Mathematically, white noise has infinite power. The bandwidth of the detector will, however, limit the amount of white noise power acquired.

The effective bandwidth of a detector, B, can be used to band-limit a white noise source (Stremler, 1990). The total photon noise, N_W, at the input to the imaging system is,

$$N_W = \left[\int_{-B}^{B} S_W(f) df\right]^{\frac{1}{2}}$$

$$N_W = \left[\int_{-B}^{B} \lambda_p \, df\right]^{\frac{1}{2}} = \sqrt{2B\lambda_p} \quad \frac{\text{photons}}{\text{sec}} \tag{5.54}$$

or

$$N_W = \left[\int_{-B}^{B} \epsilon \, I_p \, df\right]^{\frac{1}{2}} = \sqrt{2B\epsilon I_p} \quad \text{watts} \tag{5.55}$$

5.5.3 Fundamental Detection Limit

Photon noise can be considered the noise floor and defines the fundamental detection limit in laser based diagnostic systems (Eckbreth, 1996). The photon noise spectrum, shown in equation 5.53, is proportional to the mean beam power, I_p, entering a pixel. The detection limit can, therefore, be analyzed as a function of I_p.

The level of the photon noise spectrum, $S_W(f)$, is an interesting factor to consider when applying the imaging system to a pump probe absorption spectroscopy experiment. In this type of experiment, the imaging system is used to measure modulation depth contained in the probe beam. The modulation depth, α_{mod}, is evaluated as,

$$\alpha_{mod} = \frac{I_{on} - I_{off}}{I_{off}}, \tag{5.56}$$

where I_{on} is the probe beam irradiance when the pump beam is on and I_{off} is the probe beam irradiance when the pump beam is off (Settersten, 1999). The steady state probe irradiance is equal to the irradiance when the pump beam is off, I_{off}. The signal irradiance is, therefore, contained in the difference term $I_{on} - I_{off}$.

The general equation for irradiance was given in equation 5.2 and it has units of power per unit area. Multiplying the irradiance in equation 5.56 by pixel area produces a power ratio that can also be used to determine the modulation depth. In doing so, the modulation depth can be evaluated in terms of I_p,

$$\alpha_{mod} = \frac{(I_{on} - I_{off})\, A_p}{(I_{off})\, A_p} = \frac{I_A}{I_p} \tag{5.57}$$

where I_A is equal to $(I_{on} - I_{off})A_p$. I_A is considered to be the unmodulated, peak value of the signal, which is not the same as the power contained in the modulated

signal. Characteristics of the modulated signal are presented in section 5.8.

If the steady state background power, I_p, incident on a pixel is known, or is assumed, then I_A can be obtained for various modulation depths, α_{mod}.

$$I_A = \alpha_{mod} I_p \quad \text{watts} \tag{5.58}$$

The expected peak signal, I_A, can then be compared to the photon noise floor from equation 5.53. Figure 5.5 illustrates the expected peak signal for modulation depths of 10^{-2} (1.0%), 10^{-4} (0.01%), and 10^{-6} (0.0001%) over a range of steady state background conditions. The photon noise floor, in Figure 5.5, is calculated using a wavelength of 770nm (equation 5.53). Also shown in Figure 5.5, as a vertical dashed line, is the maximum I_p that can be incident on a pixel without reaching saturation. The maximum I_p is extracted from Figure 5.3.

Figure 5.5 shows that as the steady state background power is reduced, the peak signal nears the fundamental photon noise limit. An increase in the background power may, on the other hand, only lead to CCD saturation. Care must be taken to set the irradiance, or steady state background power, at a level such that the signal power is above the photon noise limit, without quickly saturating the CCD.

5.5.4 Probability Description

If more information about the random nature of photon noise is desired, then a probability model must be created. As previously stated, a Poisson distribution agrees well with discrete physical processes, such as photon noise (Dereniak & Crowe, 1984). Using a Poisson distribution, the probability that the instantaneous photon

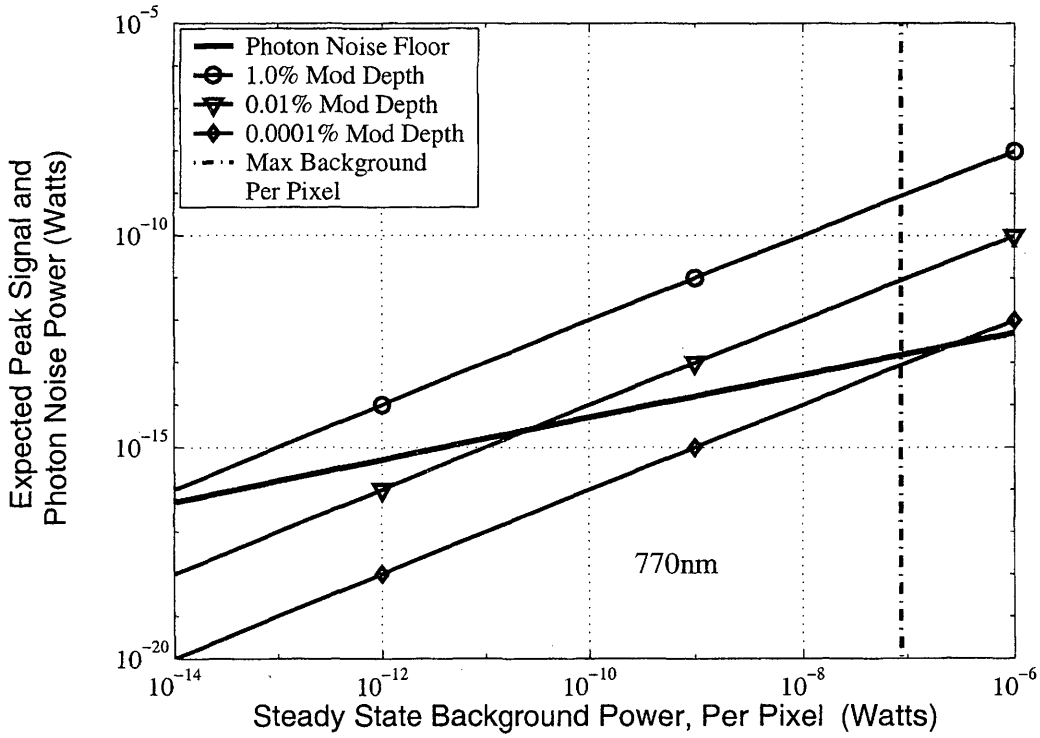

FIG. 5.5. Expected peak signal for modulation depths of 10^{-2} (1.0%), 10^{-4} (0.01%), and 10^{-6} (0.0001%),for a range of background power, compared to the photon noise limit

arrival rate $K_\lambda(t)$ is less than or equal to the possible arrival rate N is,

$$Pr\left[K_\lambda(t) \leq N\right] = \sum_{\lambda=0}^{N} \frac{(\lambda_p)^\lambda}{\lambda!} e^{-\lambda_p} \tag{5.59}$$

where λ_p is the mean arrival rate of photons, and λ is the arrival rate variable.

The distribution function for mean arrival rates of 10 and 50 are shown in Figure 5.6. The corresponding density functions, calculated numerically by taking the derivative of the distribution function with respect to the arrival rate step,

$$f_\Lambda(\lambda) = \frac{dP_\Lambda(\lambda)}{d\lambda}, \tag{5.60}$$

are also shown in Figure 5.6. Since a Poisson distribution function is used to determine the probable arrival rate, the arrival rate must be an integer value. This discrete nature is seen in both the stair step changes of the distribution function and in the discrete values of the density function.

A Gaussian density function, which is a continuous rather than a discrete function, is shown on top of the Poisson density plot in Figure 5.6. The Gaussian density function,

$$f_\Lambda(\Lambda) = \frac{1}{\sqrt{2\pi\lambda_p}} \exp\left[\frac{-(\lambda - \lambda_p)^2}{2\lambda_p}\right], \tag{5.61}$$

with the variance equal to the mean value, was used to form the overlay plot. As the arrival rate increases, it can be seen that the Gaussian density function approximates the Poisson density function very well. In fact, using the central limit theorem, the Poisson distribution approaches a Gaussian distribution at large arrival rate values (Kopeika, 1998). Since a laser source produces an extremely high photon arrival

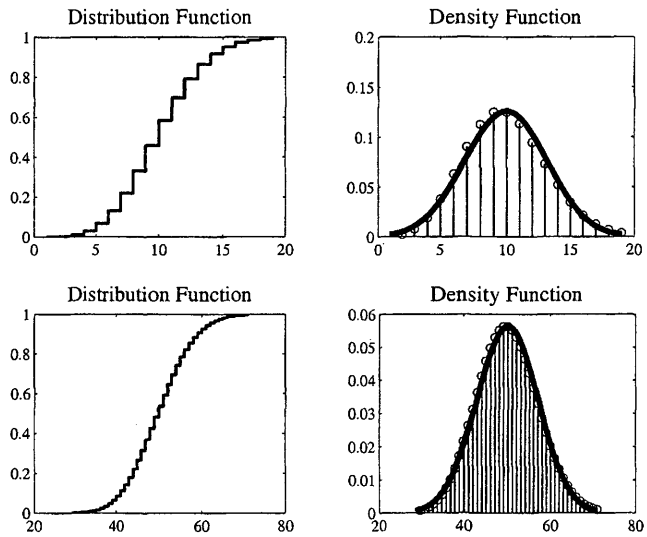

FIG. 5.6. Poisson distribution with its density function compared to a Gaussian density function

rate, a Gaussian density function can be used to describe the photon noise, should it be necessary.

5.6 $1/f$ Noise

$1/f$ noise, or low frequency noise, has been observed in transistors, diodes, average seasonal temperature, rate of traffic flow, and economic data (Halford, 1968; Keshner, 1982). It is also found in light sources and laser systems (Eckbreth, 1996). $1/f$ noise has a power spectrum, $S_{1/f}(f)$, that is proportional to the inverse of the frequency, which is raised to the power γ. The exponent, γ, is usually close to unity for most systems (Keshner, 1982).

$$S_{1/f}(f) \propto \frac{constant}{|f|^{\gamma}} \quad \text{where:} \quad 0 < \gamma < 2 \tag{5.62}$$

$1/f$ noise is a non-stationary random process (Keshner, 1982). Therefore, a

different sample set can be obtained, with different statistical properties, depending on the time origin choice. In this investigation, the $1/f$ noise is assumed to be stationary in the wide sense over a single decade of frequency. Assuming that the $1/f$ noise is stationary in the wide sense over a single decade of frequency adequately guarantees that the mean value, the mean-square value, and the variance are all constants over the single decade of frequency, independent of time origin (Cooper & McGillem, 1999).

Since stationary $1/f$ noise has a constant mean value and constant mean-square value over a decade of frequency, the total noise power in a decade of bandwidth can be determined. Integrating $1/f$ noise, with γ in equation 5.62 set to unity, from a low frequency, f_l, to a higher frequency, f_h, results in the following equation for noise power, where K_1 is a proportionality constant (Motchenbacher & Connelly, 1993).

$$\begin{aligned} N_{f_l \to f_h} &= 2K_1 \int_{f_l}^{f_h} \frac{1}{f} df \\ N_{f_l \to f_h} &= 2K_1 \left[ln(f_h) \; - \; ln(f_l) \right] + C \; = \; 2K_1 \; ln\left(\frac{f_h}{f_l}\right) + C \end{aligned} \tag{5.63}$$

Since the $1/f$ noise is assumed to be stationary in the wide sense over one decade of frequency, f_h is set equal to $10f_l$. Evaluating equation 5.63 with f_h equal to $10f_l$ shows that the $1/f$ noise power is a constant value for every decade of frequency.

$$N_{f_l \to 10f_l} \; = \; 2K_1 \int_{f_l}^{10f_l} \frac{1}{f} df \; = \; 2K_1 \; ln\left(\frac{10f_l}{f_l}\right) + C \; = \; 4.6K_1 + C \tag{5.64}$$

The noise power over any single decade of frequency is, therefore, a constant value. By making the assumption that $1/f$ noise is stationary in the wide sense over one decade also leads to the assumption that $1/f$ noise is stationary in the wide sense over every decade of frequency. In this case, each decade of frequency must have the

same noise power and rms noise value (Motchenbacher & Connelly, 1993). In fact, studies of measurements from identical systems taken at different times has shown that the spectral shape and the γ are quite consistent factors (Keshner, 1982).

5.6.1 Spectral Approximation

The strict definition for the $1/f$ noise power spectrum, in equation 5.62, is, however, not mathematically useful for this analysis. In the limit, as the frequency goes to zero, the $1/f$ noise increases to infinity. An alternate mathematical definition is used in this analysis to characterize $1/f$ noise. The power spectral density function, $S_L(f)$, defined in equation 5.65, is used as an approximation to $1/f$ noise power over all frequency. The subscript L is used to define the spectrum for $1/f$ noise since the stochastic $1/f$ noise process was previously defined as $L(\bullet)$.

$$S_L(f) = \frac{(\lambda_p)^2}{\sqrt{1 + \left(\frac{f}{f_o}\right)^{2\gamma}}} \quad f \neq 0 \quad \frac{(\text{photons/sec})^2}{\text{Hz}} \tag{5.65}$$

The mean photon arrival rate, λ_p, is incorporated into equation 5.65 so that as the frequency approaches zero, the $1/f$ noise power spectrum does not surpass the mean photon arrival rate. Also, in order to obtain the correct units, λ_p is squared in equation 5.65. In the previous section on photon noise, Figure 5.2 demonstrated that the power spectrum and the statistical parameters of the noise have units of $(\text{photons/sec})^2$. The variance, mean-square value, and the square of the mean value for the $1/f$ noise process also have units of $(\text{photons/sec})^2$.

Two parameters, a cutoff frequency f_o and an attenuation factor γ, are used in equation 5.65 to shape $S_L(f)$ in a way that approximates the laser diagnostic system's

$1/f$ noise characteristics. Figure 5.7 illustrates how f_o and γ change the shape of the $1/f$ noise spectrum. In the first plot, the cutoff frequency is held constant and the attenuation factor, γ is allowed to change. In the second plot, the attenuation factor, γ, is set to unity and the cutoff frequency varies from f_o to 0.01% of f_o.

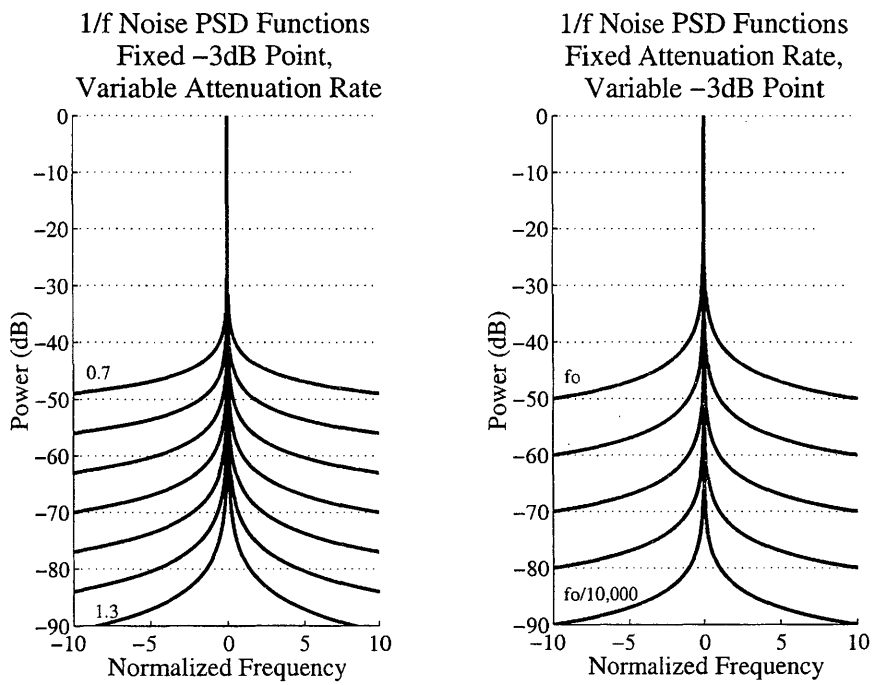

FIG. 5.7. 1/f noise power spectral density function variations

Figure 5.7 shows that the $1/f$ noise spectrum can be configured by changing the cutoff frequency, the attenuation rate, or both parameters. A closed form solution to the integral of $S_L(f)$ can be obtained when γ is an integer value (Beyer, 1978). Since the $1/f$ noise spectrum can be adequately scaled with only the cutoff frequency parameter, the spectral model is simplified by setting the attenuation factor, γ, to

unity.

$$S_L(f) = \frac{(\lambda_p)^2}{\sqrt{1 + \left(\frac{f}{f_o}\right)^2}} \quad f \neq 0 \quad \frac{(\text{photons/sec})^2}{\text{Hz}} \tag{5.66}$$

5.6.2 $1/f$ Noise Power

The variance of the $1/f$ noise process is,

$$Var\,(L\,(\bullet)) = \sigma_L^2 = \overline{L^2} - \left(\overline{L}\right)^2 \quad \text{(variance)} \tag{5.67}$$

where $\overline{L^2}$ and $\left(\overline{L}\right)^2$ are the mean-squared value and the square of the mean value respectively. Since the $1/f$ noise spectrum is undefined at zero frequency, the mean value, $\overline{L}$, of the $1/f$ noise process is zero. The variance is, therefore, equal to the mean-squared value. Thus, the variance, in this case, is found by integrating the power spectrum over a given bandwidth B.

$$\begin{aligned} \sigma_L^2 &= \int_{-B}^{B} S_L(f)\, df \\ \sigma_L^2 &= \int_{-B}^{0-} \frac{(\lambda_p)^2}{\sqrt{1 + \left(\frac{f}{f_o}\right)^2}}\, df + \int_{0+}^{B} \frac{(\lambda_p)^2}{\sqrt{1 + \left(\frac{f}{f_o}\right)^2}}\, df \quad \left[\frac{\text{photons}}{\text{sec}}\right]^2 \end{aligned} \tag{5.68}$$

Using a change of variable, $x = (f/f_o)$, and integrating over positive frequency, the integral above can be written as,

$$\sigma_L^2 = 2\int_{0+}^{B/f_o} \frac{(\lambda_p)^2 f_o}{\sqrt{1 + x^2}}\, dx \tag{5.69}$$

where $df = f_o\, dx$. The integral in equation 5.69 evaluates to (Beyer, 1978),

$$\sigma_L^2 = 2\left(\lambda_p\right)^2 f_o \left[\ln\left(\frac{B}{f_o} + \sqrt{\left(\frac{B}{f_o}\right)^2 + 1}\right) - \ln\left(\sqrt{1}\right)\right], \tag{5.70}$$

which, since $B/f_0 \gg 1$, can be written as,

$$\sigma_L^2 = 2\left(\lambda_p\right)^2 f_o \ln\left(\frac{2B}{f_o}\right) \quad \left[\frac{\text{photons}}{\text{sec}}\right]^2. \tag{5.71}$$

The total $1/f$ noise at the input to the imaging system, defined as N_L, is given in units of photons/sec in equation 5.72. Equation 5.72 can also be defined in units of watts by substituting I_p/ϵ for λ_p.

$$N_L = \sqrt{2\left(\lambda_p\right)^2 f_o \ln\left(\frac{2B}{f_o}\right)} \quad \frac{\text{photons}}{\text{sec}} \tag{5.72}$$

From previous laser beam measurements (Linne *et al.*, 1995a), it has been shown that the $1/f$ noise spectrum rolls off to the photon noise limit at frequencies on the order of 100kHz. A value for the $1/f$ noise cutoff frequency, f_o, can be determined by analyzing $S_L(f)$ at a roll-off frequency point $f = f_r$ for a specified gain factor G related to the photon noise floor. The total noise power spectrum, $S_T(f)$, can then be considered a factor G greater than the photon noise floor at f_r hertz, as shown in equations 5.73 and 5.74.

$$\begin{aligned} S_T(f_r) &= G \cdot S_W(f_r) = S_L(f_r) + S_W(f_r) \\ S_L(f_r) &= G \cdot S_W(f_r) - S_W(f_r) = S_W(f_r)\left(G - 1\right) \end{aligned} \tag{5.73}$$

$$\frac{(\lambda_p)^2}{\sqrt{1+\left(\frac{f_r}{f_o}\right)^2}} = \lambda_p (G - 1) \tag{5.74}$$

Equation 5.74 can be rearranged to solve for f_o as a function of f_r and G.

$$f_o = \frac{f_r (G-1)}{\sqrt{(\lambda_p)^2 - (G-1)^2}} \tag{5.75}$$

Setting $G = 1.5$ and $f_r = 100$kHz, in equation 5.75, and using $I_p = 0.1\text{x}10^{-6}$ watts and a wavelength of 770nm, such that λ_p is calculated from I_p/ϵ, f_o is found to be $1.29\text{x}10^{-7}$. The total $1/f$ noise, N_L, over a bandwidth of 1MHz, determined by equation 5.72, is $2.799\text{x}10^{-10}$ watts per pixel.

5.7 Total Input Noise

The total noise power spectrum is the sum of the individual spectra from the $1/f$ noise and the photon noise.

$$S_N(f) = S_L(f) + S_W(f) = \frac{(\lambda_p)^2}{\sqrt{1+\left(\frac{f}{f_o}\right)^2}} + \lambda_p \quad \left[\frac{\text{photons}}{\text{sec}}\right]^2 \tag{5.76}$$

or

$$S_N(f) = S_L(f) + S_W(f) = \frac{(I_p)^2}{\sqrt{1+\left(\frac{f}{f_o}\right)^2}} + \epsilon I_p \quad \frac{(\text{watts})^2}{\text{Hz}} \tag{5.77}$$

The total input noise power, N_T, in units of photons/sec, was given in equation 5.12. N_T is the square root of the sum of the square of the individual noise powers. The $1/f$ noise power, N_L, is given in equation 5.72, and the photon noise power, N_W, is given in equation 5.55. Combining the two results in the total noise

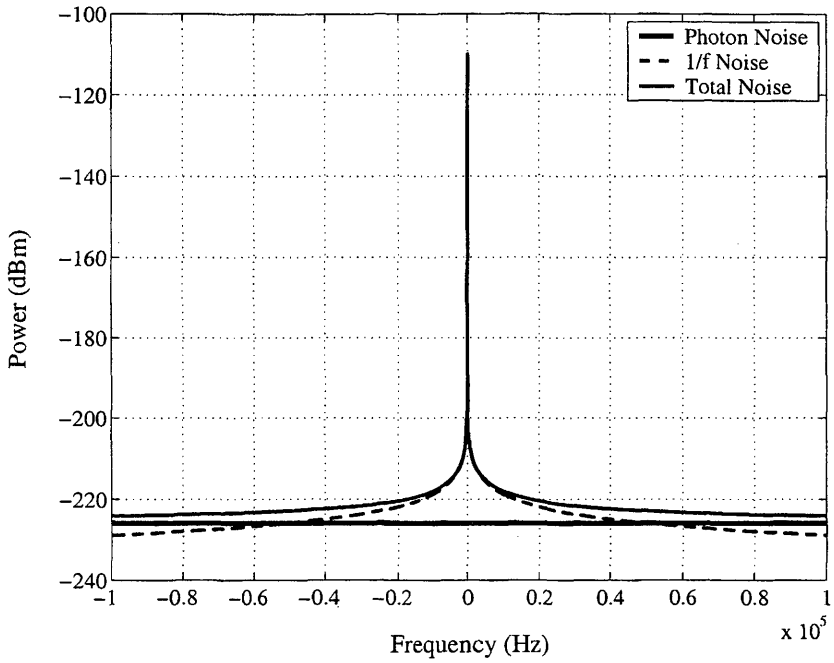

FIG. 5.8. Input noise power spectral density functions

power at the imaging system input.

$$N_T = \sqrt{(N_W)^2 + (N_L)^2}$$

$$N_T = \sqrt{2\,(\lambda_p)^2 f_o \ln\left(\frac{2B}{f_o}\right) + [2B\lambda_p]} \quad \frac{\text{photons}}{\text{sec}} \tag{5.78}$$

$$N_T = \sqrt{2\,(I_p)^2 f_o \ln\left(\frac{2B}{f_o}\right) + [2B\epsilon I_p]} \quad \text{watts} \tag{5.79}$$

As an example, I_p is set equal to 0.1μW (Figure 5.3) and is used in equation 5.77 to generate a plot of $S_N(f)$. The $1/f$ cutoff frequency, f_o, is again calculated per equation 5.75 with G set to 1.5 and f_r set to 100kHz. Using these values, f_o is $1.29\text{x}10^{-7}$ Hz. The wavelength is assumed to be 770nm, which provides a photon

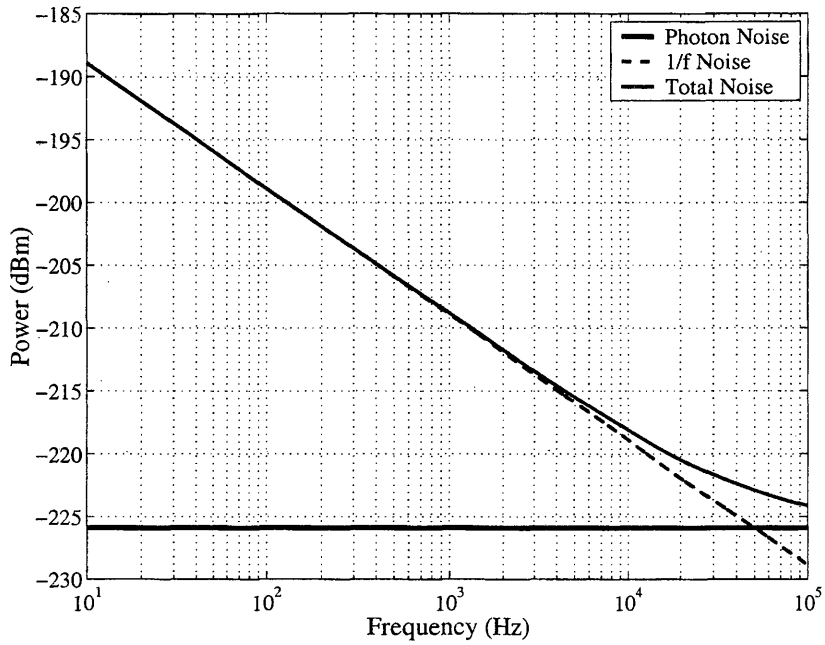

FIG. 5.9. Input noise power spectral density (positive frequency values) plotted on a logarithmic scale

energy of 2.58x10^{-19} Joules. Using these parameters, the photon noise spectrum, $S_W(f)$, the $1/f$ noise spectrum, $S_L(f)$, and the total noise spectrum, $S_N(f)$ are shown in Figures 5.8 and 5.9. Figure 5.9 plots the spectra on a log frequency scale, which illustrates the dominance of $1/f$ noise at low frequencies.

By assuming an effective bandwidth of 1MHz, the total noise can be calculated. In this case, the photon noise power, N_W, is 2.272x10^{-10} watts, the $1/f$ noise power, N_L, is 2.799x10^{-10}, for a total noise power, N_T, of 3.605x10^{-10} watts.

5.7.1 Spatial Noise

This investigation analyzes the propagation of the input through a single pixel. The analysis, therefore, assumes that each pixel is irradiated with the same input. This is not strictly the case and there are spatial variations across the array of pixels.

Spatial variations arise from both the variation in the responsivity of the detectors used to spatially sample an input and the input's spatial variation in irradiance. The responsivity of each pixel in a CCD varies slightly. The differences in responsivity create a spatial noise pattern, often called fixed pattern noise (Kopeika, 1998). The adverse effects from this type of spatial noise can be resolved with a flatfield correction pattern, saved as an image file, that normalizes the responsivity variations. This type of spatial noise was discussed in section 2.7.7 and the correction of this noise was demonstrated.

The input irradiance also varies spatially. The transverse irradiance profile of a laser beam is often approximated as a uniform, top-hat function. The irradiance does, however, vary across the diameter of a beam (Settersten, 1999). Since the $1/f$ and photon noise components were defined in terms of the average irradiance, they will also vary spatially with the average, transverse irradiance profile.

Random fluctuations in the temperature and pressure of the path through which the beam travels can also cause random spatial noise in the beam. The optics used to maneuver and direct the beam, and the environment of the samples that are investigated can cause serious variations in the beam's transverse irradiance and, therefore, spatial noise.

5.8 Information Bearing Signal

The baseband (*unmodulated*) signal of interest is an irradiance that has some mathematical relationship to a physical parameter under investigation. The signal lies in the difference between the probe beam irradiance when the pump beam is on, I_{on}, and the probe beam irradiance when the pump beam is off, I_{off}. Equation 5.57 defined I_A as the difference between I_{on} and I_{off} that enters a single pixel. The signal

I_A is now allowed to vary with time and its instantaneous value, in units of watts, is defined as $A(t)$. The signal is also defined in terms of photons/sec as $\lambda_A(t)$, which is found by dividing $A(t)$ by the energy per photon, ϵ.

The instantaneous value of the physical parameter is assumed to be random within a range of probable values. In order to develop a good mathematical model of the random physical parameter, the signal of interest is defined as the normally distributed random process $\mathrm{A}(\bullet)$ (Cooper & McGillem, 1999). The probability density function used to describe the signal is,

$$f_{\mathrm{A}}(a) = \frac{1}{\sqrt{2\pi}\sigma_{\mathrm{A}}} \exp\left[\frac{-(a-\overline{\mathrm{A}})^2}{2\sigma_{\mathrm{A}}^2}\right] \tag{5.80}$$

where $\overline{\mathrm{A}}$ is the expected value, σ_{A}^2 is the variance, σ_{A} is the standard deviation, and a is a sample from the process $\mathrm{A}(\bullet)$.

Since frequency domain analysis methods are also useful for systems with random inputs, a frequency domain representation of the random signal is also defined (Cooper & McGillem, 1999). A limit is placed on the rate at which the baseband signal's irradiance can change over time. This limit is set by defining a bandwidth in which the random signal is assumed to exist. The random signal is, therefore, assumed to be bandwidth-limited to B_{A}, which has units Hz.

Remembering, from Figure 5.2, that the power spectral density functions of the input to the imaging system have units of watts^2/Hz, requires that the information signal be squared to determine its power spectrum. For simplicity, the signal's baseband power spectrum, $S_{\mathrm{A}}(f)$, of the random signal, $A(t)$, is initially considered to be

a constant value $(\mathrm{C_A})^2$ over the bandwidth of the signal, B_A.

$$S_\mathrm{A}(f) \;=\; (\mathrm{C_A})^2 \prod\left(\frac{f}{2B_\mathrm{A}}\right) \quad \frac{(\text{watts})^2}{\text{Hz}} \tag{5.81}$$

The rectangular gate function, $\prod(\bullet)$, is introduced and defined in section 4.7.3.

The mean-square value of the signal, $A(t)$, is found by integrating the signal's power spectrum.

$$\overline{\mathrm{A}^2} \;=\; \int_{-\infty}^{\infty} S_\mathrm{A}(f)\, df \;=\; \int_{-B_\mathrm{A}}^{B_\mathrm{A}} (\mathrm{C_A})^2\, df \;=\; 2B_\mathrm{A}\,(\mathrm{C_A})^2 \quad (\text{watts})^2 \tag{5.82}$$

The variance of the random signal is the difference between its mean-square value and the square of its mean value.

$$Var\,(\mathrm{A}(\bullet)) \;=\; \sigma_\mathrm{A}^2 \;=\; \overline{\mathrm{A}^2} - \left(\overline{\mathrm{A}}\right)^2 \quad (\text{watts})^2 \tag{5.83}$$

The mean-squared value can, therefore, be defined as,

$$\overline{\mathrm{A}^2} \;=\; \sigma_\mathrm{A}^2 + \left(\overline{\mathrm{A}}\right)^2 \quad (\text{watts})^2 \tag{5.84}$$

Using equations 5.82 and 5.84, the power spectrum of $A(t)$, which is assumed uniform over the bandwidth B_A, can be defined as,

$$S_\mathrm{A}(f) \;=\; (\mathrm{C_A})^2 \prod\left(\frac{f}{2B_\mathrm{A}}\right) \;=\; \frac{\sigma_\mathrm{A}^2 + \left(\overline{\mathrm{A}}\right)^2}{2B_\mathrm{A}} \prod\left(\frac{f}{2B_\mathrm{A}}\right) \quad \frac{(\text{watts})^2}{\text{Hz}}\,. \tag{5.85}$$

Even though $A(t)$ is non-periodic, $S_\mathrm{A}(f)$ is treated as a power spectrum by assuming the process $\mathrm{A}(\bullet)$ is stationary. In order to make this assumption, a sample of $A(t)$ is selected over a duration T_A, which extends from $-T_\mathrm{A}/2$ to $T_\mathrm{A}/2$. A periodic

waveform is then generated by repeating the sample function every T_{A} seconds. The process A(•) can then be considered a power, rather than an energy, and $S_{\mathrm{A}}(f)$ can be considered a power spectral density.

Using Parseval's theorem, the power of $A(t)$ can now be set equal to the integral of its power spectral density function, $S_{\mathrm{A}}(f)$.

$$\overline{\mathrm{A}^2} = \int_{-B_{\mathrm{A}}}^{B_{\mathrm{A}}} S_{\mathrm{A}}(f)\, df = \frac{1}{T_{\mathrm{A}}} \int_{-T_{\mathrm{A}}/2}^{T_{\mathrm{A}}/2} |A(t)|^2\, dt \tag{5.86}$$

Taking the square root of $S_{\mathrm{A}}(f)$ in equation 5.85 gives the magnitude spectral representation of the information bearing signal. The magnitude spectrum, shown in equation 5.87, is used in section 5.8.2 to define the spectrum of the modulated information bearing signal.

$$F_{\mathrm{A}}(f) = \sqrt{S_{\mathrm{A}}(f)} = \frac{\sqrt{\sigma_{\mathrm{A}}^2 + \left(\overline{\mathrm{A}}\right)^2}}{\sqrt{2B_{\mathrm{A}}}} \prod\left(\frac{f}{2B_{\mathrm{A}}}\right) \quad \frac{\text{watts}}{\sqrt{\text{Hz}}} \tag{5.87}$$

Proceeding with the pump-probe absorption spectroscopy (PPAS) example, the random signal in a PPAS experiment is a fraction of the steady state background power. The measurement objective in this type of diagnostic is to determine the size of the modulated irradiance relative to the steady state background. The ratio of the random signal irradiance, $I_{on} - I_{off}$, to the steady state background irradiance, I_{off}, is the modulation depth (Settersten, 1999). Incorporating the area of a pixel, A_p, produces a power ratio, rather than an irradiance ratio, which produces the same modulation depth, α_{mod}.

$$\alpha_{mod} = \frac{I_{on} - I_{off}}{I_{off}} = \frac{A_p\left(I_{on} - I_{off}\right)}{A_p\left(I_{off}\right)} = \frac{\overline{\mathrm{A}}}{I_p} \tag{5.88}$$

Since I_{off} is the steady state irradiance entering a single pixel, the multiplication of the irradiance and the pixel area produces the steady state power entering the pixel, I_p. The baseband, expected signal power, $\overline{\mathrm{A}}$, entering a pixel, is then the difference in irradiance between I_{on} and I_{off} times the pixel area. Thus, the square of the mean value can be defined as the square of the product of α_{mod} and I_p.

$$\left(\overline{\mathrm{A}}\right)^2 = \left(\alpha_{mod} I_p\right)^2 \quad (\text{watts})^2 \tag{5.89}$$

Finally, for a PPAS diagnostic, the baseband signal power spectrum can be defined in terms of the modulation depth and the steady state background.

$$S_{\mathrm{A}}(f) = \frac{\sigma_{\mathrm{A}}^2 + \left(\alpha_{mod} I_p\right)^2}{2B_{\mathrm{A}}} \prod\left(\frac{f}{2B_{\mathrm{A}}}\right) \quad \frac{(\text{watts})^2}{\text{Hz}} \tag{5.90}$$

5.8.1 Modulation Waveforms

Two modulation waveforms are considered in this study, a pulse train modulation function, $m_p(t)$, and a purely sinusoidal modulation function, $m_s(t)$. The pulse train modulation function represents the type of modulation obtained when a mechanical chopper is used to modulate a laser beam. The sinusoidal modulation function represents the type of modulation that can be obtained when an electro-optic modulator (EO) is used to modulate a laser beam. An EO can also be used to generate a pulse train modulation function, or other arbitrary waveform, at much higher frequencies than the mechanical chopper.

Initially, a zero mean valued function $b(t)$, that varies from $-1/2$ to $1/2$, is defined as the ac portion of the modulation waveform. Since the modulation is performed optically, the waveform has an inherent dc offset, as described in section 4.4.3. Therefore, a dc value of $1/2$, as shown in equation 5.91, is added to the zero mean

valued function, $b(t)$. The result is a modulation waveform that varies in magnitude from 0 to 1.

$$m(t) = \frac{1}{2} + b(t) \tag{5.91}$$

Pulse Train Modulation If a mechanical chopper is used to modulate a laser beam, the modulation function can be considered rectangular pulse train. The zero mean valued portion of rectangular pulse train, $b_p(t)$, is defined as a symmetric function, that has an absolute magnitude of 1/2. Thus, $b_p(t)$ has a 50% duty cycle and can be defined as,

$$b_p(t) = \begin{cases} +\frac{1}{2} & if \quad \mid t \mid < \frac{T}{4}, \\ -\frac{1}{2} & if \quad \frac{T}{4} \leq \mid t \mid < \frac{T}{2}. \end{cases} \tag{5.92}$$

The pulse train modulation function, $m_p(t)$, is, therefore, the sum of $b_p(t)$ and a dc component with a magnitude of 1/2.

The time domain representation of $b_p(t)$, written as a Fourier series, is given in equation 5.93, in which T_m is the modulation period. The dc component in $b_p(t)$ is zero, thus, the Fourier series representation is the sum of all the Fourier series coefficients, except the coefficient at $n = 0$, which is the dc component.

$$b_p(t) = \frac{1}{2} \sum_{n \neq 0} Sa\left(\frac{n\pi}{2}\right) e^{j2\pi n \frac{t}{T_m}} \tag{5.93}$$

The Fourier series coefficients are the amplitude values of the waveform's frequency components. The amplitude spectrum, $B_p(f)$, which corresponds to the zero mean valued function $b_p(t)$, is the sum of the Fourier series coefficients at its frequency

harmonics, where f_m is the modulation frequency.

$$B_p(f) = \frac{1}{2}\sum_{n\neq 0} Sa\left(\frac{n\pi}{2}\right)\delta(f - nf_m) \tag{5.94}$$

Incorporating the dc offset of 1/2 into equation 5.93, results in the Fourier series representation of the pulse train modulation function, $m_p(t)$. Since the dc offset is equal to the absolute magnitude of $b_p(t)$, the dc value can be incorporated into the summation term of equation 5.93, by allowing $n = 0$ to be a part of the total summation. The Fourier series representation of the pulse train modulation function, $m_p(t)$, is, therefore,

$$m_p(t) = \frac{1}{2}\sum_{n=-\infty}^{n=\infty} Sa\left(\frac{n\pi}{2}\right)e^{j2\pi n\frac{t}{T_m}} \tag{5.95}$$

which is the summation over all harmonic components, including the dc component.

The Fourier transform of $m_p(t)$ is the amplitude spectrum $M_p(f)$. Thus, the frequency domain representation of the pulse train modulation function is

$$M_p(f) = \frac{1}{2}\sum_{n=-\infty}^{\infty} Sa\left(\frac{n\pi}{2}\right)\delta(f - nf_m) \tag{5.96}$$

If an EO modulator is used to generate the pulse train modulation function, instead of a mechanical chopper, flexibility is obtained in terms of amplitude, period (frequency), and pulse width. In order to make the modulation function definition more general, the values in equations 5.95 and 5.96 can be replaced with general variables. In the general pulse train modulation function, the amplitude is define as C_m, the period as T_m, the frequency as f_m, and the pulse duration is defined as τ_m.

The time domain representation of the general pulse train is,

$$m_p(t) = \frac{C_m \tau_m}{T_m} \sum_{n=-\infty}^{\infty} Sa\left(\pi n \frac{\tau_m}{T_m}\right) e^{j2\pi n \frac{t}{T_m}} \tag{5.97}$$

and the frequency domain representation of the general pulse train is,

$$M_p(f) = \frac{C_m \tau_m}{T_m} \sum_{n=-\infty}^{\infty} Sa(\pi f_m n \tau_m)\delta(f - nf_m). \tag{5.98}$$

A final substitution can be made to simplify the pulse train modulation function expressions. The duty cycle is the ratio of a function's pulse duration to its period. Since frequency is the inverse of the period, the duty cycle is also equal to a function's pulse duration multiplied by its frequency. The duty cycle, defined as ψ_m, can, therefore, be substituted into equations 5.97 and 5.98 to provide the following expressions for the general pulse train.

$$m_p(t) = C_m \psi_m \sum_{n=-\infty}^{\infty} Sa\left(\pi n \psi_m\right) e^{j2\pi n \frac{t}{T_m}} \tag{5.99}$$

$$M_p(f) = C_m \psi_m \sum_{n=-\infty}^{\infty} Sa(\pi n \psi_m)\delta(f - nf_m) \tag{5.100}$$

Sinusoidal Modulation If, on the other hand, a sinusoidal modulation function is desired, an EO can again be used to modulated the laser source. The modulation function, $m_s(t)$, in this case, can be defined as a positive valued sinusoidal function. Again, there must be a dc offset in the modulation function since it is performed optically.

In order to generate a sinusoidally modulated beam, the EO modulator is driven

with a function generator, that generates the desired waveform. The frequency, f_m, and phase, ϕ, terms of the waveform are controllable and, therefore, known *a priori*. Since the phase term, relative to a detection process, can be set with a phase-locked loop, it is assumed to be zero in the following descriptions. Thus, the zero mean valued portion of the function, $b_s(t)$, is defined as a sinusoidal waveform that varies from $-1/2$ to $1/2$.

$$b_s(t) = \frac{1}{2}cos(2\pi f_m t + \phi) = \frac{1}{2}cos(2\pi f_m t) \tag{5.101}$$

The Fourier transform of a sinusoid results in impulses, or delta functions, at the angular frequency of the sinusoid (Stremler, 1990). By using a complex signal representation, which implies a two sided frequency domain representation, both the positive frequency terms and negative frequency terms are obtained. Using Euler's formula, the function $b_s(t)$ can expressed in complex form.

$$b_s(t) = \frac{1}{2}cos(2\pi f_m t) = \frac{1/2}{2}\left(e^{j2\pi f_m t} + e^{-j2\pi f_m t}\right) \tag{5.102}$$

The Fourier transform, defined as $\Im[\bullet]$, of a complex exponential results in a delta function in frequency space the frequency of oscillation, f_m.

$$\Im\left[\frac{1}{2}cos(2\pi f_m t)\right] = \Im\left[\frac{1/2}{2}e^{j2\pi f_m t}\right] + \Im\left[\frac{1/2}{2}e^{-j2\pi f_m t}\right] \tag{5.103}$$

$$\Im\left[\frac{1}{2}cos(2\pi f_m t)\right] = \frac{1}{4}\delta(f - f_m) + \frac{1}{4}\delta(f + f_m) \tag{5.104}$$

Adding a dc component of $1/2$ to $b_s(t)$, defined in equation 5.101, produces the desired sinusoidal modulation function $m_s(t)$, which has the corresponding amplitude

spectrum $M_s(f)$.

$$m_s(t) = \frac{1}{2} + \frac{1}{2}cos(2\pi f_m t) \tag{5.105}$$

$$M_s(f) = \frac{1}{2}\delta(f) + \frac{1}{4}\delta(f - f_m) + \frac{1}{4}\delta(f + f_m) \tag{5.106}$$

5.8.2 Modulated Signal

In order to increase the probability of extracting the information bearing signal from the probe beam, a known frequency and phase are impressed onto $A(t)$. The signal described in section 5.8 is modulated with either the pulse train modulation waveform or the sinusoidal modulation waveform, described in section 5.8.1.

Pulse Train Modulation Multiplying $A(t)$ with the modulation function, $m_p(t)$, results in a waveform that switches on and off at the modulation frequency, f_m. Multiplying the two functions in time corresponds to convolving the two functions in the frequency domain. The result from modulating $A(t)$ with a general, pulse train modulation function from equation 5.99, with C_m set to one, is given in equations 5.107 and 5.108 for the time and frequency domains respectively.

$$A(t) \cdot m_p(t) = A(t)\psi_m \sum_{n=-\infty}^{\infty} Sa\,(n\pi\psi_m)\, e^{j2\pi n \frac{t}{T_m}} \quad \text{watts} \tag{5.107}$$

$$F_{\mathrm{A}}(f) * M_p(f) = F_{\mathrm{A}}(f) * \psi_m \sum_{n=-\infty}^{\infty} Sa\,(n\pi\psi_m)\,\delta(f - nf_m) \quad \frac{\text{watts}}{\sqrt{\text{Hz}}} \tag{5.108}$$

Since $F_{\mathrm{A}}(f)$ from equation 5.87 is convolved with $M_p(f)$ in equation 5.108, the

result is the magnitude spectrum of the modulated signal. The power spectrum, which is the square of equation 5.108, is actually more useful. The power spectrum, in units of (watts)^2/Hz is,

$$S_{\mathrm{A}}(f) * |M_p(f)|^2 = S_{\mathrm{A}}(f) * (\psi_m)^2 \sum_{n=-\infty}^{\infty} |Sa\,(n\pi\psi_m)|^2\, \delta(f - nf_m) \quad \frac{(\text{watts})^2}{\text{Hz}} \tag{5.109}$$

Thus, the signal's baseband power spectrum is replicated at each of the harmonic components contained in the modulation waveform's power spectrum, $|M_p(f)|^2$. $S_{Ap}(f)$ is now defined as the power spectrum of the signal modulated with the pulse train waveform.

$$\begin{aligned} S_{Ap}(f) &= S_{\mathrm{A}}(f) * |M_p(f)|^2 \\ S_{Ap}(f) &= (\psi_m)^2 \sum_{n=-\infty}^{\infty} |Sa\,(n\pi\psi_m)|^2\, S_{\mathrm{A}}(f - nf_m) \end{aligned} \tag{5.110}$$

From equation 5.85,

$$S_{\mathrm{A}}(f - nf_m) = \frac{\sigma_{\mathrm{A}}^2 + \left(\overline{\mathrm{A}}\right)^2}{2B_{\mathrm{A}}} \prod \left(\frac{|f - nf_m|}{2B_{\mathrm{A}}} \right) , \tag{5.111}$$

such that $S_{Ap}(f)$ is defined as the following.

$$S_{Ap}(f) = (\psi_m)^2 \frac{\sigma_{\mathrm{A}}^2 + \left(\overline{\mathrm{A}}\right)^2}{2B_{\mathrm{A}}} \sum_{n=-\infty}^{\infty} |Sa\,(n\pi\psi_m)|^2 \prod \left(\frac{|f - nf_m|}{2B_{\mathrm{A}}} \right) \tag{5.112}$$

An example of $S_{\mathrm{Ap}}(f)$ is illustrated in Figure 5.10. In Figure 5.10, $\overline{\mathrm{A}}$ is set equal to 1x10^{-9}, which in the PPAS example corresponds to an α_{mod} of 0.01 and an I_p of 0.1x10^{-6} watts. The modulation frequency, f_m, is 1.5kHz and the bandwidth of the

signal, B_A, is arbitrarily set to 600Hz. The variance of the signal, σ_A^2 is assumed to be zero.

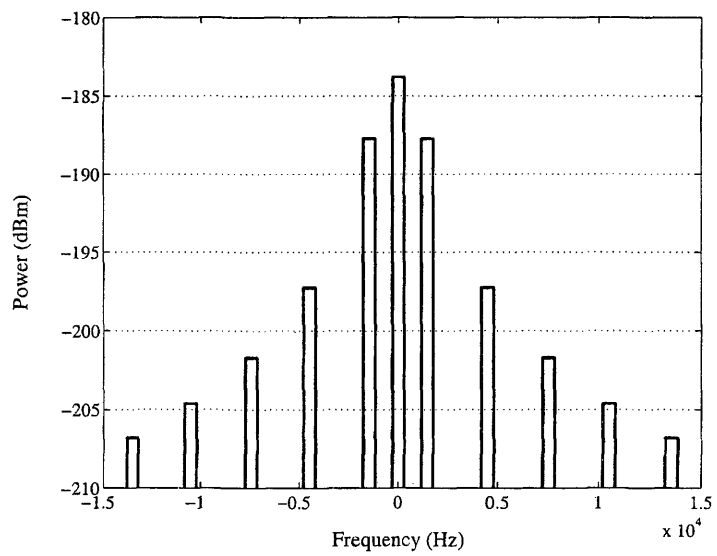

FIG. 5.10. Example power spectral density function for a pulse train modulated signal, $S_{Ap}(f)$

The complex exponential functions used to define the modulation function as a Fourier series are orthogonal in the interval from t to $t + T_m$. The integral of complex exponential functions is zero except for the case when the harmonic components are squared. Parseval's Theorem shows that the power in a function represented as a set of orthogonal functions can not only be determined by integrating the square of the time domain function, but also by summing the squared magnitude of the harmonic components, as shown in equation 5.113 (Stremler, 1990).

$$P = \frac{1}{T}\int_{-T/2}^{T/2} |f(t)|^2\, dt = \sum_{n=-\infty}^{\infty} |F_n|^2 \tag{5.113}$$

Using Parseval's theorem, the power contained in the modulated signal can be

found either by integrating over one period in time or by summing all of the spectral components in $S_{\mathrm{Ap}}(f)$. The total power, P_{Ap}, contained in $A(t) \cdot m_p(t)$ is,

$$P_{\mathrm{Ap}} = \frac{1}{T}\int_{-T/2}^{T/2} |A(t) \cdot m_p(t)|^2 \, dt = \int_{-\infty}^{\infty} S_{\mathrm{Ap}}(f) \, df. \tag{5.114}$$

In this case it is easier to calculate the total power in the time domain. Since the modulation waveform has a magnitude of one from $-\tau_m/2$ to $\tau_m/2$ and the power contained in $A(t)$ was shown to be $\overline{\mathrm{A}^2}$ in equation 5.86, the power in the modulated signal is,

$$P_{\mathrm{Ap}} = \frac{\overline{\mathrm{A}^2}}{T}\int_{-\tau_m/2}^{\tau_m/2} 1 \, dt = \frac{\overline{\mathrm{A}^2}\tau_m}{T} = \overline{\mathrm{A}^2}\psi_m = \psi_m\left[\sigma_{\mathrm{A}}^2 + \left(\overline{\mathrm{A}}\right)^2\right], \tag{5.115}$$

where ψ_m is the duty cycle of $m_p(t)$.

Sinusoidal Modulation The signal $A(t)$ can also be sinusoidally modulated with the waveform $m_s(t)$ defined in equation 5.105. In this case, the multiplication of $A(t)$ with $m_s(t)$ is given in equation 5.116 and the corresponding convolution in frequency is given in equation 5.117.

$$A(t) \cdot m_s(t) = \frac{A(t)}{2} + \frac{A(t)}{2}\cos(2\pi f_m t) \tag{5.116}$$

$$F_{\mathrm{A}}(f) * M_s(f) = \frac{1}{2}F_{\mathrm{A}}(f) + \frac{1}{4}F_{\mathrm{A}}(f - f_m) + \frac{1}{4}F_{\mathrm{A}}(f + f_m) \tag{5.117}$$

The power spectral density function of the sinusoidally modulated signal is, again, found by convolving the power spectrum of the signal with the magnitude squared of

the modulation waveform.

$$\begin{aligned} S_{\mathrm{As}}(f) &= S_A(f) * |M_s(f)|^2 \\ S_{\mathrm{As}}(f) &= \frac{1}{4}S_{\mathrm{A}}(f) + \frac{1}{16}S_{\mathrm{A}}(f - f_m) + \frac{1}{16}S_{\mathrm{A}}(f + f_m) \end{aligned} \tag{5.118}$$

Using equation 5.111, $S_{\mathrm{As}}(f)$ can written in its complete form.

$$\begin{aligned} S_{\mathrm{As}}(f) &= \frac{1}{4}\left[\frac{\sigma_{\mathrm{A}}^2 + \left(\overline{\mathrm{A}}\right)^2}{2B_{\mathrm{A}}}\prod\left(\frac{f}{2B_{\mathrm{A}}}\right)\right] + \frac{1}{16}\left[\frac{\sigma_{\mathrm{A}}^2 + \left(\overline{\mathrm{A}}\right)^2}{2B_{\mathrm{A}}}\prod\left(\frac{|f - f_m|}{2B_{\mathrm{A}}}\right)\right] \\ &+ \frac{1}{16}\left[\frac{\sigma_{\mathrm{A}}^2 + \left(\overline{\mathrm{A}}\right)^2}{2B_{\mathrm{A}}}\prod\left(\frac{|f + f_m|}{2B_{\mathrm{A}}}\right)\right] \end{aligned} \tag{5.119}$$

An example of $S_{\mathrm{As}}(f)$ is illustrated in Figure 5.11. The same parameters used to create Figure 5.10 are also used to create Figure 5.11. The dc power in both figures is the same. The power in the fundamental modulation frequency component, however, is slightly higher in Figure 5.10.

The total power contained in the sinusoidally modulated signal can, once again, be found either by integrating the time domain function or by summing the spectral components in the frequency domain. In this case, the power in the sinusoidally modulated signal, P_{As}, is easily determined by summing the spectral components.

$$\begin{aligned} P_{\mathrm{As}} &= \frac{1}{4}\int_{-B_{\mathrm{A}}}^{B_{\mathrm{A}}} S_{\mathrm{A}}(f)\,df + \frac{1}{16}\int_{f_m - B_{\mathrm{A}}}^{f_m + B_{\mathrm{A}}} S_{\mathrm{A}}(f - f_m)\,df \\ &+ \frac{1}{16}\int_{-f_m - B_{\mathrm{A}}}^{-f_m + B_{\mathrm{A}}} S_{\mathrm{A}}(f + f_m)\,df \end{aligned} \tag{5.120}$$

The integral of $S_{\mathrm{A}}(f)$, as shown in equation 5.86, is $\overline{\mathrm{A}^2}$, which results in,

$$P_{\mathrm{As}} = \overline{\mathrm{A}^2}\left(\frac{1}{4} + \frac{2}{16}\right) = \frac{3}{8}\,\overline{\mathrm{A}^2} = \frac{3}{8}\left[\sigma_{\mathrm{A}}^2 + \left(\overline{\mathrm{A}}\right)^2\right] \tag{5.121}$$

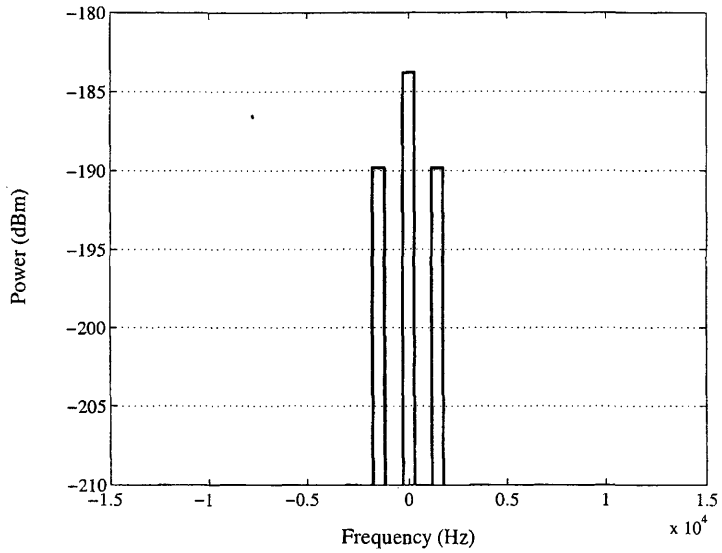

FIG. 5.11. Example power spectral density function for a sinusoidally modulated signal, $S_{\mathrm{As}}(f)$

In order to compare the differences between a pulse train modulation waveform and a sinusoidal modulation waveform, $S_{\mathrm{Ap}}(f)$, P_{Ap}, $S_{\mathrm{As}}(f)$, and P_{As} are examined. Assuming ψ_m is 50% in $S_{\mathrm{Ap}}(f)$, half of the total power in P_{Ap} resides at the dc component, 40.5% of P_{Ap} resides at the fundamental modulation frequency, and the remaining 9.5% of the power is spread over harmonics that are odd multiples of the fundamental frequency. In the case of the sinusoidal modulated signal, 66.6% of the total power in P_{As} resides at the dc component and the remaining 33.3% resides at the modulation frequency. Taking equal magnitudes of $A(t)$ into consideration, shows that the total power in the sinusoidally modulation function is 25% smaller than the total power in the pulse train modulation function. The power residing at the fundamental harmonic component, f_m, of $S_{\mathrm{Ap}}(f)$ is, therefore, about 61.7% larger than the power in $S_{\mathrm{As}}(f)$ at f_m. More signal power is, therefore, contained in the fundamental frequency component when a 50% duty cycle, pulse train waveform is

used for modulation.

5.9 Input Attributes

After determining $S_{\mathrm{Ap}}(f)$ and $S_{\mathrm{As}}(f)$, the total spectrum at the imaging system input can be can be developed through the superposition of all the spectra. The total input power spectrum, $S_T(f)$, is the sum of the steady state background, $S_B(f)$, the noise spectrum, $S_N(f)$, and the spectrum of the modulated information bearing signal, which is either $S_{\mathrm{Ap}}(f)$ or $S_{\mathrm{As}}(f)$. Using $S_{\mathrm{Ap}}(f)$, the total power spectrum at the input to the imaging system can be written as,

$$\begin{aligned} S_T(f) &= S_B(f) + S_N(f) + S_{\mathrm{Ap}}(f) \\ S_T(f) &= (I_p)^2\,\delta(f) + \frac{(I_p)^2}{\sqrt{1+\left(\frac{f}{f_o}\right)^2}} + \epsilon I_p + (\psi_m)^2\,\frac{\sigma_{\mathrm{A}}^2 + (\alpha_{mod} I_p)^2}{2B_{\mathrm{A}}} \\ &\quad \times \sum_{n=-\infty}^{\infty} |Sa\,(n\pi\psi_m)|^2 \prod\left(\frac{|f-nf_m|}{2B_{\mathrm{A}}}\right) \quad \frac{(\mathrm{watts})^2}{\mathrm{Hz}} \end{aligned} \tag{5.122}$$

or

$$\begin{aligned} S_T(f) &= (\lambda_p)^2\,\delta(f) + \frac{(\lambda_p)^2}{\sqrt{1+\left(\frac{f}{f_o}\right)^2}} + \lambda_p + (\psi_m)^2\,\frac{\sigma_{\mathrm{A}}^2 + (\alpha_{mod}\lambda_p)^2}{2B_{\mathrm{A}}} \\ &\quad \times \sum_{n=-\infty}^{\infty} |Sa\,(n\pi\psi_m)|^2 \prod\left(\frac{|f-nf_m|}{2B_{\mathrm{A}}}\right) \quad \frac{(\mathrm{photons/sec})^2}{\mathrm{Hz}} \end{aligned} \tag{5.123}$$

The signal to noise ratio (SNR) at the imaging system input, defined as SNR_{in}, is the ratio of the power contained in the modulated signal, P_{Ap} (equation 5.115) to the total noise, N_T (equation 5.79). Substituting $\alpha_{mod} I_p$ for $\overline{A}$ and assuming that the

signal variance, σ_A^2, is equal to zero, the SNR_{in} is,

$$\mathrm{SNR}_{in} = \frac{P_{\mathrm{Ap}}}{(N_T)^2} = \frac{\psi_m (\alpha_{mod} I_p)^2}{2 (I_p)^2 f_o ln\left(\frac{2B}{f_o}\right) + 2B\epsilon I_p} \tag{5.124}$$

Dividing both the numerator and the denominator in equation 5.124 by $(I_p)^2$ gives,

$$\mathrm{SNR}_{in} = \frac{\psi_m (\alpha_{mod})^2}{2 f_o ln\left(\frac{2B}{f_o}\right) + \frac{2B\epsilon}{I_p}} \tag{5.125}$$

The SNR_{in} as defined by equation 5.125 is plotted in Figure 5.12. Each line in Figure 5.12 is label with the modulation depth used in calculating SNR_{in}. The SNR_{in} is shown over a range of I_p from 10^{-10} watts to 10^{-7} watts and the bandwidth, B, is set at 1MHz. SNR_{in} in Figure 5.12 is given in units of dBm. The signal power is

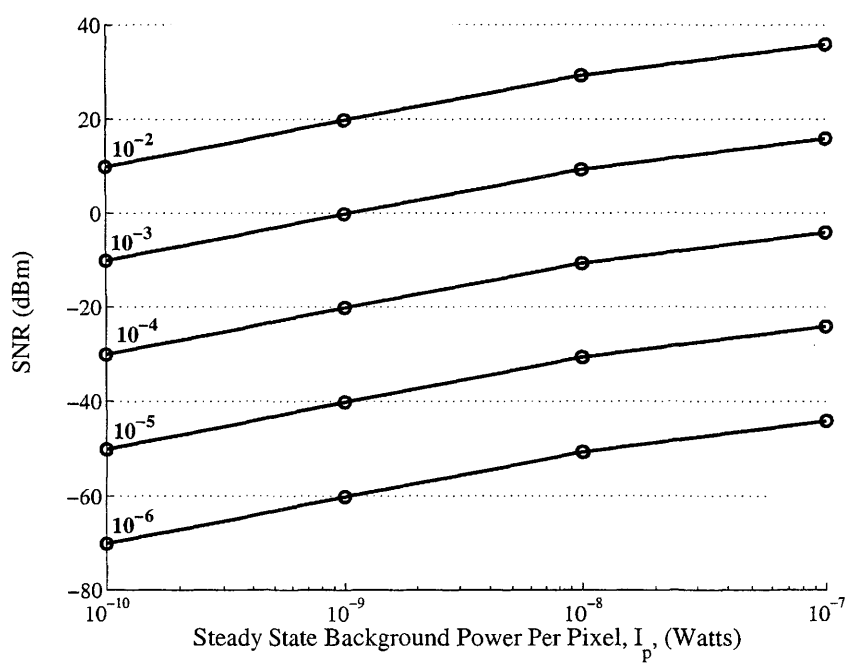

FIG. 5.12. Input signal-to-noise ratio

equal to the noise power when the SNR_{in} is equal to 0dBm. The noise power over a bandwidth of 1MHz is, therefore, larger than the signal power for modulation depths of 10^{-4} or smaller.

Another interesting attribute is the signal to background ratio (SBR). The SBR is different from the modulation depth calculation given in equation 5.88, because the signal in the SBR is modulated. The ratio of the modulated signal power, which is the same power used in equation 5.124, to the steady state background power is,

$$\mathrm{SBR}_{in} = \frac{\psi_m \left(\alpha_{mod} I_p\right)^2}{\left(I_p\right)^2} = \psi_m \left(\alpha_{mod}\right)^2 . \tag{5.126}$$

A final parameter of interest is the ratio of the power in the modulated signal's fundamental harmonic component to the power in the total noise at the modulation frequency. The ratio of the fundamental component power to the noise spectrum at f_m, as defined in equation 5.127, is a function of f_m. A 50% duty cycle, pulse train modulation function is considered and the modulated signal's fundamental component is defined as $S_{Ap}^{n=1}(f)$. Since both positive and negative frequencies are defined, the total power in the noise and in the signal's fundamental component is twice the power at f_m.

$$\mathrm{FNR}(f_m) = \frac{2\left[S_{Ap}^{n=1}(f_m)\right]}{2\left[S_T(f_m)\right]} = \frac{(\psi_m)^2 \left|\mathrm{Sa}(\pi\psi_m)\right|^2 \left(\alpha_{mod} I_p\right)^2}{2S_T(f_m)} \tag{5.127}$$

Equation 5.127 is plotted in Figure 5.13 for an f_m that ranges from 10Hz to 100kHz. The top plot in Figure 5.13 assumes a background power of 10^{-7} watts and the bottom plot assumes a background power of 10^{-10} watts. The data lines in each plot assume an α_{mod} from 10^{-2} to 10^{-6}.

Figure 5.13 shows the modulation frequency required for the signal's fundamental

component power to be equal to the noise power, for a given I_p. It is, therefore, desirable to set I_p as large as possible and modulate the signal at high frequencies. Modulation frequencies higher than 5x10^{4}Hz do not provide much improvement.

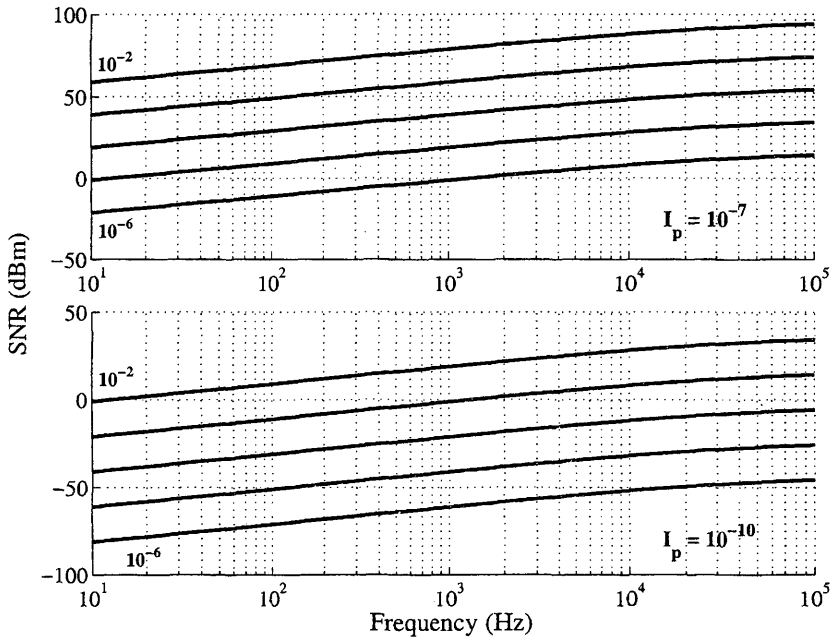

FIG. 5.13. Ratio of signal power at the fundamental frequency component to the total noise spectrum power at f_m

5.10 Imaging System Noise

Input noise sources were discussed in the previous sections. Additive noise sources from the imaging system itself also need to be considered to determine the noise properties and the SNR at the imaging system output. The noise sources are categorized as either input noise, CCD chip noise, or off-chip electronic noise. The noise sources are listed by category below and illustrated in Figure 5.14.

- Input Noise
  - 1/f Noise (photonic)
  - Photon (Shot) Noise
- CCD Chip Noise
  - Dark Charge
  - Fixed Pattern Noise
  - Charge Transfer Noise (CTE)
  - Reset Noise
  - 1/f Noise (electronic)
  - White Noise (Johnson Noise)
- Off-chip Electronic Noise
  - 1/f Noise (electronic)
  - White Noise (Johnson Noise)
  - Quantization Noise

5.10.1 Shot Noise

The photon noise from the input manifests itself as shot noise in the imaging system. Photon noise was derived and discussed in section 5.5 In determining the shape of the photon noise spectrum, in section 5.5.1, the shot noise process was

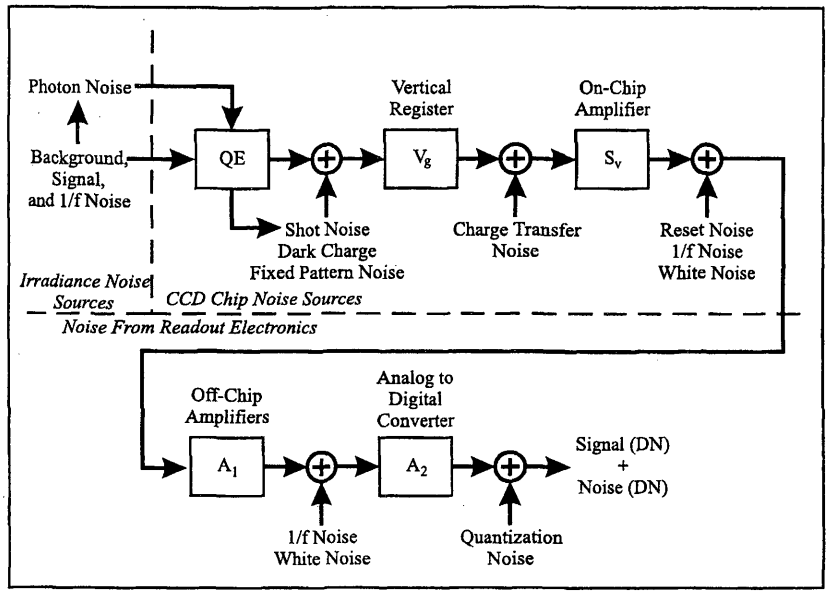

FIG. 5.14. Electronic noise sources

considered. From this analysis, the photon noise spectrum was determined to be white, as shown in equation 5.33.

As the photon noise enters the detector, it is sampled and photoelectrons are generated. The photoelectrons generated from incident noise photons are considered shot noise electrons.

The spectral density of the shot noise process was already defined in equation 5.33. Since the photon noise spectrum is white, the shape of the shot noise spectrum, defined as $S_i(f)$, depends on the impulse response of the imaging system. Thus, the shot noise spectrum is,

$$S_i(f) \;=\; S_W(f)|H(f)|^2 \;=\; (\lambda_p)^2\,|H(f)|^2 \quad \frac{(\text{photons/sec})^2}{\text{Hz}} \tag{5.128}$$

where $S_W(f)$ is the photon noise spectrum and $H(f)$ is the imaging system's detection transfer function.

The imaging system's transfer function is defined in both Chapters 6 and 7. Shot noise is derived from the photon noise and is a function of the sampling process performed by the imaging system, which is contained in the system's transfer function definition. Since shot noise is derived from the photon noise, $S_W(f)$, shot noise does not need to be specified as another additive noise source.

5.10.2 Dark Charge

Dark charge noise results from the accumulation of thermally generated electrons. The generation of thermally generated electrons is, like photon noise, governed by Poisson statistics since it is a discrete process. In most imaging conditions, the accumulation of dark charge is considerably small as compared to other sources of noise, such as photon noise (Holst, 1996).

The imaging system contains a thermoelectric Peltier cooling device, which cools the CCD chip down to -15°C. Dark charge is typically reduced by a factor of 2 for every 6°C reduction in temperature (Roper Scientific, 1998a). The system's data sheet quotes the rms dark charge noise, when the CCD is cooled to -10^oC, to be 0.05 electrons per pixel per second. Dark charge is, therefore, an important noise source to consider when imaging at long exposure time. The exposure times used in this work are on the order of microseconds or milliseconds, which are small enough to discount dark charge as a serious noise source.

5.10.3 Fixed Pattern Noise

Fixed pattern noise was previously discussed in section 2.7.7. This noise source arrises from the small pixel-to-pixel variations in gain. The gain factors for each pixel vary slightly around unity and are constant over the system's linear operating region.

The variation in gain factors can, therefore, be corrected in software.

If the variations are not corrected, at signal levels that approach saturation, the fixed pattern noise will be the dominate noise source (Janesick *et al.*, 1987). Correcting the gain variations of raw image data in software, reduces the noise to a level such that the data is shot noise limited (at signal levels above the read noise floor). Further discussion on fixed pattern noise can be found in Chapter 2.

5.10.4 Charge Transfer Noise

Charge transfer efficiency (CTE) is a measure of a device's ability to transfer charge from one potential well to the next. Charge transfer efficiency is essentially the ratio of charge transferred to the initial charge. Typically, well made, buried-channel devices have a CTE in the range of 0.99999 or greater per transfer for high signal levels (Janesick *et al.*, 1987). The remaining charge that is not transferred is either recombined in the silicon, or it is spread to trailing charge packets transferred along the same path.

Charge transfer noise is a statistical measure of the electrons *not* transferred with the original charge packet. Charge transfer noise, N_{CT}, can be calculated as,

$$N_{CT} = \sqrt{2\varepsilon n C_p} \quad \text{electrons,} \tag{5.129}$$

where ε is the transfer inefficiency, n is the number of transfers, and C_p is the amount of charge stored in the signal packet. The charge transfer inefficiency, ε is $1 - \text{CTE}$. The high CTEs that are routinely produced in CCDs make this source of noise relatively unimportant (Janesick *et al.*, 1987).

5.10.5 On-Chip and Off-Chip Amplifier Noise

The CCD's on-chip, output amplifier contains three sources of noise, which are reset noise, electronic 1/f noise, and thermal noise. Two of these noise sources, the electronic $1/f$ noise and the thermal noise are also observed in the off-chip amplifiers as well. Of these three sources, the reset noise and thermal noise sources add the majority of the total noise (Holst, 1996).

5.10.6 Reset Noise

Reset noise is the uncertainty in the CCD's output voltage after the charge from a pixel is read and the output amplifier is reset. The signal voltage is the difference between the reset voltage and the voltage a short time later when the charge from a pixel is transferred to the output capacitance node. Therefore, uncertainty in the reset voltage translates into uncertainty in the signal voltage. The reset noise, in electrons, is

$$N_R = \frac{\sqrt{k\mathrm{T}C_u}}{q} \quad \text{electrons} \tag{5.130}$$

where k is Boltzmann's constant, T is the absolute temperature, C_u is the total capacitance attached to the output node, and q is the charge of an electron (Janesick *et al.*, 1987).

Proper signal processing techniques, such as correlated double sampling (CDS) or bandpass filtering, can effectively remove reset noise (Levine, 1985; Janesick *et al.*, 1987; Solhusvik *et al.*, 1997). Since the imaging system incorporates CDS circuitry, the reset noise is assumed to be negligible.

5.10.7 Electronic $1/f$ Noise

Low frequency or $1/f$ noise, as described in section 5.6, is also present in electronic devices, albeit at lower power levels. The spectral density of low frequency noise is related to the inverse of frequency and is, therefore, larger in magnitude at very low frequencies near dc.

The $1/f$ noise generated by the laser at the input and the $1/f$ noise generated from the read out electronics effect the data differently. The $1/f$ noise at the input creates temporal uncertainty. After an image is integrated on the CCD chip, the temporal data is essentially fixed in time for a particular frame. As the frame is read from the CCD, the $1/f$ noise in the read out electronics adds $1/f$ noise across multiple pixels as they are read from the array. The electronic $1/f$ noise, therefore, adds noise spatially and creates spatial uncertainty, rather than temporally.

Much like the reset noise, the electronic $1/f$ noise can, however, be mitigated with appropriate signal processing techniques. In fact, the CDS technique used to eliminate the reset noise, can also be used to filter out much of the electronic $1/f$ noise (Levine, 1985; Solhusvik *et al.*, 1997).

5.10.8 Thermal Noise

At higher frequencies, the $1/f$ noise rolls off to the thermal noise floor of the electronics. Thermal noise, or Johnson noise, is caused by the random thermally excited vibration of charge carriers in a conductor. Since every conductor in the system has a temperature above absolute zero, it also has charge carriers that are randomly moving and vibrating. This random motion, which is a function of temperature, generates instantaneous current fluctuations, which is considered white noise in the noise bandwidth of the system.

The thermal noise power spectrum, $S_j(f)$, is a function of temperature T and equivalent circuit resistance R_{eq}. From statistical mechanical considerations, the thermal noise power spectrum is,

$$S_j(f) = 2kTR_{eq} \quad \frac{\text{watts}}{\text{Hz}} \tag{5.131}$$

where k is Boltzmann's constant (Stremler, 1990; Motchenbacher & Connelly, 1993). The mean-square value of the thermal noise voltage, defined as $\overline{V_j^2}$, is the integral of $S_j(f)$ over the noise bandwidth, B, of the circuit.

$$\begin{aligned} \overline{V_j^2} &= \int_{-B}^{B} S_j(f)\, df = \int_{-B}^{B} 2kTR_{eq}\, df \\ \overline{V_j^2} &= 4kTR_{eq}B \quad \text{watts} \end{aligned} \tag{5.132}$$

The root mean-squared (rms) thermal noise voltage is, therefore, the square root of $\overline{V_j^2}$.

$$v_j = \sqrt{\overline{V_j^2}} = \sqrt{4kTR_{eq}B} \quad \text{volts} \tag{5.133}$$

Equation 5.133 is the standard equation for rms thermal noise voltage. Since R_{eq} is fixed in the CCD's output amplifier, v_j can be reduced by either lowering the temperature or reducing the effective bandwidth. Both are accomplished by the active CCD chip cooling and the CDS processing, respectively.

5.10.9 Quantization Noise

Quantization noise, which is introduced during the system's analog to digital conversion (ADC) process, is the error that results from representing the actual analog

signal as a discrete value.

Since no value from the ADC is preferred over any other value, quantization noise has a uniform probability density function (pdf) (Cooper & McGillem, 1999). The uniform pdf for quantization noise can be written as,

$$f_{\mathrm{D}}(d) = \frac{1}{d_2 - d_1} \quad d_1 < d < d_2. \tag{5.134}$$

The mean value, $\overline{D}$, of a process that has a uniform pdf is,

$$\overline{D} = \frac{1}{2}(d_1 + d_2) \tag{5.135}$$

and the variance is (Cooper & McGillem, 1999),

$$\sigma_D^2 = \frac{1}{12}(d_2 - d_1)^2 \tag{5.136}$$

The error between the actual analog signal and the discrete representation is assumed to be uniformly spread over the interval $-\Delta d/2$ to $\Delta d/2$. Δd is defined as the difference between the two discrete values which are closest to the actual analog value. In this case, the mean is zero and the variance is equal to the mean-squared value.

A 16-bit ADC is used in the imaging system, which was described in section 2.7.2. The transfer gain of the ADC was also shown to be 1.526x10−4 volts per DN (digital number). The off-chip amplification is 4.1 volts per volt and the CCD's output amplifier conversion is 30.3μV. The ADC transfer gain can, therefore, be stated in terms of electrons as 1.228 electrons per DN. Using 1.228 electrons as Δd, the quantization

noise variance is,

$$\sigma_D^2 = \frac{1}{12}(\Delta d)^2 = \frac{1}{12}(1.228)^2 = 0.1257 \quad (\text{electrons})^2 \tag{5.137}$$

which is also equal to $0.0833(\text{DN})^2$. The rms quantization noise can, therefore, be stated as 0.354 electrons or 0.289 DN.

5.10.10 Read Noise

The read noise floor was discussed in section 2.7.4. Read noise is primarily thermal noise associated with the read out electronics. As stated in section 2.7.4, read noise is a combination of the dark charge, output amplifier noise, and noise from all other amplification stages. Read noise is the noise floor of the imaging system, below which signals are undetectable. Once the integrated image is above the read noise floor, the image is limited by shot noise. The read noise variance is 25.2 DN, which is equal to 38.0 electrons.

Chapter 6

GATED INTEGRATION SYSTEM MODEL

6.1 General Introduction

The imaging system can be operated in two detection modes, the gated integration mode and the heterodyne detection mode. The difference between the two modes lies in the frequency at which the input scene is sampled by the CCD, relative to the input signal's modulation frequency. The imaging system is operated in the gated integration mode by setting the sampling frequency equal to the modulation frequency. On the other hand, setting the sampling frequency and modulation frequency to different values places the system in the heterodyne detection mode.

This chapter analyzes the imaging system operated in the gated integration mode. The following chapter, Chapter 7, will then analyze the system under heterodyne detection operation. The input spectrum, developed in Chapter 5, is used in analyzing both operating modes.

To begin with in this chapter, the system's normal image acquisition process is presented as review. Based on the image acquisition process, mathematical functions that model the imaging system's operational capabilities are developed. A system function for the gated integration mode is then created by combining functions that describe the system's individual operations.

After applying the input spectrum to the gated integration system function, the signal and noise outputs are used to determine the signal-to-noise ratio (SNR).

Finally, the SNR is used to determine the system's detection limitations and predict the limiting modulation depth that can be resolved.

6.2 Charge Flow Under Normal Operation

A single exposure process, as performed by the interline transfer CCD, is reviewed in this section. Section 6.3 then relates the discussion in this section to linear systems models that are used to mathematically describe the individual CCD operations. The individual models are the basis for the gated integration system function, that is developed later in this chapter, and the heterodyne detection system function, developed in Chapter 7. The general interline transfer CCD illustration that was introduced in chapter 2, shown in Figure 6.1, is again used to facilitate discussion on the CCD's exposure process.

In a normal detection process, the over flow drain (OFD) barrier is initially lowered by raising the substrate voltage. This forces all charge accumulated in the sensor to immediately drain into the substrate. The OFD barrier, therefore, controls the electronic shutter mechanism. When the OFD barrier is lowered, the electronic shutter is *closed*, immediately draining photoelectrons into the substrate. When the OFD barrier is raised, the electronic shutter is *open*, creating a storage well in the sensor area that collects photoelectrons.

An image is acquired by first raising the OFD barrier. Once this barrier is raised, all photoelectrons are accumulated in the sensor area. After the desired exposure time has elapsed, which began when the OFD barrier was raised, the charge packet accumulated in the sensor is shifted to the vertical register by lowering the read out gate (ROG) barrier.

After the charge packet is stored in the vertical register, the ROG barrier is then

raised to its original level. The OFD barrier is once again lowered to drain off new photoelectrons accumulated in the sensor. Finally, the charge packet stored in the vertical register is transferred, along the y direction, out of the CCD by clocking the three vertical register phases. While the image is being read from the array, the process starts over and the next exposure is captured in the sensor.

The OFD barrier is also the mechanism that controls the anti-blooming feature. When an image is acquired and charge is integrated in the sensor, the OFD barrier level is lower than the ROG level. If the sensor well is saturated, meaning the well is full, any additional charge acquired in the sensor, will spill over the OFD and drain into the substrate. This prevents the additional charge from spilling into the vertical register or into adjacent sensor wells.

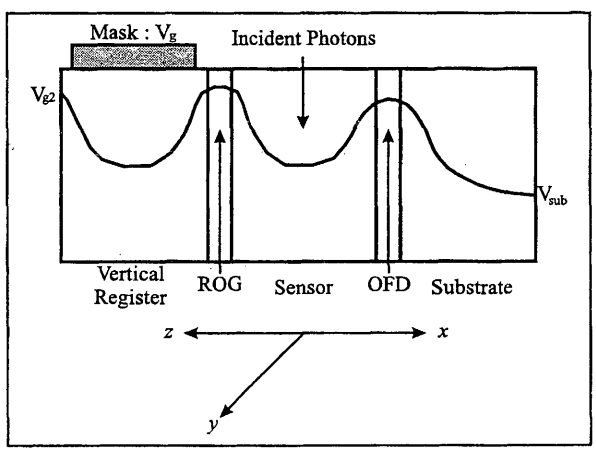

FIG. 6.1. General cross-section of the interline transfer CCD

6.3 Linear Systems Model Development

Based on the imaging process reviewed in the previous section, three fundamental functions are utilized to describe and model the imaging system's detection

process. A natural sampling function is used to model the sensor's accumulation of photoelectrons. An integrate and dump filter models the accumulation of multiple samples in the vertical register. And, a sample and hold filter is used to model the image read out process at the system's frame rate.

The natural sampling function and the integrate and dump filter are used to model the system when operated as a gated integrator. When operating as a gated integrator, the output frames contain either background, signal, and noise components or only background and noise components. It is not necessary, in this case, to retain information about the timing of an output frame with respect to another frame. It is only necessary to know whether or not the signal was present while a frame was acquired.

In order to model the system as a heterodyne detector, a sample and hold filter is added to the model, as described in Chapter 7. When operating the imaging system in a heterodyne detection mode, the background, signal, and noise components are contained in a series of frames. The sample and hold filter is, therefore, added to create a continuous time model and eliminate discontinuity between frames.

Each pixel captures a natural sample of the input and transfers the photoelectrons, or charge, from the sample to the vertical register. Initially, the vertical register is assumed to be empty (except for noise, i.e. dark charge) and the ROG barrier is set to its maximum level, which prevents charge, generated in the sensor, from flowing into the vertical register. The overflow drain (OFD) barrier is set to its minimum level to drain charge, generated in the sensor, to the substrate. Natural sampling is then accomplished by raising the OFD barrier and lowering the ROG barrier. The ROG remains low for the desired exposure time τ_s, which is the natural sample's length in time. During this time, the charge in the sensor, which varies proportionally with

the incident number of photons, flows directly into the vertical register. After the desired sample time has elapsed, the ROG barrier is raised to prevent further charge from entering the vertical register, and the OFD is lowered to drain charge from the sensor to the substrate.

After the input signal is naturally sampled, the sample is stored in the vertical register. It is also possible to acquire another sample, for the same exposure time, τ_s, and add it to the previous sample stored in the vertical register. Repeating the natural sampling process will add another sample to the sample that is already stored in the vertical register. The image is not read from the array between samples so that the sample contained in the vertical register remains in the same location as the corresponding sensor. The detector can, therefore, integrate multiple samples in the vertical register by repeating the sampling process at the sampling frequency f_s.

Integration of multiple samples can continue until the integrated charge fills the vertical register's potential well. In order to prevent saturation, however, the number of samples integrated in the vertical register should be set so that the integrated charge lies in the imaging system's linear operating range. Once the desired number of samples are integrated in the vertical register, the integrated image is readout, and the detector is reset for acquisition of the next image.

An integrate and dump filter is used to model integration of multiple samples in the vertical register. The integrate and dump filter integrates an input for a time period τ_i, which is the total time required to integrate the desired number of samples from the sensor. Once the desired number of samples are integrated, the charge in the vertical register is transferred out of the array. The integrate and dump filter, used to model the vertical register, is, therefore, reset to zero for the next integration period.

The natural sampling function and the integrate and dump filter are introduced in the following sections. The sample and hold filter, which is not used in the gated integrator system model developed in this chapter, is discussed in Chapter 7. The mathematical development of the natural sampling function and the integrate and dump filter are included in Appendices E and F respectively.

6.3.1 Natural Sampling Function

The input to the imaging system is first sampled by controlled operation of the CCD's ROG. A natural sampling function is used to model the sampling performed by the CCD's ROG. From Appendix E, the time domain Fourier series representation of the natural sampling function is,

$$q(t) = \psi_s \sum_{n=-\infty}^{\infty} \mathrm{Sa}(\pi n \psi_s) e^{j2\pi f_s n t} , \tag{6.1}$$

and the corresponding frequency domain representation is,

$$Q(f) = \psi_s \sum_{n=-\infty}^{\infty} \mathrm{Sa}(\pi n \psi_s) \delta(f - n f_s) , \tag{6.2}$$

where ψ_s is the duty cycle and f_s is the sampling frequency.

The power spectrum of the natural sampling function is found by squaring the harmonic values contained in $Q(f)$. The power spectrum of $Q(f)$ is,

$$|Q(f)|^2 = (\psi_s)^2 \sum_{n=-\infty}^{\infty} |\mathrm{Sa}\,(\pi n \psi_s)|^2 \, \delta(f - n f_s) \tag{6.3}$$

Equation 6.3 is illustrated in Figure 6.2 with ψ_s set to 50% and f_s normalized.

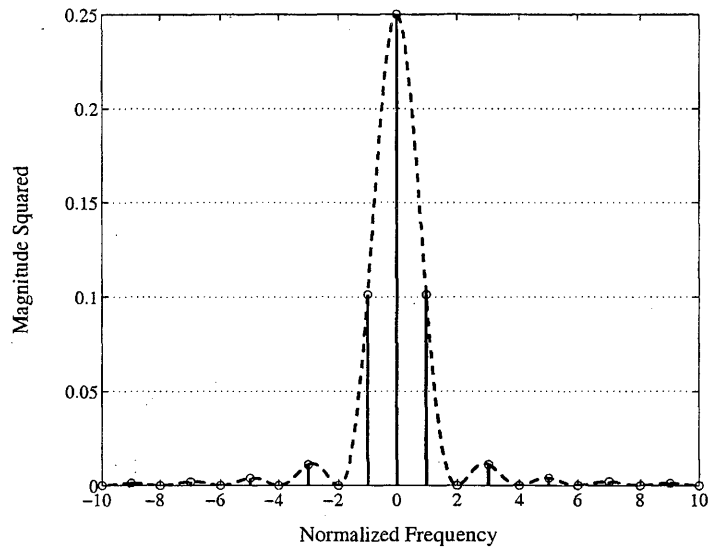

FIG. 6.2. Natural sampling function power spectrum

Natural Sampling Function Characteristics Considering a general natural sampling function, the spectral content and spectral envelope are a function of the duty cycle. More specifically, the sampling period, T_s, and dwell time, τ_s, values control the natural sampling function's spectral envelope. The dwell time is the time length of the sample pulse.

The spectral representation of the natural sampling function, defined in equation 6.2, is comprised of harmonics, located at the sampling frequency, f_s. The harmonics are scaled in amplitude by a sampling function envelope [Sa()]. They are also scaled by the constant duty cycle term, ψ_s, however, the same gain from this term is applied to all harmonics, independent of frequency. For now, only the shaping effects from Sa() are considered.

Since the sampling frequency, f_s, is the inverse of the sampling period, T_s, the spectral components are fixed if T_s is fixed. The harmonic amplitudes are then dependent on the sampling function envelope. Since the sampling function, Sa(x), is

defined as $\sin(x)/x$, it has maxima at multiples of $\pi/2$ and zeros at multiples of π. The spectral location at which the sampling function envelope crosses the abscissa, and is zero, is a function of the dwell time, τ_s. Solving for the zero crossings, the spectrum is zero at integer multiples of $1/\tau_s$ (Stremler, 1990).

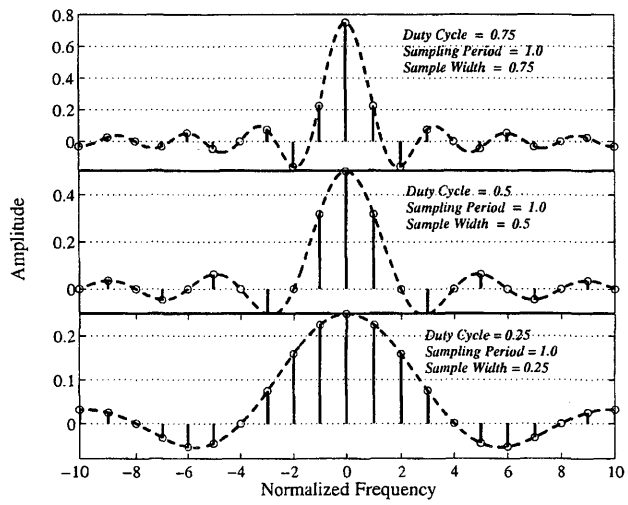

FIG. 6.3. Amplitude spectrum of periodic natural sampling function with constant sampling rate and variable dwell time

Figure 6.3 shows the amplitude spectrum of a natural sampling function for three different duty cycle values. The sampling period, T_s, is held constant and the dwell time, τ_s, is varied to obtain the desired duty cycle. The illustrations in Figure 6.3 show that the harmonics are stationary, their amplitudes change according to the sampling function envelope, and the zero crossings are located at the inverse of the dwell time.

On the other hand, the duty cycle can also be set by changing T_s and holding τ_s constant. In this case, the harmonic locations change only according to changes in the sampling period and the shape of $\mathrm{Sa}(x)$ is constant, albeit with amplitude variation. Figure 6.4 shows the spectrum for a fixed dwell time and a variable sampling period,

or sampling rate. Since the dwell time is constant, the zero crossings, in this case, are fixed at $1/\tau_s$.

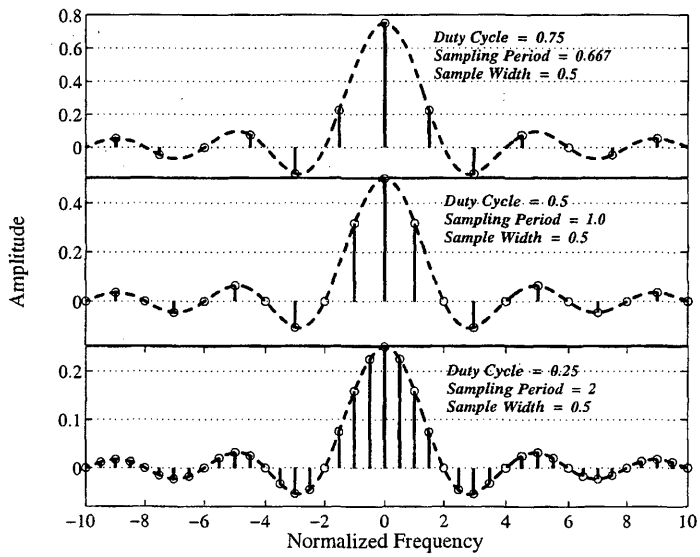

FIG. 6.4. Amplitude spectrum of periodic natural sampling function with constant dwell time and variable sampling rate

The natural sampling function's spectral envelope and harmonic placement can, therefore, be controlled by appropriately setting the values for T_s and τ_s. The period, T_s, of the natural sampling function can be set such that the harmonic components of interest are within a low noise band. The dwell time can then be used to eliminate unwanted components that reside, in frequency, at integer multiples of $1/\tau_s$. Both parameters can be configured to retain desired information and to attenuate unwanted noise.

6.3.2 Integrate And Dump Filter

After the input signal is sampled with $q(t)$ given in equation 6.1, the sampled values are integrated over an integration period τ_i. At the end of the integration

period, the final integrated value is sent to the output and the integrate and dump filter is reset. After the integrator is reset, a new integration period begins.

Based on the integrate and dump filter developments in Appendix F, the transfer function, $H_{id}(f)$, for the filter is,

$$H_{id}(f) = \tau_i \mathrm{Sa}(\pi f \tau_i) e^{-j2\pi f \frac{\tau_i}{2}} \tag{6.4}$$

The power transfer function, $|H_{id}(f)|^2$, of the integrate and dump filter is determined by multiplying the Fourier transform complex conjugates pairs. The power transfer function, given in equation 6.5, is illustrated in Figure 6.5.

$$\begin{aligned} |H_{id}(f)|^2 &= |H_{id}(f)||H_{id}^*(f)| \\ |H_{id}(f)|^2 &= \tau_i^2 \left|\mathrm{Sa}(\pi f \tau_i)\right|^2 \end{aligned} \tag{6.5}$$

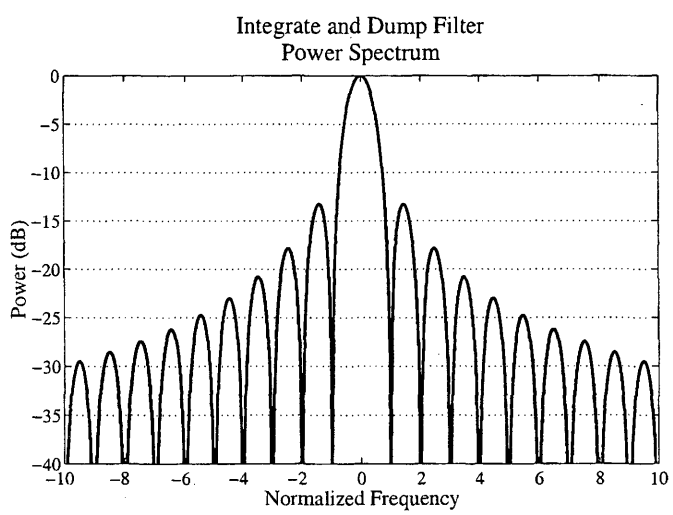

FIG. 6.5. Integrate and dump filter power response

Filter Characteristics Before concluding discussion on the integrate and dump filter, a few characteristics are discussed. Notice from Figure 6.5 the peaks and troughs, which are inherent in a sampling function, Sa(). The filter's troughs are actual zeros that eliminate power at that particular frequency value. Since the integrate and dump filter's response is defined with a sampling function [Sa()], its temporal frequency domain characteristics are similar to the spectral envelope of the natural sampling function.

The sampling function is a maximum when the argument of Sa() is a multiple of $\pi/2$, and is zero when the argument is a multiple of π. The integrate and dump filter, therefore, has peaks at,

$$\pm f = \frac{1 + 2r}{2\tau_i} \quad \text{where } r = 0, 1, 2, ... \tag{6.6}$$

and has zeros at,

$$\pm f = \frac{1 + r}{\tau_i} \quad \text{where } r = 0, 1, 2, ... \tag{6.7}$$

In Figure 6.5, both the integration period, τ_i, and the frequency are normalized. It is apparent, in this case, that the power transfer function goes to zero when f is equal to $\pm(1+r)/\tau_i$. At these points in frequency, power is eliminated at the integrate and dump filter's output.

Noise Equivalent Filter Also shown in Appendix F is the noise equivalent filter that can be used to determine the noise power at the integrate and dump filter's output. The integrate and dump filter has a noise equivalent bandwidth (NEB),

defined as B_{id}, that is equal to $1/(2\tau_i)$. The noise equivalent filter is,

$$|H_{id}^{eq}(f)|^2 = \tau_i^2 \prod \left(\frac{f}{2B_{id}}\right) = \tau_i^2 \prod (\tau_i \cdot f) = \tau_i^2 \prod \left(\frac{f}{f_i}\right) \tag{6.8}$$

where the integrate and dump frequency, f_i, is equal to $1/\tau_i$.

6.3.3 CCD Specific Gain

The imaging system's gain, which was presented in section 2.7, can also be incorporated into the system function. In section 2.7, the total gain was shown to be a combination of quantum efficiency, η, CCD output amplifier gain, S_v, the gain of the readout electronics, A_1, and the analog-to-digital conversion (ADC) factor, A_2. The system gain, G_s, used in this chapter is defined as,

$$G_s = \eta \cdot S_v \cdot A_1 \tag{6.9}$$

which excludes the ADC conversion factor. Referring to Figure 5.1 in Chapter 5, the output of the system function (defined in this chapter) will have units of either volts or (volts)^2, depending on the input definition. Incorporating the ADC conversion gain, A_2, at system function output will convert the result to a digital number (DN) of counts.

The same gain term is, however, applied to the background, the noise components, and to the signal components. When analyzing the system in terms of the output signal-to-noise ratio (SNR), the constant gain term will factor out and, therefore, is not explicitly needed in the model. If, however, the absolute power at the output is desired, then G_s can be included in the model.

6.4 Gated Integrator Model

The imaging mode analyzed in this chapter is the gated integration mode. In this mode the imaging system is either synchronized to the signal or operated completely out of phase from the signal. A minimum of two images must, therefore, be acquired to determine the modulation depth.

The system integrates multiple samples into a single image. The final integrated image either includes the information bearing signal, or excludes the signal. After acquiring two images, one with signal and one without, the modulation depth is determined by subtracting the two images and dividing by the image that does not contain signal.

The integrated image that contains signal is defined as Y_{on}^2 and the integrated image that does not contain signal is defined as Y_{off}^2. Both Y_{on}^2 and Y_{off}^2 also contain the steady state background component and noise. The modulation depth that is determined from these two images is, therefore, the mean-squared modulation depth, which is given in equation 6.10.

$$\overline{\alpha_{mod}^2} = \frac{Y_{\text{on}}^2 - Y_{\text{off}}^2}{Y_{\text{off}}^2} \tag{6.10}$$

The integrated images Y_{on}^2 and Y_{off}^2 are defined using superposition. In the sections that follow, the signal, background, and noise components are defined individually at the output of $|H_g(f)|^2$. The sum of these components then describe Y_{on}^2 and Y_{off}^2, which are used to determine the modulation depth.

6.4.1 System Function

When operated as a gated integrator, the system function is the combination of the natural sampling function and the integrate and dump filter. A block diagram of the gated integrator is shown in Figure 6.6.

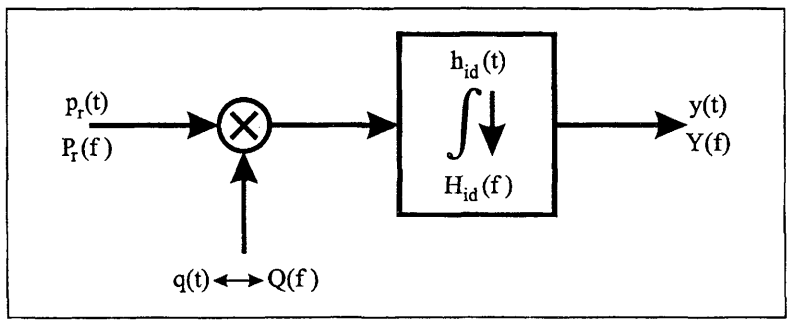

FIG. 6.6. Gated integrator block diagram

The effective system function for the gated integrator, shown in Figure 6.6, is defined as $H_g(f)$. Applying an input $P_r(f)$ to $H_g(f)$ results in an output of $Y(f)$.

The output power from the gated integrator is found by first convolving the input power spectral density function with $|Q(f)|^2$. This result is then filtered with $|H_{id}(f)|^2$ to produce the output power spectrum, $|Y(f)|^2$. For an input power spectrum $S_T(f)$, where $S_T(f)$ is equal to $|P_r(f)|^2$ from Figure 6.6, the output is,

$$|Y(f)|^2 = |H_{id}(f)|^2 \left(S_T(f) * |Q(f)|^2\right) \tag{6.11}$$

which is,

$$|Y(f)|^2 = \tau_i^2 |\mathrm{Sa}(\pi f \tau_i)|^2 (\psi_s)^2 \sum_{n=-\infty}^{\infty} |\mathrm{Sa}(\pi n \psi_s)|^2 S_T(f - nf_s) . \tag{6.12}$$

6.4.2 Input Review

The input power spectrum, $S_T(f)$, given in equation 5.123, is applied to the gated integration power transfer function, $|H_g(f)|^2$, in this chapter. As shown in Chapter 5, $S_T(f)$ is the combination of the steady state background, $S_B(f)$, the photon noise, $S_W(f)$, the $1/f$ noise, $S_L(f)$, and the modulated information bearing signal, $S_{\mathrm{Ap}}(f)$.

Two changes are made to the input spectrum when the imaging system is operating in the gated integrator mode. First, an additional variable is added to the input to model the integration threshold feature, which was introduced in section 3.4. Second, the modulation applied to the information bearing signal, contained in input spectrum, is removed because of characteristics inherent to the gated integrator.

Integration Threshold The integration threshold feature is only considered when operating in the gated integrator mode. Section 3.4 describes this mechanism as a nonlinear function that captures a portion of the steady state background irradiance.

The integration threshold (IT) is defined as,

$$\mathrm{IT} = 1 - \rho \,. \tag{6.13}$$

Based on this definition, when ρ, defined as the integration threshold coefficient, is equal to one no threshold is set and the entire input is integrated. On the other hand, when $\rho = 0$ a complete threshold is set and, in theory, the steady state background irradiance is eliminated. The amount of background that is integrated is, therefore, ρ multiplied by the arrival rate of background photons, λ_p.

Un-modulated Signal The input spectrum that is "seen" by the gated integrator is different than the input spectrum "seen" by the heterodyne detector. When

the imaging system is operated as a gated integrator, the information bearing signal spectrum does not appear modulated. In this mode, the system samples the signal only when it is present, therefore, the signal appears as a baseband, un-modulated spectrum at the input.

In order to completely resolve a particular frequency component, the component must be sampled at a frequency that is at least twice the component frequency. The Nyquist frequency is twice a particular component's frequency. The gated integrator samples at the component frequency, rather than the Nyquist frequency, therefore, the signal's modulation is not appreciated.

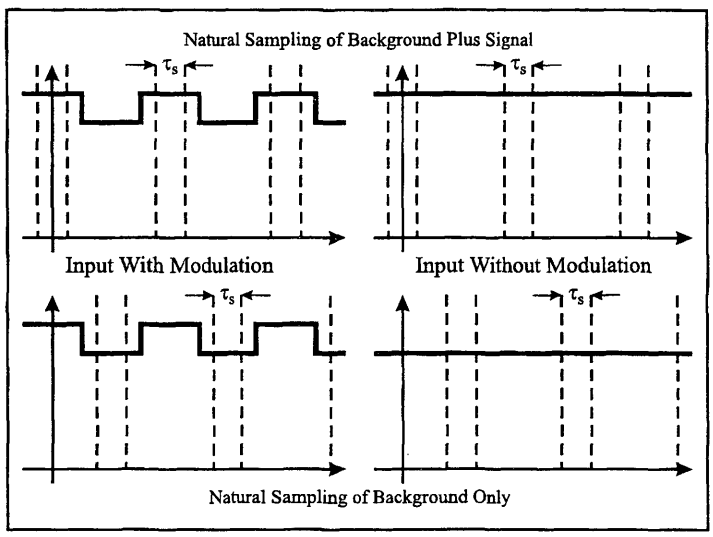

FIG. 6.7. Illustration of the natural sampling performed by the gated integrator on the input waveform

Figure 6.7 illustrates that the gated integrator does not recognize the modulation applied to the signal. Each frame from the imaging system contains either the sum of the background, signal, and noise, or the sum of only the background and noise. In either case, as shown in Figure 6.7, $|H_g(f)|^2$ can be analyzed with the baseband signal spectrum, $S_A(f)$, applied to the input, rather than the modulated spectrum,

$S_{\mathrm{Ap}}(f)$.

Even though the gated integrator does not sample at or above the Nyquist rate and does not, therefore, recognize the modulation applied to the information bearing signal, the modulation may be required by other components of the diagnostic system. In order for the laser to properly interact with a species under investigation, and to prevent population saturation, laser modulation may be required (Settersten, 1999). Besides physical constraints, modulation may also simplify data collection. A simple change of phase may be all that is required to switch from images that include the information bearing signal to images that exclude the signal.

The gated integrator analysis, contained in the following sections, is performed with an integration threshold factor, ρ, and is performed as if the signal were not modulated at the input. Also, in order to simplify the signal's spectrum, the signal variance, σ_{A}^2, is assumed to be zero and the mean value, $\overline{\mathrm{A}}$, is set equal to $\alpha\lambda_p$, where α is the modulation depth and λ_p is the steady state background entering a pixel. The signal is, therefore, assumed to be constant, which is an impulse at dc in the frequency domain. The spectral input to the gated integrator is defined as,

$$\begin{aligned} S_T(f) &= S_B(f) + S_N(f) + S_{\mathrm{A}}(f) \\ S_T(f) &= (\rho\lambda_p)^2\,\delta(f) + \frac{(\rho\lambda_p)^2}{\sqrt{1+\left(\frac{f}{f_o}\right)^2}} + \rho\lambda_p + (\alpha\lambda_p)^2\,\delta(f) \end{aligned} \tag{6.14}$$

where ρ's effect on the signal is assumed to be negligible, thus, only effecting the steady state background. Since the noise is defined as a function of the steady state background, ρ also effects the noise components.

6.5 Gated Integrator Output

In the following sections, the components of $S_T(f)$ from equation 6.14 are applied to $|H_g(f)|^2$. The outputs are defined with the same subscripts as the inputs. For example, the output is $|Y_B(f)|^2$ when $S_B(f)$ is applied to the input.

6.5.1 Signal Output

The signal is, again, represented as unmodulated when applied to the gated integrator. The signal spectrum is defined as a dc component.

$$S_{\mathrm{A}}(f) \;=\; (\alpha\lambda_p)^2\,\delta(f) \tag{6.15}$$

As the signal enters the imaging system, it is first sampled with the natural sampling function. Since it is sampled in time, it is convolved in the frequency domain, which results in,

$$S_{\mathrm{A}}(f) * |Q(f)|^2 \;=\; (\alpha\lambda_p\psi_s)^2 \sum_{n\,=\,-\infty}^{\infty} |\mathrm{Sa}\,(\pi n\psi_s)|^2\,\delta(f - nf_s) \tag{6.16}$$

where f_s is, again, the sampling frequency. The signal power is, therefore, spread out over the harmonic components created by $Q(f)$.

After sampling, the result is filtered by the integrate and dump filter. The signal's spectrum at the output of $|H_g(f)|^2$ is,

$$|Y_{\mathrm{A}g}(f)|^2 \;=\; (G_s\tau_i)^2|\mathrm{Sa}(\pi f\tau_i)|^2(\alpha\lambda_p\psi_s)^2 \sum_{n\,=\,-\infty}^{\infty} |\mathrm{Sa}\,(\pi n\psi_s)|^2\,\delta(f - nf_s) \tag{6.17}$$

where G_s is the imaging system gain and τ_i is the integration time. The subscript g on $|Y_{\mathrm{A}g}(f)|^2$ indicates the output was processed by $|H_g(f)|^2$.

The characteristics of $|H_{id}(f)|^2$ were discussed in section 6.3.2. In this section, it was shown that $|H_{id}(f)|^2$ has zero points at multiples of $1/\tau_i$. It is assumed that τ_i is set to a value that eliminates all of the harmonic components from $S_{\mathrm{A}}(f) * |Q(f)|^2$ leaving only the dc term. The integration time is, therefore, set such that,

$$\tau_i = \frac{1 + r}{f_s} \quad r = 0, 1, 2, ... \tag{6.18}$$

which sets the minimum integration time, at $r = 0$, to $1/f_s$.

Removing all harmonic components with $|H_{id}(f)|^2$ reduces the output signal spectrum to,

$$|Y_{\mathrm{A}g}(f)|^2 = (G_s \tau_i \psi_s \alpha \lambda_p)^2 \, \delta(f) \tag{6.19}$$

When analyzing noise in section 6.5.3, the sampling function's duty cycle, ψ_s, is set to 50%. In this case, the signal power at the output of $|H_g(f)|^2$ is,

$$\left(\overline{Y_{\mathrm{A}g}}\right)^2 = \frac{1}{4} (G_s \tau_i \alpha \lambda_p)^2 \ . \tag{6.20}$$

6.5.2 Background Output

Since the steady state background spectrum is the same as $S_{\mathrm{A}}(f)$, albeit with a different magnitude, the background spectrum at the output is also a dc component. The spectrum of the background component, $S_B(f)$, at the output of $|H_g(f)|^2$ is,

$$|Y_{Bg}(f)|^2 = G_s^2 |\mathrm{Sa}(\pi f \tau_i)|^2 (\rho \lambda_p \psi_s)^2 \sum_{n=-\infty}^{\infty} |\mathrm{Sa}\,(\pi n \psi_s)|^2 \, \delta(f - n f_s) \ . \tag{6.21}$$

where ρ is the integration threshold factor introduced in section 3.4.

Using the same assumptions from section 6.5.1, all of the harmonic components are eliminated and the background is naturally sampled with a 50% duty cycle waveform. Only the dc term, therefore, remains at the output.

$$\left(\overline{Y_{Bg}}\right)^2 = \frac{1}{4}\left(G_s\tau_i\rho\lambda_p\right)^2 \tag{6.22}$$

6.5.3 Noise Output

The noise at the output of the imaging system is a combination of photon noise, $1/f$ noise, and noise from the CCD and read out electronics, as discussed in section 5.10. In the following sections, the noise spectra, $S_W(f)$ and $S_L(f)$, are applied to $|H_g(f)|^2$ and the outputs are derived. The imaging system's read out noise is a constant that is added per frame. The read out noise is incorporated into the total noise power at the output, which is used in the signal-to-noise ratio (SNR) calculations in section 6.7

Photon Noise The photon noise, $S_W(f) = \rho\lambda_p$, is first sampled by the natural sampling function at the imaging system's input. If the duty cycle, ψ_s, of $Q(f)$ is 50%, then the power at the output of $Q(f)$ is half of the power at its input. Convolving the photon noise spectrum, which is white, with the natural sampling function results in photon noise power that is a function of the duty cycle.

$$S_W(f) * |Q(f)|^2 = \psi_s\rho\lambda_p = \frac{1}{2}\rho\lambda_p \tag{6.23}$$

Passing this result to the integrate and dump filter produces the output photon

noise spectrum,

$$|Y_{Wg}(f)|^2 = (G_s\tau_i)^2 \left|\mathrm{Sa}\left(\pi f \tau_i\right)\right|^2 \frac{1}{2}\rho\lambda_p \tag{6.24}$$

The total photon noise power at the output of $|H_g(f)|^2$ can be determined by integrating $S_W(f) * |Q(f)|^2$ over the integrate and dump filter's noise equivalent bandwidth (NEB). The integrate and dump filter's NEB, which is discussed in Appendix F, is $1/(2\tau_i)$. Using this NEB, the photon noise power at the output of $|H_g(f)|^2$ is,

$$\begin{aligned} \sigma^2_{Wg} &= \frac{1}{2}\left(G_s\tau_i\right)^2 \rho\lambda_p \int_{-1/2\tau_i}^{1/2\tau_i} df \\ \sigma^2_{Wg} &= \frac{1}{2} G_s^2 \tau_i \rho\lambda_p \,. \end{aligned} \tag{6.25}$$

1/f Noise The $1/f$ noise spectrum, $S_L(f)$, is, again, first mixed with $|Q(f)|^2$.

$$S_L(f) * |Q(f)|^2 = (\psi_s)^2 \sum_{n=-\infty}^{\infty} \left|\mathrm{Sa}\left(\pi n \psi_s\right)\right|^2 S_L(f - nf_s) \tag{6.26}$$

Since $S_L(f)$ is convolved with all of the harmonics contained in $|Q(f)|^2$, equation 6.26 contains the baseband $1/f$ noise spectrum and a replica of the $1/f$ noise spectrum at all of the harmonic components contained in $Q(f)$. The noise power from the harmonic components that are higher than the fundamental sampling frequency are considered negligible. Only the spectrum at dc and the spectra that is convolved to the fundamental frequency are considered. Assuming that the sampling function's duty cycle is 50%, the result is,

$$S_L(f) * |Q(f)|^2 = \frac{1}{4}S_L(f) + \frac{1}{\pi^2}S_L(f + f_s) + \frac{1}{\pi^2}S_L(f - f_s), \tag{6.27}$$

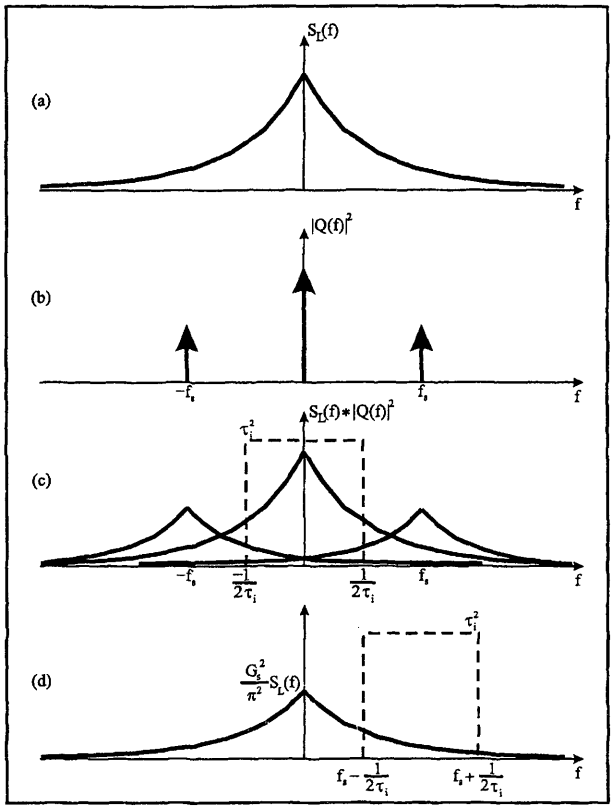

FIG. 6.8. Transfer of $1/f$ noise through gated integrator system function

since $|\mathrm{Sa}(\pi\psi_s)|^2 = 4/\pi^2$ when $\psi_s = 1/2$. The result given in equation 6.27 is illustrated in Figure 6.8(c).

After $1/f$ noise is sampled, it is then filtered with $H_{id}(f)$, producing the following noise spectrum at the output.

$$|Y_{Lg}(f)|^2 = (G_s\tau_i)^2\,|\mathrm{Sa}(\pi f\tau_i)|^2\left[\frac{1}{4}S_L(f) + \frac{1}{\pi^2}S_L(f+f_s) + \frac{1}{\pi^2}S_L(f-f_s)\right] \quad (6.28)$$

The noise power, from the $1/f$ noise, that appears at the output of $|H_g(f)|^2$ can again be determined with the integrate and dump filter's NEB. The integrate and dump filter's NEB is also shown, as a dashed line, in Figure 6.8(c). The noise within

the NEB is the sum of the noise from $S_L(f)$ and the noise from both $S_L(f+f_s)$ and $S_L(f-f_s)$.

Each of the three components inside the NEB is considered separately. The noise contribution from the dc term is found by integrating $\frac{1}{4}S_L(f)$ over the NEB and multiplying by τ_i^2, which is the gain of $|H_{id}^{eq}(f)|^2$.

$$\frac{1}{4}(G_s\tau_i)^2\int_{-1/2\tau_i}^{1/2\tau_i} S_L(f)\,df = \frac{f_o}{2}(G_s\tau_i\rho\lambda_p)^2\int_0^{1/2\tau_i}\frac{1}{\sqrt{f_o^2+f^2}}\,df$$

$$\begin{aligned}\sigma_{f=0}^2 &= \frac{f_o}{2}(G_s\tau_i\rho\lambda_p)^2\left[\ln\left(\frac{1}{2\tau_i}+\sqrt{\left(\frac{1}{2\tau_i}\right)^2+f_o^2}\right)-\ln(f_o)\right]\\ \sigma_{f=0}^2 &= \frac{f_o}{2}(G_s\tau_i\rho\lambda_p)^2\ln\left(\frac{1}{\tau_i f_o}\right) = \frac{f_o}{2}(G_s\tau_i\rho\lambda_p)^2\ln\left(\frac{f_i}{f_o}\right)\end{aligned} \tag{6.29}$$

Equation 6.29 is derived by assuming that $1/(2\tau_i)$ is much larger than f_o, and f_i is substituted for $1/\tau_i$.

Since both the $1/f$ noise spectrum and the integrate and dump filter are even functions, the limits of integration can be shifted to determine the contribution of $1/f$ noise at $\pm f_s$. Figure 6.8(d) illustrates the integration limits that are used to determine the rest of the noise that is contributed by $S_L(f\pm f_s)$.

Mathematically, the associative law of convolution is used to switch the process order. Essentially, $|H_{id}^{eq}(f)|^2$ is convolved with $|Q(f)|^2$ and then the $1/f$ noise contribution at $\pm f_s$ is found. In order to account for the negative frequency contribution, integration of the positive frequency range, shown in Figure 6.8, is doubled.

$$2\left(\frac{G_s\tau_i}{\pi}\right)^2\int_{f_s-1/2\tau_i}^{f_s+1/2\tau_i} S_L(f)\,df \;=\; 2f_o\left(\frac{G_s\tau_i\rho\lambda_p}{\pi}\right)^2\int_{f_s-1/2\tau_i}^{f_s+1/2\tau_i}\frac{1}{\sqrt{f_o^2+f^2}}\,df$$

Since $(f_s - 1/2\tau_i) \gg f_o$, the noise contribution from the $1/f$ noise at $\pm f_s$ is,

$$\sigma^2_{\pm f_s} \;=\; 2f_o\left(\frac{G_s\tau_i\rho\lambda_p}{\pi}\right)^2\ln\left(\frac{2f_s+f_i}{2f_s-f_i}\right). \tag{6.30}$$

The total $1/f$ noise power at the output of $|H_g(f)|^2$ is the sum of equations 6.29 and 6.30.

$$\sigma^2_{Lg} \;=\; 2f_o\left(G_s\tau_i\rho\lambda_p\right)^2\left[\frac{1}{4}\ln\left(\frac{f_i}{f_o}\right)+\frac{1}{\pi^2}\ln\left(\frac{2f_s+f_i}{2f_s-f_i}\right)\right] \tag{6.31}$$

6.6 Modulation Depth Determination

When operating the imaging system in the gated integrator mode, at least two frames are required to determine the modulation depth. The first frame, Y^2_{on} includes the signal, and the second frame, Y^2_{off}, does not. The noise components included in each frame are the photon noise, σ^2_{Wg}, $1/f$ noise, σ^2_{Lg}, and the imaging system's read noise, σ^2_r. The noise components in different frames are assumed to be completely uncorrelated.

$$Y^2_{\text{on}} \;=\; \left(\overline{Y_{\text{A}g}}\right)^2 \;+\; \left(\overline{Y_{Bg}}\right)^2 \;+\; \sigma^2_{Wg} \;+\; \sigma^2_{Lg} \;+\; \sigma^2_r \tag{6.32}$$

$$Y^2_{\text{off}} \;=\; \left(\overline{Y_{Bg}}\right)^2 \;+\; \sigma^2_{Wg} \;+\; \sigma^2_{Lg} \;+\; \sigma^2_r \tag{6.33}$$

The mean-square value of the modulation depth is then determined by subtracting Y^2_{off} from Y^2_{on} and then dividing the result by Y^2_{off}. Using σ^2_{Tg} as the sum of the

three noise components,

$$\sigma_{Tg}^2 = \sigma_{Wg}^2 + \sigma_{Lg}^2 + \sigma_r^2 , \tag{6.34}$$

the mean-squared modulation depth is,

$$\begin{aligned} \overline{\alpha_{mod}^2} &= \frac{Y_{\text{on}}^2 - Y_{\text{off}}^2}{Y_{\text{off}}^2} \\ \overline{\alpha_{mod}^2} &= \frac{\left[\left(\overline{Y_{\text{A}g}}\right)^2 + \left(\overline{Y_{Bg}}\right)^2 + \sigma_{Tg}^2\right] - \left[\left(\overline{Y_{Bg}}\right)^2 + \sigma_{Tg}^2\right]}{\left[\left(\overline{Y_{Bg}}\right)^2 + \sigma_{Tg}^2\right]} \end{aligned} \tag{6.35}$$

The square of the mean modulation depth is found by eliminating the noise components from the equation above.

$$\begin{aligned} \left(\overline{\alpha_{mod}}\right)^2 &= \frac{\left[\left(\overline{Y_{\text{A}g}}\right)^2 + \left(\overline{Y_{Bg}}\right)^2\right] - \left[\left(\overline{Y_{Bg}}\right)^2\right]}{\left(\overline{Y_{Bg}}\right)^2} \\ \left(\overline{\alpha_{mod}}\right)^2 &= \frac{\left(\overline{Y_{\text{A}g}}\right)^2}{\left(\overline{Y_{Bg}}\right)^2} = \frac{\frac{1}{4}\left(G_s\tau_i\alpha\lambda_p\right)^2}{\frac{1}{4}\left(G_s\tau_i\rho\lambda_p\right)^2} = \frac{\alpha^2}{\rho^2} \end{aligned} \tag{6.36}$$

If the integration threshold is not used and $\rho = 1$, then the modulation depth is the square root of equation 6.36. If, however, the integration threshold feature is utilized, the value of ρ must be known in order to calculate the modulation depth.

The modulation depth that is determined with Y_{on}^2 and Y_{off}^2 also has a variance, σ_{mod}^2, that is a function of the photon noise, $1/f$ noise, and read noise. Based on the propagation of errors, the modulation depth variance is (Bevington & Robinson,

1992),

$$\begin{aligned}
\frac{\sigma_{mod}^2}{\left(\overline{\alpha_{mod}}\right)^2} &= \frac{\sigma_{Tg}^2}{\left(\overline{Y_{\mathrm{A}g}}\right)^2} + \frac{\sigma_{Tg}^2}{\left(\overline{Y_{Bg}}\right)^2} \\
\sigma_{mod}^2 &= \left[\frac{\left(\overline{Y_{\mathrm{A}g}}\right)^2}{\left(\overline{Y_{Bg}}\right)^2}\right]\left[\frac{\sigma_{Tg}^2}{\left(\overline{Y_{\mathrm{A}g}}\right)^2} + \frac{\sigma_{Tg}^2}{\left(\overline{Y_{Bg}}\right)^2}\right] \\
\sigma_{mod}^2 &= \frac{\left(\overline{Y_{Bg}}\right)^2 \sigma_T^2 \; + \; \left(\overline{Y_{\mathrm{A}g}}\right)^2 \sigma_T^2}{\left(\overline{Y_{Bg}}\right)^4}
\end{aligned} \tag{6.37}$$

The "modulation depth-to-noise ratio" (MDNR) is the ratio of the square of the mean modulation depth to the modulation depth variance. Assuming that ρ is equal to one, the MDNR is,

$$\begin{aligned}
\mathrm{MDNR}_g &= \frac{\left(\overline{\alpha_{mod}}\right)^2}{\sigma_{mod}^2} = \left[\frac{\left(\overline{Y_{\mathrm{A}g}}\right)^2}{\left(\overline{Y_{Bg}}\right)^2}\right]\left[\frac{\left(\overline{Y_{Bg}}\right)^4}{\left(\overline{Y_{Bg}}\right)^2 \sigma_T^2 \; + \; \left(\overline{Y_{\mathrm{A}g}}\right)^2 \sigma_T^2}\right] \\
\mathrm{MDNR}_g &= \frac{\left(\overline{Y_{\mathrm{A}g}}\right)^2}{\sigma_T^2 \; + \; \left(\overline{\alpha_{mod}}\right)^2 \sigma_T^2} \approx \frac{\left(\overline{Y_{\mathrm{A}g}}\right)^2}{\sigma_T^2}
\end{aligned} \tag{6.38}$$

If the modulation depth is small, the MDNR can be approximated, as shown in equation 6.38. This approximation is, simply, the signal-to-noise ratio (SNR) of Y_{on}^2.

6.7 Signal-To-Noise Ratio

The signal-to-noise ratio (SNR) of a frame which includes the information bearing signal is given in equation 6.39. The SNR shown is per pixel and per frame.

$$\mathrm{SNR}_g = \frac{\left(\overline{Y_{\mathrm{A}g}}\right)^2}{\sigma_W^2 \; + \; \sigma_L^2 \; + \; \sigma_r^2} \tag{6.39}$$

Once the accumulation of photoelectrons surpass the read noise floor, the image is limited by photon noise (see section 5.10.10). Assuming the acquired photoelectrons

exceed the read noise floor, using equations 6.20, 6.25, and 6.31, the SNR is,

$$\mathrm{SNR}_g = \frac{\frac{1}{4}\left(G_s\tau_i\alpha\lambda_p\right)^2}{\frac{1}{2}G_s^2\tau_i\rho\lambda_p + 2f_o\left(G_s\tau_i\rho\lambda_p\right)^2\left[\frac{1}{4}\ln\left(\frac{f_i}{f_o}\right) + \frac{1}{\pi^2}\ln\left(\frac{2f_s+f_i}{2f_s-f_i}\right)\right]} \tag{6.40}$$

After factoring out G_s and dividing by both τ_i and λ_p, the SNR at the output of $|H_g(f)|^2$ is,

$$\mathrm{SNR}_g = \frac{(\alpha)^2}{2\rho\left(\tau_i\lambda_p\right)^{-1} + 8f_o\rho^2\left[\frac{1}{4}\ln\left(\frac{f_i}{f_o}\right) + \frac{1}{\pi^2}\ln\left(\frac{2f_s+f_i}{2f_s-f_i}\right)\right]}, \tag{6.41}$$

which is, again, the SNR for a single pixel in a single frame.

The SNR can be improved by averaging multiple pixels or multiple frames, or both. In general, the variance from n statistically independent samples is (Cooper & McGillem, 1999),

$$\begin{aligned}
\mathrm{Var}(\mathrm{X}) &= \frac{1}{n^2}\sum_{i=1}^{N}\sum_{j=1}^{N}\mathrm{E}\left[\mathrm{X}_i\cdot\mathrm{X}_j\right] - \left(\overline{\mathrm{X}}\right)^2 \\
\mathrm{Var}(\mathrm{X}) &= \frac{1}{n^2}\left[n\overline{\mathrm{X}^2} + \left(n^2-n\right)\left(\overline{\mathrm{X}}\right)^2\right] - \left(\overline{\mathrm{X}}\right)^2 \\
\mathrm{Var}(\mathrm{X}) &= \frac{\overline{\mathrm{X}^2} - \left(\overline{\mathrm{X}}\right)^2}{n} = \frac{\sigma_{\mathrm{X}}^2}{n}
\end{aligned} \tag{6.42}$$

Using n_p as the number of statistically independent pixels and n_f as the number of statistically independent frames, the SNR can be improved by a factor of $n_p \cdot n_f$.

$$\mathrm{SNR}_g = \frac{\left(n_p\cdot n_f\right)(\alpha)^2}{2\rho\left(\tau_i\lambda_p\right)^{-1} + 8f_o\rho^2\left[\frac{1}{4}\ln\left(\frac{f_i}{f_o}\right) + \frac{1}{\pi^2}\ln\left(\frac{2f_s+f_i}{2f_s-f_i}\right)\right]} \tag{6.43}$$

Based on equation 6.43, the SNR can be improved either by averaging or by using the integration threshold. The SNR improvement gained from using the inte-

gration threshold feature is shown in Figure 6.9. The SNR is given in decibels (dB), which is $10\log_{10}(SNR_g)$. In this figure, it is apparent that as ρ approaches 0, SNR improvement is achieved.

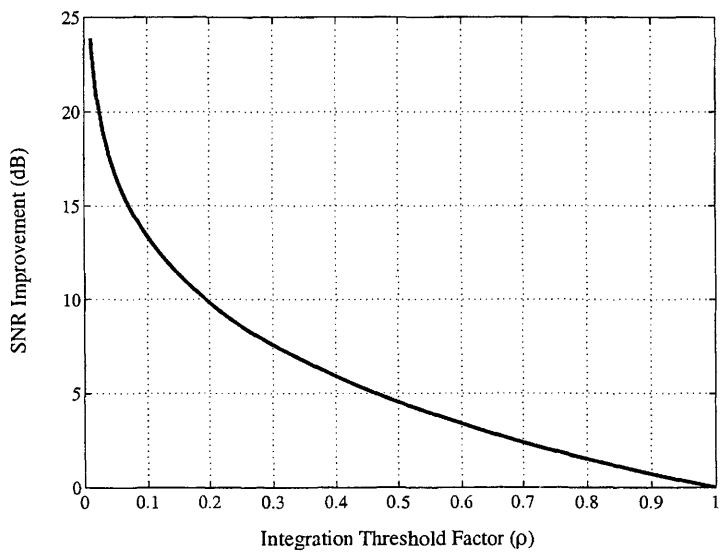

FIG. 6.9. SNR improvement gained from integration threshold factor, ρ

If it were possible, in an ideal case, to set ρ to zero, all of the background irradiance would be removed. It is not incorporated into the mathematical model, but if all the background were removed, the SNR of the output would be limited to the photon noise contained in the information bearing signal. Completely removing the steady state background is, however, impractical and ρ will not approach zero.

The SNR is also improved through temporal averaging. Gathering multiple frames and then calculating the average will improve the SNR by the number of frames gathered. Giving up spatial resolution and averaging multiple pixels together is also an effective way to improve the SNR. Figure 6.10 shows the SNR improvement, in dB, that is gained from a combination of pixel averaging and frame averaging. As an example, averaging 500 pixels and 500 frames would improve the SNR by 50dB.

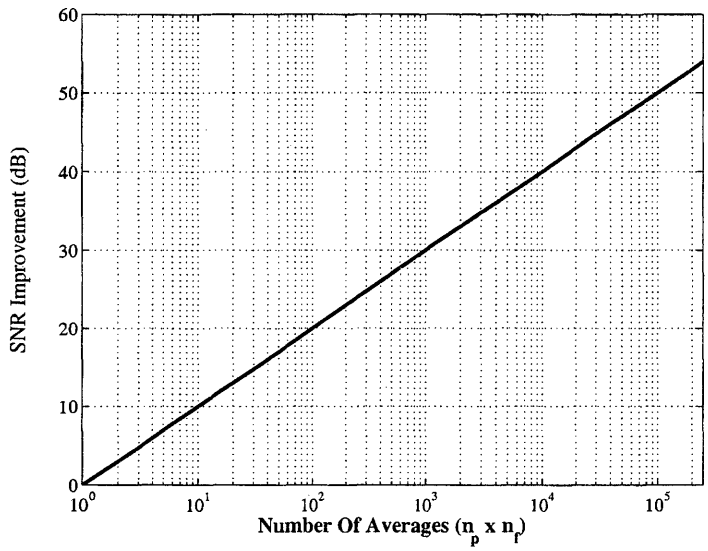

FIG. 6.10. SNR improvement gained from averaging $(n_p \cdot n_f)$

6.8 Detection Limits

The expected modulation depth detection limits for the gated integrator are presented in this section. In order to benchmark the detection limits, a comparison is made with a simple lock-in amplifier detection process. The simple lock-in amplifier, which is a basic homodyne detector, is derived in Appendix H.

Using an input spectrum, $S_T(f)$, that includes a modulated information bearing signal, $S_{\mathrm{Ap}}(f)$, the SNR at the output of the homodyne detection process is,

$$\mathrm{SNR}_o = \frac{(\alpha)^2}{\pi^3 f_c \epsilon I_p^{-1} + \pi^2 f_o \ln\left(\frac{2f_d+\pi f_c}{2f_d-\pi f_c}\right)} . \tag{6.44}$$

Derivation of the individual components is included in Appendix H.

The SNR from $|H_g(f)|^2$, given in equation 6.43 is a function of λ_p, which is multiplied by τ_i to account for the CCD's maximum well depth. Maximizing $(\tau_i \cdot \lambda_p)$ will reduce the photon noise component and, therefore, increase the SNR. Because

of the CCD has a limited well depth, $(\tau_i \cdot \lambda_p)$ has a maximum value. Since λ_p is the arrival rate of photons, the product of τ_i and λ_p must be,

$$\tau_i \lambda_p \leq \frac{e_{sat}}{\eta} \tag{6.45}$$

where e_{sat} is the electron saturation limit and η is the CCD's quantum efficiency for the particular wavelength of λ_p. The maximum value of $\tau_i \cdot \lambda_p$ is about 4.3x10^5, which is based on an e_{sat} of 34,000 electrons, and an η of 0.08 at 770nm. The quantum efficiency, η, is determined from the CCD's quantum efficiency curve, which is included in Appendix C.

In order to make a fair comparison between SNR_g, from equation 6.43, and SNR_o, from equation 6.44, a relationship between variables needs to be specified. First, the steady state background, I_p, in SNR_o is set to,

$$I_p = \frac{\epsilon \cdot e_{sat}}{\tau_i \cdot \eta} \tag{6.46}$$

which is a rearrangement of equation 6.45 that includes a substitution of I_p/ϵ for λ_p. The minimum value of τ_i is about 1μsec, which produces an I_p of 1.11x10^{-7} watts.

The frequency components of SNR_g and SNR_o are also related for a fair comparison. The demodulation frequency, f_d, in SNR_o is set equal to the sampling frequency, f_s, in SNR_g. And finally, the noise equivalent bandwidth of the lowpass filter, from Appendix H, is set equal to the noise equivalent bandwidth of the integrate and dump filter. The lowpass filter cutoff frequency is, therefore, set to,

$$f_c = \frac{1}{\pi \tau_i} \quad \text{or} \quad \frac{f_i}{\pi} \tag{6.47}$$

where $f_i = 1/\tau_i$.

The expected SNR, as a function of modulation depth, for both the gated integrator and the homodyne detector are shown in Figure 6.11. The parameter values used in Figure 6.11 are,

- $\tau_i = 1\text{x}10^{-3}$,
- $I_p = 1.109\text{x}10^{-10}$,
- $(\tau_i \lambda_p) = 429800$,
- $f_c = 318.3$,
- $f_d = f_s = 4000$,
- $f_o = 1.29\text{x}10^{-7}$,
- $\rho = 1$, and
- $(n_p \cdot n_f) = 1$.

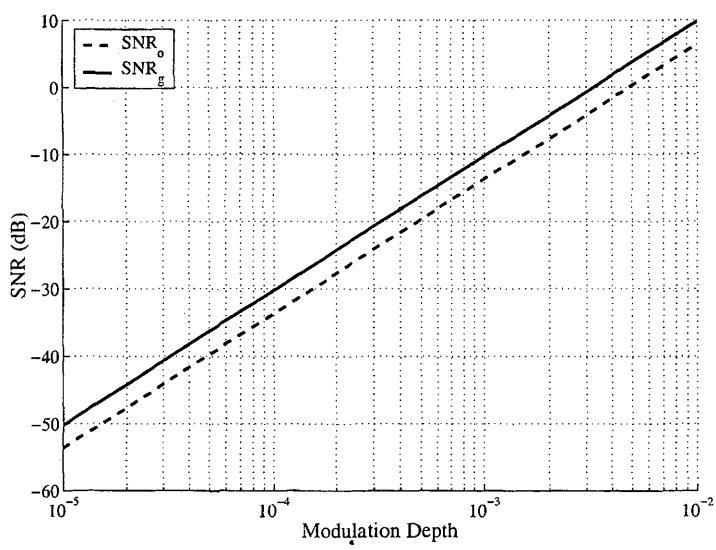

FIG. 6.11. Comparison of SNR_g with SNR_o using the same parameters

When the parameter values are comparable, as shown in Figure 6.11, SNR_g is slightly higher than SNR_o. This is because the signal power at the output of the gated integrator is larger than the signal power at the output of the homodyne detector. Half of the input signal power is obtained at the output of the gated integrator. The homodyne detector, on the other hand, captures half of the input's fundamental harmonic power at the output.

The imaging system has a limited well depth, which limits the number of photoelectrons that can be acquired prior to saturation. A lock-in amplifier, however, does not have such a constraint and would not be operated with the settings used in Figure 6.11.

Figure 6.12 shows SNR_o with I_p set to $1\mathrm{x}10^{-6}$ and f_c set to 10Hz. The parameter values for SNR_g remain the same as in Figure 6.11, because they are set to their limits. It is apparent from Figure 6.12 that the SNR of the homodyne detector improves dramatically when the input is unconstrained. A homodyne detector, such as a lock-in amplifier does not, however, have the ability to produce two-dimensional images.

6.8.1 Detection Summary

The SNR of the gated integrator can be improved with both the integration threshold feature and averaging. Figure 6.13 illustrates the SNR improvement that is obtained with the integration threshold feature. The integration threshold coefficient, ρ, is set to values less than one and equation 6.43 is plotted in Figure 6.13. The product $(n_p \cdot n_f)$, in equation 6.43, is held at unity in Figure 6.13.

The SNR improvement from averaging is illustrated in Figure 6.14. The product of n_p and n_f is varied and plotted, using equation 6.14, with ρ set to one. Figure 6.14

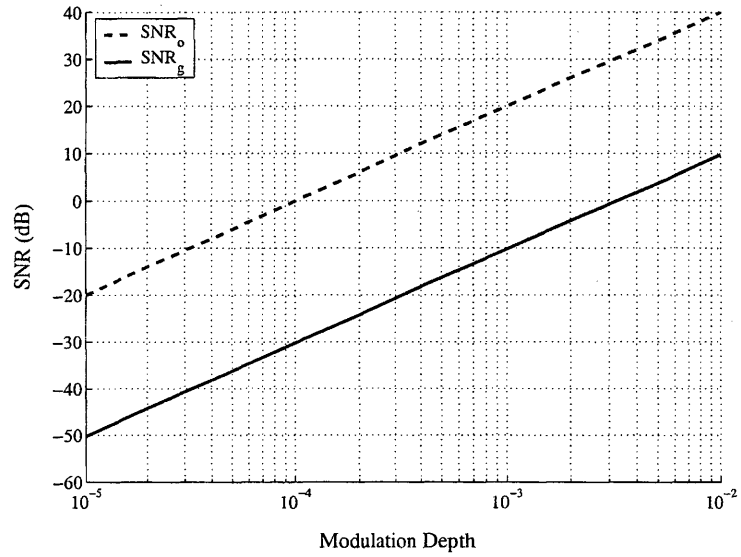

FIG. 6.12. Comparison of SNR_g with SNR_o using different constraints

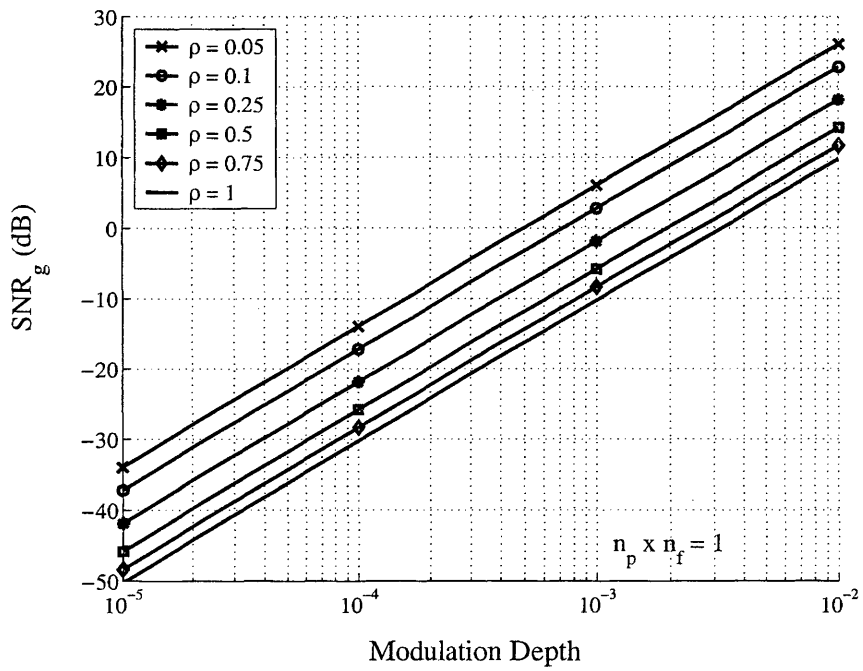

FIG. 6.13. Predicted SNR improvement when utilizing the integration threshold mechanism

shows that approximately 250,000 averages are needed to obtain an SNR of over 20dB at a modulation depth of 10^{-4}.

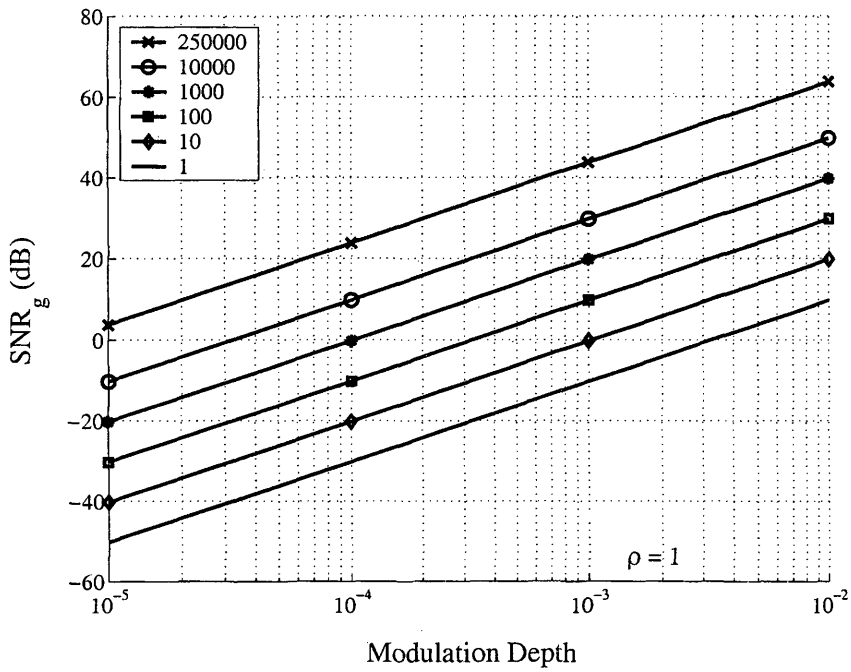

FIG. 6.14. Predicted SNR improvement when averaging

Chapter 7

HETERODYNE DETECTION SYSTEM MODEL

7.1 General Introduction

The second detection mode, the heterodyne detection mode, is analyzed in this chapter. When operating the imaging system in a heterodyne detection mode, the sampling frequency represented in the natural sampling function, $|Q(f)|^2$, is different than the modulation frequency, f_m, that is used in modulating the information bearing signal. In this mode, the modulated signal at f_m is mixed down to an intermediate frequency (IF) that is above the baseband but lower than the imaging system's frame rate. Heterodyne detection and the concept of an intermediate frequency was introduced in section 4.4.2.

Once at the intermediate frequency, the information bearing signal then oscillates over multiple frames. In order to extract, from a series of frames, the information bearing signal and the background as separate components, a final set of post processing functions are utilized. After separating the background and signal, the modulation depth is determined.

The analysis results, presented at the end of this chapter, indicate the heterodyne detection mode is not well suited for extracting weakly modulated images to measure modulation depth. The analysis in this chapter, therefore, demonstrates that other detection modes should be used when measuring very small modulation depths. Other applications, however, can benefit from an imaging system that is capable of

performing heterodyne detection. As an example, a heterodyne imaging system can extract interference patterns that can enhance industrial object recognition systems. The work presented in this chapter can, therefore, be a basis for other investigations on heterodyne detection imaging systems and their application.

7.2 Heterodyne Detection Model

The system function that describes the heterodyne detection process is divided into two stages. The first stage includes image capture functions performed by the imaging system. The second stage is comprised of post processing functions that are used to extract the desired components.

The first stage of the detection process includes a natural sampling process, $|Q(f)|^2$, an integrate and dump filter, $|H_{id}(f)|^2$, and a sample and hold filter, $|H_{sh}(f)|^2$. The image capture stage and the post processing stage of the heterodyne detection process are illustrated in Figure 7.1. Both $|Q(f)|^2$ and $|H_{id}(f)|^2$ are the same as equations 6.3 and 6.5 respectively.

In order to filter the data contained over consecutive frames the sample and hold filter is included in the heterodyne detection system function. The sample and hold filter, $|H_{sh}(f)|^2$, filters the imaging system output at the system's frame rate. The frame rate is defined as f_f, which is expressed in $|H_{sh}(f)|^2$ as T_f or $1/f_f$. The addition of the sample and hold filter completes the first stage of the heterodyne processing chain, which is illustrated in Figure 7.1.

7.2.1 Sample And Hold Filter

The sample and hold filter, which is modeled as a lowpass filter, is an additional filter included in the system function to represent the heterodyne detection process.

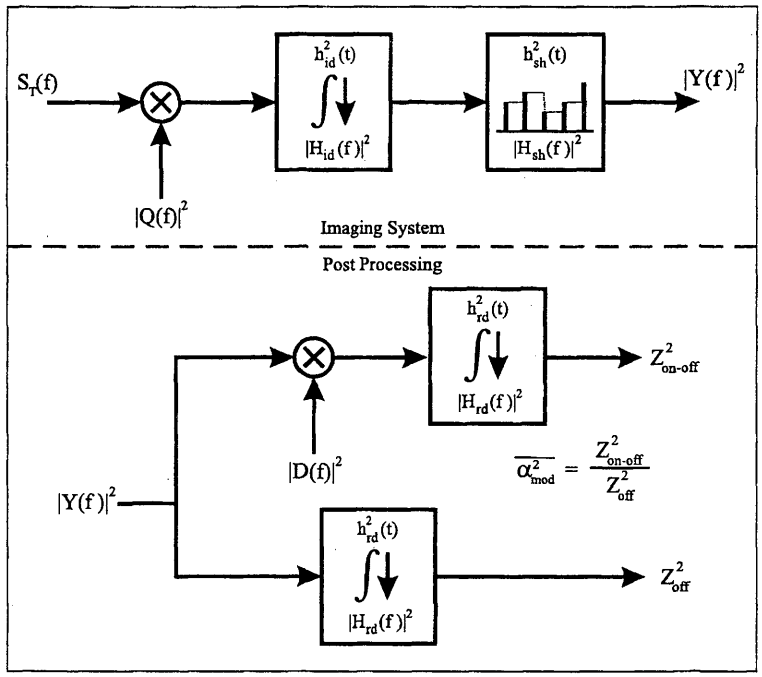

FIG. 7.1. Block diagram of the imaging system operated as a heterodyne detector with post processing functions

A mathematical description of the sample and hold filter is developed in appendix G.

From appendix G, the power transfer function, $|H_{sh}(f)|^2$, for the sample and hold filter is,

$$|H_{sh}(f)|^2 = |\mathrm{Sa}(\pi f T_f)|^2 \tag{7.1}$$

where T_f is the imaging system's frame period. The frame period is the inverse of the frame rate, f_f. The sample and hold filter's power transfer response, given in equation 7.1, is illustrated in Figure 7.2.

Filter Characteristics Much like the integrate and dump filter, the sample and hold filter has peaks and troughs across the frequency spectrum. The zeros can,

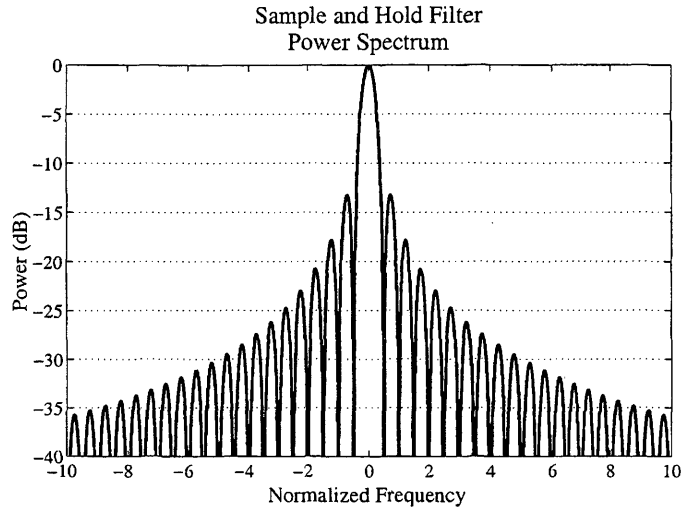

FIG. 7.2. Sample and hold filter power response

again, be used to eliminate power at specific frequencies in the output of the sample and hold filter. As shown in Figure 7.2, the sample and hold filter has peaks at,

$$\pm f = \frac{1 + 2r}{2T_f} \quad \text{where } r = 0, 1, 2, ... \tag{7.2}$$

and has zeros at,

$$\pm f = \frac{1 + r}{T_f} \quad \text{where } r = 0, 1, 2, ... \tag{7.3}$$

Noise Equivalent Filter The noise equivalent bandwidth (NEB) for the sample and hold filter is very similar to the integrate and dump filter's NEB. The NEB for the sample and hold filter, defined as B_{sh}, is equal to $1/(2T_f)$. The noise equivalent filter, $H_{sh}^{eq}(f)$, is, therefore,

$$|H_{sh}^{eq}(f)|^2 = \prod\left(\frac{f}{2B_{sh}}\right) = \prod(f\,T_f) = \prod\left(\frac{f}{f_f}\right) \tag{7.4}$$

7.2.2 Post Processing

Depending on the desired output, the demodulation function, $|D(f)|^2$, is either included or excluded from the second processing stage. Including $|D(f)|^2$ results in an output that does contain the information bearing signal. Processing the imaging system output, $|Y(f)|^2$, with $|D(f)|^2$ transfers the signal from the intermediate frequency to the baseband. At the same time, $|D(f)|^2$ also transfers the background component to the intermediate frequency. Once the signal is at the baseband, and the background is at the intermediate frequency, a final integrate and dump filter can be used to eliminate the background and retain only the signal.

Excluding $|D(f)|^2$ results in an output that does not contain the signal and only contains the background component. By not using $|D(f)|^2$ and leaving the signal at the IF, the signal is eliminated by the downstream integrate and dump filter. The signal and the background are, therefore, separated with the second processing stage through demodulation and filtering, as illustrated in Figure 7.1.

A simple homodyne detection process is included in appendix H for comparison with the other detection methods. This appendix includes further discussion on $|D(f)|^2$. The power spectrum of $|D(f)|^2$, used in this section, is,

$$|D(f)|^2 = \frac{G_d^2}{4}\delta(f + f_d) + \frac{G_d^2}{4}\delta(f - f_d) \tag{7.5}$$

where G_d is the amplitude of the sinusoidal demodulation function and f_d is the demodulation frequency.

The integrate and dump filter $|H_{rd}|^2$ is the same as the filter discussed in ap-

pendix F with different variables. The power spectrum of $|H_{rd}(f)|^2$ is,

$$|H_{rd}(f)|^2 = \tau_r^2 \left|\mathrm{Sa}(\pi f \tau_r)\right|^2 \tag{7.6}$$

where τ_r is the integration time of the filter.

Also discussed in appendix F is the noise equivalent bandwidth of an integrate and dump filter. Based on this discussion, the NEB of $|H_{rd}(f)|^2$ is $1/(2\tau_r)$ and the noise equivalent filter is,

$$|H_{rd}^{eq}(f)|^2 = \tau_r^2 \prod (f \cdot \tau_r) = \tau_r^2 \prod \left(\frac{f}{f_r}\right) \tag{7.7}$$

where $f_r = 1/\tau_r$.

7.2.3 System Function

Two effective system functions are defined to identify the two different paths in the second processing stage. The system function that includes $|D(f)|^2$ is defined as $|H_e(f)|^2$ and the system function that excludes $|D(f)|^2$ is defined as $|H_{ge}(f)|^2$. The subscript g is used in $|H_{ge}(f)|^2$, since excluding $|D(f)|^2$ results in a gated integrator system function that is similar to the one presented in Chapter 6, albeit with additional filters.

Applying an input spectrum to each of the effective system functions produces different outputs, which are diagrammed in Figure 7.3. Applying $S_T(f)$ to $|H_e(f)|^2$ produces $Z^2_{\text{on-off}}$ and applying $S_T(f)$ to $|H_{ge}(f)|^2$ produces Z^2_{off}.

$$Z^2_{\text{on-off}} = |H_{rd}(f)|^2 \left\{ \left[|H_{sh}(f)|^2 |H_{id}(f)|^2 \left(S_T(f) * |Q(f)|^2\right) \right] * |D(f)|^2 \right\} \tag{7.8}$$

$$Z^2_{\text{off}} = |H_{rd}(f)|^2 |H_{sh}(f)|^2 |H_{id}(f)|^2 \left(S_T(f) * |Q(f)|^2\right) \tag{7.9}$$

Both $Z^2_{\text{on-off}}$ and Z^2_{off} are defined below.

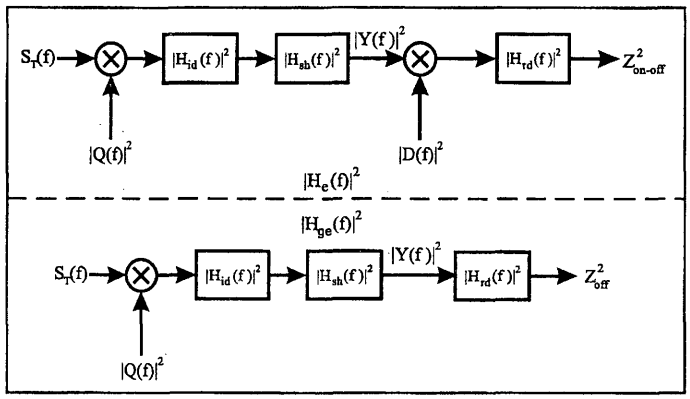

FIG. 7.3. Processing with and without $|D(f)|^2$

Applying an input spectrum, $S_T(f)$, to each of the system functions produces different results at the output, $|Z(f)|^2$. Applying $S_T(f)$ to $|H_e(f)|^2$ produces an output spectrum that is the combination of signal, photon noise, and $1/f$ noise.

$$S_T(f)|H_e(f)|^2 \;=\; |Z_{\text{A}e}(f)|^2 \;+\; |Z_{We}(f)|^2 \;+\; |Z_{Le}(f)|^2 \tag{7.10}$$

Similarly, applying $S_T(f)$ to $|H_{ge}|^2$, from equation 7.9, produces a combination of steady state background, photon noise, and $1/f$ noise.

$$S_T(f)|H_{ge}(f)|^2 \;=\; |Z_{Bge}(f)|^2 \;+\; |Z_{Wge}(f)|^2 \;+\; |Z_{Lge}(f)|^2 \tag{7.11}$$

Including $|D(f)|^2$ in $|H_e(f)|^2$ makes it possible to filter out the steady state background with $|H_{rd}|^2$. When $|D(f)|^2$ is excluded, however, the background power is retained and the signal is eliminated with $|H_{rd}(f)|^2$. Since no signal is contained in the output of $|H_{ge}(f)|^2$, the power at this output is defined as Z^2_{off}, which maintains the notation convention used in section 6.6. The power out of $|H_e(f)|^2$, which does

contain signal and does not contain background power, is defined as $Z^2_{\text{on-off}}$. Both outputs are illustrated in Figure 7.3.

Based on the output definitions, the modulation depth can be determined by dividing $Z^2_{\text{on-off}}$ by Z^2_{off}. The output of both $|H_e(f)|^2$ and $|H_{ge}(f)|^2$ contain noise as well, thus, dividing the power from each system function produces the mean-square value of the modulation depth, $\overline{\alpha^2_{mod}}$.

$$\overline{\alpha^2_{mod}} = \frac{Z^2_{\text{on-off}}}{Z^2_{\text{off}}} = \frac{\left(\overline{Z_{\text{Ae}}}\right)^2 + \sigma^2_{We} + \sigma^2_{Le} + \sigma^2_r}{\left(\overline{Z_{Bge}}\right)^2 + \sigma^2_{Wge} + \sigma^2_{Lge} + \sigma^2_r} \tag{7.12}$$

Since the imaging system's read noise, σ^2_r, is added per frame and both $Z^2_{\text{on-off}}$ and Z^2_{off} are determined from the same set of frames, the read noise in $Z^2_{\text{on-off}}$ and Z^2_{off} is correlated. When determining the modulation depth variance, the read noise will, therefore, be eliminated since the squared terms will be cancelled by the cross product terms (Bevington & Robinson, 1992).

Both the photon noise and the $1/f$ noise, however, do not cancel in equation 7.12. The noise power from $|H_e(f)|^2$ and $|H_{ge}(f)|^2$ is determined from different frequency bands. The photon noise and $1/f$ noise at different bands of frequency is uncorrelated and, therefore, does not cancel in equation 7.12. The mean-squared value of the modulation depth reduces to the following equation.

$$\overline{\alpha^2_{mod}} = \frac{Z^2_{\text{on-off}}}{Z^2_{\text{off}}} = \frac{\left(\overline{Z_{\text{Ae}}}\right)^2 + \sigma^2_{We} + \sigma^2_{Le}}{\left(\overline{Z_{Bge}}\right)^2 + \sigma^2_{Wge} + \sigma^2_{Lge}} \tag{7.13}$$

7.2.4 Input Review

The modulated signal spectrum is captured by the heterodyne detection process, thus, the modulation is included in the input spectrum. The steady state background

and noise spectral components remain the same. The input spectrum is, therefore, the same as the spectrum given in equation 5.123.

The input signal is again defined as the constant value $\alpha\lambda_p$ and σ_{A}^2 is assumed to be zero. Modulation replicates $\alpha\lambda_p$ at the harmonics contained in the modulation waveform. The modulation waveform that is considered is the rectangular pulse train function, $m_p(t)$. The total input spectrum used in this chapter's analysis is,

$$\begin{aligned} S_T(f) &= S_B(f) + S_N(f) + S_{\mathrm{Ap}}(f) \\ S_T(f) &= (\lambda_p)^2\,\delta(f) + \frac{(\lambda_p)^2}{\sqrt{1+\left(\frac{f}{f_o}\right)^2}} + \lambda_p \\ &\quad + (\alpha\lambda_p\psi_m)^2 \sum_{m=-\infty}^{\infty} |\mathrm{Sa}\,(\pi n\psi_m)|^2\,\delta(f - mf_m)\,. \end{aligned} \tag{7.14}$$

7.3 Heterodyne System Output Without Demodulation

The system function, $|H_{ge}(f)|^2$, is very similar to the system function that was used in section 6.4. In this section, $|H_{sh}(f)|^2$ and $|H_{rd}|^2$ are included to create $|H_{ge}(f)|^2$. Using these additional filters, the output of $|H_{ge}(f)|^2$ is,

$$\begin{aligned} |Z_T(f)|^2 &= |H_{rd}(f)|^2|H_{sh}(f)|^2|H_{id}(f)|^2\left(S_T(f) * |Q(f)|^2\right) \\ |Z_T(f)|^2 &= \tau_r^2\,|\mathrm{Sa}(\pi f\tau_r)|^2\,|\mathrm{Sa}(\pi fT_f)|^2\,\tau_i^2\,|\mathrm{Sa}(\pi f\tau_i)|^2 \\ &\quad \times \psi_s^2 \sum_{n=-\infty}^{\infty} |\mathrm{Sa}\,(\pi n\psi_s)|^2\,S_T(f - nf_s) \end{aligned} \tag{7.15}$$

when applying $S_T(f)$ to the input.

The noise equivalent filter for the combination of $|H_{rd}(f)|^2$, $|H_{sh}(f)|^2$, and $|H_{id}(f)|^2$ can be used to determine the noise power at the output of $|H_{ge}(f)|^2$. The integrate and dump filter, $|H_{rd}(f)|^2$, has a noise equivalent bandwidth (NEB) that is less than

the NEB for both $|H_{sh}(f)|^2$ and $|H_{id}(f)|^2$. The final integrate and dump filter, therefore, removes noise power that passes through the two other filters, which means that the NEB for $|H_{rd}(f)|^2$ is also the NEB for the combination of filters.

The gain of all three filters is included in the noise equivalent filter for the combination of filters. Since the NEB of $|H_{rd}(f)|^2$ is $1/(2\tau_r)$ (or $f_r/2$), the total noise equivalent filter is,

$$|H_{ge}^{eq}(f)|^2 = (\tau_r\tau_i)^2 \prod (\tau_r \cdot f) = (\tau_r\tau_i)^2 \prod \left(\frac{f}{f_r}\right) \tag{7.16}$$

where τ_r^2 is the gain of $|H_{rd}(f)|^2$ and τ_i^2 is the gain of $|H_{id}(f)|^2$ (the gain of $|H_{sh}(f)|^2$ is one).

In the following subsections, each component of $S_T(f)$, except for the signal component, is applied to $|H_{ge}(f)|^2$. The total output of $|H_{ge}(f)|^2$ is then developed through the use of superposition.

7.3.1 Background Output

The steady state background is a constant for all time and its spectrum, $S_B(f)$, is $(\lambda_p)^2\delta(f)$. Applying $S_B(f)$ to $|H_{ge}(f)|^2$ produces the same result that was shown in equation 6.22, with a difference in gain. The gain changes because of the additional filters. The spectral output of $|H_{ge}(f)|^2$, in this case, is,

$$|Z_{Bge}(f)|^2 = \frac{1}{4}(G_s\tau_r\tau_i\lambda_p)^2\delta(f) \tag{7.17}$$

which assumes that ψ_s, the sampling function's duty cycle, is 50% and the imaging system's gain is G_s. Since the output is simply a delta function at $f = 0$, the power

at the output is the square of the mean background.

$$\left(\overline{Z_{Bge}}\right)^2 = \frac{1}{4}(G_s\tau_r\tau_i\lambda_p)^2 \tag{7.18}$$

7.3.2 Photon Noise Output

The photon noise power and $1/f$ noise power out of $|H_{ge}(f)|^2$ are also similar to the noise power derived in section 6.5.3. As shown in section 6.5.3, sampling photon noise with $|Q(f)|^2$ results in half the photon noise power when ψ_s is 50%. Under this assumption, the photon noise spectrum at the output of $|H_{ge}(f)|^2$ is,

$$|Z_{Wge}(f)|^2 = \frac{1}{2}\lambda_p\left(G_s\tau_r\tau_i\right)^2|\mathrm{Sa}(\pi f\tau_r)|^2|\mathrm{Sa}(\pi fT_f)|^2|\mathrm{Sa}(\pi f\tau_i)|^2 \tag{7.19}$$

Using the noise equivalent filter given in equation 7.16, the photon noise power at the output of $|H_{ge}(f)|^2$ is,

$$\begin{aligned}\sigma^2_{Wge} &= \frac{1}{2}\lambda_p\left(G_s\tau_r\tau_i\right)^2\int_{-1/(2\tau_r)}^{1/(2\tau_r)} 1\cdot df \\ \sigma^2_{Wge} &= \frac{1}{2}\tau_r\lambda_p\left(G_s\tau_i\right)^2 .\end{aligned} \tag{7.20}$$

7.3.3 1/f Noise Output

Finally, the $1/f$ noise spectrum, $S_L(f)$, is applied to $|H_{ge}(f)|^2$ in this section. In doing so, $S_L(f)$ is first convolved with $|Q(f)|^2$. Just as in section 6.5.3, only the spectrum at dc and the spectra that are convolved to $\pm f_s$ by $|Q(f)|^2$ are considered. The $1/f$ noise that is convolved to the higher harmonics is considered negligible. The result of $S_L(f) * |Q(f)|^2$ is, therefore, the same as the result given in equation 6.27, assuming ψ_s is 50%.

Filtering equation 6.27 with $|H_{id}(f)|^2$, $|H_{sh}(f)|^2$, and $|H_{rd}(f)|^2$ provides the $1/f$ power spectrum at the output of $|H_{ge}(f)|^2$, which is,

$$\begin{aligned} |Z_{Lge}(f)|^2 &= (G_s\tau_r\tau_i)^2 \left|\mathrm{Sa}(\pi f\tau_r)\right|^2 \left|\mathrm{Sa}(\pi f T_f)\right|^2 \left|\mathrm{Sa}(\pi f\tau_i)\right|^2 \\ &\quad \times \left[\frac{1}{4}S_L(f) + \frac{1}{\pi^2}S_L(f+f_s) + \frac{1}{\pi^2}S_L(f-f_s)\right] . \end{aligned} \tag{7.21}$$

The $1/f$ noise power is also found using the same methodology that was outlined in section 6.5.3. The noise equivalent bandwidth is now changed to $1/(2\tau_r)$ and the gain is slightly different. Based on these changes, the $1/f$ noise power at the output of $|H_{ge}(f)|^2$ is,

$$\sigma^2_{Lge} = 2f_o\left(G_s\tau_r\tau_i\lambda_p\right)^2\left[\frac{1}{4}\ln\left(\frac{f_r}{f_o}\right) + \frac{1}{\pi^2}\ln\left(\frac{2f_s+f_r}{2f_s-f_r}\right)\right] . \tag{7.22}$$

7.3.4 Combined Output

The spectral output of $|H_{ge}(f)|^2$ is a combination of background, photon noise, and $1/f$ noise. Since the power out of $|H_{ge}(f)|^2$ contains only background power and no signal power, it has been defined as Z^2_{off}. Thus, Z^2_{off} is,

$$\begin{aligned} Z^2_{\text{off}} &= \left(\overline{Z_{Bge}}\right)^2 + \sigma^2_{Wge} + \sigma^2_{Lge} \\ Z^2_{\text{off}} &= (G_s\tau_r\tau_i)^2\left\{\frac{1}{4}\lambda_p^2 + \frac{\lambda_p}{2\tau_r}\right. \\ &\quad \left. + 2f_o\lambda_p^2\left[\frac{1}{4}\ln\left(\frac{f_r}{f_o}\right) + \frac{1}{\pi^2}\ln\left(\frac{2f_s+f_r}{2f_s-f_r}\right)\right]\right\} . \end{aligned} \tag{7.23}$$

7.4 Heterodyne System Output With Demodulation

In this section the demodulation function, $|D(f)|^2$ is included in the second stage of the detection process. When including $|D(f)|^2$, which changes the system function definition to $|H_e(f)|^2$, the output of the system function is,

$$|Z_T(f)|^2 = |H_{rd}(f)|^2 \left\{ \left[|H_{sh}(f)|^2 |H_{id}(f)|^2 \left(S_T(f) * |Q(f)|^2 \right) \right] * |D(f)|^2 \right\} . \quad (7.24)$$

In the following subsections, the signal and noise components of $S_T(f)$ are applied individually to $|H_e(f)|^2$. The total output power is, again, developed through superposition.

7.4.1 Signal Output

As $S_{\mathrm{Ap}}(f)$, from equation 7.14, enters the imaging system it is convolved with $|Q(f)|^2$. Since this mode is a heterodyne mode, the sampling frequency is different than the modulation frequency. Convolving $S_{\mathrm{Ap}}(f)$ with $|Q(f)|^2$ will transfer the signal in frequency to all of the sum and difference terms $\pm m f_m \pm n f_s$, where m and n are all integer values from $-\infty$ to ∞.

$$\begin{aligned} S_{\mathrm{Ap}}(f) * |Q(f)|^2 &= (\psi_m \psi_s \alpha \lambda_p)^2 \sum_{m=-\infty}^{\infty} \sum_{n=-\infty}^{\infty} |\mathrm{Sa}\,(\pi m \psi_m)|^2 \\ &\quad \times |\mathrm{Sa}\,(\pi n \psi_s)|^2 \, \delta(f - m f_m - n f_s) \end{aligned} \quad (7.25)$$

The intermediate frequency, f_I, which was introduced in section 4.4.2, is the absolute value of the difference of f_s and f_m, where $|m|$ and $|n|$ are both one. Convolving $S_{\mathrm{Ap}}(f)$ with $|Q(f)|^2$ will, therefore, transfer the signal component at f_m to the intermediate frequency, f_I. The intermediate frequency needs to be chosen in accordance

with downstream filtering processes to allow f_I to propagate to the output. If f_I is not properly set, downstream filtering may eliminate the desired signal component.

After filtering with $|H_{id}(f)|^2$ and $|H_{sh}(f)|^2$, the only components of $S_{\mathrm{Ap}}(f) * |Q(f)|^2$ that are not severely attenuated are the dc component and the difference terms between f_s and f_m. Incorporating the filters, the output of the imaging system is,

$$\begin{aligned}
|Y_{\mathrm{Ae}}(f)|^2 &= (G_s\tau_i\psi_m\psi_s\alpha\lambda_p)^2|\mathrm{Sa}(\pi f T_f)|^2|\mathrm{Sa}(\pi f\tau_i)|^2 \\
&\quad \times \sum_{n=-1}^{1} |\mathrm{Sa}\,(\pi n\psi_m)|^2\,|\mathrm{Sa}\,(\pi n\psi_s)|^2\,\delta(f+nf_m-nf_s) \\
|Y_{\mathrm{Ae}}(f)|^2 &= (G_s\tau_i\psi_m\psi_s\alpha\lambda_p)^2|\mathrm{Sa}(\pi f T_f)|^2|\mathrm{Sa}(\pi f\tau_i)|^2 \\
&\quad \times \sum_{n=-1}^{1} |\mathrm{Sa}\,(\pi n\psi_m)|^2\,|\mathrm{Sa}\,(\pi n\psi_s)|^2\,\delta(f-nf_I) \qquad (7.26)
\end{aligned}$$

The sample and hold filter, which has a smaller pass band than the integrate and dump filter, sets the limits on f_I. Actually, the limit is set by the imaging system's maximum frame rate, f_f, which is $1/T_f$. The maximum frame rate, for a very small region of interest (ROI), is approximately 30Hz. The first zero point in the sample and hold filter's spectrum, therefore, is at 30Hz.

In order for the signal, that is modulated at f_m, to pass through $|H_{sh}(f)|^2$, f_I in equation 7.26 must be less than 30Hz. As an alternative, the intermediate frequency can also be set greater than $1/T_f$ as long as it is set to one of the peaks in $|H_{sh}(f)|^2$. The intermediate frequency should, therefore, be set to,

$$f_I = |f_s - f_m| < \frac{1}{T_f} = f_f \qquad (7.27)$$

or

$$f_I = |f_s - f_m| = \frac{1+2r}{2\cdot T_f} \quad r = 0,1,2,... \qquad (7.28)$$

From equation 7.26, the only components from $S_{\mathrm{Ap}}(f) * |Q(f)|^2$ that will pass through $|H_{id}(f)|^2$ and $|H_{sh}(f)|^2$ without serious attenuation will be the dc term and the components at $|f_s - f_m|$. The product of the modulation function and the natural sampling function at $n = 0$, which is the dc term is one. Assuming both ψ_m and ψ_s are 50% the product of the modulation function and the natural sampling function at $\pm f_I$ is,

$$\psi_m^2 \left| \frac{\sin(\pi\psi_m)}{\pi\psi_m} \right|^2 \cdot \psi_s^2 \left| \frac{\sin(\pi\psi_m)}{\pi\psi_m} \right|^2 = \frac{1}{\pi^2} \cdot \frac{1}{\pi^2} . \tag{7.29}$$

The signal spectrum at the output of the first stage of $|H_e(f)|^2$ can, therefore, be written as the following equations.

$$\begin{aligned} |Y_{\mathrm{A}e}(f)|^2 &= (G_s\tau_i\psi_m\psi_s\alpha\lambda_p)^2\,\delta(f) + \left(\frac{G_s\alpha\lambda_p}{\pi^2}\right)^2 |H_{id}(|f_s - f_m|)|^2\,|H_{sh}(|f_s - f_m|)|^2 \\ &\quad \times\ [\delta(f + |f_s - f_m|) + \delta(f - |f_s - f_m|)] \\ &\quad \text{which is,} \\ |Y_{\mathrm{A}e}(f)|^2 &= \frac{1}{16}\,(G_s\tau_i\alpha\lambda_p)^2\,\delta(f) + \left(\frac{G_s\tau_i\alpha\lambda_p}{\pi^2}\right)^2 |\mathrm{Sa}(\pi f_I\tau_i)|^2\,|\mathrm{Sa}(\pi f_I T_f)|^2 \\ &\quad \times\ [\delta(f + f_I) + \delta(f - f_I)] \end{aligned} \tag{7.30}$$

The subscript e on $|Y_{\mathrm{A}e}(f)|^2$ indicates the output is from the heterodyne detection process.

In order to extract just the information bearing signal that resides at f_I and eliminate the steady state background component that lies at $f = 0$, $|Y_{\mathrm{A}e}(f)|^2$ is first mixed with $|D(f)|^2$ and then filtered with $|H_{rd}(f)|^2$. Mixing $|Y_{\mathrm{A}e}(f)|^2$ with $|D(f)|^2$ will transfer any component at f_d, which is the demodulation frequency in $|D(f)|^2$, down to the baseband. In order to recover the signal at f_I, the demodulation frequency, f_d, is, therefore, set equal to f_I. Convolving $|Y_{\mathrm{A}e}(f)|^2$ with $|D(f)|^2$, and

setting $f_d = f_I$, produces the following result.

$$\begin{aligned} |Y_{\mathrm{Ae}}(f)|^2 * |D(f)|^2 &= \frac{1}{64}\left(G_d G_s \tau_i \alpha \lambda_p\right)^2 \left[\delta(f+f_I) + \delta(f-f_I)\right] \\ &\quad + 2\left(\frac{G_d G_s \tau_i \alpha \lambda_p}{2\pi^2}\right)^2 |\mathrm{Sa}(\pi f_I \tau_i)|^2 \, |\mathrm{Sa}(\pi f_I T_f)|^2 \, \delta(f) \end{aligned} \tag{7.31}$$

Not only is the dc component of the information bearing signal transferred to f_I, as shown in equation 7.31, but the steady state background component is also transfered to f_I. The final integrate and dump filter, $|H_{rd}(f)|^2$, is then used to remove the background component that is transferred in frequency to f_I. This is accomplished by setting $1/\tau_r = f_I = f_d$, which creates a zero at f_I.

This is the same reason the signal is eliminated at the output of $|H_{ge}(f)|^2$, which does not perform the convolution in equation 7.31. If $|Y_{\mathrm{Ae}}(f)|^2$ is not convolved with $|D(f)|^2$, the signal remains at f_I. The signal, that remains at f_I in this case, is eliminated by $|H_{rd}(f)|^2$, which has a zero at f_I. The final integrate and dump filter, therefore, eliminates the signal from $|H_{ge}(f)|^2$ and eliminates the steady state background from $|H_e(f)|^2$.

After equation 7.31 is filtered with $|H_{rd}(f)|^2$, the only remaining term is the dc term. The signal's spectrum at the output of $|H_e(f)|^2$ is, therefore,

$$|Z_{\mathrm{Ae}}(f)|^2 = \frac{1}{2\pi^4}\left(G_d G_s \tau_r \tau_i \alpha \lambda_p\right)^2 |\mathrm{Sa}(\pi f_I \tau_i)|^2 \, |\mathrm{Sa}(\pi f_I T_f)|^2 \, \delta(f) \tag{7.32}$$

where τ_r is the gain of $|H_{rd}(f)|^2$. Since only the dc component remains, the signal power is the square of the mean signal power at the output.

$$\left(\overline{Z_{\mathrm{Ae}}}\right)^2 = \frac{1}{2\pi^4}\left(G_d G_s \tau_r \tau_i \alpha \lambda_p\right)^2 |\mathrm{Sa}(\pi f_I \tau_i)|^2 \, |\mathrm{Sa}(\pi f_I T_f)|^2 \tag{7.33}$$

7.4.2 Photon Noise Output

The noise at the output of the first stage of the heterodyne detection process is, essentially, the same as the noise out of the gated integrator. The sample and hold filter is added to the spectrum given in equation 6.24, to produce the photon noise spectrum at the output out of the first stage of the heterodyne detection process.

$$|Y_{We}(f)|^2 = (G_s\tau_i)^2 \left|\mathrm{Sa}\left(\pi f \tau_i\right)\right|^2 \left|\mathrm{Sa}\left(\pi f T_f\right)\right|^2 \frac{1}{2}\lambda_p \,. \tag{7.34}$$

The photon noise spectrum at the output of the second stage, $|Z_{We}(f)|^2$, is determined by mixing $|Y_{We}(f)|^2$ with $|D(f)|^2$ and then filtering the result with $|H_{rd}(f)|^2$.

$$\begin{aligned}
|Z_{We}(f)|^2 &= |H_{rd}(f)|^2 \left[|Y_{We}(f)|^2 * |D(f)|^2\right] \\
|Z_{We}(f)|^2 &= \frac{\lambda_p}{8}\left(G_d G_s \tau_r \tau_i\right)^2 \left|\mathrm{Sa}(\pi f \tau_r)\right|^2 \Big[\left|\mathrm{Sa}\left[\pi(f+f_d)\tau_i\right]\right|^2 \left|\mathrm{Sa}\left[\pi(f+f_d)T_f\right]\right|^2 \\
&\quad + \left|\mathrm{Sa}\left[\pi(f-f_d)\tau_i\right]\right|^2 \left|\mathrm{Sa}\left[\pi(f-f_d)T_f\right]\right|^2 \Big]
\end{aligned} \tag{7.35}$$

The symmetrical shape of both $|Y_{\mathrm{A}e}(f)|^2$ and the noise equivalent filter for $|H_{rd}(f)|^2$ can, again, be used to simplify the noise power calculation. Using the NEB for $H_{rd}(f)$ and changing the integration limits to include f_d, the photon noise power at the output of $H_e(f)$ is,

$$\sigma^2_{We} = \frac{1}{4}\lambda_p \left(G_d G_s \tau_r \tau_i\right)^2 \int_{f_d - f_r/2}^{f_d + f_r/2} \left|\mathrm{Sa}\left(\pi f \tau_i\right)\right|^2 \left|\mathrm{Sa}\left(\pi f T_f\right)\right|^2 \, df \tag{7.36}$$

The demodulation frequency, f_d, is set equal to the intermediate frequency, f_I, to transfer the signal to the baseband. The final filter's first zero at f_r is also set equal to f_I. The demodulation frequency, f_d, is, therefore, also equal to f_r. In this case, equation 7.36 can be simplified by substituting f_d for f_r. The photon noise power at

the output of $|H_e(f)|^2$ is then a function of f_d.

$$\sigma_{We}^2 = \frac{1}{4}\lambda_p \left(G_d G_s \tau_r \tau_i\right)^2 \int_{f_d/2}^{(3f_d)/2} |\mathrm{Sa}\left(\pi f \tau_i\right)|^2 \left|\mathrm{Sa}\left(\pi f T_f\right)\right|^2 \, df \tag{7.37}$$

or

$$\sigma_{We}^2 = \frac{1}{4}\lambda_p \left(G_d G_s \tau_r \tau_i\right)^2 K_W(f_d) \tag{7.38}$$

where

$$K_W(f_d) = \int_{f_d/2}^{(3f_d)/2} |\mathrm{Sa}\left(\pi f \tau_i\right)|^2 \left|\mathrm{Sa}\left(\pi f T_f\right)\right|^2 \, df \, . \tag{7.39}$$

The numerical integration of $K_W(f_d)$, defined in equation 7.39, is shown in Figure 7.4. For the numerical integration shown in this figure, the demodulation frequency ranges from 1Hz to 75Hz, the integration time, τ_i, is set to 1/200 seconds, and the frame period, T_f, is set to 1/30 seconds.

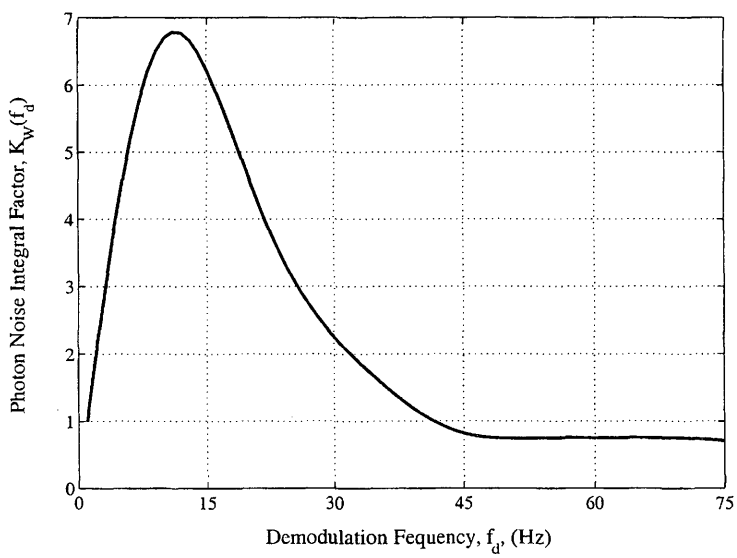

FIG. 7.4. Numerical integration of $K_W(f_d)$

7.4.3 1/f Noise

Determining the $1/f$ noise at the output of the first stage of the heterodyne detector is, again, the same as for the gated integrator. The $1/f$ noise at the output of the first stage is the same as shown in equation 6.28, with the addition of the sample and hold filter.

$$\begin{aligned} |Y_{Le}(f)|^2 &= (G_s\tau_i)^2 \left|\mathrm{Sa}(\pi f \tau_i)\right|^2 \left|\mathrm{Sa}(\pi f T_f)\right|^2 \\ &\quad \times \left[\psi_s^2 S_L(f) + \frac{1}{\pi^2} S_L(f+f_s) + \frac{1}{\pi^2} S_L(f-f_s)\right] \end{aligned} \tag{7.40}$$

Using the noise equivalent filter from equation 7.16, the $1/f$ noise at the output of the first stage is,

$$\sigma_L^2 = 2f_o\left(G_s\tau_i\lambda_p\right)^2 \left[\psi_s^2 \ln\left(\frac{f_f}{f_o}\right) + \frac{1}{\pi^2}\ln\left(\frac{2f_s+f_f}{2f_s-f_f}\right)\right] \tag{7.41}$$

which is the same as equation 6.31, however, using f_f from $|H_{sh}(f)|^2$ instead of f_i.

The total $1/f$ noise at the output is comprised of the baseband $1/f$ noise and the $1/f$ noise that is convolved to f_s by $Q(f)$. The ratio of the noise from $S_L(f \pm f_s)$ to the total noise, as given by equation 7.42, is shown graphically in Figure 7.5.

$$S_L(f \pm f_s) \text{ Contribution } = \left[\frac{\frac{1}{\pi^2}\ln\left(\frac{2f_s+f_f}{2f_s-f_f}\right)}{\psi_s^2 \ln\left(\frac{f_f}{f_o}\right) + \frac{1}{\pi^2}\ln\left(\frac{2f_s+f_f}{2f_s-f_f}\right)}\right] \times 100 \tag{7.42}$$

In Figure 7.5, f_s is set to 4kHz, ψ_s is set to 50%, and the $1/f$ noise cutoff frequency, f_o, is set to 1.29x10^{-7}Hz. The imaging system frame rate, f_f, is varied from 1Hz to 100Hz.

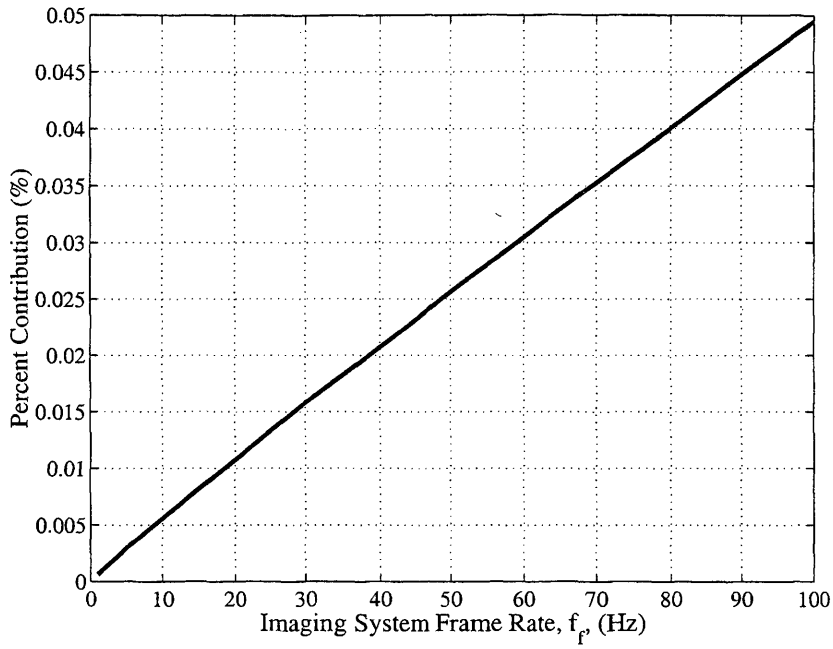

FIG. 7.5. Ratio of noise contribution from $S_L(f \pm f_s)$ to the total $1/f$ noise

It is apparent from Figure 7.5, that most of the $1/f$ noise at the output of the first stage is from the baseband $1/f$ noise. Since the additional noise from $S_L(f \pm f_s)$ is quite small, compared to the noise from $S_L(f)$, the $1/f$ noise at the output of the first stage is approximated with only the baseband contribution.

$$|Y_{Le}(f)|^2 \approx \frac{1}{4}(G_s\tau_i)^2 \left|\mathrm{Sa}(\pi f \tau_i)\right|^2 \left|\mathrm{Sa}(\pi f T_f)\right|^2 S_L(f). \tag{7.43}$$

The $1/f$ noise spectrum at the output of $|H_e(f)|^2$ is found by first convolving $|Y_{Le}(f)|^2$ and then filtering the result with the final integrate and dump filter.

$$\begin{aligned}
|Z_{Le}(f)|^2 &= |H_{rd}(f)|^2 \left[|Y_{\mathrm{Ae}}(f)|^2 * |D(f)|^2\right] \\
|Z_{Le}(f)|^2 &= \frac{1}{16}(G_d G_s \tau_r \tau_i)^2 \Big[S_L(f+f_d)\left|\mathrm{Sa}\left[\pi(f+f_d)\tau_i\right]\right|^2 \left|\mathrm{Sa}\left[\pi(f+f_d)T_f\right]\right|^2 \\
&\quad + S_L(f-f_d)\left|\mathrm{Sa}\left[\pi(f-f_d)\tau_i\right]\right|^2 \left|\mathrm{Sa}\left[\pi(f-f_d)T_f\right]\right|^2\Big]
\end{aligned} \tag{7.44}$$

In order to determine the $1/f$ noise power, the noise equivalent filter, $|H_{rd}^{eq}(f)|^2$ can be substituted for $|H_{rd}(f)|^2$. Since the functions in equation 7.44 are all even functions, $|H_{rd}^{eq}(f)|^2$, instead of $|Y_{\mathrm{A}e}(f)|^2$, can be convolved with $|D(f)|^2$.

$$|Z_{Le}(f)|^2 = |Y_{\mathrm{A}e}(f)|^2 \left[|H_{rd}^{eq}(f)|^2 * |D(f)|^2\right] \tag{7.45}$$

By convolving $|H_{rd}^{eq}(f)|^2$ with $|D(f)|^2$, the limits of integration, over the NEB, include f_d. The $1/f$ noise power at the output of $|H_e(f)|^2$ can, therefore, be determined with the following equation.

$$\sigma_{Le}^2 = \frac{f_o}{8}\left(G_d G_s \tau_r \tau_i \lambda_p\right)^2 \int_{f_d - f_r/2}^{f_d + f_r/2} \frac{|\mathrm{Sa}\,(\pi f \tau_i)|^2 \, |\mathrm{Sa}\,(\pi f T_f)|^2}{\sqrt{f_o^2 + f^2}}(f)\, df \tag{7.46}$$

Just as in the photon noise case, f_d can be substituted for f_r. After substitution, the $1/f$ noise power is,

$$\sigma_{Le}^2 = \frac{f_o}{8}\left(G_d G_s \tau_r \tau_i \lambda_p\right)^2 \int_{f_d/2}^{(3f_d)/2} \frac{|\mathrm{Sa}\,(\pi f \tau_i)|^2 \, |\mathrm{Sa}\,(\pi f T_f)|^2}{\sqrt{f_o^2 + f^2}}(f)\, df \tag{7.47}$$

or

$$\sigma_{Le}^2 = \frac{f_o}{8}\left(G_d G_s \tau_r \tau_i \lambda_p\right)^2 K_L(f_d) \tag{7.48}$$

where

$$K_L(f_d) = \int_{f_d/2}^{(3f_d)/2} \frac{|\mathrm{Sa}\,(\pi f \tau_i)|^2 \, |\mathrm{Sa}\,(\pi f T_f)|^2}{\sqrt{f_o^2 + f^2}}(f)\, df \tag{7.49}$$

The results from numerically integrating $K_L(f_d)$, with f_d ranging from 1Hz to 75Hz, are plotted in Figure 7.6. The integration time, τ_i is, again, set to 1/200 seconds and the frame period, T_f is set to 1/30 seconds.

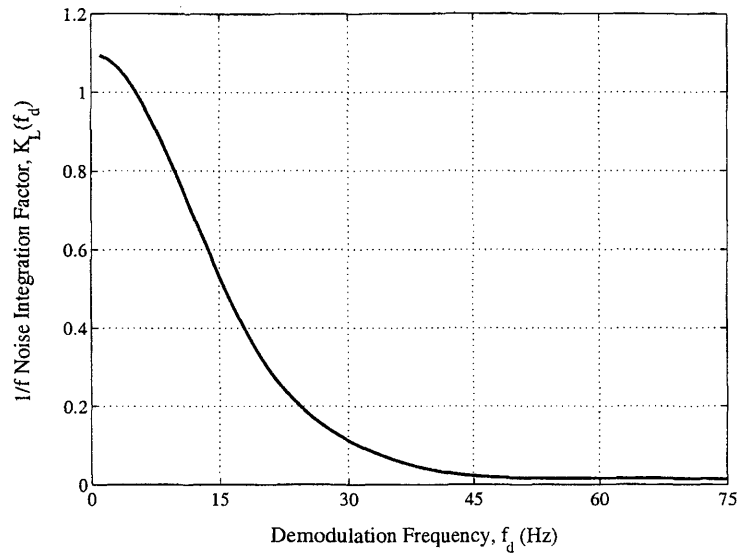

FIG. 7.6. Numerical integration of $K_L(f_d)$

7.4.4 Combined Output

The output power from $|H_e(f)|^2$ is the combination of signal power, photon noise power, and $1/f$ noise power. Since no background power is resolved, the total output of $|H_e(f)|^2$ is, again, defined as $Z^2_{\text{on-off}}$.

$$\begin{aligned} Z^2_{\text{on-off}} &= \left(\overline{Z_{\text{Ae}}}\right)^2 + \sigma^2_{We} + \sigma^2_{Le} \\ Z^2_{\text{on-off}} &= \left(G_d G_s \tau_r \tau_i\right)^2 \left[\frac{1}{2\pi^4}\left(\alpha\lambda_p\right)^2 \left|\text{Sa}(\pi f_I \tau_i)\right|^2 \left|\text{Sa}(\pi f_I T_f)\right|^2 \right. \\ &\quad \left. + \frac{1}{4}\lambda_p K_W(f_d) + \frac{1}{8} f_o \lambda_p^2 K_L(f_d)\right] \end{aligned} \tag{7.50}$$

7.5 Modulation Depth Determination

The modulation depth is determined with a similar method to the one shown in section 6.6. The signal is, however, extracted through demodulation, thus, the

background does not need to be subtracted out. The ratio of the signal to the background will, in this case, provide the modulation depth. The mean-square value of the modulation depth is,

$$\overline{\alpha_{mod}^2} = \frac{Z_{\text{on-off}}^2}{Z_{\text{off}}^2} = \frac{\left(\overline{Z_{\text{Ae}}}\right)^2 + \sigma_{We}^2 + \sigma_{Le}^2}{\left(\overline{Z_{Be}}\right)^2 + \sigma_{Wge}^2 + \sigma_{Lge}^2} \tag{7.51}$$

The mean-square value of the modulation depth is the sum of the square of the mean modulation depth, $(\overline{\alpha_{mod}})^2$, and the modulation depth variance, σ_{mod}^2. The squared mean value is,

$$(\overline{\alpha_{mod}})^2 = \frac{\left(\overline{Z_{\text{Ae}}}\right)^2}{\left(\overline{Z_{Be}}\right)^2} = \frac{\frac{1}{2\pi^4}\left(G_d\alpha\lambda_p\right)^2 \left|\text{Sa}(\pi f_I \tau_i)\right|^2 \left|\text{Sa}(\pi f_I T_f)\right|^2}{\frac{1}{4}\lambda_p^2}, \tag{7.52}$$

after canceling the like terms in equations 7.23 and 7.50. Taking the square root of equation 7.52 produces the mean modulation depth that is measured by the imaging system.

$$\overline{\alpha_{mod}} = \frac{\sqrt{2}}{\pi^2} G_d \alpha \left|\text{Sa}(\pi f_I \tau_i)\right| \left|\text{Sa}(\pi f_I T_f)\right| \tag{7.53}$$

Since the gain of $|D(f)|^2$, which is G_d, is only applied to the signal, it can be set such that α is extracted. In order for $\overline{\alpha_{mod}}$ to be equal to α, G_d is set to,

$$G_d = \frac{\pi^2}{\sqrt{2}\left|\text{Sa}(\pi f_I \tau_i)\right| \left|\text{Sa}(\pi f_I T_f)\right|} \tag{7.54}$$

7.6 Signal-To-Noise Ratio

Since $Z^2_{\text{on-off}}$ contains the signal power, the signal-to-noise ratio (SNR) can be defined as

$$SNR = \frac{\left(\overline{Z_{\text{Ae}}}\right)^2}{\sigma^2_{We} + \sigma^2_{Le} + \sigma^2_r} \tag{7.55}$$

which contains the read noise power, σ^2_r. The read noise power is only canceled when the modulation depth is determined.

Measuring the modulation depth, rather than the signal power, is, however, the objective. A more useful figure of merit is, therefore, the modulation depth-to-noise ratio (MDNR). The MDNR is the ratio of $(\overline{\alpha_{mod}})^2$ and σ^2_{mod}. The MDNR is different than the SNR because of the propagation of errors through the calculation performed in equation 7.51.

Since the noise from $|H_e(f)|^2$ and the noise from $|H_{ge}(f)|^2$ are determined over different spectral ranges, the photon noise powers are uncorrelated. It is assumed that the $1/f$ noise power from the two system functions will have some correlation. The correlation in $1/f$ noise is, however, ignored, which produces a worst case scenario. If the $1/f$ noise has in fact some correlation, the actual MDNR will only be better.

Based on the propagation of errors, the modulation depth variance is (Bevington & Robinson, 1992),

$$\frac{\sigma^2_{mod}}{(\overline{\alpha_{mod}})^2} = \frac{(\sigma^2_{We} + \sigma^2_{Le})}{\left(\overline{Z_{\text{Ae}}}\right)^2} + \frac{\left(\sigma^2_{Wge} + \sigma^2_{Lge}\right)}{\left(\overline{Z_{Bge}}\right)^2} \tag{7.56}$$

Since $\left(\overline{\alpha_{mod}}\right)^2$ is $\left(\overline{Z_{\mathrm{A}e}}\right)^2 / \left(\overline{Z_{Bge}}\right)^2$, the modulation depth variance is,

$$\sigma_{mod}^2 = \frac{\left(\overline{Z_{Bge}}\right)^2 \left(\sigma_{We}^2 + \sigma_{Le}^2\right) \; + \; \left(\sigma_{Wge}^2 + \sigma_{Lge}^2\right)}{\left(\overline{Z_{Bge}}\right)^4} \tag{7.57}$$

The MDNR is then found by dividing equation 7.53 by equation 7.57.

$$\begin{aligned} \mathrm{MDNR} &= \frac{\left(\overline{\alpha_{mod}}\right)^2}{\sigma_{mod}^2} \\ \mathrm{MDNR} &= \frac{\left(\overline{Z_{\mathrm{A}e}}\right)^2}{\left(\overline{Z_{Bge}}\right)^2 \left(\sigma_{We}^2 + \sigma_{Le}^2\right) \; + \; \left(\sigma_{Wge}^2 + \sigma_{Lge}^2\right)} \end{aligned} \tag{7.58}$$

The MDNR is plotted in Figure 7.7, for modulation depths of 10^{-2}, 10^{-3}, 10^{-4}, and 10^{-5}. The MDNR is shown as a function of the demodulation frequency, f_d, which is also the intermediate frequency, f_I, or the frequency difference between f_m and f_s. The integration time, τ_i is set to 2.5ms, thus, 10 samples of a 4kHz input are integrated per frame. The system frame rate is assumed to be 30Hz, therefore, T_f is set to 1/30 seconds. Also, the input λ_p is set such that the system is just below saturation after integrating the 10 samples per frame.

7.7 Detection Limits

The MDNR shown in Figure 7.7 is much lower than the SNR shown in Figure 6.11 for the gated integrator detection mode. The MDNR is much lower because the signal power at the output of $|H_e(f)|^2$ is much lower than the signal power obtained with the gated integrator, $|H_g(f)|^2$.

The ratio of signal power out of the heterodyne detection mode, from equation 7.33, to the signal power out of the gated integrator mode, from equation 6.20, is plotted in Figure 7.8. This figure shows that the signal power obtained at the output

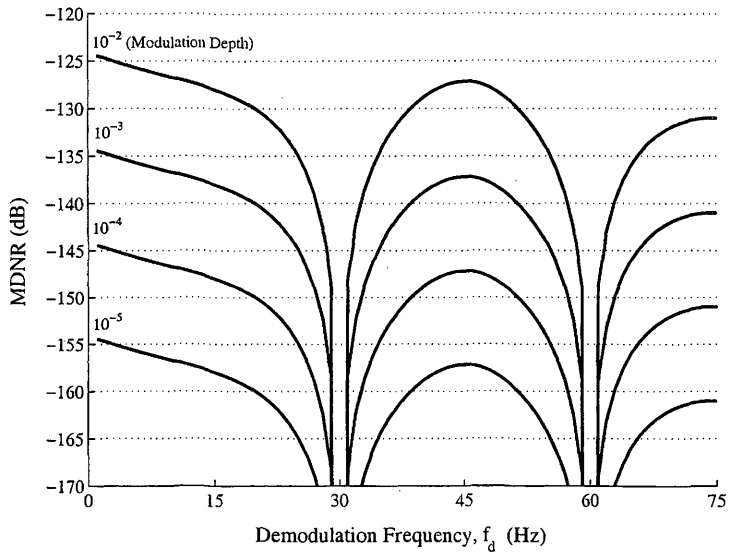

FIG. 7.7. Modulation depth-to-noise ratio (MDNR) as a function of demodulation frequency, f_d

of the heterodyne detection system is much smaller. The reduction in signal power accounts for the reduction in SNR, or in this case MDNR.

The noise power from both system functions remains essentially the same. Since the natural sampling function has a dc component, the low frequency noise remains at the baseband. The input signal power at the modulation frequency, f_m, is mixed down to the intermediate frequency, f_I. Since the imaging system has such a low frame rate, f_I must be a low frequency (~30Hz) located in a large portion of the $1/f$ noise. Since the $1/f$ noise remains at its baseband and is not convolved to a higher frequency band by the natural sampler, the heterodyne detection process can be thought of as a lock-in detection process that uses a 30Hz modulation frequency.

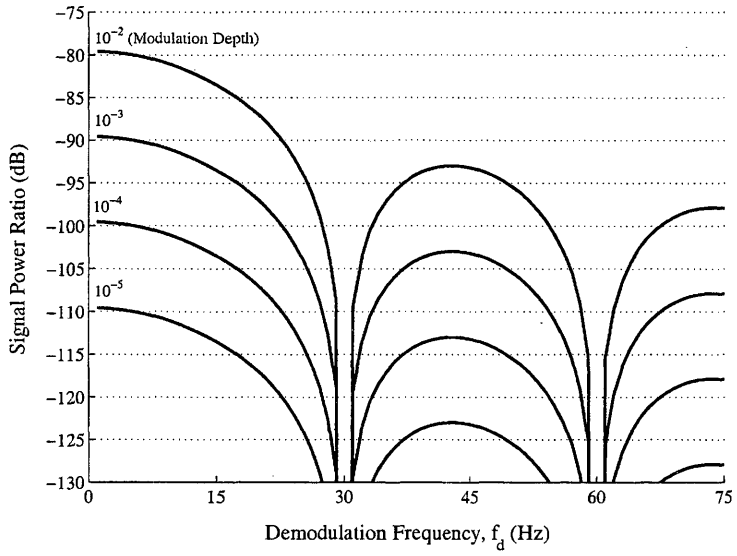

FIG. 7.8. Ratio of signal power from $|H_e(f)|^2$ to the signal power from $|H_g(f)|^2$

7.8 Applications

The results indicate that the imaging system's heterodyne detection mode is not well suited for making measurements used to calculate modulation depth. The gated integration mode, discussed in Chapter 6, transfers more signal power to the output and is, therefore, more applicable to the problem of extracting a weakly modulated image.

The heterodyne detection mode can, however, enhance images used in other applications. Not discussed in this analysis is the fact that phase information is also retained at the output, $|Y(f)|^2$, of the imaging system. Phase information in images can be used to calculate distances in the object plane and generate topographical images.

Besides three-dimensional mapping, phase information may also be used in selected background free laser diagnostics. As an example, the ability to determine the

phase difference between an excitation source and the resulting fluorescence from a paint sample can extend the measurement options in pressure sensitive paint diagnostics.

Chapter 8

PROCESSING DEMONSTRATION

8.1 General Introduction

As an indication of the imaging system's potential, its processing capabilities are demonstrated in this chapter. The system's ability to perform on-chip integration of multiple exposures is first shown in section 8.3. Then, in section 8.4, the results from testing the integration threshold function are presented.

After demonstrating the system's ability to perform on-chip integration, the results from modulation depth experiments are outlined. In these experiments, the gated integration mode, from Chapter 6, is used to measure a simulated probe beam irradiance. The simulated probe beam irradiance is generated with a controllable light-emitting-diode (LED) array. Modulation depth, from the simulated probe beam, as measured with the imaging system is compared to the modulation depth, from the same LED, as measured by the combination of a lock-in amplifier and a dc volt meter.

This chapter then concludes with demonstrations that could prove valuable to alternate applications. Using the gated integrator mode, fringe analysis is shown as a method for object and shape recognition. Finally, the heterodyne detection mode, presented in Chapter 7, is demonstrated and possible applications are discussed.

8.2 Experiment Configuration

Most of the results are generated from the experimental setup shown in Figure 8.1. An LED array is used as a controllable irradiance source. In the LED array electronics, a dc input, a noise input, and a signal input, can be summed together to produce the desired irradiance from the LEDs.

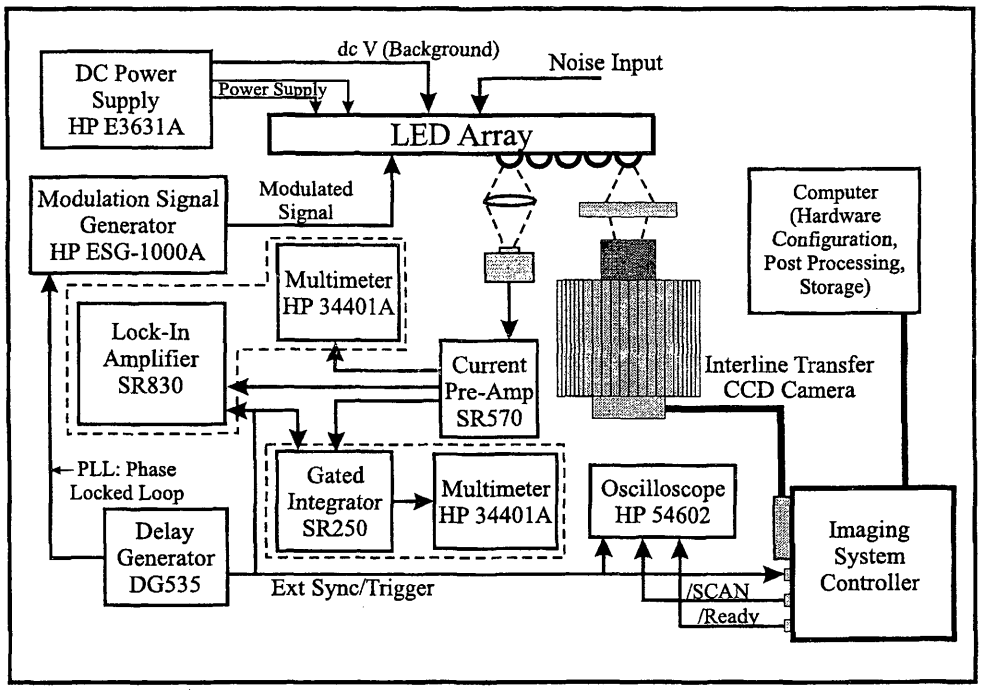

FIG. 8.1. Equipment and instrumentation used to demonstrate and test the imaging system's functions

A lock-in amplifier (Stanford Research Systems (SRS) SR830), a gated integrator (SRS SR250), and a multimeter (Hewlett-Packard (HP) 34401A) are used to acquire baseline data, for comparison with the data from the imaging system. The irradiance from an LED is detected with a photodiode (Thor-Labs DET110), amplified with a current pre-amplifier (SRS SR570), and then set to a combination of instruments for measurement. Although Figure 8.1 shows that different LEDs are used for the

baseline measurements and the imaging system measurements, the same LED was used for both.

When performing measurements with the photodiode, a lens was used to focus the irradiance onto the photodiode element. An optical diffuser was used to make the LED irradiance more uniform for the imaging system. The uniform irradiance created by the diffuser made it possible to collect data across a larger area of pixels.

8.2.1 Light Source

An LED array was developed as the excitation source for testing the imaging system. The array consists of an 8x8 square matrix of LEDs. The LED array is energized with a dc voltage, a signal voltage, and a noise voltage, which are summed together. Figure 8.2 is a block diagram of the circuitry used in the LED array.

The dc input and the signal input are used to simulate a small modulated signal that is superimposed on a large steady state background (dc), similar to the probe beam irradiance introduced in Figure 1.3. A dc power supply (HP E3631A) was used to generate the dc input and a digital signal generator (HP ESG-1000A) was used to produce the modulated signal waveform. For the results given in this chapter, a 50 ohm terminator was connected to the noise input to create a noise floor created with Johnson noise. Additional noise from, for example, an active noise generator was supplied.

The LEDs used in the array are blue-green emitters (Hewlett-Packard, HLMP-CE23-R0000) that have, based on the data sheet, a typical peak wavelength of 502nm and a spectral halfwidth of 35nm. The wavelength of light emitted by the LED array was scanned using a monochromater. The results of the scan are shown in Figure 8.3. The peak wavelength is very close to the wavelength given in the data sheet. At a

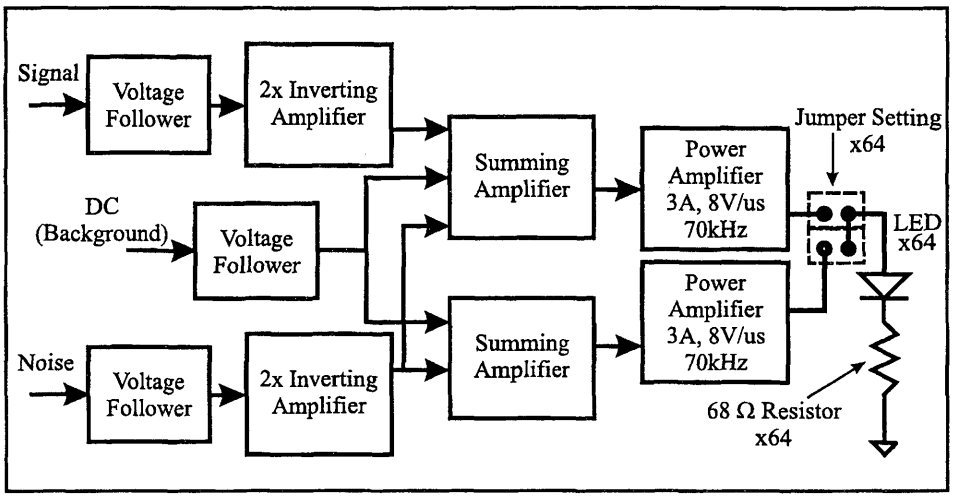

FIG. 8.2. Block diagram of LED array

wavelength of 500nm, the imaging system has a quantum efficiency (QE) of about 45%, which is obtained from the QE curve in Appendix C.

The LEDs begin to conduct when the dc voltage is 3V or greater, as shown in Figure 8.4. The dc voltage used during the tests shown in the following sections ranges from 3V to 6V.

8.3 On-chip Integration

The imaging system's ability to integrate multiple exposures is demonstrated in this section. A single LED is imaged onto a 100x100 region of interest (ROI). The dc voltage applied to the LED is set at 3V, 4V, 5V, and 6V. At each voltage setting, the number of integrated exposures is increased until the imaging system saturates.

Figure 8.5 is a graph of the number of exposures that can be integrated when the exposure time is set to 10μs. The maximum number of exposures that can be integrated is 4000, which is a limit that is set by the digital logic configured in the controller. The imaging system will not reach saturation when the exposure time is

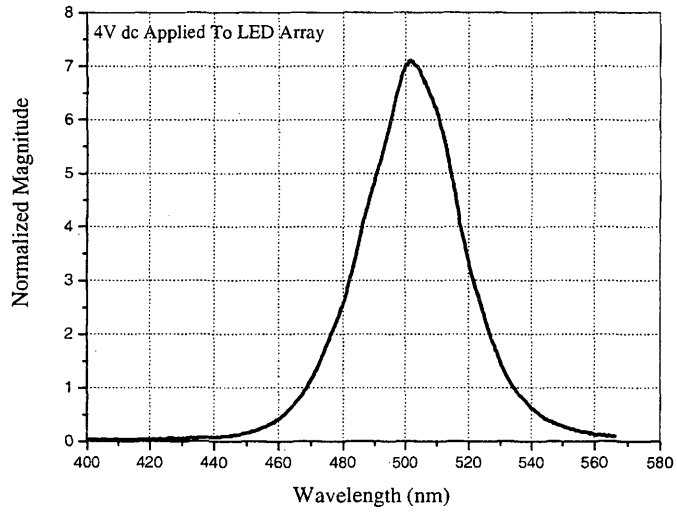

FIG. 8.3. Wavelength scan of LED Array

set at 10μs and the dc voltage applied to the LED is 3V.

It was determined, in Chapter 2, that the imaging system saturates at approximately 28,000 counts (DN). The count values plotted in Figures 8.5, 8.6, and 8.7 are mean values across the 100x100 ROI. The mean data in the figures only approaches 16,000 counts (DN) because some pixels were near saturation and data collection was terminated.

Figures 8.6 and 8.7 are also graphs of the integrated exposures for exposure times of 100μs and 500μs respectively. Obviously, as shown in Figures 8.5, 8.6, and 8.7, the maximum number of exposures that can be integrated decreases as the irradiance increases. In the same respect the number of exposures that can be integrated decreases as the duration of each exposure increases.

Independent of the exposure time, integrating exposures on the CCD chip is a fairly linear process. As shown in Figure 8.5, a 4V dc input to the LED and

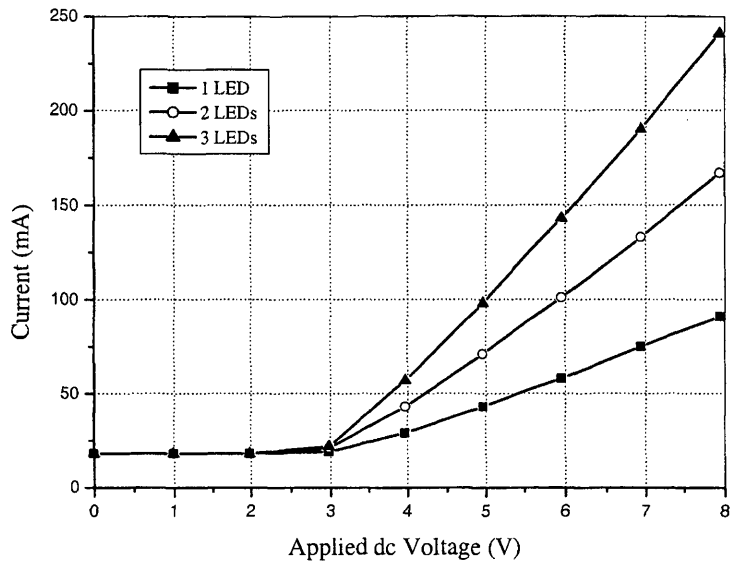

FIG. 8.4. Applied dc voltage vs. total LED current draw

an exposure time of 10μs produces about 14,000 counts (DN) at the output after integrating 2500 exposures. The output is determined by averaging over the 100x100 ROI.

After increasing the exposure time by an order of magnitude to 100μs, the number of integrated exposures required to obtain the same output acquired by integrating 10μs exposures should, correspondingly, decrease by an order of magnitude. Figure 8.6 shows, in fact, for a dc voltage of 4V and an exposure duration of 100μs, the output reaches about 14,000 counts (DN) after integrating 250 exposures.

The same correlation is apparent in Figure 8.7 as well. Using an exposure time of 500μs requires, as expected, 50 integrated exposures to reach approximately 14,000 counts (DN) at the output, when the dc voltage applied to the LED is 4V.

Using the 4V dc data from Figures 8.5, 8.6, and 8.7, the integration rate, in

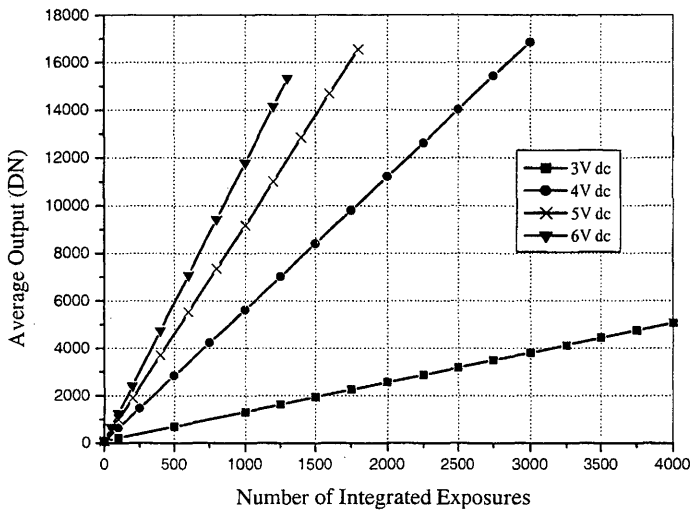

FIG. 8.5. On-chip exposure integration using 10μs exposure time

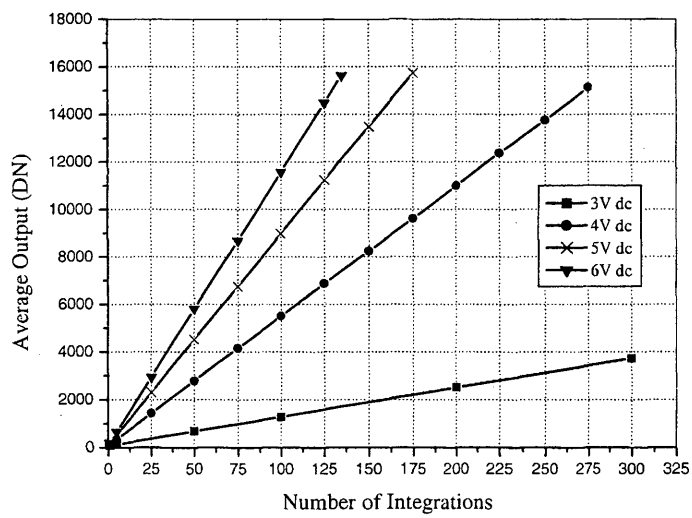

FIG. 8.6. On-chip exposure integration using 100μs exposure time

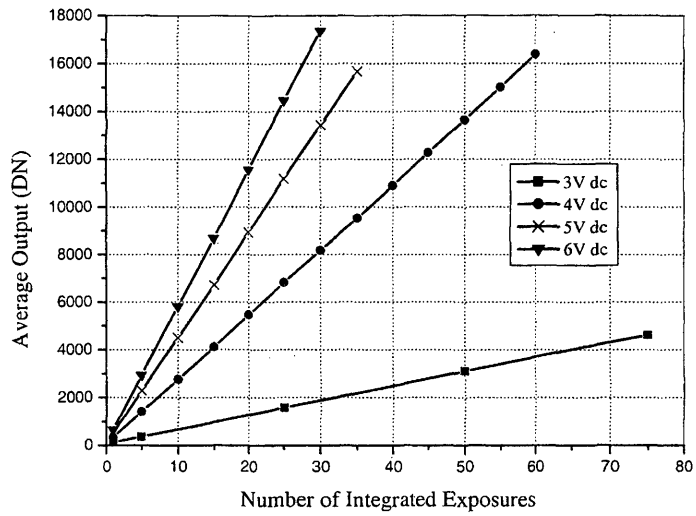

FIG. 8.7. On-chip exposure integration using 500μs exposure time

terms of digital counts per second, is determined and shown in Figure 8.8. Once the integrated value becomes larger than about 4000 counts, the mean integration rate becomes fairly constant. The same is true for LED dc supply voltages of 5V and 6V, which are not shown.

The mean integration rate, given in Figures 8.8, is shown to be higher when the exposure time is 10μs. This effect is probably caused by an emphasis in noise that occurs at very short exposure times. Charge, in the form of noise, from mask bleedthrough can add to the total charge at the output. The ratio of the charge collected during an exposure to noise charge is small when using a short exposure time. The mean integration rate, shown in Figure 8.8, does not account for noise and, therefore, increases as the exposure time decreases.

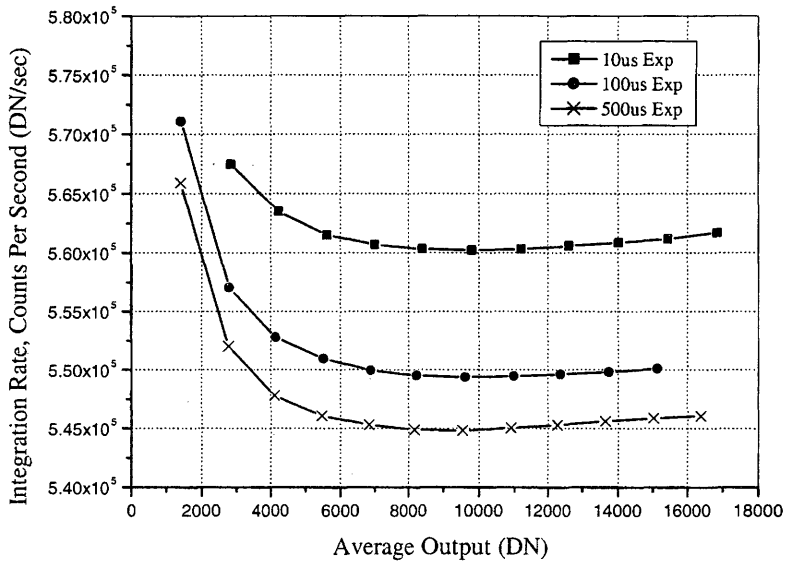

FIG. 8.8. Input arrival rate when applying 4V dc to the LED array

8.4 Integration Threshold

The integration threshold (IT) feature is demonstrated in this section. The same 100x100 ROI discussed in section 8.3 is used again to image a single LED. The dc voltage applied to the LED is held constant at 4V. Also, only a single exposure is taken and multiple exposures are not integrated.

The dead-band, created with the IT feature, is controlled by the voltage applied to the read out gate (ROG) barrier during an exposure. The maximum voltage that can be applied to the ROG barrier is 12.75V. In the following analysis, the dead-band threshold level is represented as a percentage of the maximum voltage that can be applied. The dead-band threshold is, therefore, created by applying less than 100% of the maximum voltage to the ROG barrier, and it is represented as this percentage.

Figure 8.9 shows the integrated output as the ROG barrier voltage is lowered

from 75% to 18%. The expected output when the ROG voltage is set to 100% is shown on the abscissa and the actual output when the ROG voltage is less than 100% is plotted along the ordinate.

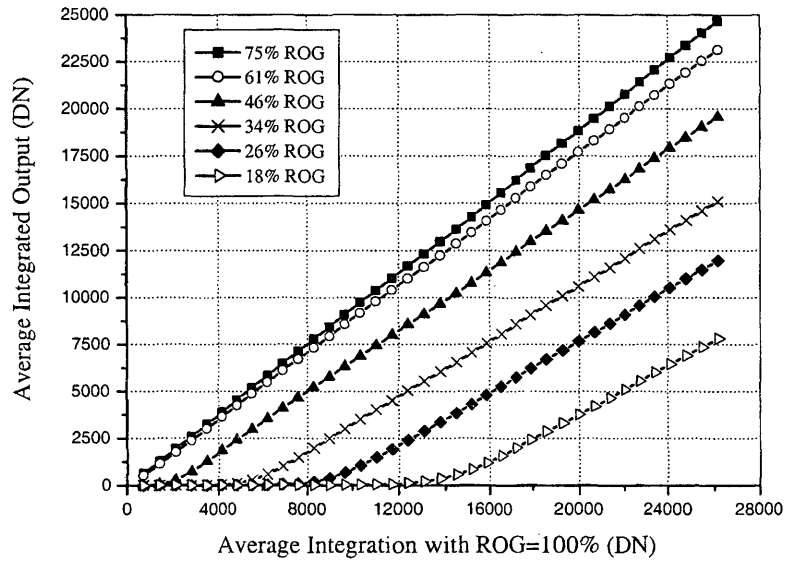

FIG. 8.9. Mean integration per read out gate (ROG) voltage setting

As expected, lowering the ROG voltage does in fact create a dead-band in the integration process. The amount of charge accumulated per exposure must exceed the dead-band threshold before it is integrated into the vertical register.

The integration threshold coefficient (ρ), which was defined in equation 6.13, is given in Figure 8.10 for various ROG settings. The threshold coefficient is plotted as a function of the average output when the ROG voltage were set to 100%.

Figure 8.10 shows that the integration threshold coefficient is not a constant, which would make it difficult to determine the actual modulation depth as given by equation 6.36. The integration threshold coefficient, ρ, is determined by dividing the

actual output (with ROG set less than 100%) by the expected output when ROG is 100%. As the average output with the ROG set to 100% increases, ρ levels off and approaches a steady state value. If integration is performed in a region in which ρ reaches a steady state value, it is possible, according to the data in Figure 8.10, to use the integration threshold to improve the SNR.

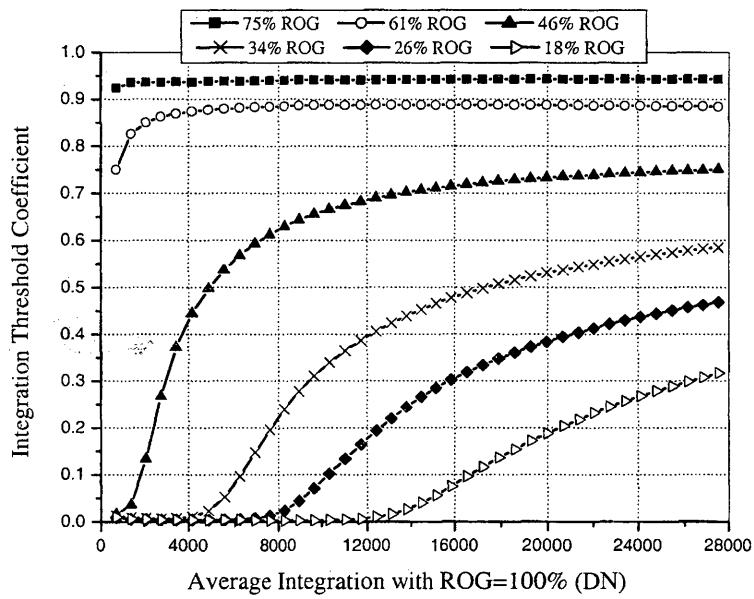

FIG. 8.10. Integration threshold coefficient (ρ) determination

The dead-band threshold does not appear to be a constant, however, at every pixel over the region of interest. Noise from pixel-to-pixel variations dramatically increases as the threshold is raised. Figures 8.11 and 8.12 show the noise power obtained when the dead-band threshold is raised. Figure 8.11 shows ROG settings of 100%, 75%, and 61%, and Figure 8.12 shows results for ROG settings of less than 50%. The photon noise limit is also incorporated into Figures 8.11 and 8.12 for comparison.

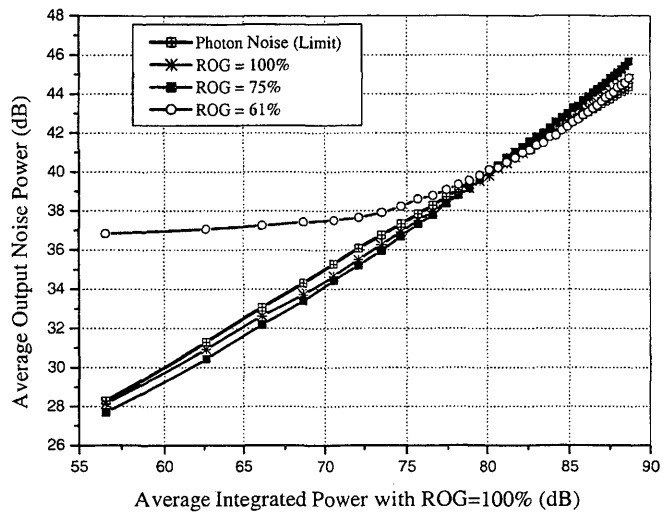

FIG. 8.11. Noise power per read out gate (ROG) voltage setting

When the ROG voltage is set below 61% of the maximum, the noise power (in dB referenced to counts) becomes quite large and appears to be signal dependent. It also appears that, when using the integration threshold, the noise power is dependent on the integrated input. At all the ROG settings, the noise power dropped back down to the photon noise limit when the integrated value reached about 87.5dB, which is about 23,700 counts (DN).

All of the images at each dead-band threshold setting were processed with the flat-field correction file that was created for 100% ROG operation. The flat-field correction file may account for some of the anomalous results shown in Figures 8.11 and 8.12. In some cases, the data is lower than the photon noise limit, which is suspected to be an overcorrection caused by the flat-field correction data file. Even though the flat-field correction factor data file was generated by averaging images taken at multiple steps over imaging system's linear operating region, it may be the

cause of the strange shape in the noise curves.

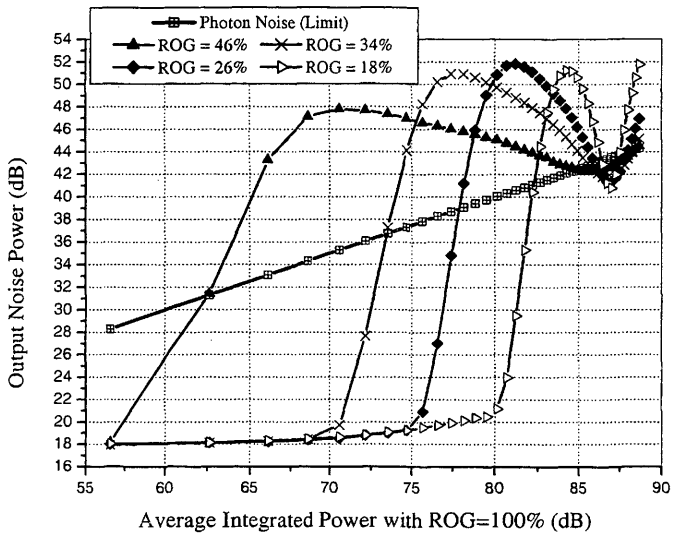

FIG. 8.12. Noise power per read out gate (ROG) voltage setting

The pixel-to-pixel uniformity appears to be dependent on the ROG barrier voltage, which is a CCD trait that has also been documented by Janesick (1987). Based on equation 6.36, integration threshold nonuniformity across the array, which is the same as nonuniformity in ρ, would make it very difficult to determine the modulation depth at each pixel. It is, therefore, not advisable to use the integration threshold when determining modulation depth.

8.5 Modulation Depth

Based on the modeling results in Chapters 6 and 7, the gated integration mode, rather than the heterodyne detection mode, offers better performance expectations when attempting to determine modulation depth. In this section, the gated integration mode from Chapter 6, without the integration threshold, is used to measure

the irradiance from a single LED and demonstrate the system's ability to determine modulation depth.

8.5.1 Source Configuration

In order to set-up a test probe irradiance that contains a modulated information bearing signal, an LED is excited with the sum of a dc voltage and a modulated signal voltage, as shown in Figure 8.2. The irradiance from the LED is passed through a diffuser and then imaged onto a 100x100 pixel ROI in the CCD array, creating 10,000 data points per frame.

The dc voltage applied to the LED ranges from 3V to 6V. A zero mean valued square wave is used as the modulating signal. The modulating signal amplitude ranges from ± 20mV to ± 1mV. Since the modulating signal has a zero mean value, it both adds to and subtracts from the dc voltage. The noise input is grounded through 50 ohms.

8.5.2 Calibration Measurements

In order to measure the captured signal's modulation depth with the imaging system, the modulation depth created with the LED needs to first be known. The modulation depth created with the LED cannot, however, be determined with the conventional technique used to determine the modulation depth in an actual probe beam from a PPAS experiment (Settersten, 1999). Instead, a method for calculating modulation depth from a combination of measurements with both a lock-in amplifier and a multimeter was developed.

Conventionally, in a PPAS experiment, only the power in the fundamental harmonic is measured with a lock-in amplifier to determine modulation depth (Settersten,

1999). First, the pump beam is blocked and the noise floor (no signal present because pump is blocked) at the fundamental harmonic (which is phase and frequency locked to the modulated signal) is measured with a lock-in amplifier. This value is set at the 0% modulation depth point. The modulation is then impressed directly onto the probe beam (normally by inserting a mechanical chopper in the probe beam's path) and the power at the fundamental harmonic component is again measured. This second value is set as the 100% modulation depth point. A linear calibration equation is fitted between the 0% and the 100% modulation depth points. The experiment is then performed (modulation is impressed onto the pump beam) and the power at the fundamental harmonic component is measured. The linear calibration is then used to determine the actual modulation depth occurring in the experiment.

The conventional measurement technique, described in the previous paragraph, uses the fact that the steady state background is a constant value and the modulation depth can be determined from changes in the fundamental harmonic component's power. The 0% and 100% modulation depth points cannot, however, be measured with the test probe irradiance from the LED. Because the modulating signal, in the test irradiance, has a zero mean value, it lowers the dc voltage (steady state background) by the negative portion of the square wave modulation signal. The steady state background in the test irradiance, therefore, changes based on the magnitude of the modulating signal.

Since both the steady state background irradiance and the irradiance in the fundamental harmonic component change with changes in modulation signal magnitude, the modulation depth is determined from both components. As introduced in section 1.3.1, the modulation depth is the ratio of the power in the modulated portion of the irradiance to the power in the steady state background irradiance. In order to ob-

tain baseline data, an equation was developed to calculate the modulation depth from measurements of both the dc component and the fundamental harmonic component. The derivation and further explanation of this calculation is given in Appendix I.

To determine the actual modulation depth emitted by an LED, the irradiance from that LED was focused onto a photodiode and measured with both a multimeter (HP 34401A) and a lock-in amplifier (SRS SR830). The multimeter was used to measure the steady state background, or dc irradiance, from the LED. The lock-in amplifier was referenced to the modulation signal and was used to measure the power in the fundamental harmonic component. The values from these measurements were then used to calculate the modulation depth using equation I.26.

The calculated modulation depth from measurements at LED dc voltage settings from 3V to 6V and modulation voltages of ±20mV, ±10mV, and ±5mV are plotted in Figure 8.13. With these voltages applied to the LED, the modulation depth ranged from just over 0.1 to $2\text{x}10^{-3}$.

In order to verify the data obtained with the lock-in amplifier, multimeter, and calculation from Appendix I, measurements were also performed with a boxcar averager (SRS SR250). The boxcar averager was used in a gated integration mode to integrate samples of only the steady state background (I_{off} from equation 1.1) and then to integrate samples of both the steady state background and the signal (I_{on} from equation 1.1). The values from the boxcar averager were then used in equation 1.1 to determine the modulation depth. The results are also shown in Figure 8.13.

Based on the inclusion of the boxcar averager measurements in Figure 8.13, the modulation depth results determined with measurements from the lock-in amplifier and multimeter are more convincing. The lock-in amplifier and multimeter are, therefore, used to acquire baseline modulation depth data, with which the data from the

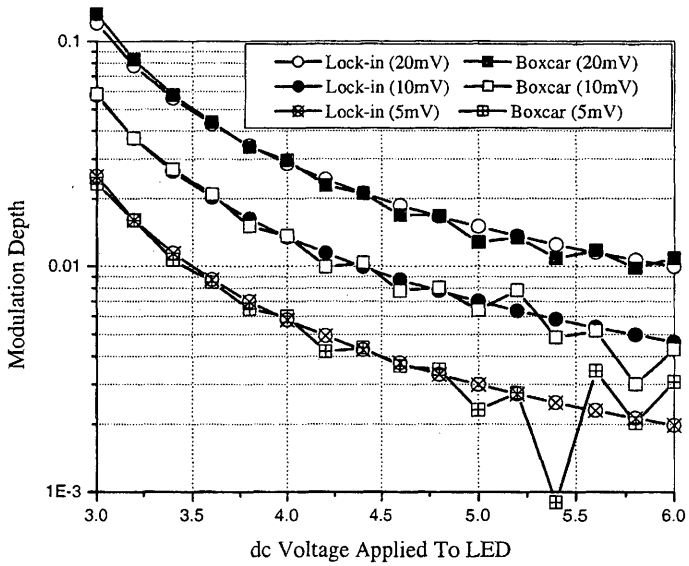

FIG. 8.13. Modulation depth measurements with a lock-in amplifier and a boxcar averager

imaging system is compared. Figure 8.14 shows the baseline modulation depth data, which ranges from about 0.1 to $2\text{x}10^{-5}$.

8.5.3 Imaging System Results

The imaging system was then used, in the gated integration mode, to determine the modulation depth created by the same LED that was analyzed in Figure 8.14. The dc voltage applied to the LED ranged from 3V to 6V in 1V increments. The modulated signal amplitude was set to 20mV, 5mV, 2mV, and 1mV. The modulation frequency was set to 1500Hz, which was the frequency at which the irradiance appeared, on a spectrum analyzer (HP 89410), to roll off to the noise floor. Each exposure was set to 125μs and, depending on the dc voltage, the number of integrations was set such that the final integrated output was in the linear operating range

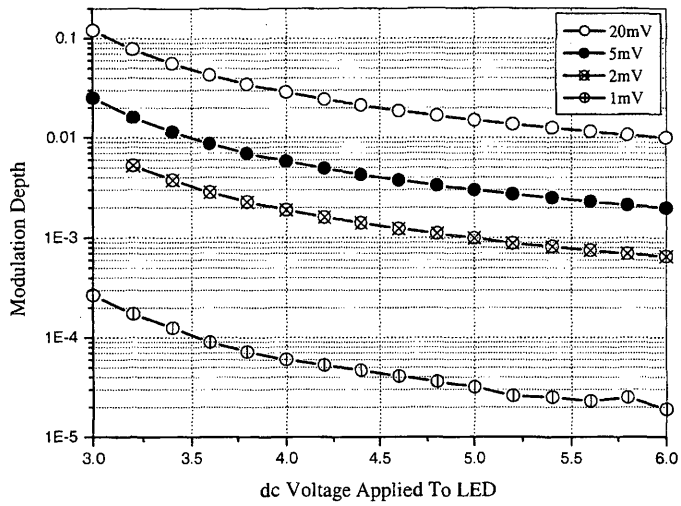

FIG. 8.14. Modulation depth measurement with the combination of a lock-in amplifier and a multimeter

around 20,000 counts (DN).

Multiple image sets per dc voltage setting and per modulation voltage setting were acquired with the imaging system. As described in Chapter 3, the integration of exposures is phase locked to the modulated signal. Using a delay generator (SRS DG535), that is phase locked to the digital function generator, either an image that contains signal (I_{on}) can be acquired or an image that contains no signal (only steady state background, I_{off}) can be acquired. The images that contain signal are considered in-phase images and the images that do not contain signal are considered anti-phase images. Changing the delay in the trigger, generated by the DG535, that initiates an exposure relative to the modulation signal, provides a means for selecting between in-phase and anti-phase images.

Once the in-phase image and the anti-phase image are acquired, the modulation depth is determined, on a pixel by pixel basis, using a two-dimensional form of equa-

tion 1.1. Prior to calculating the modulation depth, multiple frames are also averaged together.

The modulation depth calculations from imaging system measurements are shown in Figures 8.15, 8.16, 8.17, and 8.18. Also included in the figures is the baseline modulation depth that was determined with the lock-in amplifier and multimeter, from Figure 8.14. The data in Figure 8.15 is based on a 20mV modulation signal. Figures 8.16, 8.17, and 8.18 are based on modulation signal voltages of 5mV, 2mV, and 1mV respectively.

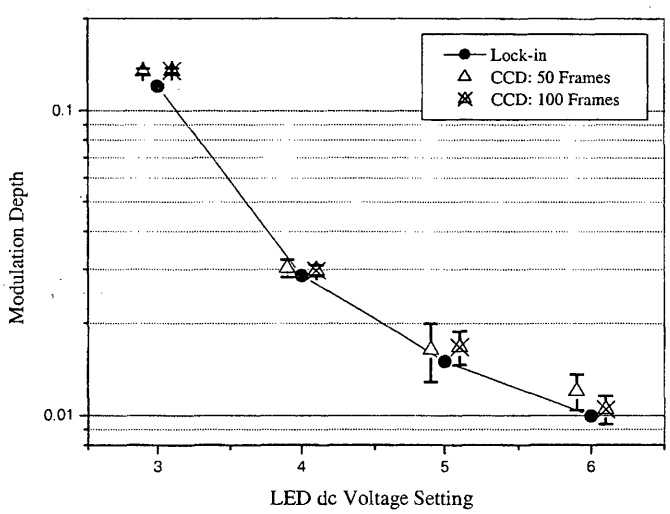

FIG. 8.15. Modulation depth measurement with 20mV input signal modulation

The modulation depth data point shown for the imaging system measurements is the average value over the 100x100 pixel region of interest (ROI). The error bars indicate the range of modulation depth values that were calculated over the ROI. Error bars that do not extend below the mean indicate that negative values were present in the ROI, which are probably caused by $1/f$ noise or drifts in the dc voltage.

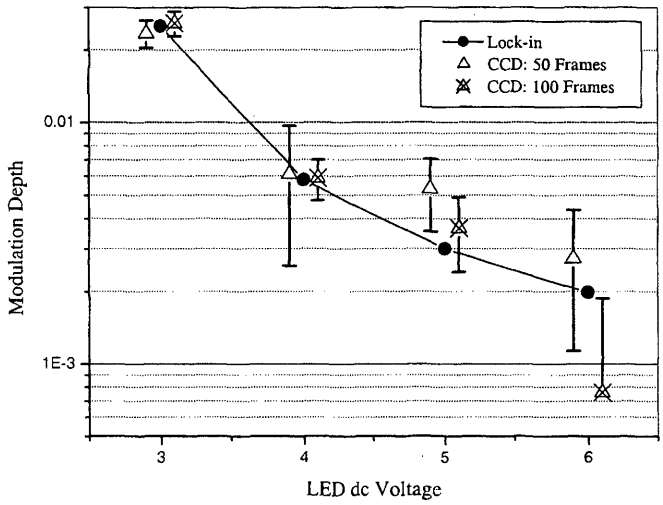

FIG. 8.16. Modulation depth measurement with 5mV input signal modulation

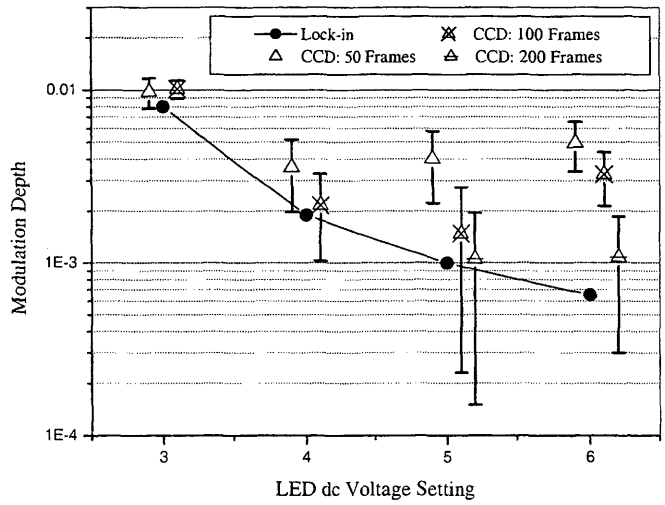

FIG. 8.17. Modulation depth measurement with 2mV input signal modulation

The discrepancy between the baseline modulation depth data and the modulation depth determined with the imaging system becomes very large in Figure 8.18. The modulation depth error is larger than 100% for many data points in Figure 8.18.

Figure 8.18 only shows the results that were feasible. Some of the results, when using a 1mV modulation signal, were returned as negative values. Modulation depth, as defined by equation 1.1, cannot be a negative value, thus, any negative results were discarded.

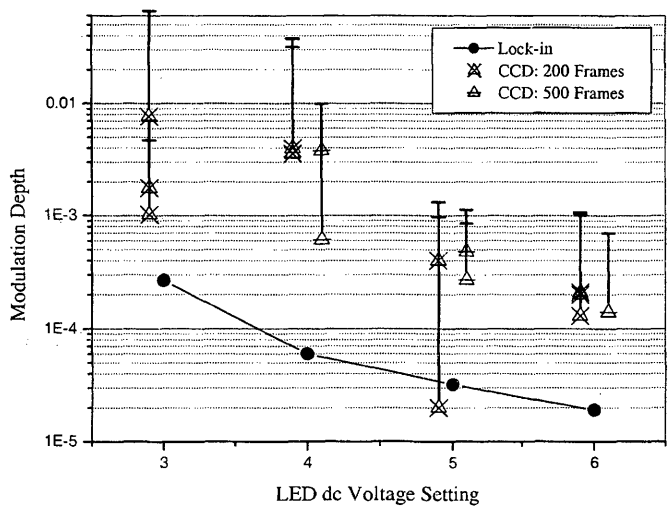

FIG. 8.18. Modulation depth measurement with 1mV input signal modulation

Negative valued modulation depth results are probably due to drifts in the dc voltage (steady state background). While acquiring a set of anti-phase images, the dc voltage likely drifted higher, or when acquiring a set of in-phase images, the dc voltage likely drifted lower. This seems especially reasonable when averaging a set of 100, 200, or 500 images, which takes quite a long period of time and is more suseptible to dc drift ($1/f$ noise).

8.5.4 Detection Limit

Based on the data in Figures 8.17 and 8.18, the imaging system's ability to determine modulation depth appears to be limited to $1\text{x}10^{-3}$. As shown in Figure 8.14, a modulation depth of 10^{-5} was, however, obtainable with the lock-in amplifier. The modulation depth, whether determined with the imaging system or the lock-in amplifier, is limited by the amount of signal power and noise power that manifests itself at the measurement system's output. The amount of signal and noise power produced at the measurement system's output is not only dependent on the system's processing functions but is also dependent on the amount of signal and noise power introduced at the measurement system's input.

The irradiance incident on one of the CCD's pixels can be determined from the integration rate, shown in Figure 8.8, the imaging system's gain, given in equation 6.9, and the ADC conversion gain, A_2, which is not incorporated into the system gain. The integration rate, that was calculated in section 8.3 and is defined here as ν_I, has units of counts or DN (digital number) per second. The ADC gain, A_2, has units of DN per volt. The system gain, G_s, which is a function of the quantum efficiency (η), CCD output amplifier gain (S_v), and the transfer gain (A_1), has units of volts per photon. The arrival rate of photons per pixel, λ_p, can, therefore, be calculated by multiplying the integration rate by the inverse of A_2 and the inverse of G_s. The average, per pixel, arrival rate of photons is, therefore,

$$\nu_I \cdot \frac{1}{A_2} \cdot \frac{1}{G_s} = \lambda_p \tag{8.1}$$

which in terms of units is,

$$\left[\frac{\text{DN}}{\text{sec}}\right] \cdot \left[\frac{\text{Volts}}{\text{DN}}\right] \cdot \left[\frac{\text{photons}}{\text{volt}}\right] = \left[\frac{\text{photons}}{\text{sec}}\right]$$

The parameter values for the system gain are given in section 2.7. The ADC conversion gain is 6.553DN/mV, the CCD output amplifier gain is 30.3μV/electron, and the transfer gain is 4.1V/V. Based on a 500nm wavelength, which is the approximately the peak shown in Figure 8.3, the quantum efficiency is about 45% (Appendix C). Using the values listed produces a system gain, G_s, of about 5.59x10^{-5}.

The integration rate, shown in Figure 8.8, is the average rate of integration per pixel with the LED dc voltage set to 4V. The integration rate becomes fairly constant after integrating approximately 4000 counts (DN). Since the exposure time used to determine modulation depth was set at 125μs, the integration rate calculated at an exposure time of 100μs, as shown in Figure 8.8, was considered in the following analysis. The average integration rate for LED dc voltage settings of 3V, 4V, 5V, and 6V, was calculated for integrations over 4000 counts (DN). These values were then multiplied by the inverse of the ADC gain and the system gain to determine the average arrival rate of photons, as given in equation 8.1.

The average input arrival is considered to be the average steady state background, I_p, incident on each pixel. The average input arrival rate can be converted to irradiance in watts by multiplying by the energy per photon (equation 5.6). Using 500nm as the wavelength, the average arrival rate of photons, per pixel, is converted to the steady state background in watts by multiplying λ_p with ϵ. Table 8.1 lists the results, along with the corresponding standard deviation, from converting the average integration rate to the average steady state background irradiance per pixel.

The steady state background, I_p, given in Table 8.1, is the average irradiance incident on each pixel of the CCD. Since a 100x100 region of interest was used, the average irradiance over the entire array was approximately 10,000 times the values shown in Table 8.1. The average irradiance over the entire array is used as an estima-

LED dc V	ν_I	$\Delta\nu_I$	λ_p	$\Delta\lambda_p$	I_p	ΔI_p
	(DN/sec)		(photons/sec)		(watts)	
3	$1.24\text{x}10^5$	$7.23\text{x}10^2$	$3.37\text{x}10^5$	$1.97\text{x}10^3$	$1.34\text{x}10^{-13}$	$7.85\text{x}10^{-16}$
4	$5.49\text{x}10^5$	$3.04\text{x}10^3$	$1.50\text{x}10^6$	$8.31\text{x}10^3$	$5.95\text{x}10^{-13}$	$3.30\text{x}10^{-15}$
5	$8.96\text{x}10^5$	$5.87\text{x}10^3$	$2.45\text{x}10^6$	$1.60\text{x}10^4$	$9.72\text{x}10^{-13}$	$6.37\text{x}10^{-15}$
6	$1.15\text{x}10^6$	$6.94\text{x}10^3$	$3.15\text{x}10^6$	$1.89\text{x}10^4$	$1.25\text{x}10^{-12}$	$7.52\text{x}10^{-15}$

Table 8.1. Calculation of photon arrival rate (λ_p) and steady state background irradiance (I_p) from the integration rate (ν_I) on a per-pixel basis

tion to the irradiance that was focused onto the photodiode element, which was the transducer for the lock-in amplifier measurements. Under the same LED dc voltage conditions, the steady state background power incident on the photodiode is, therefore, assumed to be 10,000 times larger than the background power incident on a single CCD pixel.

In section 5.5.3 the expected signal power is compared to the photon noise limit for a range of steady state background powers. The comparison is shown graphically in Figure 5.5. The calculated steady state background power per pixel, given in Table 8.1, is incorporated into this comparison and is shown in Figure 8.19. Also shown in Figure 8.19 is the estimated steady state background power incident on the photodiode element.

Figure 8.19 shows that the experimental modulation depth detection limit quoted above is set by the source (LED) rather than by the imaging system. For the average steady state background power that was incident on a single pixel, the minimum expected signal that remains greater than the photon noise limit is about 10^{-3}. The modulation depth data given in Figures 8.17 and 8.18 does, if fact, become noise limited around modulation depths of 10^{-3}.

Figure 8.19 also shows that the lock-in amplifier measurement technique, which uses the photodiode, becomes photon noise limited at a modulation depth of about

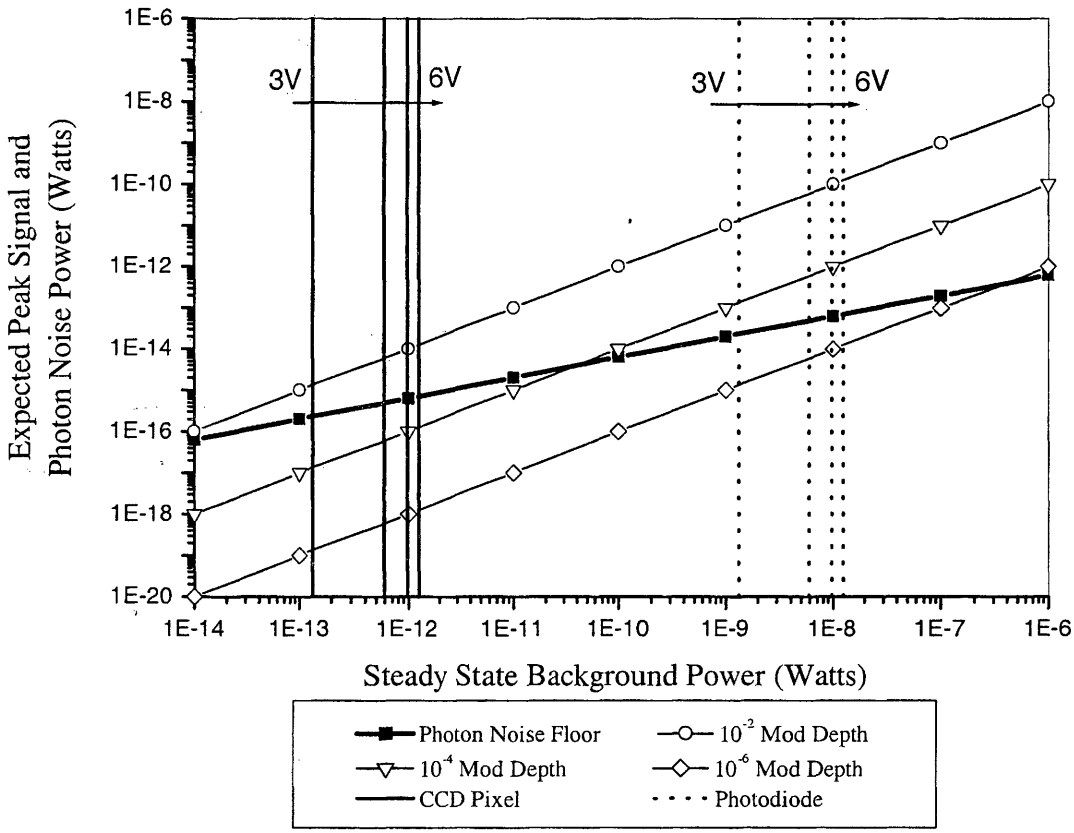

FIG. 8.19. Calculated steady state background irradiance for both a single pixel and the photodiode, compared to the expected peak signal value for modulation depths of 10^{-2}, 10^{-4}, and 10^{-6}, and compared to the photon noise limit

10^{-5}. Figure 8.14 does show that a modulation depth close to 10^{-5} was calculated from measurements with the lock-in amplifier.

Based on Figure 8.19, the LED array does not provide adequate irradiance for testing the imaging system on modulation depths below 10^{-3}. The data in Figures 8.15, 8.16, 8.17, and 8.18 indicates that the minimum detectable modulation depth is photon noise limited. Based on the mathematical models, which are shown graphically in Figures 5.5 and 6.14, the imaging system should be capable of resolving a modulation depth of at least 10^{-4}, if an adequate irradiance source (one that supplies at least 10^{-10} watts per pixel) is utilized.

8.6 Alternate Applications

Besides the ability to measure modulation depth, the imaging system may be applied in other arenas. For example, the gated integration mode could be used in industrial applications for object recognition. The other detection mode, heterodyne detection, may prove useful in imaging applications that require phase information.

8.6.1 Object Recognition

Fringe analysis is an optical technique that can be used for object measurement and object recognition in industrial applications (Arai *et al.*, 1996a). In order to show the systems ability to extract a fringe pattern from an object, a simple experiment was performed using the gated integration mode.

A simple interference pattern (fringe pattern), setup by the constructive and destructive interference from two coherent beams, was focused onto an integrated circuit package, as illustrated in Figure 8.20 (Fisher *et al.*, 1999). One of the beams is a steady state beam and the other is modulated with a mechanical chopper. The

gated integration is, again, phase locked to the modulated beam.

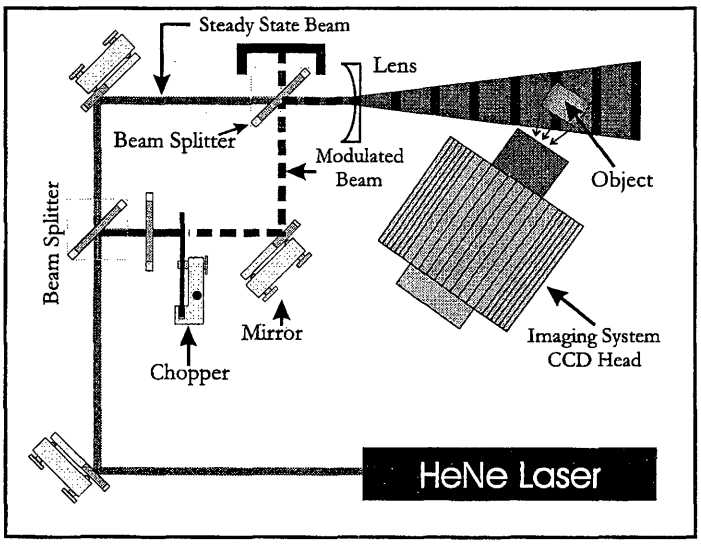

FIG. 8.20. Experimental configuration for fringe analysis

An image with modulation and an image without modulation is acquired by the system. The interference pattern, or fringe pattern, is obtained by differencing the two images. The resulting fringe pattern is shown in Figure 8.21. Since interference exists only in the area where both beams exist, which is in this case on the integrated circuit package, the fringe pattern emphasizes the shape of the object. The background, which does not contain a fringe pattern, becomes a fairly constant value.

The gated integration mode, therefore, may also find application in fringe analysis methods. These methods may prove useful in two-dimensional object recognition and measurement systems. The initial result indicates that further investigation into the use of the imaging system gated integration mode may prove valuable.

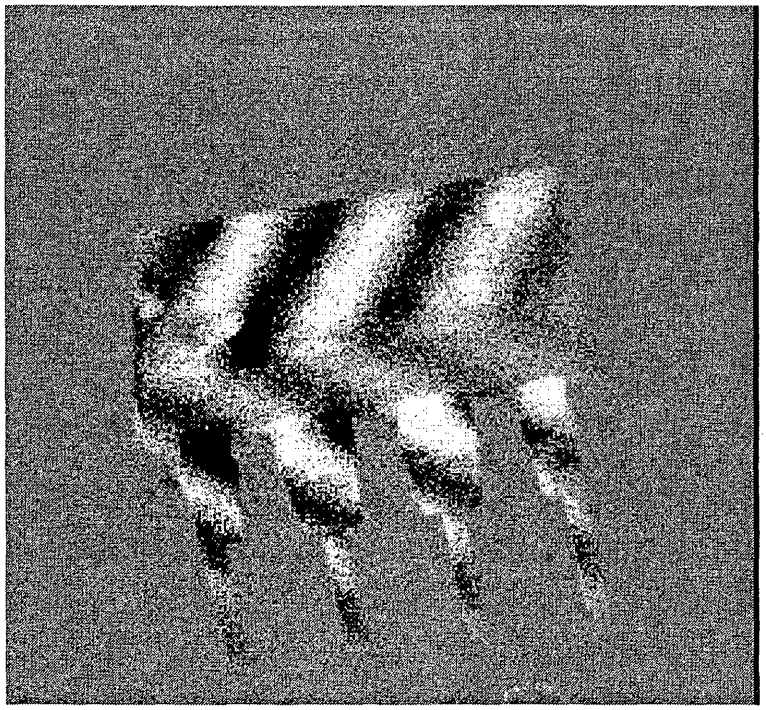

FIG. 8.21. Fringe analysis example

8.6.2 Heterodyne Detection

The heterodyne detection process, described in Chapter 7, did not appear to be applicable to modulation depth measurements in PPAS. It may, however, prove useful to other applications. Unlike the gated integration mode, the heterodyne detection mode retains phase information. The ability to resolve phase data is necessary in range finding instruments, such as LIDAR. Phase information can also enhance diagnostics such as pressure sensitive paint measurements.

The irradiance from an LED is, in this case, set as the combination of a small background (a dc voltage of 3V to surpass the LED's break down voltage, Figure 8.4) and a relatively large modulated signal. The imaging system is, again, phase locked to the modulated signal. The sampling process performed on the CCD chip is, however,

set at a slightly different frequency than the frequency of the modulated signal. The difference in frequency is the intermediate frequency, which is explained in Chapter 7.

In order to acquire data at a rate faster than the intermediate frequency, the number of pixels that can be incorporated into the region of interest (ROI) is quite small. A single row of 100 pixels is set as the ROI to achieve a frame rate of about 30Hz.

Figure 8.22 shows the output from the imaging system in the heterodyne detection mode. In this example, the modulated signal's frequency is set to 4kHz. The sampling performed on the CCD chip is set to 3998Hz, which sets the intermediate frequency to 2Hz. The output of 100 frames, each a row of 100 pixels, is shown in Figure 8.22.

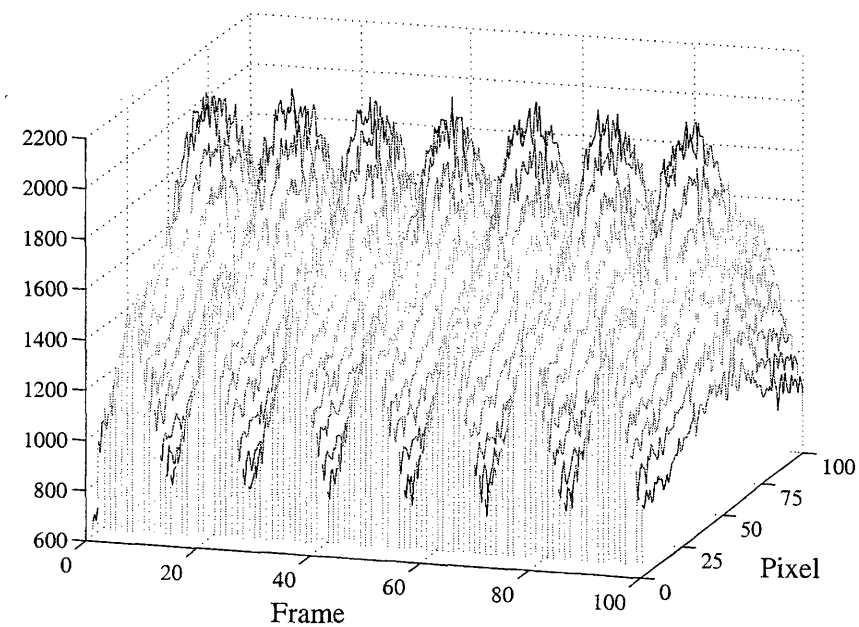

FIG. 8.22. Heterodyne detection output with difference between sampling frequency and modulation frequency set to 2Hz

The power spectral density of the data in Figure 8.22 is determined and shown

in Figure 8.23. The output from the imaging system is, in fact, at the intermediate frequency of 2Hz. Also present in Figure 8.23 are harmonics of the intermediate frequency. These harmonics probably appear because the sampling performed by the imaging system is not purely sinusoidal. Sampling performed by the imaging system was defined in equations 6.1 and 6.2 as a natural sampling function that has frequency components that are harmonics of the sampling frequency.

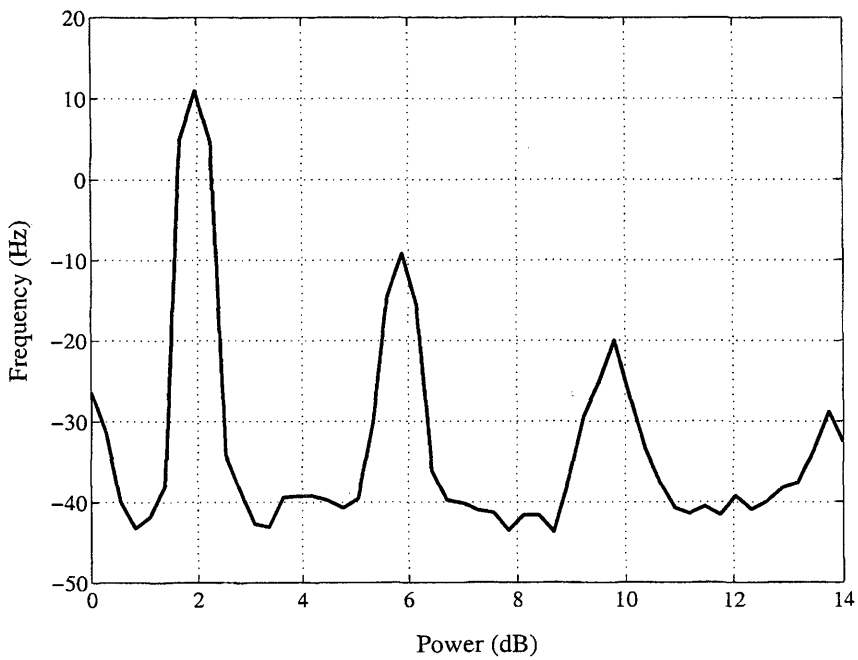

FIG. 8.23. Power spectrum of the 2Hz IF example from Figure 8.22

The primary advantage of the heterodyne detection process, as shown in Figure 8.22, is that the phase information is retained. If for example, multiple signals were present, rather than a single modulated signal, the phase relative to other signal could be determined. This type of information could prove valuable to 3-D depth imaging and harsh environment imaging applications.

Chapter 9

DISCUSSION AND OBSERVATIONS

9.1 System Performance

The imaging system performs well, given the fact that the focal plane processing has been incorporated into a commercially available system, not specifically designed for focal plane processing. A demonstration has shown that a modulation depth of 10^{-3} can be resolved with the imaging system and mathematical modeling suggests that 10^{-4} is obtainable.

The processing functions incorporated into the imaging system are by no means optimized in terms of the signal-processing functions most suitable for extracting modulation depth (Fowler, 2000). In order for an imaging system to accurately resolve modulation depths lower than 10^{-4}, sophisticated processing circuitry must be incorporated at the focal plane.

The level of processing implemented in the interline transfer CCD, which is limited by the architecture itself, was sufficient enough to extract a weakly modulated image from a large background and determine modulation depth. Sophisticated processing implemented in an imaging system specifically designed to resolve modulation depth should be able to perform better and achieve a higher SNR than that achieved with the imaging system in this work. An imaging system specifically designed to remove the steady state background and synchronously extract the information bearing signal could extend two-dimensional modulation depth measurements to at least

10^{-5}.

9.2 Industrial Collaboration

Collaboration with Roper Scientific, Inc., (Princeton Instruments) provided significant momentum for this investigation. The opportunity to obtain a scientific imaging system, gather an understanding of its design, and the ability to modify the design has proved to be invaluable. Both the hardware resources and intellectual property provided by Roper Scientific, Inc., have greatly enhanced this project.

Results from this investigation and joint efforts with Roper Scientific, Inc., have led to the development of other imaging systems. An imaging system, based on the same CCD architecture, that captures two full frame images separated by a short temporal delay has been developed. This imaging system has been demonstrated at university laboratories and is now available as a commercial system. This commercial system is currently being applied to pressure sensitive paint research at the Colorado School of Mines.

Not only has this work directly influenced the development of a commercially available device, but the results have also influenced the design of a new active pixel device. Collaboration with a semiconductor design house has been initiated and a CMOS active pixel sensor has been designed specifically for extracting weakly modulated images from a large background irradiance. As of this writing, the prototype device is in production.

9.3 Project Breadth

In order to complete this investigation, selected fundamentals from a variety of technological disciplines were incorporated. Interdisciplinary topics required in-

vestigation in order to obtain an understanding of the imaging system's role as the transducer in a diagnostic system. In order to develop this understanding, breadth in technological fundamentals was required. A fundamental understanding of

- analog circuitry design and hardware development,
- digital logic design and hardware implementation,
- communications and linear systems analysis fundamentals,
- optics fundamentals,
- semiconductor technology specific to CCDs and CMOS active pixel sensors,
- fundamentals of laser diagnostics and spectroscopy,
- image processing techniques,
- statistical and probabilistic systems analysis, and
- measurement and instrumentation technology,

was incorporated at multiple stages of this investigation.

A particular important result is the fact that much of the analysis performed in this work is actually not specific to pump-probe absorption spectroscopy or the interline transfer imaging system. The models were formulated to conform to their parameters and follow their attributes and functions. Nothing about the framework of the analysis is, however, specific to laser diagnostics or imaging.

This work, therefore, contains a solid analytical treatment and a collection of pragmatic tools that can be used to analyze technical systems. This tool-set not only includes the mathematical fundamentals from linear systems theory but also methodologies aimed at understanding the parts of a technical device or process as sub-systems.

Chapter 10

CONCLUSIONS

10.1 General Summary

An imaging system that extracts a weakly modulated image that is superimposed on a large background and is embedded in noise has been developed and investigated. In order to complete this task, application specific functions, that operate at the focal plane, have been incorporated into an imaging system. The functionality of the imaging system has been modeled. A separate model of the input irradiance was also developed and was used in the analysis of the imaging system.

After the system was modeled, the application specific functions were then demonstrated. This demonstration showed that the proposed integration threshold is not generally viable as a mechanism for improving the signal-to-noise ratio (SNR) beyond the SNR obtained without the integration threshold. The system was shown, however, to have the capability to extract a weakly modulated image from a large background irradiance. Based on the imaging system's ability and the demonstration of its processes, other applications have also become apparent.

10.2 Contributions of this Work

The result of this work contributes to not only the field of detection for laser diagnostics but also to a selection of other imaging applications. Primarily, the application specific CCD functions, the related mathematical models, and the mathemati-

cal model of the input irradiance can prove useful to two-dimensional laser diagnostic investigations and to the design of new detection systems for these diagnostic investigations. The contributions are further outlined in the following sections.

10.2.1 Two-Dimensional Gated Integration with a CCD

A commercial interline transfer CCD is used as a two-dimensional gated integrator. Synchronizing the CCD's exposure mechanism with a signal's frequency and phase produces a imaging system that can be operated as a gated integrator. In the gated integrator mode the input irradiance is either integrated or rejected at the focal plane.

10.2.2 Integration Threshold Implementation and Investigation

An integration threshold feature is implemented and investigated in the interline transfer CCD architecture. A potential barrier between the CCD's sensor and storage well is used to create a dead-band threshold, which accumulated charge in the sensor must surpass before it is integrated in a storage well. The process is similar to anti-blooming, which is implemented with another potential barrier and the substrate potential well.

The results show that an integration threshold can be implemented in a commercially available interline transfer CCD, even though it is not designed for such an application. The integration threshold does, in fact, introduce a dead-band that reduces the amount of charge integrated per exposure, thus, eliminating some of the steady state background. As a result, a greater number of exposures can be integrated prior to reaching saturation.

The integration threshold feature is, however, not recommended as a process for

increasing the signal-to-noise ratio (SNR). As the threshold barrier is increased, the pixel-to-pixel spatial noise increases dramatically. The amount of irradiance reduction, indicated by the integration threshold coefficient, also varies across the array and is signal dependent. The integration threshold is, therefore, not suitable for precise measurements, such as modulation depth, that require the threshold coefficient be known.

Because it was possible to introduce a dead-band into a device not specifically designed for such a feature, the integration threshold could be more attractive if it is considered in the design stage of a new device. The integration threshold could perform quite well if it were designed into the architecture of an applications specific device. Incorporating CMOS APS technology would provide enhanced focal plane processing capability that could be used to refine the integration threshold feature.

10.2.3 Heterodyne Detection with a CCD

The interline transfer CCD can also be operated as a heterodyne detector. The CCD's exposure mechanism is again synchronized to a signal's phase. The frequency of exposures is, however, different than the frequency of the signal. Using this type of detection method transfers the signal to an intermediate frequency, that can be set below the imaging system's frame rate.

Operating the imaging system in this mode produces a set of frames that contain both the signal's frequency and the signal's phase information. The phase information can then be used, as another parameter, in measuring a characteristic in the object plane.

10.2.4 Input Irradiance Model Development

The input irradiance, used in analyzing the imaging system, is modeled as the linear sum of probe beam components. Defining the input irradiance as the sum of individual spectra provides both flexibility and convenience in analyzing the imaging system. With these definitions, it is possible to investigate the spectral composition of each component before it enters a detection system and after it has been processed by a detection system. The definition of the input irradiance developed in this work is general, flexible, and can easily be used in the design and analysis of other detection systems.

10.2.5 Imaging System Model Development

Mathematical models of the imaging system are presented and analyzed. The foundation for the models is built from communications and linear systems theory. The model development practice and analysis procedure provides insight to the detection process at a systems level. The detection parameters are investigated and specified to improve performance.

A laser diagnostic and an imaging system are modeled and analyzed with linear mathematical models, which are founded on fundamental communications theories. These models and this analysis shows its flexible nature, effectiveness, and benefits obtained from investigating a technical system with this approach. The system's parameters can be analyzed individually and prescribed to improve performance. Since the approach has been beneficial to the analysis of the combination of a laser diagnostic and an imaging system, it can also be useful to many other, unrelated technical systems.

10.2.6 Diagnostic Imaging Performance Prediction

The imaging system's performance is defined in the context of modulation depth measurement for pump-probe absorption spectroscopy diagnostics. Using the gated integration mode, the imaging system can extract a weakly modulated image from both a large background irradiance and noise. The ratio of the magnitude of the modulated image to the magnitude of the background irradiance is defined as the modulation depth. Modulation depth of 10^{-4} or less can be used in spectroscopic calculations to determine species number density.

It is shown, that the imaging system can extract modulated images and that a modulation depth of 10^{-3} can be obtained. The measurements were limited by the irradiance source used for calibration and testing. Had the irradiance been adequate, models of the irradiance and imaging system indicate that a modulation depth of 10^{-4} can be resolved.

Since the imaging system has been shown to have the ability to extract a modulation depth of 10^{-3}, it can also be utilized in other applications that have less stringent measurement requirements. Interference patterns can be resolved with the imaging system operated in the gated integration mode. Such measurements can be used for object recognition.

10.3 Limitations of this Work

The noise analysis of the input irradiance did not include spatial noise. The irradiance source was not entirely adequate. The imaging system was not applied directly to the laser diagnostic analyzed and post-processing the images to enhance signal extraction was not investigated further. Recommendations to continue this investigation and expand on the findings are outlined in the following sections.

10.3.1 Spatial Noise Considerations

Spatial noise, which is a random fluctuation in irradiance across the profile of the probe beam, was not considered as a source of noise in the analysis. It was assumed that each pixel across the imaging array was incident with the same irradiance. The model of the input irradiance, and the imaging system model, should be extended to include the effects of stochastic spatial variations. This extension would enhance the models and provide an investigation that is closer to the system's actual performance.

Along these lines, an analysis of spatial noise may lead to the implementation of other signal-processing techniques, possibly including spatial filters. Image processing algorithms could be incorporated that account for low frequency spatial variations and, essentially, register respective images for calculations. Some type of spatial modulation may also be attractive. Spatially modulating the signal, in addition to the temporal modulation, may move the signal to a spatial frequency that is not affected by random low frequency spatial drifts.

10.3.2 Irradiance Source

The irradiance test source did not produce adequate irradiance for resolving a modulation depth lower than 10^{-3}. The input irradiance was photon limited around this range. The imaging system could, therefore, only perform to the photon noise limit.

Another irradiance source needs to be developed that both produces adequate irradiance (to allow calibration and measurement at or below 10^{-5}) and is configurable. The source must have outputs (electronic) that can be used for synchronization and the irradiance that is produced must be controllable.

10.3.3 Diagnostic Application

The imaging system was applied to a pump-probe absorption spectroscopy experiment. Conclusions were, however, unattainable from the images acquired during the experiment. Since the characteristics of the imaging system were at the time unknown, an apparatus that could be configured, accurately controlled, and repeated, was needed to characterize the imaging system. Since the imaging system is now characterized, it should now be applied to an actual diagnostic.

10.3.4 Signal Enhancement with Image Processing Algorithms

Image processing algorithms, performed in software after obtaining images, were not extensively considered as a method to further enhance the final image data. Image processing should be considered as an important tool that can be used to enhance the image data and improve the overall system's ability to resolve modulation depth.

10.4 Suggestions For Future Work

Besides the suggestions included in the previous section, an extension of the interline transfer architecture is suggested for further investigations. An interline frame transfer CCD, which is an architecture that is a combination of the interline transfer and frame transfer architectures may provide more flexibility. In the normal interline transfer CCD, integration, both in the gated integration mode and the heterodyne detection mode, cannot commence until the previous image is completely read from the array. A combination of interline transfer and frame transfer architectures could be used to quickly transfer the image to a mask area, where it would then be read from the array, while integration of the next consecutive image has been initiated.

10.5 Conclusion

An imaging system that uses an interline transfer CCD as the transducer can operate in both a gated integration mode and a heterodyne detection mode. These functional modes are accomplished by synchronizing focal plane mechanisms with the input signal's frequency and phase. An integration threshold can also be incorporated into an interline transfer CCD, however, the noise from such an implementation precludes its effectiveness. In a test application, the imaging system can measure a modulation depth of 10^{-3}. Based on the modeling and analysis performed, lower modulation depths may be obtainable with the imaging system.

The modeling approach used in this work is flexible and effective. Based on the analysis performed in this investigation, it is apparent that many other and unrelated technical systems can also benefit from the underlying framework of analysis in this thesis.

REFERENCES

Amelio, G. F., Tompsett, M. F., & Smith, G. E. 1970. Experimental Verification of the Charge Coupled Device Concept. *The Bell System Technical Journal*, **49**(4), 593–600.

Arai, Yasuhiko, Yokozeki, Shunsuke, Shiraki, Kazuhiro, & Yamada, Tomoharu. 1996a. High-speed fringe analysis method using frequency demodulation technology. *Optical Engineering*, **35**(8), 2341–2344.

Arai, Yasuhiko, Yokozeki, Shunsuke, Shiraki, Kazuhiro, & Yamada, Tomoharu. 1996b. High-speed two-dimensional fringe analysis using frequency demodulation. *Pages 377–384 of: Optical Inspection and Micromeasurements*, vol. 2782. Proc. SPIE.

Barbe, David F. 1975. Imaging Devices Using the Charge-Coupled Concept. *Proceedings Of The IEEE*, **63**(1), 38–67.

Bevington, Philip R., & Robinson, D. Keith. 1992. *Data Reduction And Error Analysis For The Physical Sciences.* Second edn. New York, NY: The McGraw-Hill Companies, Inc.

Beyer, William H. 1978. *CRC Standard Mathematical Tables.* Twenty-fourth edn. West Palm Beach, FL: CRC PRESS, Inc.

Boyle, W. S., & Smith, G. E. 1970. Charge Coupled Semiconductor Devices. *The Bell System Technical Journal*, **49**(4), 587–593.

Burgess, Arthur E. 1999. The Rose Model, revisited. *J. Opt. Soc. Am. A*, **16**(3), 633.

Burke, Barry E., & Dan L. Smythe, Jr. 1983. A CCD Time-Integrating Correlator. *IEEE Journal Of Solid-State Circuits*, **18**(6), 736–744.

Burns, Peter D. 1989. Image Signal Modulation and Noise Characteristics of Charge-Coupled Device Imagers. *Pages 144–152 of: Optical Sensors and Electronic Photography*, vol. 1071. Proc. SPIE.

Burns, Peter D. 1990. Signal-To-Noise Ratio Analysis Of Charge-Coupled Device Imagers. *Pages 187–194 of: Charge-Coupled Devices and Solid State Optical Sensors*, vol. 1242. Proc. SPIE.

Chitti, Yasmina. 1997. Detection of Small Local Intensity Changes in CCD Images with Nonuniform Illumination and Large Signal Dependent Noise. *Graphical Models and Image Processing*, **59**(2), 139–148.

Cooper, George R., & McGillem, Clare D. 1999. *Probabilistic Methods of Signal and System Analysis.* New York, NY: Oxford University Press, Inc.

Couch, Leon W. 1995. *Modern Communication Systems: Principles and Applications.* Upper Saddle River, NJ: Prentice Hall, Inc.

Cunningham, Ian A., & Shaw, Rodney. 1999. Signal-to-noise optimization of medical imaging systems. *J. Opt. Soc. Am. A*, **16**(3), 621.

Dereniak, Eustace L., & Crowe, Devon G. 1984. *Optical Radiation Detectors.* New York, NY: John Wiley & Sons, Inc.

Drouillard, Thomas F. 1998. *Mathematical Analysis of PIV Image Data, and Analysis*

Implementation and Image Rendering On a PC. M.S. thesis, Colorado School of Mines, Golden, CO.

Drouillard, Thomas F., Fisher, Chad W., Linne, Mark A., Middleton, Nigel T., Fiechtner, Gregory J., Goss, Larry P., & Gord, James R. 2000. Evaluation of New Camera Architectures for Pressure Sensitive Paint Measurements. the 21st AIAA Aerodynamic Measurement Technology and Ground Testing Conference, nos. Invited Paper No. AIAA–2000–2524.

Eckbreth, A. C. 1996. *Laser Diagnostics for Combustion Temperature and Species.* 2 edn. Amsterdam: Gordon and Breach.

Eklund, Jan-Erik, Svensson, Christer, & Aström, Anders. 1996. VLSI Implementation of a Focal Plane Image Processor - A Realization of the Near-Sensor Image Processing Concept. *IEEE Transactions On Very Large Scale Integration (VLSI) Systems*, **4**(3), 322.

Fiechtner, G.J., & Linne, M.A. 1994. Absolute Concentrations of Potassium by Picosecond Pump/Probe Absorption in Fluctuating, Atmospheric Flames. *Combustion Science and Technology*, **100**, 11–27.

Fisher, C.W., Linne, M.A., & Middleton, N.T. 1999. Phase Sensitive Imaging In Flows. 37th AIAA Aerospace Sciences Meeting & Exhibit, nos. AIAA–99–0771.

Fossum, Eric R. 1989. Architectures for focal plane image processing. *Optical Engineering*, **28**(8), 865–871.

Fossum, Eric R. 1993. Active Pixel Sensors: Are CCD's Dinosaurs? *Pages 2–14 of: Charge-coupled devices and solid state optical sensors*, vol. 1900. Proc. SPIE.

Fossum, Eric R., & Barker, Richard Clark. 1984. A Linear and Compact Charge-Coupled Charge Packet Differencer/Replicator. *IEEE Transactions On Electron Devices*, **31**(12), 1784–1789.

Fowler, John B. 2000. *Signal Processing Studies of Detector Systems for use in Single-Point Pump/Probe Absorption Spectroscopy.* M.S. thesis, Colorado School of Mines, Golden, CO.

French, T.E. 1996. *The Development of Fluorescence Lifetime Imaging and An Application in Immunology.* Ph.D. thesis, University of Illinois at Urbana-Champaign.

Frey, M. 1995. A finite point process model of shot noise. *In: Computational Stochastic Mechanics.* BR Rotterdam, Netherlands: A. A. Balkema Publishers.

Haas, W. H., Dixon, G. S., & Soon, N. Y. 1979. Performance of mosaic sensor dim-target detection algorithms. *Pages 25–32 of: Smart Sensors*, vol. 178. Proc. SPIE.

Hakkarainen, J. Mikko, & Lee, Hae-Seung. 1993. A 40x40 CCD/CMOS Absolute-Value-of-Difference Processor for Use in a Stereo Vision System. *IEEE Journal Of Solid-State Circuits*, **28**(7), 799–807.

Halford, Donald. 1968. A General Mechanical Model for $|f|^{\alpha}$ Spectral Density Random Noise with Special Reference to Flicker Noise $1/|f|$. *Proceedings Of The IEEE*, **56**(3), 251–258.

Hanson, R. K. 1986. Combustion Diagnostics: Planar Imaging Techniques. *Page 1677 of: 21st International Symposium on Combustion.* The Combustion Institute, Pittsburgh, PA.

Harada, Yasuhiro, Asakura, Toshimitsu, & Murakami, Terutoshi. 1992. Spatial and temporal analysis of solid-state imaging systems. *Applied Optics*, **31**(23), 4758–4768.

Helstrom, Carl W. 1991. *Probability And Stochastic Processes For Engineers.* New York, NY: Macmillan Publishing Company.

Holst, Gerald C. 1996. *CCD Arrays, Cameras, and Displays.* Winter Park, FL: JDC Publishing.

Horenstein, Mark N. 1990. *Microelectronic Circuits & Devices.* Englewood Cliffs, NJ: Prentice-hall, Inc.

Horowitz, Paul, & Hill, Winfield. 1989. *The Art of Electronics.* New York, NY: Cambridge University Press.

Janesick, James R., Klaasen, Kenneth, & Elliott, Tom. 1985. CCD charge collection efficiency and the photon transfer technique. *Pages 7–19 of: Solid State Imaging Arrays*, vol. 570. Proc. SPIE.

Janesick, James R., Elliott, Tom, Collins, Stewart, Blouke, Morley M., & Freeman, Jack. 1987. Scientific charge-coupled devices. *Optical Engineering*, **26**(8), 692–714.

Johnson-Cole, H., & Clark, R.L. 1991. A Validated CCD Camera Model. *Pages 203–211 of: Infrared Imaging Systems: Design, Analysis, Modeling, and Testing II*, vol. 1488. Proc. SPIE.

Johnston, Gregory E. 1995. Nonlinear Control of Charge Coupled Device Sensors. vol. 2432. Proc. SPIE.

Keshner, Marvin S. 1982. $1/f$ Noise. *Proceedings Of The IEEE*, **70**(3), 212–218.

Kopeika, Norman S. 1998. *A System Engineering Approach To Imaging.* Bellingham, Washington: Proc. SPIE.

Levine, Peter A. 1985. Low-Noise CCD Signal Recovery. *IEEE Transactions on Electron Devices*, **32**(8), 1534–1537.

Linne, M.A., Morse, D.C., Skilowitz, J.L., Fiechtner, G.J., & Gord, J.R. 1995a. Two-dimensional Pump/Probe Imaging in Reacting Flows. *Optics Letters*, **20**(23), 2414.

Linne, Mark, Lyon, Torsten, Gord, James, Weaver, William L., & Fiechtner, Gregory. 1995b. *Noise and Tuning Properties of Regeneratively Mode-Locked Ti:sapphire Lasers for Combustion Spectroscopy.* Tech. rept. Colorado School of Mines, Golden, CO.

Marshall, G. F., & Collins, S. 1998. A High Dynamic Range Front End for Automatic Image Processing Applications. *In: EUROPTO Conference on Advanced Focal Plane Arrays and Electronic Cameras II*, vol. 3410. Proc. SPIE.

Mendis, Sunetra K., Kemeny, Sabrina E., Gee, Russell C., Pain, Bedabrata, Staller, Craig O., Kim, Quiesup, & Fossum, Eric R. 1997. CMOS Active Pixel Image Sensors for Highly Integrated Imaging Systems. *IEEE Journal Of Solid-State Circuits*, **32**(2), 187–197.

Motchenbacher, C. D., & Connelly, J. A. 1993. *Low-Noise Electronic System Design.* New York, NY: John Wiley & Sons, Inc.

O'Malley, Mark, & O'Mongain, Eon. 1992. Charge-coupled devices: frame adding as an alternative to long integration times and cooling. *Optical Engineering*, **31**(3), 522–526.

Oppenheim, Alan V., & Willsky, Alan S. 1997. *Signals & Systems*. 2 edn. Upper Saddle River, NJ: Prentice-Hall, Inc.

Pain, Bedabrata, Mendis, Sunetra K., Schober, Robert C., Nixon, Robert H., & Fossum, Eric R. 1993. Low-power low-noise analog circuits for on-focal-plane signal processing of infrared sensors. *Pages 365–374 of: Infrared Detectors and Instrumentation*, vol. 1946. Proc. SPIE.

Pallás-Areny, Ramón, & Webster, John B. 1991. *Sensors And Signal Conditioning*. New York, NY: John Wiley & Sons, Inc.

Paul, P. H. 1991. The Application of Intensified Array Detectors to Quantitative Planar Laser-Induced Fluorescence Imaging. AIAA/SAE/ASME/ASEE 27th Joint Propulsion Conference, nos. AIAA–91–2315.

Pelli, Denis G., & Farell, Bart. 1999. Why use noise? *J. Opt. Soc. Am. A*, **16**(3), 647.

Pierret, Robert F. 1996. *Semiconductor Device Fundamentals*. Reading, MA: Addison-Wesley Publishing Co., Inc.

Povel, Hanspeter. 1995. Imaging Stokes polarimetry with piezoelastic modulators and charge-coupled device image sensors. *Optical Engineering*, **34**(7), 1870–1878.

Povel, Hanspeter, Aebersold, Hans, & Stenflo, Jan O. 1990. Charge-coupled device image sensor as a demodulator in a 2-D polarimeter with a piezoelastic modulator. *Applied Optics*, **29**(8), 1186–1190.

Ratzlaff, Kenneth L., & Paul, Steven L. 1979. Characterization of a Charge-coupled Device Photoarray as a Molecular Absorption Spectrophotometric Detector. *Applied Spectroscopy*, **33**(2), 240–245.

Roper Scientific, Inc. (Princeton Instruments). 1998a. *MicroMAX System Manual.* 3, b edn. Trenton, NJ.

Roper Scientific, Inc. (Princeton Instruments). 1998b. *WinView User's Manual.* 2, b edn. Trenton, NJ.

Schroder, Dieter K. 1987. *Advanced MOS Devices.* Modular Series On Solid State Devices, vol. 7. Reading, MA: Addison-Wesley Publishing Co., Inc.

Seitz, P., Leipold, D., Kramer, J., & Raynor, J. M. 1993. Smart optical and image sensors fabricated with industrial CMOS/CCD semiconductor processes. *Pages 21–30 of: Charge-Coupled Devices and Solid State Optical Sensors*, vol. 1900. Proc. SPIE.

Seitz, P., Spirig, T., Vietze, O., & Metzler, P. 1995a. The Lock-In CCD And The Convolver CCD - Applications Of Exposure-Concurrent Photo-Charge Transfer In Optical Metrology And Machine Vision. vol. 2415. Proc. SPIE.

Seitz, Peter. 1996. Smart Image Sensors: An Emerging Key Technology For Advanced Optical Measurement And Microsystems. *Pages 276–284 of: Micro-optical Technologies For Measurement, Sensors, and Microsystems*, vol. 2783. Proc. SPIE.

Seitz, Peter, Spirig, Thomas, Vietze, Oliver, & Engelhardt, Kai. 1995b. Smart sensing using custom photo-application-specific integrated circuits and charge-coupled device technology. *Optical Engineering*, **34**(8), 2299–2308.

Séquin, Carlo H., & Tompsett, Michael F. 1975. *Charge Transfer Devices.* Advances In Electronics And Electron Physics, vol. 8. New York, NY: Academic Press, Inc.

Settersten, T. B. 1999. *Picosecond Pump-Probe Diagnostics For Combustion.* Ph.D. thesis, Colorado School of Mines.

Snyder, Donald L., Hammoud, Abed M., & White, Richard L. 1993. Image recovery from data acquired with a charge-coupled-device camera. *J. Opt. Soc. Am. A*, **10**(5), 1014–1023.

Solhusvik, Johannes, Lavernhe, Francis, Montseny, Gérard, & Farré, Jean A. 1997. A New Low-Noise CCD Signal Acquisition Method Based on a Commutable Band-Pass Filter. *IEEE Transactions On Circuits and Systems II: Analog and Digital Signal Processing*, **44**(3), 164–173.

Sony. 1998. *CCD Camera System, Semiconductor Selection Guide.* www.sony-semi.com.

Spirig, T., Seitz, P., Vietze, O., & Heitger, F. 1995. The Lock-In CCD – Two-Dimensional Synchronous Detection of Light. *IEEE Journal Of Quantum Electronics*, **31**(9), 1705–1708.

Spirig, Thomas, Marley, Michael, & Seitz, Peter. 1997. The Multitap Lock-In CCD with Offset Subtraction. *IEEE Transactions On Electron Devices*, **44**(10), 1643–1647.

Stanford Research Systems, SRS. 1999. *Scientific And Engineering Instruments Manual.* Sunnyvale, CA.

Stremler, Ferrel G. 1990. *Introduction to Communication Systems.* 3 edn. Reading, MA: Addison-Wesley Publishing Co., Inc.

Takeda, Mitsuo, & Kitoh, Masahiro. 1991. Spatio-temporal frequency-multiplex heterodyne interferometry. *Pages 66–71 of: Laser Interferometry IV: Computer-Aided Interferometry*, vol. 1553. Proc. SPIE.

Tao, T. F., Hilmers, D., Evenor, B., & Yehoshua, D. Bar. 1979. Focal plane processing techniques for background clutter suppression and target detection. *Pages 2–12 of: Smart Sensors*, vol. 178. Proc. SPIE.

Taub, Herbert, & Schilling, Donald L. 1986. *Principles of Communication Systems.* 2 edn. New York, NY: The McGraw-Hill Companies, Inc.

Wang, H., Hengstermann, T., Reuter, R., & Willkomm, R. 1992. Robust Improvement In The Signal-to-Noise Of A Laser Fluorosensor Through Selectively Averaging Signals. *Review of Scientific Instruments*, **63**(3), 1877–1879.

Winzer, Peter J. 1997. Shot-noise formula for time-varying photon rates: a general derivation. *J. Opt. Soc. Am. B*, **14**(10), 2424–2429.

APPENDIX A

Cooled CCD Cameras

based on the Sony 1300 × 1030 Interline CCD

MicroMAX-1300Y

These cameras are ideal for high resolution fluorescence microscopy applications requiring high blue-green sensitivity, but not requiring high frame rates.

These cameras are recommended for GFP imaging, FISH and general fluorescence imaging.

The key features include:

- High QE in the blue-green
- Smallest pixel: 6.7 µm, 1.3 million pixels
- Electronic shuttering
- Programmable readout capabilities (subregion, binning)
- 100% duty cycle
- Fast focus video signal

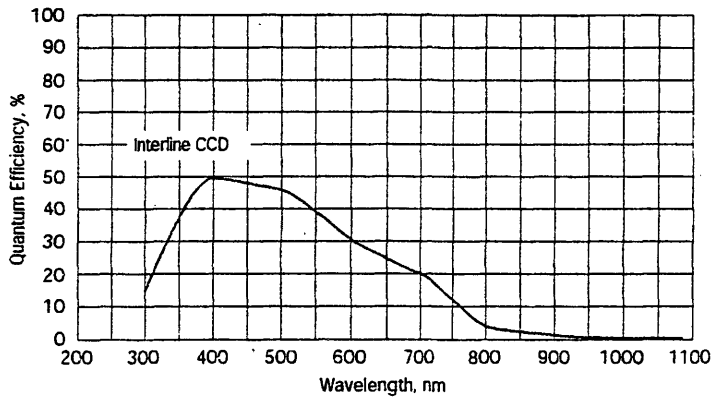

CCD Array
Sony ICX061

CCD Format
1300 × 1030; 8.71 × 6.90 mm overall; 6.7 × 6.7 µm pixels center-to-center

Full Well Capacity
20,000 electrons typical; 40,000 with 2 × 2 binning

Readout Noise
6-9 electrons at 1 MHz

Spectral Range
300-800 nm

Dynamic Range
11-12 bits

Response Nonlinearity
<1%

Blemish Specifications
Grade 0, no point, cluster, or column defects. These specifications are based exclusively on the manufac-turer's cosmetic blemish definitions.

Operating Temperature
-10 °C for RTE/CCD with TE cooling

Thermostating Precision
±0.040 °C over entire temperature range

Typical Dark Charge
0.05 electrons/pixel-second at -10 °C

Scan Rate
1 MHz

Readout Rates (frames per second)

Binning	Region 1300×1030	400×400	200×200	100×100
1×1	0.7	2.6	5.4	9
2×2	1.9	5.4	9	14
3×3	3.2	7.5	12	17
4×4	4.3	9	14	19

QE values presented above are average for the entire pixel area, including the effect of microlenses with nearly collimated light (as output from a microscope). Effective QE may decline slightly in low f/# systems.

Lumogen coating is not recommended on this CCD.

Although no mechanical shutter is required on this camera, a mechanical shutter is available either mounted on the camera or for the use elsewhere in the optical path for special operating modes.

APPENDIX B

BURIED-CHANNEL CCD CONCEPT

B.1 Charge Collection in a Semiconductor

The Poisson equation, which relates electrostatic potential and charge density in electricity and magnetism, is often used as a starting point when analyzing semiconductor devices and obtaining quantitative solutions to the electrostatic variables (Pierret, 1996). The three dimensional Poisson relationship is

$$\nabla^2\phi = \frac{-\rho}{\kappa} \tag{B.1}$$

where ϕ is the electrostatic potential, ρ is charge density, and κ is a dielectric constant. Simplifying the equation to a single dimension and applying it specifically to a semiconductor material gives

$$\frac{\partial^2\phi}{\partial x^2} = \frac{-\rho}{\kappa_s\epsilon_o} \tag{B.2}$$

where x is the semiconductor material depth, ρ is the charge density in the material, κ_s is the dielectric constant for the semiconductor material, and ϵ_o is the permittivity of free space.

Knowing that the electric field, in three dimensions, is

$$E = -\nabla\phi \tag{B.3}$$

which in a single dimension is

$$E = -\frac{\partial\phi}{\partial x} \tag{B.4}$$

allows us to find the electric field across a semiconductor by integrating the charge density as a function of distance (Dereniak & Crowe, 1984).

$$E(x) = \int \frac{\rho}{\kappa_s \epsilon_o}\, dx \tag{B.5}$$

Finally, the potential distribution along the depth of the semiconductor material can be found by integrating the electric field with respect to the depth x.

$$\phi(x) = \int E(x)\, dx \tag{B.6}$$

The P-type region, as shown in figure B.1(b), is completely depleted of holes by holding it at the negative potential ϕ_c. The charge density, $\rho(x)$, in the P-type region from $x = 0$ to $x = x_p$ is, thus, a uniform function of the acceptor doping,

$$\rho(x) = -qN_a \qquad 0 < x \leq x_p \tag{B.7}$$

where q is the charge on an electron ($q = 1.602 \text{ x } 10^{-19}\ C$) and N_a is the total number of doped acceptor atoms. The charge density in the N-type region from $x = x_p$ to

$x = x_p + x_d$ also has a uniform distribution with respect to the doping,

$$\rho(x) \;=\; qN_d \qquad x_p < x \leq x_p + x_d \tag{B.8}$$

where N_d is the total number of doped donor atoms.

The distance x_d is the depletion depth and is determined by both the doping density and the charge, Q_g, at the gate. The integrated charge across the entire structure must be neutral (Dereniak & Crowe, 1984). Therefore, the charge on the gate determines x_d by

$$Q_g \;=\; qN_a x_p - qN_d x_d \tag{B.9}$$

which can be rewritten as

$$x_d \;=\; \frac{N_a x_p - \frac{Q_g}{q}}{N_d}. \tag{B.10}$$

From equation B.5, we find the electric field across the structure, as shown in figure B.1(c), by integrating the charge distribution, $\rho(x)$, along the depth of the material. From $x = x_o$ to $x = 0$, the electric field is

$$E(x) \;=\; \int \frac{\rho}{\kappa_o \epsilon_o}\, dx \;=\; \frac{1}{\kappa_o \epsilon_o} \int Q_g.\delta(x + x_o)\, dx \tag{B.11}$$

which integrates to a step function and shows that the electric field in the silicon dioxide, SiO_2, region is a constant.

$$E_1(x) \;=\; \frac{Q_g}{\kappa_o \epsilon_o} \qquad -x_o < x \leq 0 \tag{B.12}$$

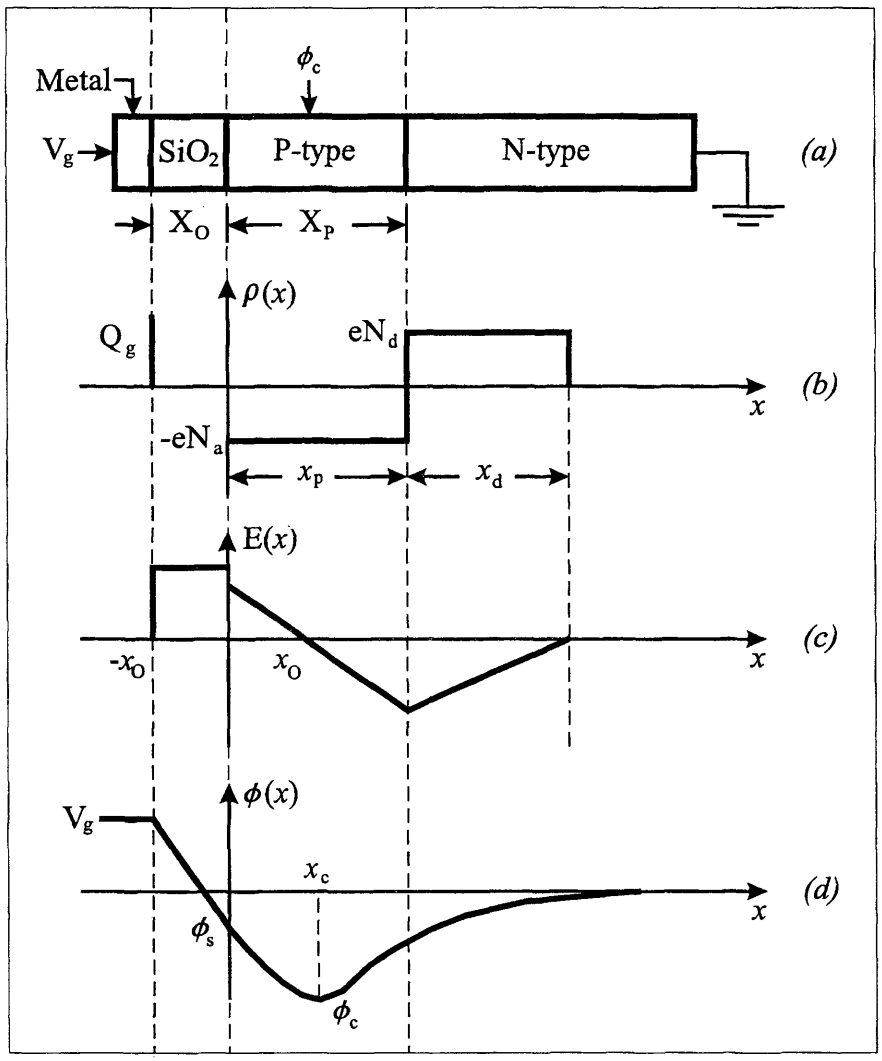

FIG. B.1. Buried-Channel CCD Illustration: (a) semiconductor structure, (b) charge density profile, (c) electric field profile, (d) potential profile.

The constant κ_o, in equation B.12, is the dielectic constant for SiO_2.

The electric field from $x = 0$ to $x = x_p$ is a function of x given by,

$$E(x) = \int \frac{\rho}{\kappa_s \epsilon_o} dx = \frac{1}{\kappa_s \epsilon_o} \int -qN_a \, dx \tag{B.13}$$

which, after including the initial condition at $x = 0$ from the charge Q_g, integrates to a linear function of depth.

$$E_2(x) = \frac{Q_g - qN_a x}{\kappa_s \epsilon_o} \qquad 0 < x \leq x_p \tag{B.14}$$

The dielectric constant for silicon, Si, is now used since we are integrating the charge density in the P-type region.

The electric field from $x = x_p$ to $x = x_p + x_d$ is also a function of x given by,

$$E(x) = \frac{1}{\kappa_s \epsilon_o} \int qN_d \, dx \tag{B.15}$$

which, after including the condition at x_p, becomes

$$E_3(x) = \frac{Q_g - qN_a x + qN_d(x - x_p)}{\kappa_s \epsilon_o} \qquad x_p < x \leq x_p + x_d. \tag{B.16}$$

After finding the electric field profile, the potential profile can be found by integrating the electric field with respect to the semiconductor depth, as shown in equation B.6. The integrated potential must also be neutral, thus, we must have

$$0 = V_g - \int_{-x_o}^{x_p + x_d} E(x) \, dx \tag{B.17}$$

which says we must use the negative of the integrated electric field to find the potential

profile as a function of depth.

From $x = -x_o$ to $x = 0$, the potential in the SiO_2 layer, as shown in figure B.1(d), is found by integrating the electric field, defined in equation B.12, over the oxide layer.

$$\phi(x) = \frac{-1}{\kappa_o \epsilon_o} \int_{-x_o}^{x} Q_g \, dx \tag{B.18}$$

Since the initial condition for the gate potential at $x = -x_o$ is V_g,we find

$$\phi_1(x) = V_g - \frac{Q_g(x + x_o)}{\kappa_o \epsilon_o} \qquad -x_o < x \leq 0. \tag{B.19}$$

The potential profile in the P-type and N-type material varies quadratically with respect to the depth as shown in figure B.1(d). Integrating equation B.14, which is the electric field in the P-type region from $x = 0$ to $x = x_p$,

$$\phi(x) = \frac{-1}{\kappa_s \epsilon_o} \int_{0}^{x} Q_g - qN_a x \, dx \tag{B.20}$$

and incorporating the initial conditions from evaluating equation B.19 at $x = 0$,

$$\phi(0) = V_g - \frac{Q_g x_o}{\kappa_o \epsilon_o} \qquad x = 0 \tag{B.21}$$

results in the following:

$$\phi_2(x) = V_g - \frac{Q_g x_o}{\kappa_o \epsilon_o} - \frac{1}{\kappa_s \epsilon_o}\left[Q_g x - \frac{1}{2} qN_a x^2\right] \qquad 0 < x \leq x_p. \tag{B.22}$$

In the remaining part of the structure, $x > x_p$, the potential profile is again found by

integrating final electric field section.

$$\phi(x) \;=\; \frac{-1}{\kappa_s \epsilon_o} \int_{x_p}^{x_p+x} Q_g - qN_a x + qN_d(x - x_p)\; dx \tag{B.23}$$

Evaluating the integral gives us

$$\phi(x) \;=\; \frac{-1}{\kappa_s \epsilon O}\Big[Q_g x \;-\; qN_a x x_p \;+\; \frac{1}{2} qN_a x^2 \;+\; \frac{1}{2} qN_d x^2\Big] \tag{B.24}$$

and since,

$$\frac{qN_d x_p^2}{2\kappa_s \epsilon_o} \;=\; \frac{qN_a x_p^2}{2\kappa_s \epsilon_o} \tag{B.25}$$

the potential for $x > x_p$ evaluates to

$$\phi_3(x) \;=\; V_g - \frac{Q_g x_o}{\kappa_o \epsilon_o} - \frac{1}{\kappa_s \epsilon_o}\Big[Q_g - qN_a x x_p + \frac{1}{2} qN_a x_p^2 + \frac{1}{2} qN_d (x - x_p)^2\Big]. \tag{B.26}$$

APPENDIX C

SONY ICX085 CCD QUANTUM EFFICIENCY CURVE

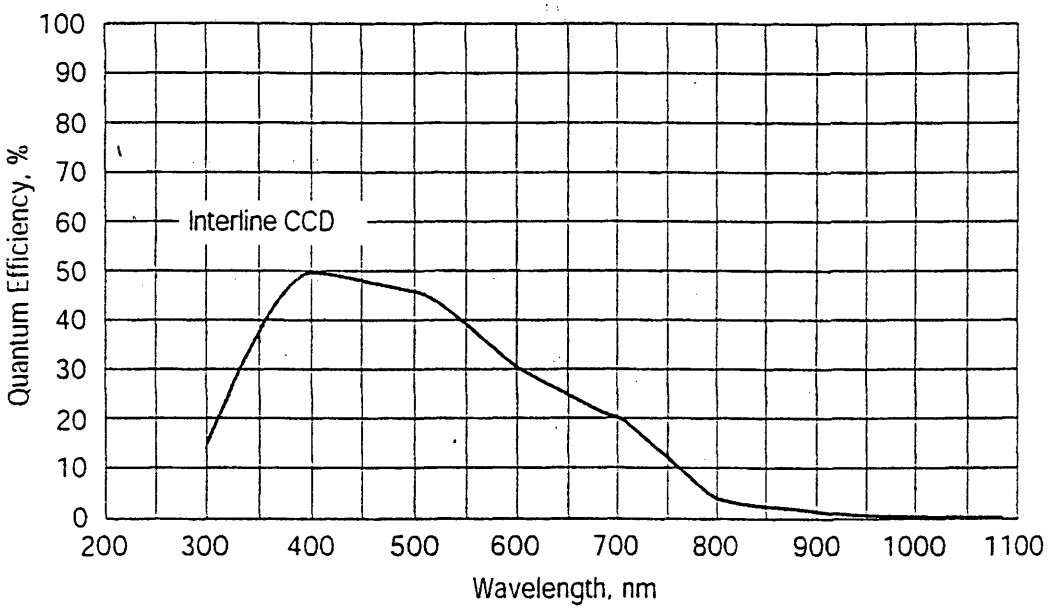

APPENDIX D

PHOTON TRANSFER TECHNIQUE

D.1 Photon Transfer Technique

The photon transfer technique is a tool for evaluating a CCD's performance in absolute units (Janesick *et al.*, 1985; Janesick *et al.*, 1987). This technique provides a way to measure the CCD's output sensitivity, S_v, in volts per electron (V/e^-).

For an ideal CCD detector system that is illuminated with a diffuse, uniform light source, the average signal value, $S(DN)$ (in digital number, DN, units) over all the affected pixels is found with the system's signal value transfer function. Graphically this transfer chain is illustrated in figure D.1.

$$S(DN) = P.QE_I.\eta_i.S_v.A_1.A_2 \tag{D.1}$$

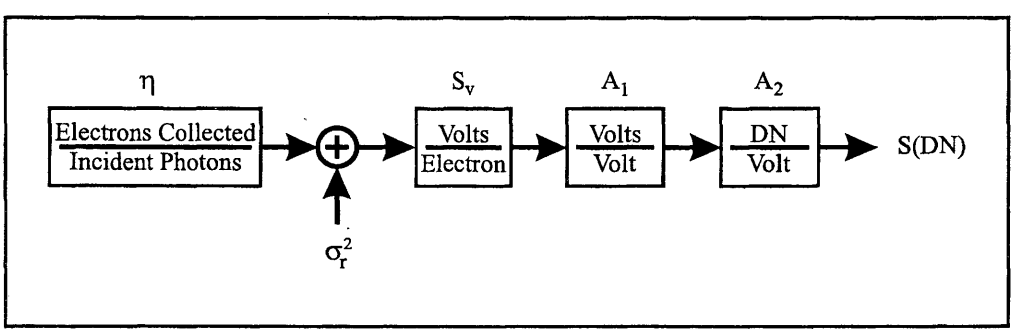

FIG. D.1. CCD signal conversion factor representation

In equation D.1, P is the mean number of incident photons per pixel, QE_I is the interacting quantum efficiency, η_i is the ideal quantum yield, S_v is the CCD's output sensitivity, A_1 is the cameras electronic gain, and A_2 is the analog-to-digital converter (ADC) gain.

Two factors are defined for converting the output signal, $S(DN)$, into fundamental physical units of either signal electrons or interacting photons.

$$K = \frac{1}{S_v.A_1.A_2} \quad (e^-/DN) \tag{D.2}$$

$$K = \frac{1}{\eta_i.S_v.A_1.A_2} \quad (interactingphotons/DN) \tag{D.3}$$

For wavelengths above 300nm, only one electron-hole pair are generated per photon (Janesick *et al.*, 1985). Therefore, in the diagnostic imaging system, the quantum yield, η_i, is unity, which means that there is only one signal electron generated for each interacting photon. In this case the conversion factors K and J are equal.

Incorporating only the number of interacting photons, P_I, which is the number of incident photons, P, times the interacting quantum efficiency, QE_I, gives a new equation for $S(DN)$ in terms of interacting photons, or signal electrons.

$$S(DN) = P_I.S_v.A_1.A_2 \tag{D.4}$$

Equation D.4 can also be written in terms of the conversion factor K.

$$S(DN) = \frac{P_I}{K} \tag{D.5}$$

APPENDIX E

NATURAL SAMPLING FUNCTION

E.1 Natural Sampling Function Model

As the optical waveform, $p_r(t)$, enters the detector, it is first sampled by the natural sampling function $q(t)$. The function $q(t)$ is a periodic train of rectangular sampling windows. The sampling rate is f_s and the width of each sampling window is defined as τ_s.

$$q(t) = \begin{cases} 0 & \frac{-T_s}{2} \leq t < \frac{-\tau_s}{2} \\ 1 & \frac{-\tau_s}{2} \leq t < \frac{\tau_s}{2} \\ 0 & \frac{\tau_s}{2} \leq t < \frac{T_s}{2} \end{cases} \tag{E.1}$$

A time domain illustration for $q(t)$ is shown in Figure E.1. The natural sampling function is very similar to the pulse train modulation function defined in section 5.8.1. The sampling function has an inherent dc offset in its mathematical description. Since the input to the natural sampler is always positive, the output from the sampler will always be positive and, therefore, contain a dc component.

Since the sampling function is periodic, the function can be written as Fourier

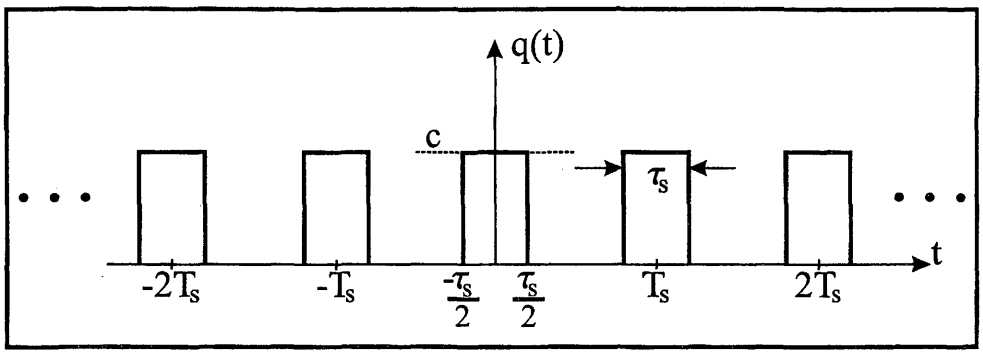

FIG. E.1. Time domain illustration of the natural sampling function

series, which has the form,

$$q(t) = \sum_{n=-\infty}^{\infty} Q_n e^{j2\pi n \frac{t}{T_s}} \tag{E.2}$$

The Fourier series coefficients, Q_n, are found by integrating the function, multiplied by the complex conjugate, over the period of the waveform. Since it is a power waveform, it is also multiplied by the inverse of the period.

$$Q_n = \frac{1}{T_s} \int_{-T_s/2}^{T_s/2} q(t) e^{-j2\pi f_s n t}\, dt \tag{E.3}$$

The integral from equation E.3 can be divided into the sum of three integrals with integration boundaries set by the time domain representation's nonlinear changes in amplitude. Since the amplitude changes from zero to c at $\pm\tau_s/2$, equation E.3 can be written as,

$$\begin{aligned} Q_n = & \frac{1}{T_s} \int_{-T_s/2}^{-\tau_s/2} 0 \cdot e^{-j2\pi f_s n t}\, dt + \frac{1}{T_s} \int_{-\tau_s/2}^{\tau_s/2} c \cdot e^{-j2\pi f_s n t}\, dt \\ & + \frac{1}{T_s} \int_{\tau_s/2}^{T_s/2} 0 \cdot e^{-j2\pi f_s n t}\, dt. \end{aligned} \tag{E.4}$$

The sampling function $q(t)$ is zero in both the range $-T_s/2$ to $-\tau_s/2$ and the range $\tau_s/2$ to $T_s/2$, thus, the Fourier coefficient integrals in these two ranges evaluate to zero. The Fourier coefficients for $q(t)$ can be found by integrating only over the time range from $-\tau_s/2$ to $\tau_s/2$.

$$Q_n = \frac{1}{T_s}\int_{-\tau_s/2}^{\tau_s/2} c \cdot e^{-j2\pi f_s n t}\, dt \tag{E.5}$$

Performing the integration above results in equation E.6, which can be rearranged into equation E.7.

$$Q_n = \frac{-c}{j2\pi f_s n T_s}\left[e^{-j2\pi f_s n\left(\frac{\tau_s}{2}\right)} - e^{j2\pi f_s n\left(\frac{\tau_s}{2}\right)}\right] \tag{E.6}$$

$$Q_n = \frac{c}{\pi f_s n T_s}\left[\frac{e^{j2\pi f_s n\left(\frac{\tau_s}{2}\right)} - e^{-j2\pi f_s n\left(\frac{\tau_s}{2}\right)}}{2j}\right] \tag{E.7}$$

Using an Euler identity, the portion of equation E.7 that is in brackets is equal to $\sin(\pi f_s n \tau_s)$. The Fourier coefficients can, therefore, be written as,

$$Q_n = \frac{c\tau_s}{T_s}\left[\frac{\sin(\pi f_s n \tau_s)}{\pi f_s n \tau_s}\right]. \tag{E.8}$$

A final simplification can be made by incorporating the definition for a sampling function.

$$Q_n = \frac{c\tau_s}{T_s}\mathrm{Sa}(\pi f_s n \tau_s) \tag{E.9}$$

where the sampling function is defined as

$$\mathrm{Sa}(x) = \frac{\sin(x)}{x} \tag{E.10}$$

Once the Fourier series coefficients are determined, a periodic waveform can be

represented by the exponential Fourier series in the time domain as equation E.11 and in the frequency domain as equation E.12.

$$q(t) = \sum_{n=-\infty}^{\infty} Q_n \, e^{j2\pi f_s n t} \tag{E.11}$$

$$Q(f) = \sum_{n=-\infty}^{\infty} Q_n \, \delta(f - n f_s) \tag{E.12}$$

Using the Fourier coefficients, Q_n, and setting the amplitude, c, to one, the natural sampling function is represented in time with equation E.13 and is represented in frequency with equation E.14.

$$q(t) = \frac{\tau_s}{T_s} \sum_{n=-\infty}^{\infty} \mathrm{Sa}(\pi f_s n \tau_s) e^{j2\pi f_s n t} \tag{E.13}$$

$$Q(f) = \frac{\tau_s}{T_s} \sum_{n=-\infty}^{\infty} \mathrm{Sa}(\pi f_s n \tau_s) \delta(f - n f_s) \tag{E.14}$$

The two equations above can be written in a shorter form by defining a variable to represent the duty cycle. The duty cycle is the ratio of the sampling pulse width, τ_s, to the sampling period, T_s. If the sampling function's duty cycle is defined as ψ_s, then τ_s/T_s and $f_s \tau_s$, in equations E.13 and E.14, can be replaced with ψ_s.

$$q(t) = \psi_s \sum_{n=-\infty}^{\infty} \mathrm{Sa}(\pi n \psi_s) e^{j2\pi f_s n t} \tag{E.15}$$

$$Q(f) = \psi_s \sum_{n=-\infty}^{\infty} \mathrm{Sa}(\pi n \psi_s) \delta(f - n f_s) \tag{E.16}$$

The amplitude spectrum of a sampling function, which has unity amplitude in the time domain and a 50% duty cycle, is illustrated in Figure E.2. The harmonic coefficients exist at the dc component, the fundamental component, and at odd multiples of the fundamental component. The sampling function's spectral envelope is also shown in Figure E.2 to illustrate the zero magnitude components at even multiples of the fundamental harmonic component.

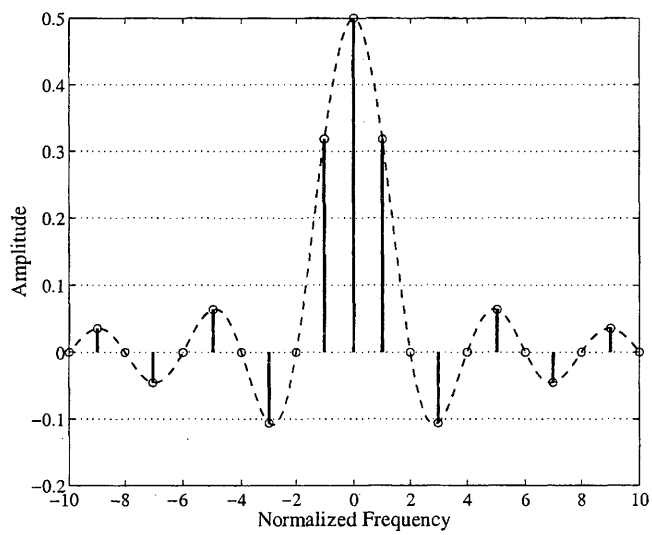

FIG. E.2. Spectral coefficients and spectral envelope of the natural sampling function

The power spectrum is obtained by squaring the absolute value of natural sampling function's harmonic coefficients. Since the natural sampling function can be represented as the sum of discrete harmonic components, the squared magnitude of the discrete harmonic components is equivalent to its power spectral density function, $|Q(f)|^2$ (Taub & Schilling, 1986). The power spectral density of the natural sampling

function is illustrated in Figure E.3.

$$|Q(f)|^2 = \sum_{n=-\infty}^{\infty} |Q_n|^2 \delta(f - nf_s) = (\psi_s)^2 \sum_{n=-\infty}^{\infty} |\mathrm{Sa}(\pi n \psi_s)|^2 \delta(f - nf_s) \quad \text{(E.17)}$$

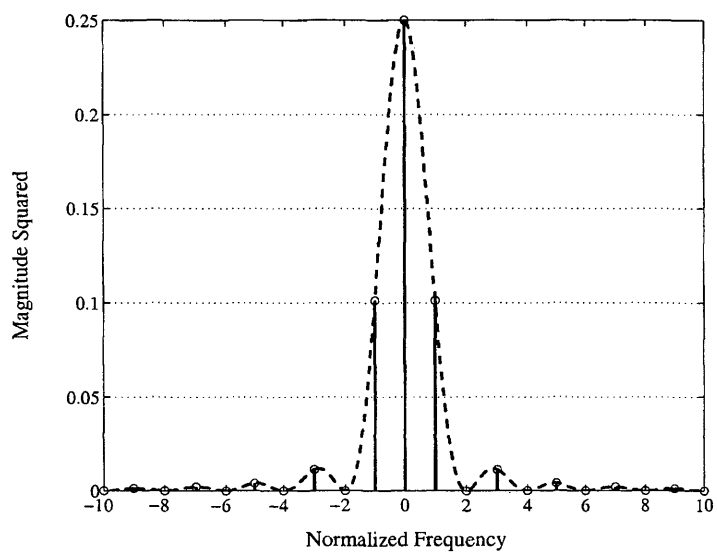

FIG. E.3. Natural sampling function: magnitude squared spectrum

APPENDIX F

INTEGRATE AND DUMP FILTER

F.1 Integrate and Dump Filter Model

In order to find the parameters that describe the integrate and dump function, a qualitative discussion is first presented. An integrator sums all input signal values over a specified time with a time resolution dt. If, for example, a square pulse signal with an area of one enters the integrator, the integrator's output will increase linearly until the output is unity. The output will remain the same until another signal enters the integrator, or the integrator is reset.

By reducing the width of the unit area pulse that enters the integrator to dt, the function's impulse response is obtained. If the input, $x_{id}(t)$, is equal to a delta function, $\delta(t)$, then, from convolution, the impulse response, $h_{id}(t)$, is received at the integrator's output (Stremler, 1990).

$$y_{id}(t) \;=\; x_{id}(t) * h_{id}(t) \;=\; \int_{-\infty}^{+\infty} x_{id}(\tau) h_{id}(t-\tau)\, d\tau \tag{F.1}$$

$$y_{id}(t) \;=\; h_{id}(t) \qquad \text{IF} \qquad x_{id}(t) \;=\; \delta(t) \tag{F.2}$$

Since the area of a delta function is unity, the output of the integrator will also be unity. The output remains at unity until the integration period, τ_i is complete and

the integrator is reset. A reset delta function at time τ_i, that is negative and has a magnitude equal to the input delta function, is required to force the output back to the integrator's initial state, which existed at time t less than zero.

$$h_{id}(t) = \int_0^{\tau_i} \delta(t) - \delta(t - \tau_i)\, dt \tag{F.3}$$

Evaluating the integral of a delta function at $t = 0$ and an opposite polarity delta function at $t = \tau_i$, results in two unit step functions, one a time t and the other at time $t - \tau_i$. The difference between the two step functions produces the temporal representation of the integrate and dump function, given in equation F.4 and illustrated in Figure F.1.

$$h_{id}(t) = [u(t) - u(t - \tau_i)] \tag{F.4}$$

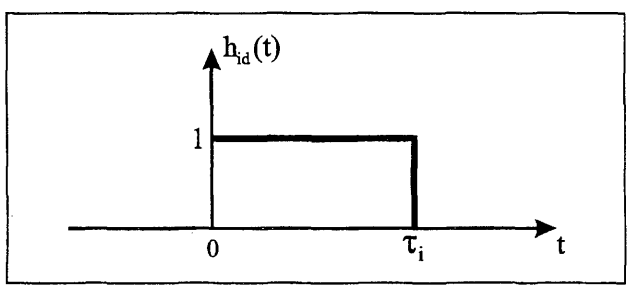

FIG. F.1. Causal impulse response of the integrate and dump filter

Often, the time function shown in figure F.1 is defined as $\prod(\bullet)$, which is a gate function. The function $\prod(\bullet)$ is defined in equation F.5, and it is used to define the

integrate and dump filter's impulse response in equation F.6.

$$\prod\left(\frac{t}{T}\right) \equiv \begin{cases} 1 & |t| \leq \frac{T}{2} \\ 0 & |t| > \frac{T}{2} \end{cases} \tag{F.5}$$

$$h_{id}(t) = \prod\left(\frac{t}{\tau_i}\right) \tag{F.6}$$

Besides finding the impulse response for the integrate and dump filter, determining the frequency response, or transfer function, $H_{id}(f)$, is also useful for analyzing the detection system. The transfer function of a filter is the Fourier transform of its impulse response. In order to simplify the Fourier transform calculation of equation F.6, the temporal impulse response, $h_{id}(t)$, is first time shifted by $\tau_i/2$, in the $(-t)$ direction. The shift in time creates a non-causal, even function that simplifies the Fourier series evaluation over the symmetric interval from $-\tau_i/2$ to $\tau_i/2$, and provides the real frequency spectrum components (Stremler, 1990).

$$h_{id}(t) = \prod\left(\frac{t-(\tau_i/2)}{\tau_i}\right) \tag{F.7}$$

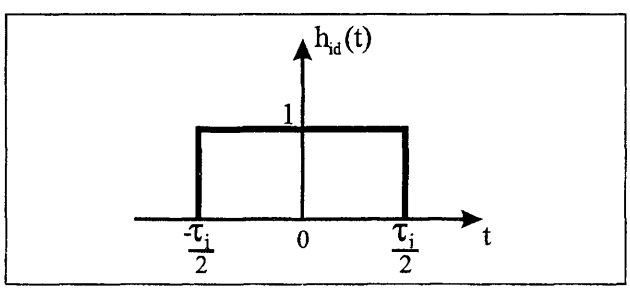

FIG. F.2. Non-causal integrate and dump impulse response

It is also noted, in equation F.8, that the Fourier transform of a time-shifted function is the Fourier transform of the unshifted function multiplied by a phase delay term. Incorporating the phase delay term after determining the Fourier transform of the non-causal impulse response, will incorporate the imaginary frequency spectrum components with the real spectrum components producing a total spectrum for the causal integrate and dump filter (Stremler, 1990).

$$x(t - t_o) \iff X(f)e^{-j2\pi f t_o} \tag{F.8}$$

The Fourier transform of a non-periodic function is calculated much the same way as the Fourier coefficients are, for a periodic function. The Fourier transform is found by assuming the non-periodic function is periodic and then taking the limit at the function's period T goes to infinity. As the fundamental period T goes to infinity, the frequency step, which is the inverse of the period, $1/T$, becomes infinitely small, and the Fourier transform becomes a continuous frequency function. This is in contrast to a periodic signal's spectrum, as shown in Figure E.2, which is the sum of spectral impulses at integer multiples of the fundamental frequency (Taub & Schilling, 1986).

Taking the limit as the period T goes to infinity, we find the Fourier transform of a general time function $f(t)$ can be found as shown in equation F.9.

$$F(f) = \lim_{T \to \infty} \frac{1}{T} \int_{-T/2}^{T/2} f(t)e^{-j2\pi n \frac{t}{T}}\, dt = \int_{-\infty}^{\infty} f(t)e^{-j2\pi f t}\, dt \tag{F.9}$$

Since the integrate and dump filter's impulse response, $h_{id}(t)$, is zero for all $t > |\tau_i/2|$, the integral need only be evaluated over the interval from $-\tau_i/2$ to $\tau_i/2$.

$$H_{id}(f) = \int_{-\infty}^{\infty} h(t)e^{-j2\pi f t}\, dt = \int_{-\tau_i/2}^{\tau_i/2} (1)e^{-j2\pi f t}\, dt \tag{F.10}$$

Evaluating the integral and utilizing an Euler identity, produces the real components of the integrate and dump filter's frequency response.

$$H_{id}(f) \;=\; \tau_i \cdot \mathrm{Sa}(\pi f \tau_i) \tag{F.11}$$

In order to simplify the procedure used to find the integrate and dump filter's Fourier transform, the filter was first transferred into a non-causal function by time shifting $h_{id}(f)$ in equation F.7. The Fourier transform for the causal integrate and dump filter must, therefore, include the time delay given in equation F.8.

$$H_{id}(f) \;=\; \tau_i \cdot \mathrm{Sa}(\pi f \tau_i) e^{-j2\pi f \frac{\tau_i}{2}} \tag{F.12}$$

The squared magnitude or power transfer function of the integrate and dump filter is determined by multiplying the Fourier transform complex conjugates pairs.

$$|H_{id}(f)|^2 \;=\; |H_{id}(f)||H^*_{id}(f)| \tag{F.13}$$

Squaring complex conjugate pairs that are orthogonal functions produces a zero value for the cross-product terms. Also, the phase term from the product of positive and negative frequency terms evaluates to unity. Using the power transfer function will produce, at the filter's output, information about the propagation of energy or power density and will not provide phase difference information. The integrate and dump filter's power transfer function is given by equation F.14, and a graphical illustration is shown in Figure F.3.

$$|H_{id}(f)|^2 \;=\; |\tau_i \cdot \mathrm{Sa}(\pi f \tau_i)|^2 \tag{F.14}$$

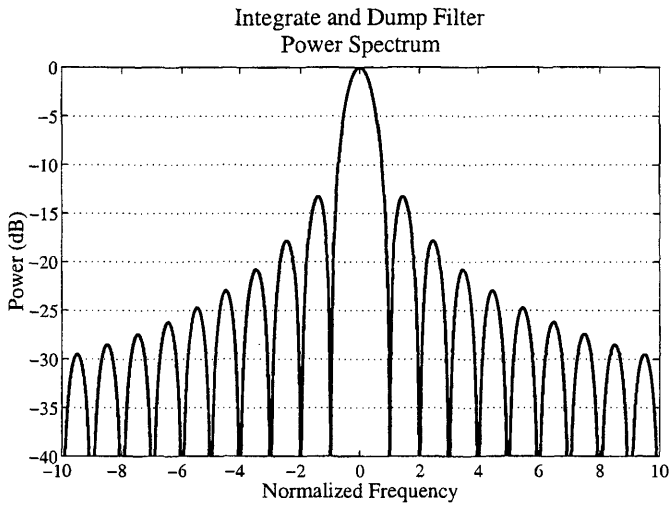

FIG. F.3. Integrate and dump filter power response

F.1.1 Noise Equivalent Bandwidth

The noise equivalent bandwidth (NEB) of the integrate and dump filter is also useful in determining the noise power obtain at the filter's output based on an input noise power. The method for calculating the NEB of a real filter is discussed in section 4.7.3.

The NEB for the integrate and dump filter, defined as B_{id}, is

$$B_{id} = \frac{\int_0^\infty |H_{id}(f)|^2 \, df}{|H_{id}(0)|^2} = \frac{\tau_i^2}{\tau_i^2} \int_0^\infty \frac{\sin^2(\pi f \tau_i)}{(\pi f \tau_i)^2} = \frac{1}{\pi^2 \tau_i^2} \int_0^\infty \frac{\sin^2(\pi f \tau_i)}{(f)^2} \tag{F.15}$$

The integral is definite as shown by (Beyer, 1978),

$$\int_0^\infty \frac{\sin^2(xf)}{f^2} \, df = x \left(\frac{\pi}{2}\right). \tag{F.16}$$

The NEB for the integrate and dump filter is, therefore,

$$B_{id} = \frac{1}{\pi^2\tau_i^2}\int_0^\infty \frac{\sin^2(\pi f\tau_i)}{(f)^2} = \left(\frac{1}{\pi^2\tau_i^2}\right)\left(\frac{\pi^2\tau_i}{2}\right) = \frac{1}{2\,\tau_i}. \tag{F.17}$$

The noise equivalent filter, $H_{id}^{eq}(f)$, rather than the actual integrate and dump filter, can be used to determine the noise power at the output of the integrate and dump filter. The noise equivalent filter for the integrate and dump filter is,

$$|H_{id}^{eq}(f)|^2 = \tau_i^2 \prod\left(\frac{f}{2B_{id}}\right) = \tau_i^2 \prod(f\tau_i) \tag{F.18}$$

or

$$|H_{id}^{eq}(f)|^2 = \tau_i^2 \prod\left(\frac{f}{f_i}\right), \tag{F.19}$$

where f_i is equal to $1/\tau_i$.

APPENDIX G

SAMPLE AND HOLD FILTER

G.1 Sample and Hold Filter Model

In order to analyze the sample and hold filter, a flat-top sampler is first developed. A flat-top sampling function is initiated with an impulse sampler. During a flat-top sampling procedure, an input is first sampled with a unit impulse train. Equation G.1 represents an arbitrary signal, $f(t)$ that is sampled by an impulse train $k(t)$. After sampling $f(t)$ with an impulse train, the result is an impulse train that has as its magnitudes, the magnitude of $f(t)$ at the sampling period T_f (Couch, 1995).

$$f(t) \cdot k(t) \;=\; f(t) \cdot \sum_{n=-\infty}^{\infty} \delta(t - nT_f) \tag{G.1}$$

The frequency domain representation of the impulse train is also a series of impulses over all frequency, separated by the sampling frequency, f_f, which has an inverse relationship with the sampling period, $1/T_f$. The magnitude of the frequency domain components are also scaled by the inverse of the sampling period. The Fourier transform pair for an impulse train is given in equation G.2.

$$k(t) = \sum_{n=-\infty}^{\infty} \delta(t - nT_f) \iff \frac{1}{T_f} \sum_{n=-\infty}^{\infty} \delta(f - nf_f) = K(f) \tag{G.2}$$

The Fourier transform of the impulse train $k(t)$ is another impulse train with

a frequency $f_f = 1/T_f$ and it is scaled by the magnitude $1/T_f$. Since the signal $f(t)$ is sampled in the time domain, it is convolved in the frequency domain. The spectrum of the impulse sampled function $f(t)$ is, therefore, the Fourier transform of $f(t)$ replicated in frequency at integer values of the sampling frequency, f_f (Couch, 1995).

$$F(f) * K(f) = F(f) * \frac{1}{T_f} \sum_{n=-\infty}^{\infty} \delta(f - nf_f) = \frac{1}{T_f} \sum_{n=-\infty}^{\infty} F(f - nf_f) \tag{G.3}$$

In order to generate a flat-top sample of the arbitrary function $f(t)$, the impulse samples need to be stretched over time. This is accomplished by convolving the time domain impulse samples with a rectangular pulse, $r(t)$, that has a width equal to the desired flat-top sample pulse width, τ_h, and an amplitude of one. Since the impulse samples are convolved with $r(t)$, the amplitudes of the impulse samples are retained during the width of the rectangular pulse. The pulse width (τ_h) is, therefore, the time during which the output of the impulse sampling function is held constant.

A general flat-top sampling pulse for stretching the impulse samples over time is given in equation G.4, as $r(t)$.

$$r(t) = \prod \left(\frac{t - \frac{\tau_h}{2}}{\tau_h} \right) \tag{G.4}$$

The corresponding power spectrum of $r(t)$ is a continuous frequency function, defined as $|R(f)|^2$.

$$|R(f)|^2 = |\tau_h \cdot \mathrm{Sa}(\pi f \tau_h)|^2 \tag{G.5}$$

In order to obtain the flat-top sampling function, $f(t) \cdot k(t)$ is convolved with

$r(t)$, in the time domain, which is the same as multiplying the frequency domain representation. The power output of the flat-top sampler, $|Y(f)|^2$, is found by multiplying the power spectrum of the flat-top pulse, $|R(f)|^2$, with the magnitude squared of the sampled input.

$$|Y(f)|^2 = \left|\frac{\tau_h}{T_f}\mathrm{Sa}(\pi f \tau_h)\right|^2 \sum_{n=-\infty}^{\infty} |F(f - nf_f)|^2 \tag{G.6}$$

If the flat-top pulse width, τ_h, is stretched out further in time, so it is the same length as the sampling period, T_f, then the sample will be held at its sampled value until the next sample is taken. By extending τ_h to T_f, the harmonic components of the sampled input, at integer multiples of the sampling frequency (f_f), are forced to zero. It is assumed that by extending τ_h to T_f the sampled components of the input are severely attenuated and can be discarded. It is, therefore, assumed that,

$$|Y(f)|^2 = \left|\frac{T_f}{T_f}\mathrm{Sa}(\pi f T_f)\right|^2 \sum_{n=-\infty}^{\infty} |F(f - nf_f)|^2 \rightarrow 0 \qquad n \neq 0$$

such that the power output is

$$|Y(f)|^2 = |\mathrm{Sa}(\pi f T_f)|^2 \cdot |F(f)|^2 \tag{G.7}$$

By making this assumption, the sample and hold function can be approximated as a lowpass filter. The power response of the filter, $|H_{sh}(f)|^2$, is

$$\frac{|Y(f)|^2}{|F(f)|^2} = |H_{sh}(f)|^2 = |\mathrm{Sa}(\pi f T_f)|^2 \tag{G.8}$$

and the corresponding impulse response is

$$h_{sh}(t) = \frac{1}{T_f}\prod\left(\frac{t}{T_f}\right). \tag{G.9}$$

The power response of $|H_{sh}(f)|^2$ is shown in Figure G.1. As shown in the figure, the sample and hold filter is in fact approximated with a lowpass filter.

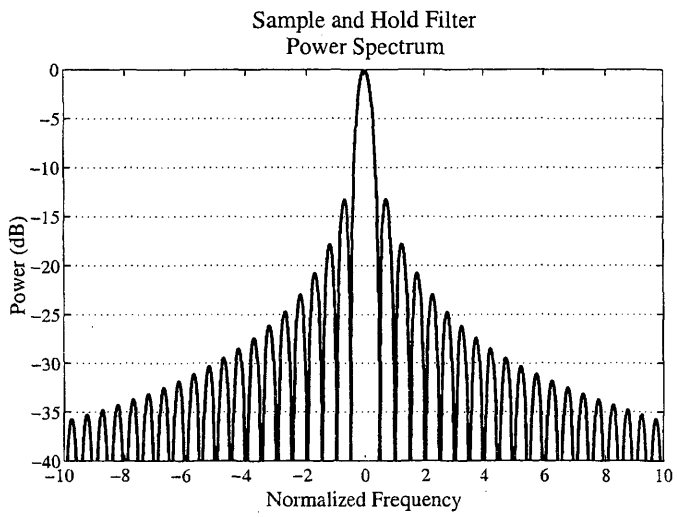

FIG. G.1. Sample and hold filter power response

G.1.1 Noise Equivalent Bandwidth

The noise equivalent bandwidth (NEB) for the sample and hold filter is very similar to the NEB for the integrate and dump filter from appendix F. The NEB for the sample and hold filter, defined as B_{sh}, is,

$$B_{sh} = \frac{1}{\pi^2 T_f^2} \int_0^\infty \frac{\sin^2(\pi f T_f)}{(f)^2}\, df = \left(\frac{1}{\pi^2 T_f^2}\right)\left(\frac{\pi^2 T_f}{2}\right) = \frac{1}{2\,T_f}. \qquad \text{(G.10)}$$

The noise equivalent filter, $H_{sh}^{eq}(f)$, for the sample and hold filter, however, has no gain term and is defined as,

$$|H_{sh}^{eq}(f)|^2 = \prod\left(\frac{f}{2B_{sh}}\right) = \prod(f\,T_f) \tag{G.11}$$

or

$$|H_{sh}^{eq}(f)|^2 = \prod\left(\frac{f}{f_f}\right), \tag{G.12}$$

where f_f is equal to $1/T_f$.

APPENDIX H

SIMPLIFIED LOCK-IN AMPLIFIER (HOMODYNE DETECTION)

A homodyne detection process is used to simulate a very simple lock-in amplifier. The homodyne detection system function is developed in this appendix for comparison with both the gated integrator and heterodyne detection system functions. Essentially, the homodyne detector is the second stage of the heterodyne detection process, discussed in Chapter 7. The system function in this appendix processes, however, the original input, $S(f)$.

H.1 Homodyne Detection System Function

The homodyne detection system function is comprised of a sinusoidal mixer, $D(f)$, and a second order lowpass filter, $H_{lp}(f)$. The system function is illustrated in Figure H.1.

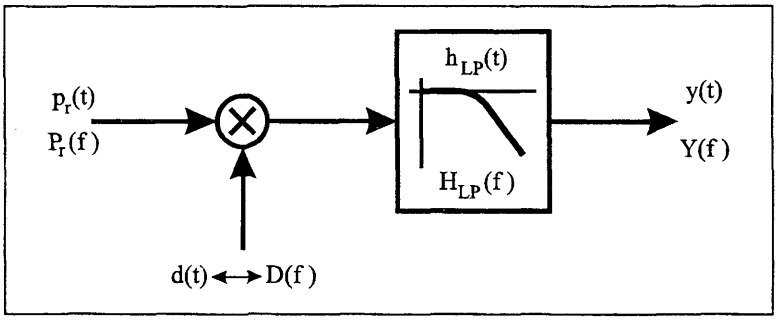

FIG. H.1. Simplified lock-in amplifier (homodyne detector) block diagram

H.1.1 Sinusoidal Mixer

The sinusoidal mixer is defined in the time domain as,

$$d(t) = G_d \cos(2\pi f_d t + \phi_d) \tag{H.1}$$

where G_d is the gain of the mixer, f_d is the demodulation frequency, and ϕ_d is the sinusoid's phase. Since a lock-in amplifier performs in-phase (I) and quadrature (Q) detection, then calculates the result as the square root of the sum of the squares, the phase term, ϕ_d, is assumed to be zero.

Taking the Fourier transform of $d(t)$ and squaring the result, gives the power spectrum of the sinusoidal mixer, which is,

$$|D(f)|^2 = \frac{G_d^2}{4}\delta(f + f_d) + \frac{G_d^2}{4}\delta(f - f_d) \tag{H.2}$$

H.1.2 Lowpass Filter

A second order lowpass filter is used to filter the output of the sinusoidal mixer, as shown in Figure H.1. The transfer function of the lowpass filter, $H_c(f)$, is given as

$$H_c(f) = \frac{G_c}{\sqrt{1 + \left(\frac{f}{f_c}\right)}} \tag{H.3}$$

where G_c is the lowpass filter gain, and f_c is the -3dB cutoff frequency. The power transfer function is the squared magnitude of $H_c(f)$, which is,

$$|H_c(f)|^2 = \frac{(G_c f_c)^2}{f_c^2 + f^2} \tag{H.4}$$

When analyzing noise passed through $|H_c(f)|^2$, the noise equivalent bandwidth

(NEB) can be utilized. The NEB of the lowpass filter is $B_c = f_c(\pi/2)$. The noise equivalent filter is,

$$|H_c^{eq}(f)|^2 = G_c^2 \prod\left(\frac{f}{2B_c}\right) = G_c^2 \prod\left(\frac{f}{\pi f_c}\right). \tag{H.5}$$

The output of $|H_o(f)|^2$, based on an input power spectrum $S(f)$, which is, from Figure H.1, $|P_r(f)|^2$, is,

$$|Y(f)|^2 = |H_c(f)|^2 \left(S(f) * |D(f)|^2\right) \tag{H.6}$$

$$|Y(f)|^2 = |H_c(f)|^2 \left(\frac{G_d^2}{4} S(f+f_d) + \frac{G_d^2}{4} S(f-f_d)\right) \tag{H.7}$$

H.2 System Output

Input Review The input applied to $|H_o|^2$ is the power spectrum defined in equation 5.122. The total input is,

$$\begin{aligned} S_T(f) &= S_B(f) + S_N(f) + S_{\mathrm{Ap}}(f) \\ S_T(f) &= (I_p)^2\,\delta(f) + \frac{(I_p)^2}{\sqrt{1+\left(\frac{f}{f_o}\right)^2}} + \epsilon I_p + (\psi_m)^2 \frac{\sigma_{\mathrm{A}}^2 + \left(\overline{A}\right)^2}{2B_{\mathrm{A}}} \\ &\quad \times \sum_{n=-\infty}^{\infty} |Sa\,(n\pi\psi_m)|^2 \prod\left(\frac{|f-nf_m|}{2B_{\mathrm{A}}}\right) \quad \frac{(\mathrm{watts})^2}{\mathrm{Hz}}. \end{aligned} \tag{H.8}$$

H.2.1 Signal Output

At the input to $|H_o(f)|^2$, the signal, $S_{Ap}(f)$, is mixed with $|D(f)|^2$. Since $S_{Ap}(f)$ is mixed with a sinusoid, only the components of $S_{Ap}(f)$ that are involved in the mixing process and are of interest at the output are considered. The dc component and the fundamental harmonic component are, therefore, the only portion of $S_{Ap}(f)$

that is applied to $|D(f)|^2$. Using only the dc and fundamental harmonic components, the input is,

$$S_{Ap}(f) = (\psi_m)^2 \frac{\sigma_{\mathrm{A}}^2 + \left(\overline{A}\right)^2}{2B_{\mathrm{A}}} \sum_{n=-1}^{1} |Sa\,(n\pi\psi_m)|^2 \prod \left(\frac{|f - nf_m|}{2B_{\mathrm{A}}}\right) \tag{H.9}$$

The signal's variance, σ_A^2, is assumed to be zero and the mean value $\overline{A}$ is set equal to αI_p, which is the steady state background multiplied by the modulation depth. The measurement system's goal is to then extract α. Since the signal is assumed to be a constant value, it is now represented as a delta function, such that the unmodulated signal is $S_A(f) = (\alpha I_p)^2 \delta(f)$. The modulated signal's three components of interest at the input is, therefore,

$$S_{Ap}(f) = (\alpha I_p \psi_m)^2\, \delta(f) + \frac{(\alpha I_p)^2}{\pi^2} \left[\delta(f + f_m) + \delta(f - f_m)\right] \tag{H.10}$$

Since the dc signal component in equation H.10 is assumed to be buried by the steady state background and noise at low frequency, which is the reason for modulating the signal in the first place, the signal must be obtained from the modulated components. In order to resolve the signal that resides at the modulation frequency, $\pm f_m$, the demodulation frequency, f_d, in $|D(f)|^2$ is set equal to f_m. Convolving $S_{Ap}(f)$ with $|D(f)|^2$, with f_d set equal to f_m, gives the following six components.

$$\begin{aligned} S_{Ap}(f) * |D(f)|^2 &= \frac{G_d^2}{4} \Bigg\{ (\alpha I_p \psi_m)^2 \delta(f + f_d) + \left(\frac{\alpha I_p}{\pi}\right)^2 \left[\delta(f + 2f_d) + \delta(f)\right] \\ &+ (\alpha I_p \psi_m)^2 \delta(f - f_d) + \left(\frac{\alpha I_p}{\pi}\right)^2 \left[\delta(f - 2f_d) + \delta(f)\right] \Bigg\} \end{aligned} \tag{H.11}$$

Once the signal at f_m is transferred to the baseband, it is recovered at the output

of $|H_o(f)|^2$ by filtering equation H.11 with $|H_c|^2$. It is assumed that f_m is set high enough and f_c, from the lowpass filter, is set low enough to attenuate all components, except for the baseband component, to a negligible level. Based on this assumption, the $\delta(f \pm f_d)$ and $\delta(f \pm 2f_d)$ components in equation H.11 are eliminated, resulting in the following at the output.

$$\begin{aligned}
|Y_{A_o}(f)|^2 &= |H_c(f)|^2 \left[S_{Ap}(f) * |D(f)|^2\right] \\
|Y_{A_o}(f)|^2 &= \left(\frac{G_c G_d}{2}\right)^2 \left[\left(\frac{\alpha I_p}{\pi}\right)^2 \delta(f) + \left(\frac{\alpha I_p}{\pi}\right)^2 \delta(f)\right] \\
|Y_{A_o}(f)|^2 &= \frac{1}{2}\left(\frac{G_c G_d \alpha I_p}{\pi}\right)^2 \delta(f) \qquad \text{(H.12)}
\end{aligned}$$

H.2.2 Background Output

The steady state background, $S_B(f)$, is also mixed with $D(f)$ and then lowpass filtered. The output, $|Y_{B_3}(f)|^2$, in this case, is,

$$|Y_{B_o}(f)|^2 = |H_c|^2 (G_d I_p)^2 \left[\delta(f + f_d) + \delta(f - f_d)\right]. \qquad \text{(H.13)}$$

Based on the assumption made in section H.2.1 about the modulation frequency and the lowpass filter's cutoff frequency, the steady state background components at $\delta(f \pm f_d)$ are eliminated. The resulting output is zero.

$$|Y_{B_o}(f)|^2 = 0 \qquad \text{(H.14)}$$

H.2.3 Noise Output

The noise at the input is the combination of photon noise and $1/f$ noise. The noise obtained at the output of $|H_o|^2$ is discussed in this section.

Photon Noise The photon noise at the input has the constant power spectrum $S_W(f)$. Mixing $S_W(f)$ with $|D(f)|^2$ gives,

$$S_W(f) * |D(f)|^2 = \frac{G_d^2}{4} S_W(f + f_d) + \frac{G_d^2}{4} S_W(f - f_d)$$

Since $S_W(f)$ is white, $S_W(f \pm f_d) = S_W(f)$, which results in,

$$S_w(f) * |D(f)|^2 = \frac{G_d^2}{2} S_W(f) = \frac{1}{2} G_d^2 \epsilon I_p \tag{H.15}$$

Applying the lowpass filter, $|H_c(f)|^2$, to equation H.15, gives the photon noise spectrum at the output of the homodyne detection system.

$$|Y_{Wo}(f)|^2 = |H_c(f)|^2 \left[S_W(f) * |D(f)|^2\right] = \frac{(G_c G_d f_c)^2 \epsilon I_p}{2\,(f_c^2 + f^2)} \tag{H.16}$$

In order to determine the power of the photon noise that exits the detection process, the NEB for $|H_c(f)|^2$ is used. Applying the noise equivalent filter, from equation H.5, to equation H.15 results in the photon noise power, σ_{Wo}^2, at the output of $|H_o(f)|^2$.

$$\sigma_{Wo}^2 = \frac{(G_c G_d)^2 \epsilon I_p}{2} \int_{-f_c \frac{\pi}{2}}^{f_c \frac{\pi}{2}} df = \frac{1}{2} (G_c G_d)^2 \pi f_c \epsilon I_p \tag{H.17}$$

$1/f$ **Noise** The analysis of $1/f$ noise as it passes through $|H_o(f)|^2$ is performed much the same way as the analysis of photon noise in the previous section. The $1/f$ noise at the input is first mixed with $|D(f)|^2$ and then filtered with $|H_c(f)|^2$.

Mixing the $1/f$ noise spectrum, $S_L(f)$, with the sinusoid at the input gives,

$$S_L(f) * |D(f)|^2 = \frac{G_d^2}{4} S_L(f + f_d) + \frac{G_d^2}{4} S_L(f - f_d). \tag{H.18}$$

Applying the lowpass filter produces the spectrum of the $1/f$ noise at the system's output.

$$|Y_{Lo}(f)|^2 = \frac{(G_c G_d f_c)^2}{4\,(f_c^2 + f^2)}\,[S_L(f+f_d) + S_L(f-f_d)] \tag{H.19}$$

Figure H.2 illustrates $S_L(f)$, $|D(f)|2$, and the convolution of the two spectra. The $1/f$ noise power at the output is determined with the noise equivalent filter, $|H_c^{eq}(f)|^2$, which is also shown, as a dashed line, in Figure H.2(c).

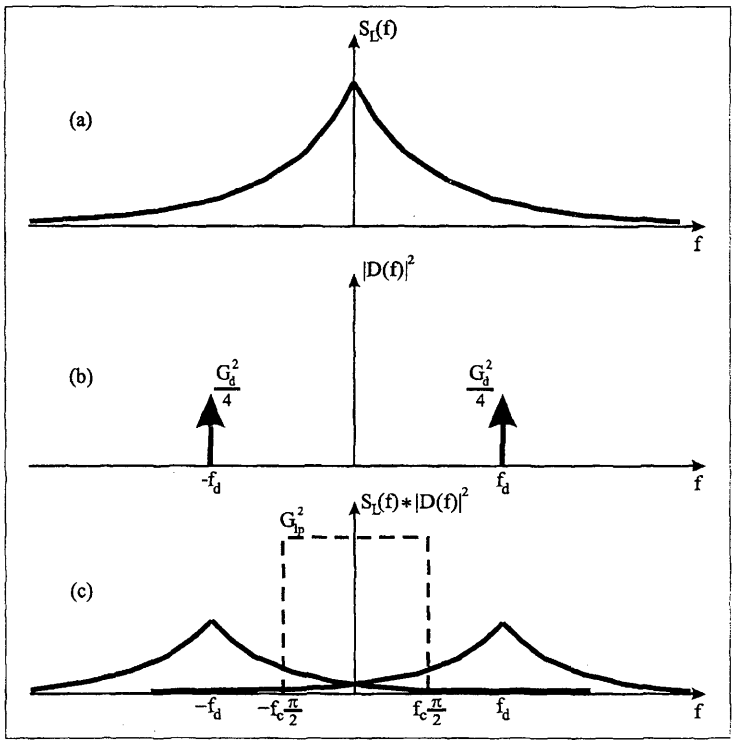

FIG. H.2. Transfer of $1/f$ noise through the simplified lock-in amplifier system function

Instead of integrating $S_L(f \pm f_d)$ to find the output power, the noise equivalent filter can be transferred to f_d and the integration can be performed on $S_L(f)$. The limits of integration are shifted to center around f_d and a multiplication factor of two

is included to account for both positive and negative frequency contributions. The $1/f$ noise power at the output can, therefore, be determined by,

$$\begin{aligned}\sigma_{Lo}^2 &= 2\left(\frac{G_c^2 G_d^2}{4}\right)\int_{f_d - f_c\frac{\pi}{2}}^{f_d + f_c\frac{\pi}{2}} S_L(f)\,df \\ &= \frac{(G_c G_d I_p)^2 f_o}{2}\int_{f_d - f_c\frac{\pi}{2}}^{f_d + f_c\frac{\pi}{2}} \frac{1}{\sqrt{f_o^2 + f^2}}\,df. \end{aligned} \tag{H.20}$$

Since $f_d - f_c(\pi/2) \gg f_o$, the noise contribution at the output is,

$$\sigma_{Lo}^2 = \frac{f_o}{2}(G_c G_d I_p)^2 \ln\left(\frac{2f_d + \pi f_c}{2f_d - \pi f_c}\right) \tag{H.21}$$

H.3 Signal-To-Noise Ratio

The signal-to-noise ratio (SNR) at the output of $|H_o(f)|^2$ is the ratio of $|Y_{A_o}(f)|^2$ to the total output noise power. The total noise at the output is the sum of $\sigma_{W_o}^2$ and $\sigma_{L_o}^2$.

$$\begin{aligned}\sigma_{To}^2 &= \sigma_{W_o}^2 + \sigma_{Lo}^2 \\ \sigma_{To}^2 &= \frac{1}{2}G_c^2 G_d^2\left[\pi f_c \epsilon I_p + f_o I_p^2 \ln\left(\frac{2f_d + \pi f_c}{2f_d - \pi f_c}\right)\right] \end{aligned} \tag{H.22}$$

The SNR at the output of the homodyne detection system is,

$$\mathrm{SNR}_o = \frac{|Y_{A_o}(f)|^2}{\sigma_{T_o}^2} \tag{H.23}$$

which after canceling G_c and G_d is,

$$\mathrm{SNR}_o = \frac{(\alpha I_p)^2}{\pi^3 f_c \epsilon I_p + \pi^2 f_o I_p^2 \ln\left(\frac{2f_d + \pi f_c}{2f_d - \pi f_c}\right)}. \tag{H.24}$$

Dividing through by the steady state background power, I_p^2, gives,

$$\mathrm{SNR}_o \;=\; \frac{(\alpha)^2}{\frac{1}{I_p}\pi^3 f_c \epsilon \;+\; \pi^2 f_o \ln\left(\frac{2f_d+\pi f_c}{2f_d-\pi f_c}\right)} \,. \tag{H.25}$$

APPENDIX I

MODULATION DEPTH DETERMINATION FROM FOURIER COMPONENTS

I.1 Determination of Modulation Depth

In general, the probe signal, in a pump-probe absorption spectroscopy (PPAS) experiment, can be illustrated as a square wave that has a dc offset, as shown in figure I.1. The waveform in figure I.1 represents the change in probe intensity which

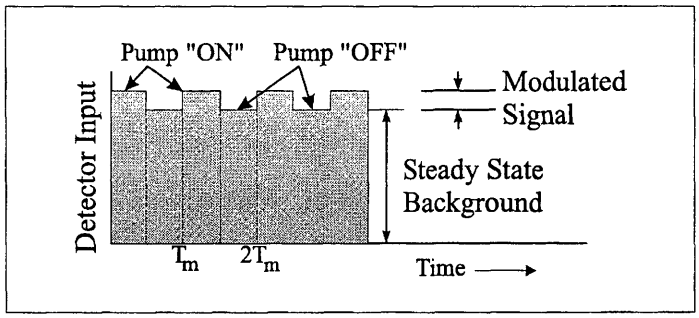

FIG. I.1. General probe intensity along a time axis

results from a change in a sample's absorptivity. Since both beam's, the probe beam and the pump beam, pass throught the same sample volume, the sample's absorptivity is changed by the pump beam, since it passes through the sample volume prior to the probe beam. Therefore, a modulated pump beam will modulate the sample's absorptivity, which, in turn, will modulate the probe beam intensity. The modulation that appears on the probe beam is assumed to contain the same modualtion

characteristics, which include frequency and phase, or waveshape, that were applied directly to the pump beam.

The measurement objective, in a PPAS diagnostic, is modulation depth, α_{mod}. From Figure I.1, modulation depth the ratio of the difference in the probe beam intensity when the pump beam is 'ON' and the probe beam intensity when the pump beam is 'OFF' over the probe beam intensity when the pump beam is 'OFF' (Settersten, 1999). Modulation depth is given in equation I.1. The modulation depth can then be used in spectroscopic calculations to determine physical characteristics, such at molecular number density, temperature, or pressure (Settersten, 1999).

$$\alpha_{mod} = \frac{I_{pr}^{on} - I_{pr}^{off}}{I_{pr}^{off}} \tag{I.1}$$

The detection system must, therefore, take, at the input, the waveform from Figure I.1, and produce, at the output, the modulation depth, α_{mod}. In order to design and develop a detector that will satisfy the detection requirements, a linear mathematical model of the input is developed in this appendix. Specifically, the relationships between the input waveform, from Figure I.1, the waveform's frequency components, and the modulation depth calculation, in equation I.1, are developed.

I.1.1 Waveform Definition

First, the waveform shown in Figure I.1 is defined in more general terms that simplify the equations that are developed. The intensity of the probe beam when the pump is 'ON' is defined as d. The intensity of the probe beam when the pump is 'OFF' is defined as c. Figure I.2 illustrates the variable relationships.

The waveform in Figure I.2 represents a general input to the detection system.

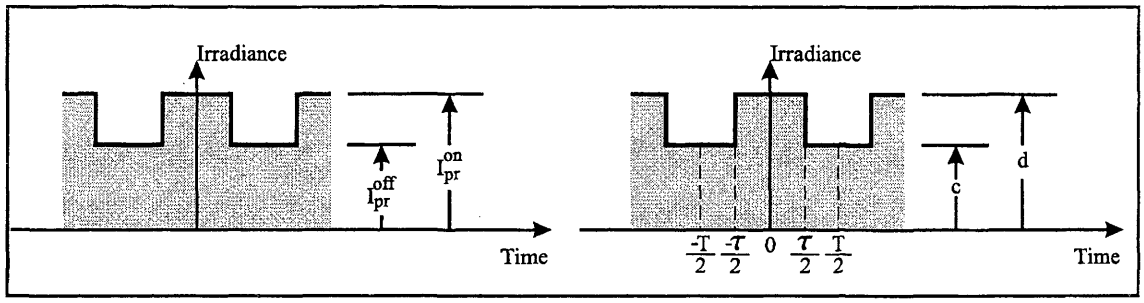

FIG. I.2. General detection system input waveform

The desired output, modulation depth, can now be defined in terms of c and d.

$$\alpha_{mod} = \frac{I_{pr}^{on} - I_{pr}^{off}}{I_{pr}^{off}} = \frac{d-c}{c} \tag{I.2}$$

I.1.2 Fourier Series Representation

Next, we investigate the waveform's harmonic content, which will prove useful in extracting the modulation depth from the detected waveform. In other words, the values of the harmonic components will provide insight to the desired irradiance values c and d.

Since the input waveform has periodic characteristics, the waveform can be written as a Fourier series. In general, the Fourier series for a function $v(t)$ is,

$$v(t) = \sum_{n=-\infty}^{\infty} V_n e^{j2\pi n \frac{t}{T_o}} \tag{I.3}$$

The Fourier series coefficients, or spectral amplitudes, are found by integrating the function, $v(t)$, multiplied by the complex conjugate, over one period, and then divid-

ing by that period.

$$V_n = \frac{1}{T_o}\int_{\frac{-T_o}{2}}^{\frac{T_o}{2}} v(t)e^{-j2\pi f_s nt}dt \tag{I.4}$$

A periodic signal is comprised of discrete harmonic components, that when summed together, produce the periodic signal. If a signal is expressed in time by the general Fourier series representation in equation I.3, then it's amplitude spectrum is expressed by equation I.5.

$$V(f) = \sum_{n=-\infty}^{\infty} V_n\ \delta(f - nf_o) \tag{I.5}$$

The waveform in Figure I.2 is defined as the time varying function $v(t)$. The spectral amplitudes are found by integrating $v(t)$ over one period from $-T_m/2$ to $T_m/2$. The value T_m is the modulation period, and, thus, the modulation frequency, f_m, is the inverse of the period. The value τ_m is the width of the pulse and, therefore, defines the duty cycle, which is τ_m/T_m.

$$V_n = \frac{1}{T_m}\left[\int_{\frac{-T_m}{2}}^{\frac{-\tau_m}{2}} (c)e^{-j2\pi f_m nt}dt + \int_{\frac{-\tau_m}{2}}^{\frac{\tau_m}{2}} (d)e^{-j2\pi f_m nt}dt + \int_{\frac{\tau_m}{2}}^{\frac{T_m}{2}} (c)e^{-j2\pi f_m nt}dt\right] \tag{I.6}$$

The spectral components, V_n, are equal to the sum of the three integrals defined above, which as a whole equate to one period. Each intergral can be evaluated serperately and then summed with the results from the other integrals, in order to find the spectral components. Evaluating the first integral, defining its result as V_n^1, over the time $-T_m/2 \leq t < -\tau/2$, gives,

$$V_n^1 = \frac{1}{T_m}\int_{\frac{-T_m}{2}}^{\frac{-\tau_m}{2}} (c)e^{-j2\pi f_m nt}\,dt \tag{I.7}$$

which is,

$$
\begin{aligned}
V_n^1 &= \frac{-c}{j2\pi f_m n T_m}\left[e^{j\pi f_m n \tau_m} - e^{j\pi f_m n T_m}\right] \\
V_n^1 &= \frac{c}{j2\pi f_m n T_m}\left[e^{j\pi f_m n T_m} - e^{j\pi f_m n \tau_m}\right] \ .
\end{aligned} \tag{I.8}
$$

Evaluating the third integral, defining its result as V_n^3, over the time $\tau_m/2 \leq t < T_m/2$, gives,

$$
V_n^3 = \frac{1}{T_m}\int_{\frac{\tau_m}{2}}^{\frac{T_m}{2}} (c)e^{-j2\pi f_m n t}\, dt \tag{I.9}
$$

which is,

$$
\begin{aligned}
V_n^3 &= \frac{-c}{j2\pi f_m n T_m}\left[e^{-j\pi f_m n T_m} - e^{-j\pi f_m n \tau_m}\right] \\
V_n^3 &= \frac{c}{j2\pi f_m n T_m}\left[e^{-j\pi f_m n \tau_m} - e^{-j\pi f_m n T_m}\right] \ .
\end{aligned} \tag{I.10}
$$

Combining equations I.8 and I.10, which is now defined as $V_N^{1,3}$, results in,

$$
\begin{aligned}
V_n^{1,3} &= \frac{c}{j2\pi f_m n T_m}\left[\left(e^{j\pi f_m n T_m} - e^{-j\pi f_m n T_m}\right) - \left(e^{j\pi f_m n \tau_m} - e^{-j\pi f_m n \tau_m}\right)\right] \\
V_n^{1,3} &= \frac{c}{\pi f_m n T_m}\left[\left(\frac{e^{j\pi f_m n T_m} - e^{-j\pi f_m n T_m}}{2j}\right) - \left(\frac{e^{j\pi f_m n \tau_m} - e^{-j\pi f_m n \tau_m}}{2j}\right)\right]
\end{aligned} \tag{I.11}
$$

which can be simplified to,

$$
V_n^{1,3} = cSa(\pi n) - \frac{\tau_m c}{T_m} Sa\left(\pi n \tau_m f_m\right) \ , \tag{I.12}
$$

where $Sa(\bullet)$ is the sampling function, defined as $sin(x)/x$. Returning to the original equation and evaluating the second integral, defining its result as V_n^2, over the time

$-\tau/2 \leq t < \tau/2$, gives,

$$V_n^2 = \frac{1}{T_m}\int_{\frac{-\tau_m}{2}}^{\frac{\tau_m}{2}} (d)e^{-j2\pi f_m n t}\, dt \tag{I.13}$$

which integrates to,

$$\begin{aligned} V_n^2 &= \frac{-d}{j2\pi f_m n T_m}\left[e^{-j\pi f_m n \tau_m} - e^{j\pi f_m n \tau_m}\right] \\ V_n^2 &= \frac{d}{\pi f_m n T_m}\left[\frac{e^{j\pi f_m n \tau_m} - e^{-j\pi f_m n \tau_m}}{2j}\right] \end{aligned} \tag{I.14}$$

Equation I.14 can be simplified to,

$$V_n^2 = \frac{\tau_m d}{T_m} Sa(\pi n \tau_m f_m) \tag{I.15}$$

The harmonic coefficients, V_n, are finally found by summing the results from the three integrals. Summing equations I.12 and I.15 gives,

$$\begin{aligned} V_n &= V_n^1 + V_n^2 + V_n^3 = cSa(\pi n) - \frac{\tau_m c}{T_m} Sa\left(\pi n \tau_m f_m\right) + \frac{\tau_m d}{T_m} Sa(\pi n \tau_m f_m) \\ V_n &= cSa(\pi n) + \frac{\tau_m}{T_m}\left(d - c\right) Sa\left(\pi n \tau_m f_m\right) \end{aligned} \tag{I.16}$$

The waveform in Figure I.2 can now be written as a Fourier series in the time domain and a corresponding summation of spectral amplitudes in the frequency domain.

$$v(t) = \sum_{n\,=\,-\infty}^{\infty} \left[cSa(\pi n) + \psi_m\left(d - c\right) Sa\left(\pi n \psi_m\right)\right] e^{j2\pi n \frac{t}{T_m}} \tag{I.17}$$

$$V(f) = \sum_{n=-\infty}^{\infty} \left[cSa(\pi n) + \psi_m (d-c)\, Sa\,(\pi n \psi_m)\right] \delta(f - nf_m) \tag{I.18}$$

The duty cycle, which is τ_m/T_m or $\tau_m f_m$, is represented by ψ_m in the equations above.

I.1.3 Harmonic Relation To Modulation Depth

The spectal components for the waveform in Figure I.2 are defined in equation I.18 as a function of both c and d. The assumption is now made that it is possible to extract the dc component, V_0, and the fundamental harmonic component, V_1, which is at the modulation frequency, f_m. The spectral components can, for example, be measured using a photondiode and a spectrum analyzer.

Evaluating equation I.18 at $n = 0$ and at $n = 1$ produces the dc component, V_0, and the fundamental component, V_1, respectively.

$$V_0 = c + \psi_m(d-c) \tag{I.19}$$

$$V_1 = \psi_m(d-c)Sa(\pi\psi_m) \tag{I.20}$$

Equation I.19 can be rearranged such that,

$$(d-c) = \frac{V_0 - c}{\psi_m}\,. \tag{I.21}$$

Equation I.20 can also be rearranged such that,

$$(d-c) = \frac{V_1}{\psi_m Sa(\pi\psi_m)}\,. \tag{I.22}$$

Equations I.21 and I.22 can then be set equal to each other, which provides a way to solve for c.

$$\begin{aligned} \frac{V_0 - c}{\psi_m} &= \frac{V_1}{\psi_m Sa(\pi\psi_m)} \\ c &= V_0 - \frac{V_1}{Sa(\pi\psi_m)} \end{aligned} \tag{I.23}$$

Equation I.23 is substituted into equation I.19, which is then used to solve for d.

$$d = \frac{(1-\psi_m)\frac{V_1}{Sa(\pi\psi_m)} + \psi_m V_0}{\psi_m} \tag{I.24}$$

The modulation depth can now be determined from the dc component and the fundamental spectral component, which is at the modulation frequency. A slight change is made in the calculation based on the period definition of the signal in Figure I.2. In this figure, the I_{pr}^{off} is defined as c. If there is 100% absorption in an experiment, then the irradiance of the probe beam when the pump beam is 'OFF' would be zero. In the modulation depth calculation, dividing by zero would indicate that the modulation depth tends toward infinity. The denominator, in the modulation depth calculation, is, therefore, changed to d. In this case,

$$\begin{aligned} \alpha_{mod} &= \frac{d-c}{d} \\ \frac{d-c}{d} &= \frac{\frac{V_1}{\psi_m Sa(\pi\psi_m)}}{\frac{(1-\psi_m)\frac{V_1}{Sa(\pi\psi_m)} + \psi_m V_0}{\psi_m}} \end{aligned}$$

such that

$$\alpha_{mod} = \frac{V_1}{V_0\psi_m Sa(\pi\psi_m) + V_1(1-\psi_m)} \tag{I.25}$$

The modulation depth calculation, based on the dc component and the funda-

mental harmonic component, is dependent the modulation imposed. Whether the modulaiton is a gain term or a loss term, determines which calculation for modulation depth is utilized. If the waveform has a modulated loss, then the modulation depth is,

$$\alpha_{mod_L} = \frac{V_1}{V_0\psi_m Sa(\pi\psi_m) + V_1(1-\psi_m)} \,. \tag{I.26}$$

If, on the other hand, the waveform has an additional modulated gain, then the modulation depth is,

$$\alpha_{mod_G} = \frac{V_1}{V_0\psi_m Sa(\pi\psi_m) - V_1\psi_m} \,. \tag{I.27}$$

An example of modulated loss is a steady light source that is directly modulated with a mechanical chopper or other optical modulator. A mechanical chopper can only eleminate the transmission of light to create a square wave modulation function. Thus, the chopper imposes a loss in the resulting light emitted at the chopper's output.

An example of modulated gain can be taken from pump probe absorption spectroscopy. Under steady state conditions, the probe beam has a mean irradiance value after passing through a sample volume. If a pump beam passes through the sample volume just prior to the probe beam's interaction, the sample volume will have less absorbing capability when the probe beam enters the sample. Thus, the probe beam exits the sample volume with a slightly higher irradiance than its mean irradiance. In this case a gain is seen in the probe beam, which in this case occurs at the modulation that is placed on the pump beam, and the probe beam is, therefore, gain modulated.

Equations I.26 and I.27 are used in modulation depth calculations for a range of

values for c (which is I_{pr}^{off}) and d (which is I_{pr}^{on}). The results are shown in Table I.3. The first and last set of values depict modulated loss and equation I.26 is shown to correctly calculate the modulation depth, while equation I.27 does not. The second and third set of values represent modulated gain and, accordingly, equation I.27 correctly calculates the modulation depth.

I.1.4 Determiniation of Fundamental Harmonic

The magnitude at the fundamental frequency is actually $2|V_1|$, since both the positive and negative frequencies need to be considered. Assuming, however, that the signal is demodulated with a sinusoid, $d(t)$ that varies from +1 to -1.

$$d(t) = cos(2\pi f_d) \tag{I.28}$$

$$D(f) = \frac{1}{2}\delta(f - f_d) + \frac{1}{2}\delta(f + f_d) \tag{I.29}$$

The frequency f_d is assumed to be equal to the modulation frequency f_m. From the spectrum of the demodulation signal, $D(f)$, we see that half of the power is at the positive frequency and half of the power is at the negative frequency. Thus, when we demodulate the waveform $v(t)$ (cosidering only the fundamental harmonic component) we get:

$$V_1 * D(f) = \frac{V_1}{2}(f - 2f_d) + 2\left[\frac{V_1}{2}(0)\right] + \frac{V_1}{2}(f + 2f_d) \tag{I.30}$$

Therefore, only $|V_1|$ is measured after demodulation, eventhough, $2|V_1|$ actually exists at the fundamental spectral component.

Ioff c	Ion d	Modulation Depth	DC Value	Fundamental Harmonic Value	Modulating Loss (depth)	Modulating Gain (depth)
0.000	1.0	100.00%	0.7500	0.225079	**100.000%**	#DIV/0!
0.250	1.0	75.00%	0.8125	0.168809	**75.000%**	300.000%
0.500	1.0	50.00%	0.8750	0.112540	**50.000%**	100.000%
0.750	1.0	25.00%	0.9375	0.056270	**25.000%**	33.333%
0.900	1.0	10.00%	0.9750	0.022508	**10.000%**	11.111%
0.990	1.0	1.00%	0.9975	0.002251	**1.000%**	1.010%
0.999	1.0	0.10%	0.9998	0.000225	**0.100%**	0.100%
0.999	1.0	0.10%	0.9998	0.000225	**0.100%**	0.100%
0.9999	1.0	0.01%	1.0000	0.000023	**0.010%**	0.010%
1.0	1.0001	0.01%	1.0001	0.000023	0.010%	**0.010%**
1.0	1.001	0.10%	1.0008	0.000225	0.100%	**0.100%**
1.0	1.010	1.00%	1.0075	0.002251	0.990%	**1.000%**
1.0	1.100	10.00%	1.0750	0.022508	9.091%	**10.000%**
1.0	1.250	25.00%	1.1875	0.056270	20.000%	**25.000%**
1.0	1.500	50.00%	1.3750	0.112540	33.333%	**50.000%**
1.0	1.750	75.00%	1.5625	0.168809	42.857%	**75.000%**
1.0	2.000	100.00%	1.7500	0.225079	50.000%	**100.000%**
1.0001	1.0	0.01%	1.0001	0.000023	0.010%	**0.010%**
1.001	1.0	0.10%	1.0008	0.000225	0.100%	**0.100%**
1.010	1.0	1.00%	1.0075	0.002251	0.990%	**1.000%**
1.100	1.0	10.00%	1.0750	0.022508	9.091%	**10.000%**
1.250	1.0	25.00%	1.1875	0.056270	20.000%	**25.000%**
1.500	1.0	50.00%	1.3750	0.112540	33.333%	**50.000%**
1.750	1.0	75.00%	1.5625	0.168809	42.857%	**75.000%**
2.000	1.0	100.00%	1.7500	0.225079	50.000%	**100.000%**
1.0	0.000	100.00%	0.7500	0.225079	**100.000%**	#DIV/0!
1.0	0.250	75.00%	0.8125	0.168809	**75.000%**	300.000%
1.0	0.500	50.00%	0.8750	0.112540	**50.000%**	100.000%
1.0	0.750	25.00%	0.9375	0.056270	**25.000%**	33.333%
1.0	0.900	10.00%	0.9750	0.022508	**10.000%**	11.111%
1.0	0.990	1.00%	0.9975	0.002251	**1.000%**	1.010%
1.0	0.999	0.10%	0.9998	0.000225	**0.100%**	0.100%
1.0	0.999	0.10%	0.9998	0.000225	**0.100%**	0.100%
1.0	0.9999	0.01%	1.0000	0.000023	**0.010%**	0.010%

FIG. I.3. Modulation depth calculation using the dc component and the fundamental modulation frequency component

APPENDIX J

INTEGRATION THRESHOLD CIRCUIT DESIGN

J.1 Integration Threshold Circuit

This Appendix provides information about the integration threshold circuit. This circuit is connected to the camera head and controls the voltage applied to the read out gate (ROG) barrier during an exposure. When the system is not acquiring an exposure, the ROG barrier voltage is set to its nominal value.

The circuit obtains power from the camera head. Two 8-bit DACs are used to set and control the ROG barrier voltage. Setting the ROG barrier to a desired level, which is accomplished with the DACs, is discussed in Appendix K. Once the DACs are set, the setting remains the same for all exposures, until a change is made through the software when the system is not acquiring an image.

The voltage from the DACs are amplified through two operational amplifier stages. An analog switch is then used to control the ROG barrier voltage. During an exposure, the analog switch allows the voltage from the DACs to propagate to the camera head. When an exposure is not taking place, the analog switch allows a nominal voltage to propagate to the camera head. Either voltage, after passing through the analog switch, is inverted and amplified with a final op-amp stage.

The analog switch is driven with a simple AND logic gate. A jumper is used to invoke the integration threshold or leave the threshold off, operating the system in its normal configuration. When the threshold is utilized, a logic signal from the camera

head's digital logic (EPLD) controls the analog switch, through the AND gate.

A schematic of the circuit is first presented. Printed circuit board (PCB) layouts for the top and bottom layers follow respectively. Finally, a bill of materials (BOM) is given.

J.2 Circuit Design

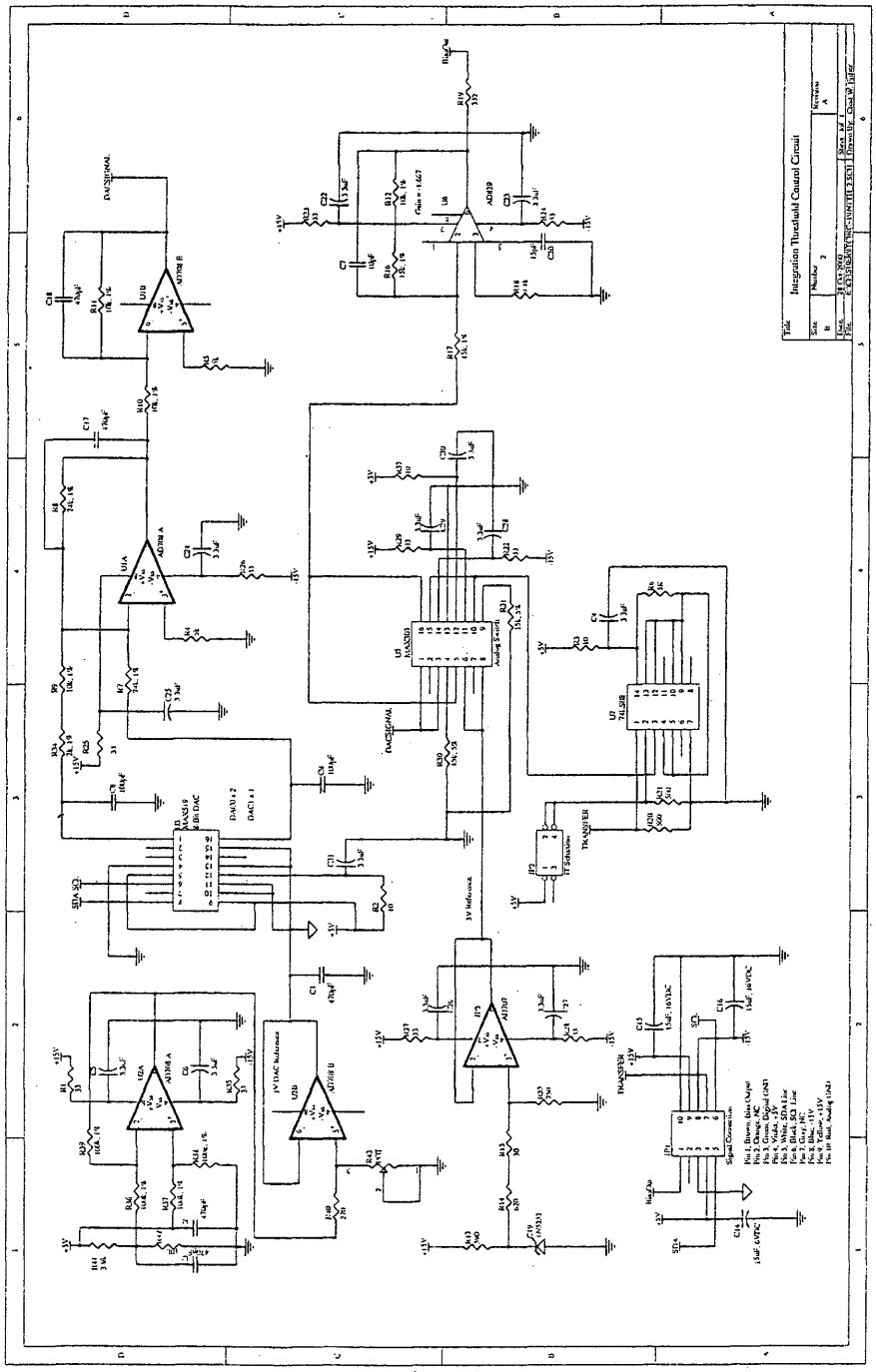

J.3 PCB Layout

J.3.1 Top Layer

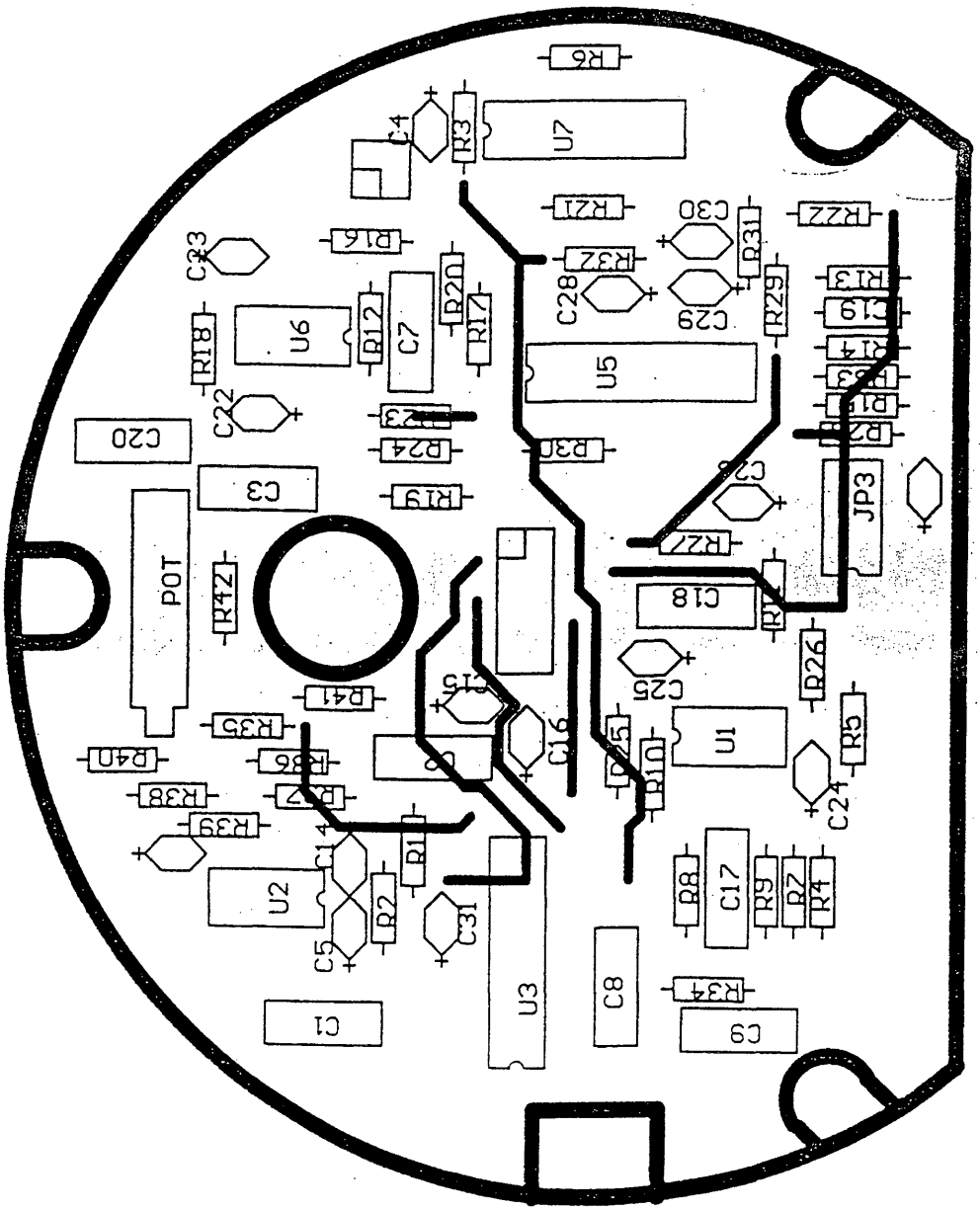

J.3.2 Bottom Layer

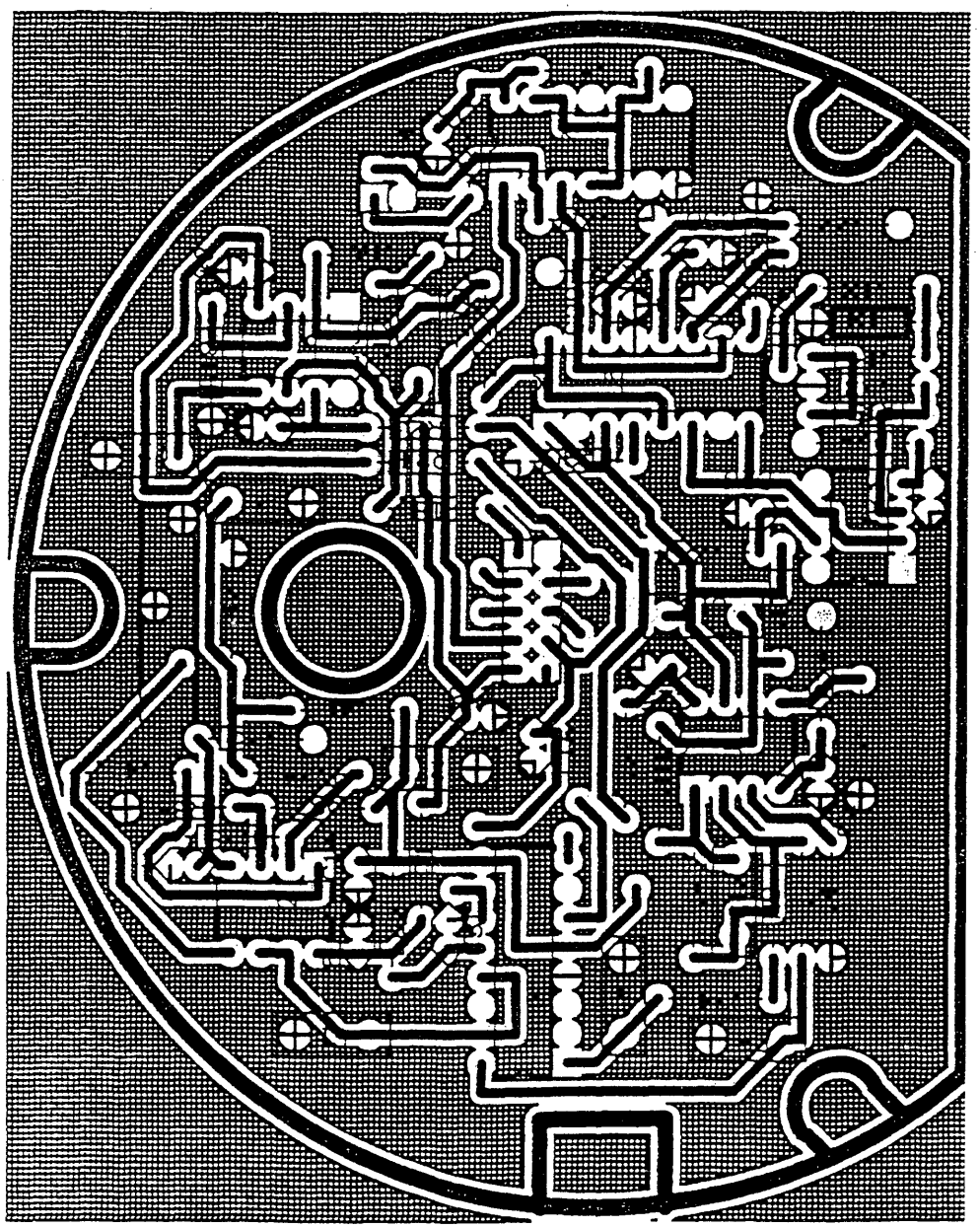

Part Type	Designator	Footprint	Description
1N5232	C19	DIODE0.4	Zener Diode
POT	R43	VR1	Variable Resistor
10	R2	AXIAL0.4	Resistor
10	R3	AXIAL0.4	Resistor
10	R32	AXIAL0.4	Resistor
100k, 1%	R38	AXIAL0.4	Resistor
100k, 1%	R39	AXIAL0.4	Resistor
100k, 1%	R36	AXIAL0.4	Resistor
100k, 1%	R37	AXIAL0.4	Resistor
10k	R42	AXIAL0.4	Resistor
10k, 1%	R10	AXIAL0.4	Resistor
10k, 1%	R11	AXIAL0.4	Resistor
10k, 1%	R9	AXIAL0.4	Resistor
10k, 1%	R12	AXIAL0.4	Resistor
15k, 1%	R16	AXIAL0.4	Resistor
15k, 1%	R17	AXIAL0.4	Resistor
15k, 5%	R31	AXIAL0.4	Resistor
15k, 5%	R30	AXIAL0.4	Resistor
24k, 1%	R8	AXIAL0.4	Resistor
24k, 1%	R7	AXIAL0.4	Resistor
270	R40	AXIAL0.4	Resistor
2k, 1%	R34	AXIAL0.4	Resistor
3.9k	R41	AXIAL0.4	Resistor
30	R15	AXIAL0.4	Resistor
33	R35	AXIAL0.4	Resistor
33	R1	AXIAL0.4	Resistor
33	R29	AXIAL0.4	Resistor
33	R24	AXIAL0.4	Resistor
33	R23	AXIAL0.4	Resistor
33	R22	AXIAL0.4	Resistor
33	R25	AXIAL0.4	Resistor
33	R28	AXIAL0.4	Resistor
33	R27	AXIAL0.4	Resistor
33	R26	AXIAL0.4	Resistor
332	R19	AXIAL0.4	Resistor
390	R13	AXIAL0.4	Resistor
500	R20	AXIAL0.4	Resistor
500	R21	AXIAL0.4	Resistor
5k	R5	AXIAL0.4	Resistor
5K	R6	AXIAL0.4	Resistor
5k	R4	AXIAL0.4	Resistor
620	R14	AXIAL0.4	Resistor
750	R33	AXIAL0.4	Resistor
9.1k	R18	AXIAL0.4	Resistor
IT Selection	JP2	IDC4	Jumper
100pF	C8	RAD0.26	Capacitor
100pF	C9	RAD0.26	Capacitor
10pF	C7	RAD0.26	Capacitor

FIG. J.1. Bill of materials (BOM)

Part Type	Designator	Footprint	Description
15pF	C20	RAD0.26	Capacitor
15uF, 16VDC	C16	RB0.1	Capacitor
15uF, 16VDC	C15	RB0.1	Capacitor
15uF, 6VDC	C14	RB0.1	Capacitor
3.3uF	C23	RB0.1	Capacitor
3.3uF	C22	RB0.1	Capacitor
3.3uF	C30	RB0.1	Capacitor
3.3uF	C29	RB0.1	Capacitor
3.3uF	C25	RB0.1	Capacitor
3.3uF	C24	RB0.1	Capacitor
3.3uF	C28	RB0.1	Capacitor
3.3uF	C31	RB0.1	Capacitor
3.3uF	C26	RB0.1	Capacitor
3.3uF	C4	RB0.1	Capacitor
3.3uF	C5	RB0.1	Capacitor
3.3uF	C27	RB0.1	Capacitor
3.3uF	C6	RB0.1	Capacitor
470pF	C2	RAD0.26	Capacitor
470pF	C18	RAD0.26	Capacitor
470pF	C1	RAD0.26	Capacitor
470pF	C3	RAD0.26	Capacitor
470pF	C17	RAD0.26	Capacitor
74LS08	U7	DIP14	AND Gate
AD707	JP3	DIP8	Analog Devices Op Amp
AD708	U1	DIP8	Analog Devices Op Amp
AD708	U2	DIP8	Analog Devices Op Amp
AD829	U6	DIP8	Analog Devices High Speed Op Amp
Signal Connection	JP1	IDC10	Input/Output Connection Block
MAX519	U3	DIP16	Maxim I2C 8-bit DAC
MAX303	U5	DIP16	Maxim Analog Switch

FIG. J.2. Bill of materials (BOM)

APPENDIX K

DIAGNOSTIC IMAGING SYSTEM USER MANUAL

K.1 Application Manual

In order to use the application specific features, proper settings need to be made in software. Settings for both the integration dead-band threshold and the number of integrated exposures are entered in the WinView/32 software interface. WinView/32 is developed by Roper Scientific, Inc., (Princeton Instruments) and distributed with their scientific imaging systems (Roper Scientific, 1998b).

This appendix provides instructions for configuring the level of the dead-band threshold and the number of integrated exposures. Only the two application specific features are discussed in this appendix. Information on conventional settings, such as exposure time, region of interest, timing mode, can be found in the WinView/32 User's Manual from Roper Scientific (Roper Scientific, 1998b). In order to use the application specific features, the system must be set in the 'Ext Sync' (external synchronous) timing mode. This mode is set under the 'Experiment Setup' control panel, which is under the 'Acquisition' menu.

Both application specific features are configured in control panels under the 'Diagnostics' menu. As shown in Figure K.1, the 'Diagnostics' menu is found under the main 'Setup' menu.

The exposure time resolution is first configured. Under 'Diagnostics', as shown in Figure K.1, selected the 'Get/Set Parameter' control panel. This control panel

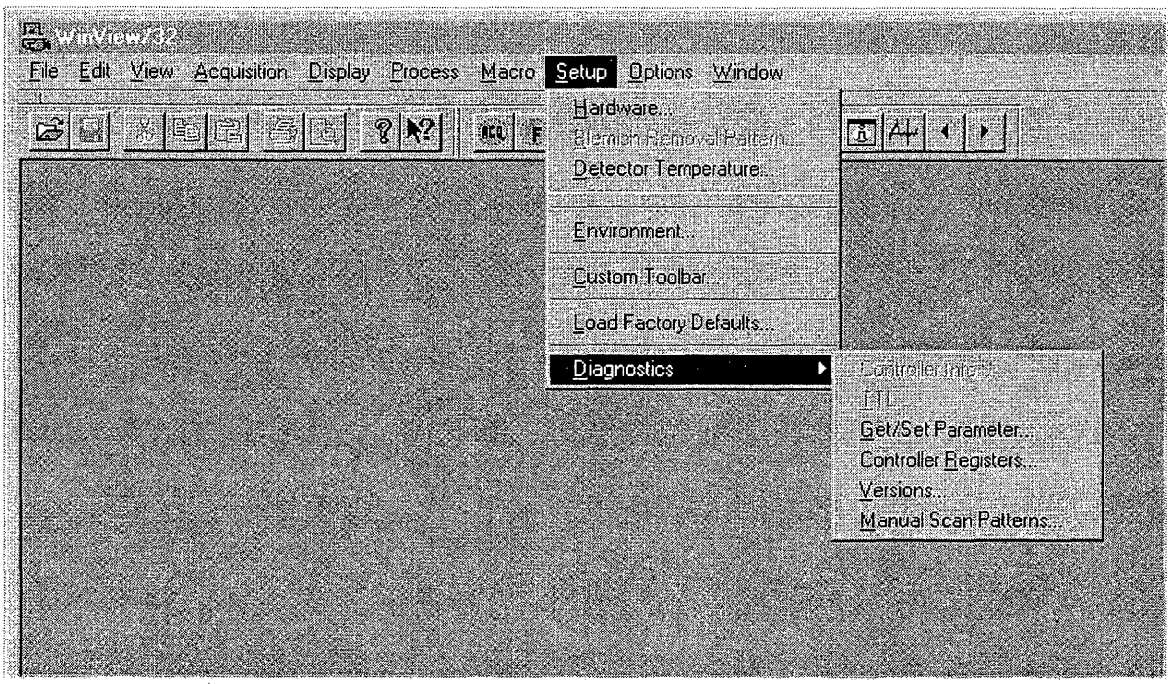

FIG. K.1. WinView/32 menu for application specific settings

looks like the one shown in Figure K.2. The parameter ID for setting the exposure time resolution is 75, which should be entered in the appropriate space. Entering a parameter value of '0' will configure the system with 1ms exposure time resolution. Entering a parameter value of '1' will configure the system with 1μ exposure time resolution. Enter the desired parameter value and then press the 'SET' button. Leave this control panel open; it will be used to set the integration threshold as well.

Once the exposure time resolution is configured, the appropriate resolution will appear in the 'Experiment Setup' control panel, which is under the 'Acquisition' menu.

The same 'Get/Set Parameters' control panel is used to configure the dead-band threshold. The dead-band threshold is raised by lowering the voltage applied to the read out gate (ROG) barrier. The ROG barrier voltage is controlled with the digital-to-analog converter (DAC) presented in Appendix J.

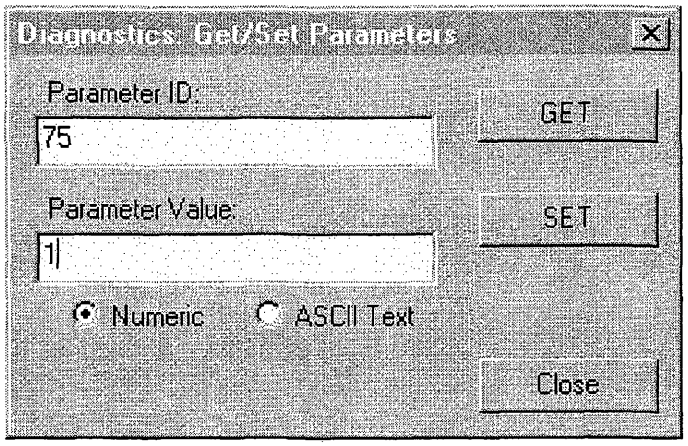

FIG. K.2. Exposure time resolution setting

The two 8-bit DACs are set through the 'Get/Set Parameters' control panel. DAC0 has a parameter ID of 231 and DAC1 has a parameter ID of 232. Since they are both 8-bit DACs, any integer value from 0 to 255 may be entered as a parameter value. Figure K.3 shows an entry that will set DAC0 to its maximum value. Once a parameter ID and a parameter value are entered, press the 'SET' button.

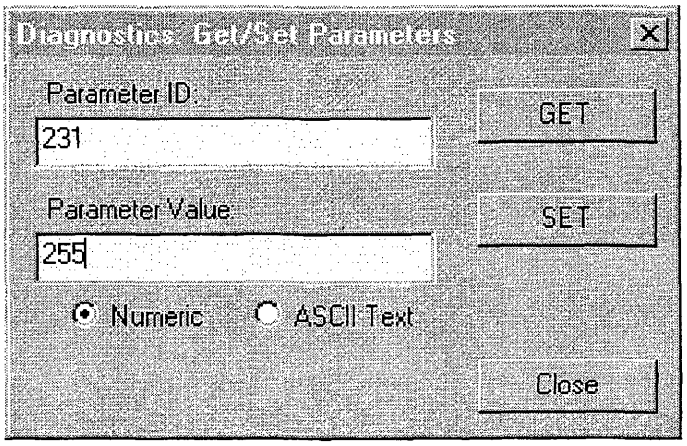

FIG. K.3. Integration dead-band threshold setting

The ROG barrier is set as a percentage of its maximum value. Figure K.4

provides the parameter values that should be entered for both DAC0 and DAC1 to configure the ROG barrier.

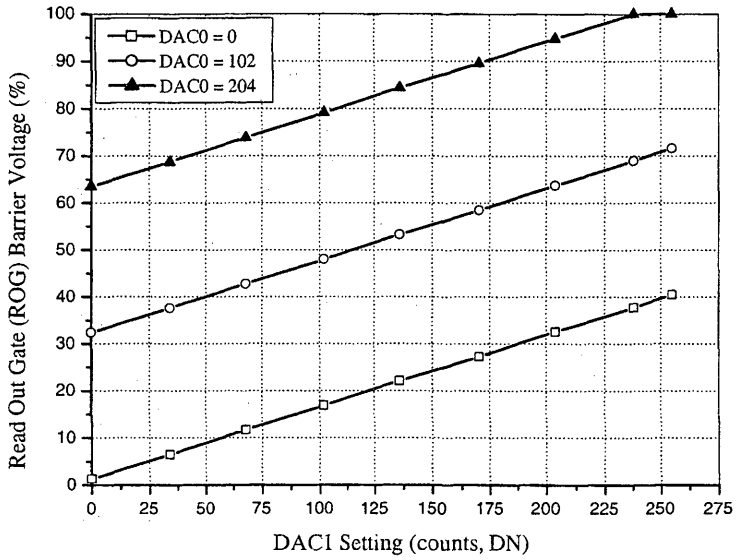

FIG. K.4. ROG barrier voltage as a function of digital-to-analog converter settings (DAC)

The number of integrated exposures is set in the 'Controller Registers' control panel, which is shown in Figure K.5. This control panel is also found under the 'Diagnostics' menu, which is under the main 'Setup' menu, as shown in Figure K.1. Once the 'Controller Registers' panel is open, set the hexadecimal mode. Then enter '3E' in the 'Register' dialog box. This register in the controller's digital logic sets the exposure integration counter.

The '3E' register is a 16-bit register. Only 13 of the 16 bits are used in this configuration. Four hexadecimal values are entered into the 'Register Value' dialog box. The first hex value is either '0' or '1'. This hex value corresponds to the exposure time resolution. If ms resolution is set, enter '0' in the first hex value, or enter '1' , if

μs resolution is set.

The number of integrated exposures is set with the last three hex values (12-bit). The minimum number of integrated exposures is 1, set as 'x001', where 'x' is either '0' or '1' depending on the exposure time resolution. The maximum number of integrated exposures is 4095, set as 'xFFF'. Any number in the range 1-4095 is set according to its hex value. Figure K.5 illustrates a setting of 100 integrated exposures. Once the desired number is entered in the 'Register Value' dialog box, press the 'REG. WRITE' button.

Leave this control panel open. The number of integrated exposures can be changed any time the system is not acquiring images.

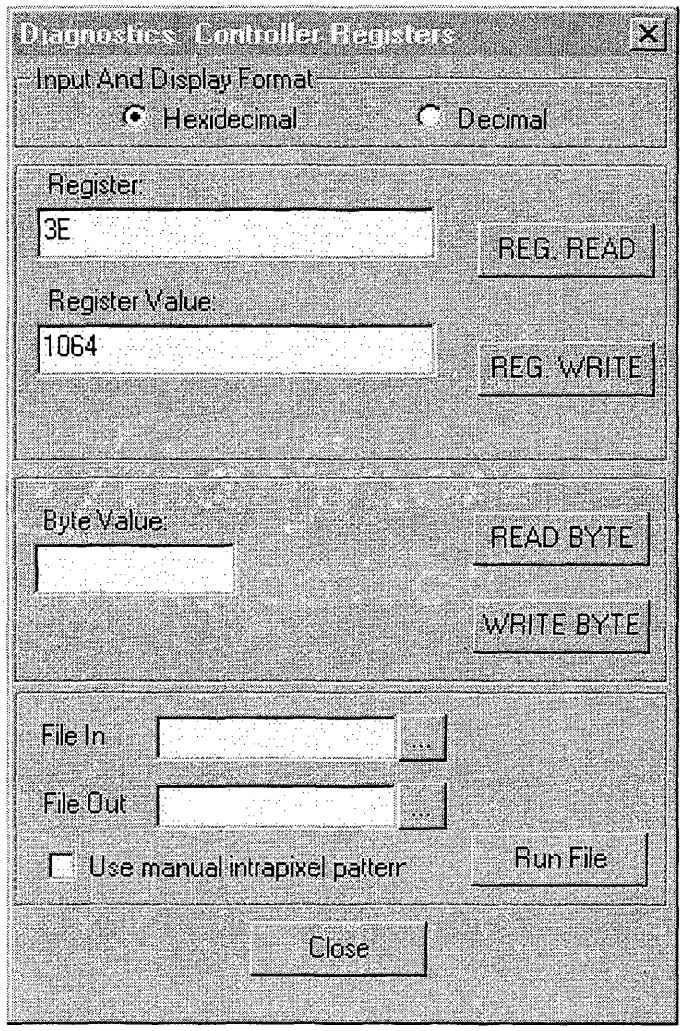

FIG. K.5. Setting the number of integrated exposures

351033